Attenuation of Turbulent Boundary Layer Induced Interior Noise Using Integrated Smart Foam Elements

by

John Patrick D'Angelo

Dissertation submitted to the faculty of Virginia Polytechnic Institute and State University in partial fulfillment of the requirements for the degree of

Doctor of Philosophy
in
Mechanical Engineerng

Approved:
Chris R. Fuller, Chair
Ricardo A. Burdisso
Marty E. Johnson
Jamie Carneal
William T. Baumann

August 30, 2004
Blacksburg, Virginia

Keywords: Active Noise Control, Aircraft, Interior Noise, Near Field Sensing, Spatial Sensing, Turbulent Boundary Layer

Attenuation of Turbulent Boundary Layer Induced Interior Noise Using Integrated Smart Foam Elements

John P. D'Angelo
Committee Chair: C. R. Fuller

Abstract

Research presented herein involved the use of a smart skin treatment used for the attenuation of turbulent boundary layer induced interior noise. The treatment consisted of several Smart Foam actuators each having a reference and error sensor along with a feed forward, filtered–x controller.

Studies were performed to determine if the use of multiple instances of single input, single output (SISO) control systems could be implemented with success given the difficulty of actively suppressing turbulent boundary layer induced interior noise. Further, this research will lead to the development of an integrated Smart Foam element consisting of a Smart Foam actuator, reference sensor, error sensor and SISO controller in one complete, stand–alone unit.

Several topics were studied during this effort: reference sensing, error sensing, actuator design, controller causality, correlation of turbulent flow and resulting plate vibration, and coherence between plate vibration and the interior noise field. Each study was performed with the goal of improving the performance of active attenuation of turbulent boundary layer induced interior noise.

Depending on the configuration of the control system, control was performed using either experiments or simulations based on experimental data. Within the desired control band of 400–800 Hz, attenuation of up to -3.1 dB_A was achieved at the error sensors and up to -1.4 dB_A within the observer plane relative to the uncontrolled case. However, over a band of greater coherence from 480–750 Hz, attenuation of up to -4.8 dB_A was achieved at the error sensors and up to -2.6 dB_A within the observer plane. Further, peak attenuation of up to -12 dB_A was achieved within the observer plane.

Studies were also conducted to increase the low frequency performance of the Smart Foam treatment. These experiments used tuning masses placed on the tops of the integrated Smart Foam elements to tune them to the fundamental mode of the vibrating plate. This treatment was used to reactively attenuate plate vibration such that the radiated acoustic field would be minimized. These experiments resulted in -6 dB_A global attenuation at the plate fundamental resonance. Further, it was shown that the reactive treatment did not inhibit active control.

For my parents.

Acknowledgements

The author would like to acknowledge NASA—Langley Research Center for sponsoring this research project and those at The Boeing Company who have contributed to research related to this effort. In addition, the author would like to thank his advisor, and committee members for their time contributed during preliminary and final examinations. In addition, I would like to offer my sincere appreciation to Mr. Chris Park for offering me the use his control simulation code, *lmsfilterx*.

I could never have gotten through this "odyssey" of sorts without the good friends I have met while in Blacksburg. To Greg, Barry, Steve, Zachary and the rest of the crew best of luck and keep in touch.

Although far from campus, my parents and sister deserve much recognition. Their encouragement and unconditional love has been instrumental in all of my accomplishments and neither has ever been, nor will ever be, taken for granted.

I owe my parents a sincere debt of gratitude; I recognize the sacrifices which they made to better my opportunities throughout life. My mother's efforts have molded me into the person that I am. I realize that without her guidance and encouragement I would never have finished my Freshman year in college, much less my doctorate. Thank you Mom.

I recognize my father for preparing me for life itself. He has been not only a guiding hand and a role model, but also a great inspiration. My father has taught me the meaning of *work* and *honor* and *pride* not through his words but through his efforts and his resulting accomplishments. He has shown me that with much hard work and determination, and perhaps even a pinch of good luck, you may accomplish any goal you aim for. Thank you Dad.

The invariable mark of wisdom
is to see the miraculous in the common.

–Ralph Waldo Emerson

Contents

List of Figures

List of Tables

Chapter 1

Introduction

The fascination of sound has undoubtedly intrigued man since the first time he banged a stick against a hollowed–out tree trunk. According to Lindsay [1], however, the first person to *study* the origin of musical sounds was the Greek philosopher Pythagoras while working at his school in Crotone, Italy in the 6th century B.C. The legend states that Pythagoras was fascinated by the fact that when strings of varying length, fixed at both ends, were plucked they each emitted different tones. He discovered that strings of shorter length emit a higher pitch. Further, a string twice the length of another produced a tone being one octave lower than the shorter one.

Over the past twenty–five hundred years since Pythagoras acted upon his curiosity, the fascination of acoustics has evolved into a science capable of not only reproducing but also modifying the sounds around us. Aircraft interiors, for instance, have several noise sources. These sources may be engine intake and exhaust, movement of mechanical devices such as control surfaces and landing gear, and the turbulent flow over the fuselage.

Interior noise in aircraft has always been a concern for aircraft designs due to it's ability to fatigue passengers and crew as well as inhibit their comfort. In addition, excessive turbulent boundary layer induced noise and vibration may also induce structural wear.

Exterior noise reduction has focussed on jet aircraft since the 1960's while interior noise research has been given more attention to turbo–prop craft. Recently, though, there has been increased interest in interior noise generated by turbulent boundary layers. For this thesis, an active control approach was used to reduce interior noise due to a turbulent flow.

The problem statement and the approach used are defined in the following section. Following the problem statement are several sections presenting surveys of previous research and the theory of the feed forward control algorithm used for this research. The surveys of the previous research efforts are of passive noise control, reactive noise control using distributed vibration absorbers, active noise control, control specific to TBL induced interior noise, and a survey of previous research performed using Smart Foam. The chapter concludes with objectives and contributions made by this research effort along with an outline of the thesis structure.

1.1 Problem Statement

This research effort focuses on the latter source of noise—that induced by turbulent boundary layers (TBLs). TBL induced noise is a broadband disturbance. Further, it is both spatially and temporally random. For commercial aircraft, TBL noise is considered to be both a nuisance and a detriment, being a cause of fatigue and discomfort which may lead to loss of concentration [2]. The troublesome interior noise frequencies usually occur from 100 Hz to 1000 Hz, peaking in magnitude around 400 Hz [3] and being upwards of 80–90 dB [4]. To date, commercial aircraft have resorted to simple, passive methods to deal with interior noise. Only the SAAB 340B and SAAB 2000 commuter aircraft use active control to deal with propeller noise, and no aircraft use active systems to deal with random noise induced by turbulent flow.

Figure 1.1 presents an aircraft fuselage subjected to a turbulent boundary layer flow. The figure shows the cross section of an aircraft fuselage with the flow normal to the page. This turbulent boundary layer flow is shown to induce vibration in the plate. Plate vibration then radiates acoustic energy into the interior noise field.

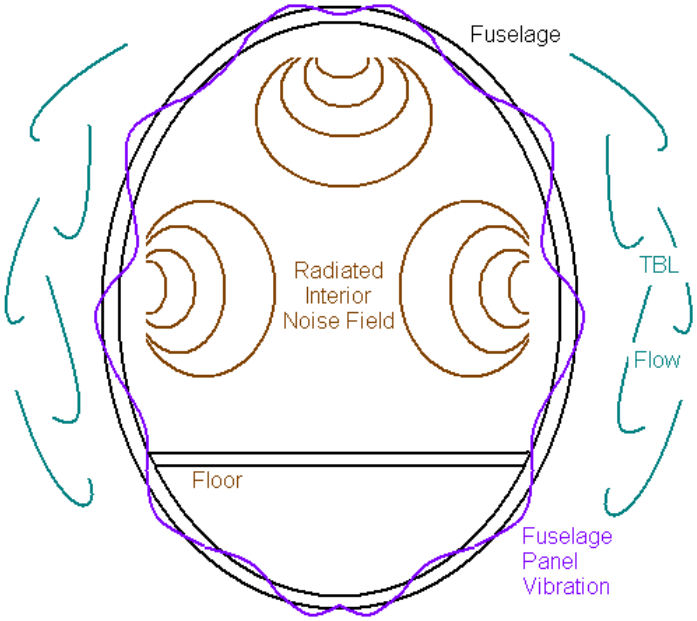

Figure 1.1: Problem statement–Turbulent boundary layer induced interior noise of an aircraft. Note, the flow is normal to the page.

The above problem was reproduced using a wind tunnel having a small, flat, flexible aluminum plate mounted in a side wall of the duct to represent the fuselage panel of an aircraft. When subjected to a turbulent boundary layer flow the plate radiated into the anechoic box where noise control was performed. This configuration is shown in Figure 1.2.

The turbulent flow within the duct perturbs the plate which then radiates into the anechoic enclosure similar to the process observed of an aircraft in flight. Smart Foam elements, used as the secondary noise sources, are mounted directly to the vibrating plate. Plate vibration is measured by transducers (accelerometers or PVDF sheets) located under each Smart Foam element. Microphone arrays, used to obtain error signals, were located 75 mm from the tops of the Smart Foam elements. Performance within the anechoic enclosure was monitored using several observer microphones placed in a plane as shown well above the microphone arrays. Note that observer microphones were not used in the control process and simply monitored global performance.

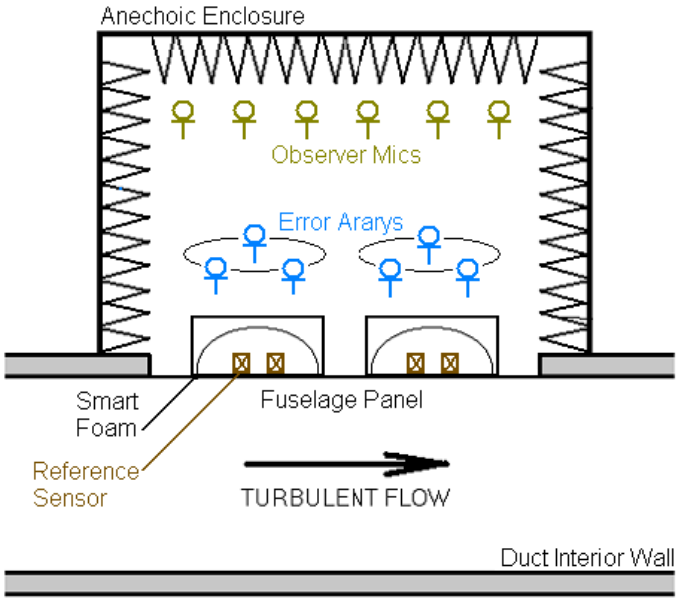

Figure 1.2: General approach to TBL induced interior noise control.

Research has been performed on many noise reduction techniques for various noise problems. Both passive and active methods have been investigated by numerous researchers as well as hybrid active/passive noise reduction systems. Below is presented a brief summary of some of these methods for a variety of problems. Of particular interest to this effort, a survey of research performed on the attenuation of TBL-induced interior noise is presented in the section entitled **Previous Developments in the Attenuation of TBL-Induced Interior Noise**.

1.2 Passive Noise Control

Passive noise control involves the reduction of noise levels without injecting energy into the system. Therefore, passive control techniques are inherently stable. Several means of passive noise control have been studied and used in commercial applications. Works presented here include blanket treatments and damping layers.

Acoustic Blankets

Acoustic blankets may be placed over a surface adjacent to a noise field. The presence of the blankets reduces the noise field by absorption. And, if the blanket is placed on the radiating structure, the added benefit of structural damping is present. At frequencies below the first panel resonance, the transmission loss is governed by the stiffness. Above this resonance, but below the coincidence region, the transmission loss is accounted for by the mass law where an increase in transmission loss of 6 dB per octave occurs. Within the coincidence region, damping is the primary mechanism for transmission loss.[5]

Several studies have been conducted on the use of acoustic blankets in rocket payload fairings to absorb sound energy and increase transmission loss during ascent [6, 7, 8]. Long et al [8] used various configurations of blankets in a Delta IV payload fairing to study how effective blankets were in reducing the interior noise field during ascent. This research effort was performed specifically for the launch of the Cassini space craft, therefore, clearance requirements within the payload fairing were well defined. The blankets used a baseline blanket of 3 inches thickness (0.21 lb/ft^2) and two other modified blankets of 5 inch (1.29 lb/ft^2) and 6 inch (0.80 lb/ft^2) thicknesses. Although maximum coverage would theoretically give the best performance, it was not possible to attain full coverage because of the clearance limitations for this application. Therefore, both full and partial coverage configurations were tested with the satellite removed.

The blankets were shown to have varying performance in reducing both fairing vibration and interior noise levels. Fifty percent blanket coverage resulted in a maximum vibration reduction of 7 dB, while full coverage resulted in up to a 10 dB reduction. At frequencies below 200 Hz, the weight of the modified blankets had no effect on vibration reduction with respect to the baseline blanket. However, at 100 Hz, the heavier blanket (5 inches thick) resulted in an additional 1.2 dB attenuation of vibration when compared to the mid–weight blanket (6 inches thick) and 6.5 dB more than the light blanket (3 inches thick). Above 200 Hz, the difference in vibration was reported to be within 1 dB.

Structural damping

Structural vibration may be reduced in order to minimize the sound energy radiating from the structure. Several methods for passive attenuation of structural vibration exist including constrained layer damping, viscous damping, and the transformation of mechanical energy into thermal energy using piezoelectric transducers.

Constrained layer damping is performed by alternating layers of structural and viscoelastic materials. According to Lu, et al [9] the three layer viscoelastic sandwich is "the most weight– and cost–effective method for incorporating a viscoelastic material." The damping mechanism is due to the shear strain within the viscoelastic layer due to the flexural vibration of the structure. This shear strain dissipates energy. Since strain is greatest on resonance, constrained layer damping is very effective for reducing the noise field due to a structure having a high modal participation. For this case, Lu et al presented a method of predicting the resonances and loss factors for a three–layered, viscoelastic sandwich and confirmed their theory with experiments. The first three modes of a three–layer beam were determined to be 37.3 Hz, 81.3 Hz, and 139.8 Hz with modal loss factors of 0.107, 0.201, and 0.278, respectively. Experiments suggested their method was accurate by predicting the first three modes to be 36.5 Hz, 78.6 Hz, and 130.1 Hz with loss factors of 0.098, 0.143, and 0.204, respectively. Unfortunately, no baseline comparison was made for these results.

Another approach to constrained layer damping is to manufacture the laminate as one piece using composite materials having anisotropic stiffness. Nadella and Rao [10] studied this technique and cited that the benefit of using viscoelastic layers in composite materials is that there is a lesser stiffness reduction when compared with conventionally sandwiched constraining layers. In addition, the anisotropic nature of composite material was shown to be, by Mukhopadyay and Kingsbury [11], that "when a composite sandwich plate undergoes flexural deformation, the anisotropic facings will not only deform under normal strain, but also undergo shear deformation in their own planes." Therefore, the damping effect is increased because of the additional shear strain. In [10] it was shown that by varying the composite layup, or orientation of the fibrous layers, and the viscoelastic material, the resonant frequencies and corresponding loss factors could be easily tuned.

Another means of damping modes is to convert vibration (mechanical energy) to heat (thermal energy) by means of piezoelectric patches bonded to the vibrating surfaces. Here, the shear strain induced by the structure deforms the piezoelectric patch. The work required to do this deformation is then converted into an electric charge by the electro–mechanical nature of the piezoelectric material. Then, this charge may be dissipated by connecting an electric circuit across the terminals of the piezoelectric material. Shunting with a resistor makes the piezoelectric patch act much like a viscoelastic material. However, combined with the capacitance of the piezoelectric material, the addition of an inductor and resistor in series makes the circuit act like a damped, tuned mass absorber creating an electrical resonance. Matching an electrical resonance of the piezo circuit to a mechanical resonance of the structure produces an efficient mechanical–to–electrical energy transformation resulting in maximum structural damping for that resonance.

Hagood and Von Flowtow [12] stated that the "high loss factor, high stiffness, and temperature stability [of piezoelectric shunts] makes them an attractive alternative to viscoelastic materials." Experiments were performed on a cantilever beam measuring 29.3 cm by 2.55 cm by 3.17 mm thick. Two shunted, piezoelectric patches, measuring 6.2 cm by 2.55 cm, were bonded on either surface by the beam's root and a second pair of piezoelectric patches, used for the disturbance, were bonded 2.15 cm away. A pseudo–random excitation

was used to excite the beam and the shunting circuit was tuned to the fundamental bending resonance of 33 Hz. Tuning the shunting circuit to the beam resulted in a 35 dB attenuation of the fundamental resonance.

Edberg et al [13] developed a theory for the simultaneous damping of two modes using a single, passive, piezoelectric patch. Hollkamp [14] then compared the theory and confirmed it with experiment. Here, Hollkamp used a single circuit with several piezoelectric patches. These patches were arranged and the circuit was tuned such that the troublesome modes would be effectively damped. The first three modes were at 8.3 Hz, 52.9 Hz, and 149.1 Hz. Since the required inductance for damping the first mode was very high, Hollkamp focussed on damping the second and third modes. For these modes, he achieved peak response reductions of 19 dB and 12 dB, respectively.

1.3 Reactive Control Using Distributed Vibration Absorbers

Smart Foam performance is shown in following chapters to be lacking at low frequencies. In an attempt to increase the low frequency ($\leq$ 200 Hz) performance of the small Smart Foam actuators, a tuning mass layer was used. This uniform mass layer, applied to the top of the actuator, was used to tune the Smart Foam element to have a fundamental bouncing mode equal to that of the plate (1,1) mode. This section presents the theory of how distributed vibration absorbers work and follows with an overview of previously performed research on the topic.

Mechanical impedance for an absorber of this design is shown in equation 1.1 [15].

$$Z_a = j\alpha m_a \omega_r \frac{1 + \frac{j\alpha}{Q}}{1 - \alpha^2 + \frac{j\alpha}{Q}} \tag{1.1}$$

where ω is the drive frequency (radians/second), k_a the stiffness of the absorber, m_a the effective lumped mass of the absorber, and $\alpha = \omega/\omega_r$. The resonant frequency may be expressed as

$$\omega_r = \sqrt{\frac{k_a}{m_a}} \tag{1.2}$$

and

$$Q = \frac{m_a \omega_r}{c_a} \tag{1.3}$$

where c_a is the coefficient of damping of the absorber

Figure 1.3 depicts a vibrating, single degree of freedom (SDOF) base structure with some surface velocity having impedance Z_b and free (no absorber affect) surface velocity, $V_{b,f}$. The development herein is of a lumped, SDOF system being driven at its resonant frequency ($\alpha = 1$).

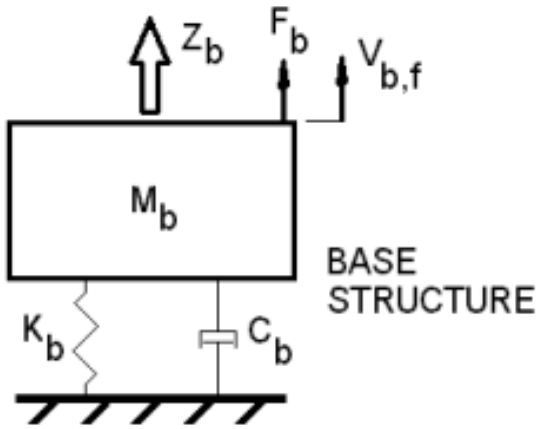

Figure 1.3: Dynamics of Base Structure

Equation 1.4 expresses the relationship between mechanical impedance, Z, velocity, V, and force, F.

$$Z = \frac{F}{V} \tag{1.4}$$

Adding a tuned mass absorber of impedance Z_a to the free structure of impedance Z_b (1.4) gives the force balance as shown in equation 1.5.

$$Z_b V_b = Z_b V_{b,f} - Z_a V_b \tag{1.5}$$

Rearranging equation 1.5 we have

$$\frac{V_b}{V_{b,f}} = \frac{Z_b}{Z_a + Z_b} \tag{1.6}$$

Therefore, by equation 1.6 it is shown that the reduction of the base velocity, V_b, is directly proportional to the mechanical impedance of the tuned mass absorber. Increasing the absorber impedance, Z_a, reduces the structure vibration and so noise radiation is decreased.

Squaring both sides of equation 1.6 is more representative of the attenuating affect since sound pressure level is related to the square of the surface velocity of the radiating structure.

$$SPL = 10 \log_{10} \frac{P_{rms}^2}{P_{ref}^2} \tag{1.7}$$

and

$$P_{rms}^2 = \frac{1}{2} \left(\frac{V}{\rho} \right)^2 \tag{1.8}$$

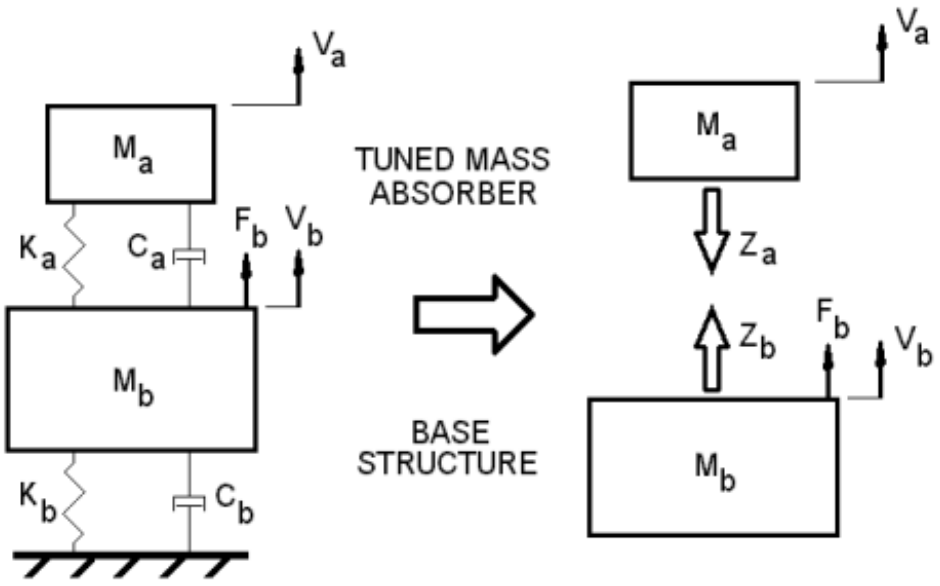

Figure 1.4: Base Structure with Tuned Mass Absorber

where ρ is the density of acoustic medium, c the phase speed within the acoustic medium, and P_{ref} the reference pressure $(2(10)^{-5}$ Pa for all work presented herein). Expressing equation 1.1 for $\alpha = 1$ gives

$$Z_a = m_a \omega_r Q + j m_a \omega_r \tag{1.9}$$

Simplifying the expression in equation 1.9, the mechanical impedance of the absorber may be written as in equation 1.10 [15].

$$Z_a = C_a + j\left(\omega m_a - \frac{k_a}{\omega}\right) \tag{1.10}$$

By equation 1.10, we see that an increase of absorber mass, m_a or a decrease of absorber stiffness, k_a results in a greater absorber impedance, Z_a. Therefore, the rule of thumb for designing an effective absorber would be to use larger absorber mass or softer foam (for example, thicker foam).

Theoretical and experimental development of the passive, distributed vibration absorber (DVA) concept has been performed by several authors including [16] [17] and [18].

In [16], Jolly and Sun use dynamic vibration absorbers, tuned to resonant frequencies of high structural response, placed at anti-nodes of corresponding modes. However, rather than applying the treatment to high vibration response in the hopes of achieving a reduced acoustic radiation, the analysis observed the structural-acoustic interaction. This allows for the development of tuned vibration absorber treatment capable of attenuating structural

modes which are well coupled to the acoustic environment [16]. It was shown that tuning of the DVA's to a critical mode of the radiating panel results in attenuation not only at that frequency but also at lower frequencies. Structure responses at higher frequency resonances benefit from increased damping provided by the TVA's. Although performance was achieved, noise levels did increase over certain bands depending on the application. In addition, it should be noted that no results were stated for performance over the band of application.

Sun, et al [17] applied DVA's to aircraft panels to increase their transmission loss. Their analysis used both Statistical Energy Analysis (SEA) and modal analysis for the development of DVA's and to determine their optimal placement on aircraft panels. Vibration reduction was 30 dB on resonance at the 101 Hz tuning frequency with good agreement between predicted and experimental results on resonance. However, off resonance, these results varied by several dB. In addition, transmission loss at the same frequency was 10 dB. Predicted and experimental results for sound transmission loss were in discrepancy by up to 5 dB off resonance.

Huang and Fuller [18] applied the DVA concept numerically to the vibration of a cylindrical shell and its coupled interior sound field. By means of substructure synthesis and modal expansion, [18] showed that the use of several DVA's, applied and correctly positioned on a cylindrical shell, will both reduce the shell vibration response and the resulting interior noise field. It was shown, for the point force excitation, the best placement of DVA's was to use a single large one near the disturbance location with several smaller DVA's located around it. However, for uniformly distributed perturbations, [18] showed the use of several smaller DVA's achieved better attenuation of interior sound.

The active counterpart to the DVA is the Distributed Active Vibration Absorber (DAVA). This treatment makes use of active control to tune the characteristics of the treatment such that its performance is increased as desired. Several efforts have been conducted on this topic with a brief survey [19] [20] [21] [22] and [23] presented here.

Abè and Igusa [19] developed the theory for a semi–active, distributed vibration absorber for suppressing the impulse vibration response of a structure. Advantages of this approach, compared to the passive DVA treatment, were the ability to alter the damping characteristics of the semi-active treatment and also the initial displacement such that "optimal performance" may be achieved while still maintaining "unconditional stability" [19]. Abè and Igusa determined that "the optimal initial displacement is a monotonically increasing function of damping [19]".

Fuller et al [20] developed a method for optimally tuning vibration absorbers placed on a cylindrical shell such that the radiated noise field would be reduced. Tuning mass was determined based on the modal mass of the structure and was not optimized. This development used an active structural acoustic control (ASAC) approach such that the frequency ratio of vibration absorbers would be optimally tuned. Nagaya and Li [21] referenced [20] stating the determination of tuning masses based on modal analysis of the structure "do not always give optimal values". Nagaya and Li then furthered the work of Fuller et al by also tuning the absorbers to have optimal mass for treatment used to reduce sound radiated from a plate using electromagnetic vibration absorbers. Their effort developed a neural net-

work capable of optimizing the parameters of the vibration absorbers by minimizing the cost function of radiated sound and also showed that optimal tuning required the use of fewer absorbers. For a flat plate, Nagaya and Li achieved by experiment a reduction in sound pressure level of "22.5 dB for the first mode, 18.9 dB for the second mode, 12.6 dB for the third mode, 19.8 dB for the fourth mode, and 18.0 dB for the fifth mode [21]".

Marcotte et al [22] developed theory and demonstrated by experiment the use of DAVA's and the ability to spatially tune them using a varied mass and/or stiffness distribution. Broadband performance in the passive configuration was reported to be up to 13 dB reduction of the mean square velocity of a steel beam over a band of 100–1600 Hz using a mass distribution consisting of small lead plates supported by a curled PVDF layer. The active configuration achieved up to 19 dB for the same beam. Applying this technique to a clamped, flat, aluminum plate using a foam/PVDF layer allowed 15 dB passive attenuation from 20–1600 Hz. Active performance was not reported for this case. In addition, the use of three foam/PVDF DAVA's placed on a flat aluminum plate having free end conditions achieved 10 dB passive attenuation from 5–400 Hz. The weight penalty was reported to be 14%.

Marcotte et al [23] furthered efforts of [22] by using genetic algorithms and the Rayleigh–Ritz method to optimize the design and configuration of the DAVA treatment while using a maximum weight penalty of 10%. It was shown that "a higher loss factor of the DAVA elastic layer leads to better broadband attenuations [23]". "The power dissipated by the DAVA is primarily from the normal stretching of the foam element" and "the shearing of the elastic layer is not a significant source of energy dissipation"[23]. This then allows the DAVA to be used in "any frequency bandwidth, since the DAVA can be tuned to any given frequencies"[23].

1.4 Theory of Feed Forward Control

Active control involves sensing and controlling a variable of interest such that its characteristics may be tailored as desired. For instance, in noise control, the controlled variable may be mean square sound pressure with the intent of minimizing its magnitude.

Control may be implemented using one of two strategies—feed back control or feed forward control. In feed back control, "the error sensor signal is returned back through an amplifier with magnitude and phase response designed to produce cancellation at the sensor. The undesired sound can be reduced through the use of a very high loop gain [2]". The high feed back gain generally results in stability problems since "error in the controller phase response can change the desired negative feed back into unstable positive feed back." Feed forward control, however, is "generally more robust than feed back" particulary when "the feed forward system has a reference input isolated from the secondary source". In feed forward control, "the undesired signal [or reference signal] is sensed [and is used] to generate a signal which produces a secondary noise that is 180^o out of phase with the disturbance, thereby cancelling the unwanted noise.

Active noise control systems may then be categorized into either feed back control or

feed forward control. Feed back control "acts to change the system response by changing the system resonant frequencies and damping. Relatively high gains in the feed back loop are necessary [making] this type of controller prone to instability if any parameters describing the physical system change slightly [5]." Feed forward control, on the other hand, monitors the "disturbance[1] sufficiently far ahead in time for it to be used to generate the required control signal for the control source." These systems generally use the inverse of the measured system model which is then multiplied by the disturbance, or reference, to generate the secondary excitation. The plant model for a practical feed forward system is adaptable such that changes in the plant may be accounted.

The control algorithm may be implemented either in the frequency domain or in the time domain. In the frequency domain, the error path filters are the transfer functions between the actuators and the error sensors. The control filter may then be determined knowing the primary disturbance, the error path filters, and the reference signals. Time domain feed forward control systems require that the coefficients of the control filter be adapted until the correct model is determined. This technique results in a control filter which approximates the ideal control filter and so is an approximation to the frequency domain control system. Therefore, the time domain, feed forward control system has less than optimal performance. However, in most cases, the time domain approach is the only method that may be used for reasons discussed below.

The wiring diagram for the error path of the frequency domain, feed forward, single input, single output (SISO) controller is shown in Figure 1.5 with the corresponding expression for error expressed in equation 1.11.

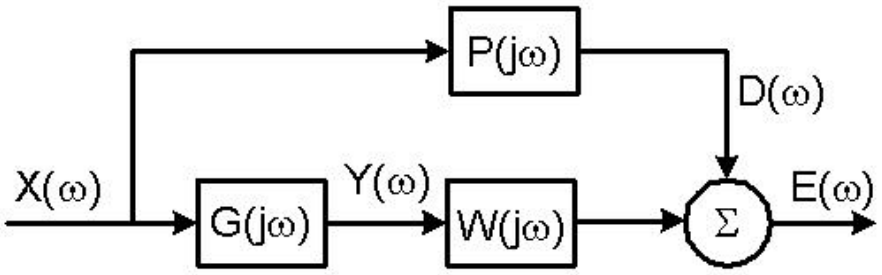

Figure 1.5: Error path for feed forward controller.

$$E(\omega) = D(\omega) + W(j\omega)G(j\omega)X(\omega) \tag{1.11}$$

where P($j\omega$) is the plant or primary path, D(ω) the primary disturbance field, W($j\omega$) the controller, G($j\omega$) the error paths, and X(ω) the reference signal. Note, that linearity is

[1]For this research effort, the disturbance source, or reference, was the TBL–induced panel vibration.

assumed thus making possible the superposition of the primary and secondary fields. The ideal control filter may then be calculated by setting the error signal to zero giving

$$W(j\omega) = -D(\omega)G(j\omega)X(\omega)^{-1} \tag{1.12}$$

leading to complete attenuation of the primary field. However, this depends directly on proper modelling of the plant and the presence of unit coherence between the reference and error (plant or primary path) signals. The coherence between the error and reference signals directly relates to the maximum amount of control. This concept is discussed in Chapter 6—Causality and Multiple Coherence Studies.

In the time domain, the controller must be determined using one of several algorithms capable of determining the filter coefficients in an adaptive manner. Since this is typically performed digitally, the use of the z–transform is required. The z–transform is a mathematical relation used for analyzing linear systems and is the discrete time analogy to the LaPlace transform [24] [25]. Z–transforms are important for the determination of discrete time domain filters used in adaptive control and may be expressed as

$$X(z) = \sum_{n=-\infty}^{\infty} x(n)z^{-n} \tag{1.13}$$

where z is a complex variable and n is an integer denoting the time step. For a sample time, T, the time at which the sample occurred may be expressed as $t = nT$. Note, too, the relation between the z–transform and the LaPlace transform is simply $z = e^{sT}$ and the z–transform of an input sequence, $x(n)$, delayed by one sample, $x(n-1)$ may be expressed as

$$\sum_{n=-\infty}^{\infty} x(n-1)z^{-n} = \sum_{n=-\infty}^{\infty} x(m)z^{-(m+1)} = z^{-1}X(z) \tag{1.14}$$

and, therefore, a delay of one sample is simply z^{-1}. Ratios may be expressed using the z–transform by expressing both the numerator and denominator in terms of z

$$X(z) = \frac{N(z)}{D(z)} \tag{1.15}$$

where the poles and zeros of $X(z)$ are the roots of $D(z)$ and the roots of $N(z)$, respectively. Returning to the time domain from the z domain, is achieved by performing an inverse z–transform using the contour integral [26]

$$x(n) = \frac{1}{2\pi j} \oint \frac{X}{z}(z)z^n \, \mathrm{d}z \tag{1.16}$$

Digital filters are referred to as *causal* if their response is zero for all inputs prior to $x(1)$ and *acausal* should their response be described requiring knowledge of future events [27]. A schematic of a digital filter in Figure 1.6 shows the relation between the input, $x(n)$, the filter, H, and the resulting output, $y(n)$, and is expressed mathematically as

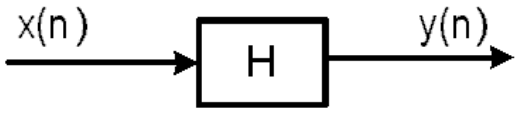

Figure 1.6: Error path for a feed forward controller.

$$y(n) = \sum_{i=0}^{\infty} h_i x(n-i) \tag{1.17}$$

suggesting that the response is affected by all previous values of the input and is stable given a bounded input.

In practice there is only a finite number of coefficients permissible for describing a digital filter, otherwise, an infinite amount of time would be required to determine the conditioned output. Two methods are used to implement the digital filter: the finite impulse response (FIR) filter and the infinite impulse response (IIR) filter. The FIR filter, when subjected to an impulse input, has a finite duration response and may be expressed as

$$y(n) = \sum_{i=0}^{I-1} w_i x(n-i) \tag{1.18}$$

where w_i are the I filter weights or coefficients. This form supposes the response, $y(n)$, depends on the current input, $x(n)$, and therefore the filter must respond instantaneously. Assuming a delay of only one sample, the FIR filter may be expressed as

$$y(n) = \sum_{i=0}^{I} w_i x(n-i) \tag{1.19}$$

More samples of delay result given the presence of other instrumentation such as analog–to–digital and digital–to–analog converters, and anti–aliasing and reconstruction filters. The FIR filter, shown schematically in Figure 1.7, is also referred to as a moving average (MA) filter and as a transversal or non–recursive filter. FIR filters are always stable provided their coefficients are bounded and the resulting response is small given small changes in the values of the coefficients.

Infinite impulse response filters have infinitely long response given an impulse disturbance. Although they typically require fewer coefficients than an FIR filter, the IIR filter, also referred to as a pole–zero, recursive, or autoregressive moving average (ARMA) filter, may be unstable since their poles may exist anywhere in the z–plane. In addition, the IIR is best suited for representing lightly damped systems having clearly defined resonances whereas FIR filters are best used to describe highly damped or spectrally flat systems. Therefore, for this research, the FIR filters are best suited.

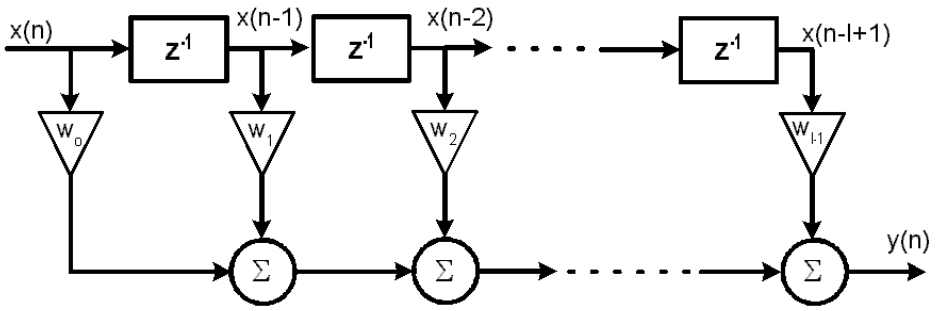

Figure 1.7: The finite impulse response (FIR) filter may be described knowing its filter coefficients and the delay operator, z^{-1}.

The control techniques used the least mean squares (LMS) method (an FIR filter) for determining the control filter coefficients. Implementation in the time domain allows for continually updating the control filters thus allowing sufficient performance for slowly time varying systems, however it does not allow for development of a control filter capable of absolute control. In addition, time domain techniques are also free from the need of generating matrix inverses of large systems—a computationally intensive procedure that is also subject to numerical instabilities if the matrix is ill–conditioned. The block diagram of the time domain representation of the SISO LMS algorithm is shown in Figure 1.8 having an error signal of

$$e(n) = d(n) + \mathbf{w}^T \mathbf{x}(n) \tag{1.20}$$

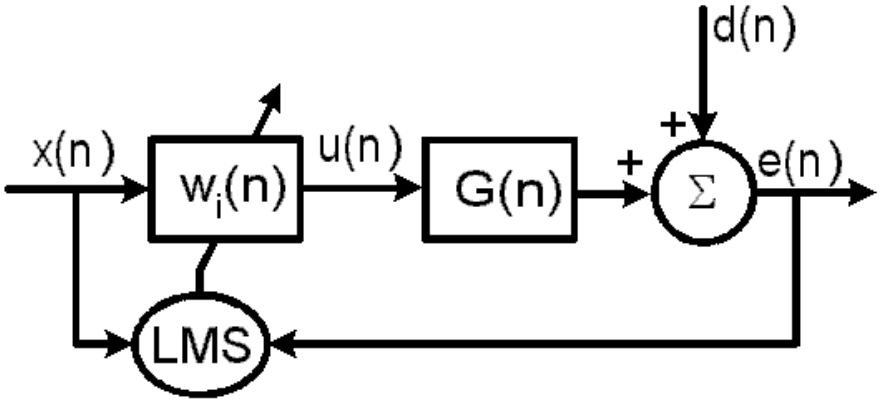

Figure 1.8: Block diagram of the LMS algorithm.

The Least Mean Squares algorithm uses sequential sets of data to adaptively adjust coefficients of the control filters such that the error signals are minimized. With sufficient iterations, the LMS approach will converge to the optimal control filters [25]. In addition, an adaptive filter is capable of adjusting the coefficients to track non–stationary disturbances whose character changes slowly with respect to the convergence time of the adaptive filters. Many adaptive filter algorithms use the *steepest descent* method for converging filter coefficients. Here, the gradient of a cost function is determined and filter coefficients adjusted such that the cost function is minimized. However, successful implementation of the steepest descent method requires that "the expectation value of the product of the error signals with the delayed reference signals would need to be estimated by time averaging over a large segment of data, and so the filter coefficients could be updated rather infrequently." The LMS technique instead uses a *stochastic gradient* technique where an instantaneous estimate of the cost function gradient allows for updating the coefficients with every sample of data. The cost function we choose to minimize is

$$J = e^2(n) \tag{1.21}$$

and the gradient may then be expressed as

$$\frac{\partial e^2(n)}{\partial w} = -2\mathbf{x}(n)e(n) \tag{1.22}$$

the derivative of the instantaneous error with respect to the filter coefficients. The adaptation algorithm is then expressed as

$$w(n+1) = w(n) + \alpha\mathbf{x}(n)e(n) \tag{1.23}$$

where $\alpha = 2\mu$ is the convergence coefficient and μ is referred to as the convergence factor. Note that the product of reference and error signals are used for the adaptation process and is an estimate of the cross–correlation between the measured error and measured reference signals. Quick convergence of the filter is necessary to effectively track and minimize non–stationary disturbances making proper selection of the convergence coefficient, α, crucial. From the reference signals, the autocorrelation matrix may be determined by

$$A = E\left[x(n)x(n)^T\right] \tag{1.24}$$

where $E\,[]$ is *the expectation of* or simply the mean of the term inside the brackets. Assuming A is symmetric, diagonalizing gives

$$A = Q\Lambda Q^T \tag{1.25}$$

giving orthonormal eigenvectors such that $QQ^T = I$ and eigenvalues of $\Lambda = diag\,[\lambda_1, \lambda_2, \ldots, \lambda_I]$.

Knowing the difference, $\epsilon(n)$, between the mean of the filter coefficients and the optimal, or Wiener, filter coefficients, the equation of the mean evolution of the filter coefficients is

$$\epsilon(n+1) = [\mathbf{I} - \alpha\mathbf{A}]\,\epsilon(n) \tag{1.26}$$

which may then be rotated to correspond with the principal axes

$$\mathbf{Q}^T\epsilon(n+1) = [\mathbf{I} - \alpha\Lambda]\,\mathbf{Q}^t\epsilon(n) \tag{1.27}$$

and may be rewritten as

$$\mathbf{v}(n+1) = [\mathbf{I} - \alpha\Lambda]\,\mathbf{v}(n) \tag{1.28}$$

or, for each i

$$v_i(n+1) = (1 - \alpha\lambda_i)\,v_i(n) \tag{1.29}$$

Equation 1.29 represents I independent equations each being a mode of the LMS algorithm. Therefore, the convergence of each mode is independent and depends only on λ_i and the modal error, $v_i\,(n)$, decays to zero provided

$$0 < \alpha < 2/\lambda_i \tag{1.30}$$

Or, to ensure global convergence

$$0 < \alpha < 2/\lambda_{max} \tag{1.31}$$

A popular variation of the LMS algorithm is known as the filtered reference, or filtered–x, LMS algorithm identical to the LMS algorithm with one additional multiplication; the reference signal, $x(n)$, is pre–multiplied by a model of the plant, $\hat{G}(x)$, giving the filtered reference, $r(n)$, prior to being implemented in the LMS adaptation scheme. The filtered–x, LMS algorithm is shown in Figure 1.9 and may be expressed mathematically as

$$e(n) = d(n) + \mathbf{w}^T\mathbf{r}(n) \tag{1.32}$$

where $\mathbf{r}(n)$ is referred to as the filtered reference or filtered–x since x is commonly used to denote the unconditioned reference signal. LMS algorithms "adapt the filter coefficients in the opposite direction of the mean–square error with respect to the coefficients" and so for the filtered–x technique

$$\frac{\partial e^2(n)}{\partial w} = 2e(n)\frac{\partial e(n)}{\partial w} = 2e(n)r(n) \tag{1.33}$$

leading to the filtered–x LMS algorithm

$$w(n+1) = w(n) - \alpha\mathbf{r}(n)e(n) \tag{1.34}$$

Convergence properties are then dependent on the autocorrelation matrix $A = E\left[r(n)r(n)^T\right]$ similarly to equation 1.24. However, since the filtered reference signal is a product of the

actual reference and the plant model, the actual filtered reference must be approximated by $\hat{\mathbf{r}}(n) = \hat{G}(z)x(n)$ giving

$$w(n+1) = w(n) - \alpha\hat{\mathbf{r}}(n)e(n) \tag{1.35}$$

Model adaptation is achieved by "detecting the residual sound field [with the error sensors] after control to provide a signal to the control algorithm which adjusts the weights of the filter."

Unlike with the ordinary LMS algorithm which suffers from a time mismatch between the reference and error signals, the filtered–x LMS algorithm first prefilters the reference signal so that "the measured error signal and the filtered reference signal are aligned in time to give a valid cross–correlation estimate [25]".

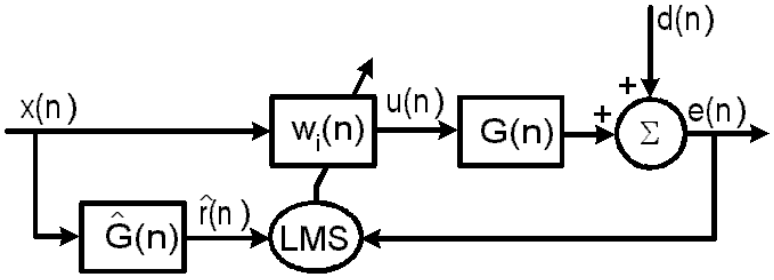

Figure 1.9: Block diagram of the filtered–x LMS algorithm.

Estimation of the plant is necessary for the adaptation process of the filtered–x since the reference signals must first be conditioned by the plant model. The plant model would be a transfer function between the output of each reference sensor to the error sensor response, or in the case of the time domain controller, it would be a filter of a sufficient number of coefficients. Often, a control system may be able to update the plant model on–line, or during control implementation, thus allowing for sufficient performance even for non–stationary systems. According to Elliott [25], the filtered–x LMS control algorithm is stable given a plant model whose phase is within $\pm 40^o$ of the actual plant for a given frequency. The error path may also be determined similarly by measuring the error signal due to a known input to the actuators. For MIMO systems, white noise, filtered over the desired control band, is typically input to one actuator and the resulting secondary error signal measured at each error sensor. The transfer function or filter of sufficient length may then be determined and used in the algorithm.

During control, it is generally possible that the actuators may affect the reference signal. If the effect is significant, the actuator–to–reference feed back must be accounted for in the control algorithm. This transmission path would be modelled similar to modelling the error path by measuring the reference signal due to each independently excited actuator.

Knowing the effect of feed back, it may be modelled as shown in Figure 1.10 which is an extension of Figure 1.9. Mathematically, the feed back path of a SISO controller is modelled

$$\frac{u}{x} = \frac{W}{1 - FW} \tag{1.36}$$

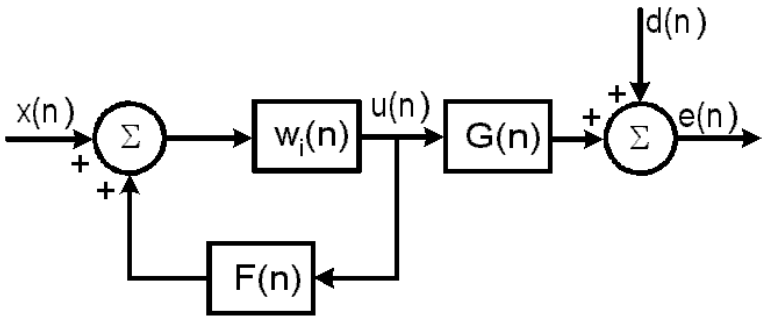

Figure 1.10: Block diagram of feed forward control with actuator–to–reference feed back path.

Large control systems can be computationally intensive and prohibitively complex for practical use. Using many SISO control units may provide similar performance levels while drastically reducing computational overhead and system complexity. Presented here is an analysis of a fully coupled, feed forward, filtered–x, MIMO control system [28] along with a discussion regarding the use of multiple SISO control units.

The schematic of a fully coupled, multiple channel, filtered–x controller may be represented as shown in Figure 1.11 with appropriate block diagram in Figure 1.12. For MIMO control, the error may be expressed in the frequency domain similar to the SISO approach as

$$\mathbf{e}(j\omega) = \mathbf{d}(j\omega) + \mathbf{G}(j\omega)\,\mathbf{u}(j\omega) \tag{1.37}$$

where $\mathbf{d}$ and $\mathbf{e}$ are the column vectors of primary and combined errors, respectively, each of length L, $\mathbf{u}$ the vector of actuator signals of length M, and $\mathbf{G}$ the matrix of error paths of size (L,M). The vector of actuator signals of length M may be determined by

$$\mathbf{u}(j\omega) = \mathbf{W}(j\omega)\,\mathbf{x}(j\omega) \tag{1.38}$$

with $\mathbf{x}$ the column vector of unconditioned references of length K and $\mathbf{W}$ the control filter matrix of size (M,K). Combining equations 1.37 and 1.38 and expanding gives

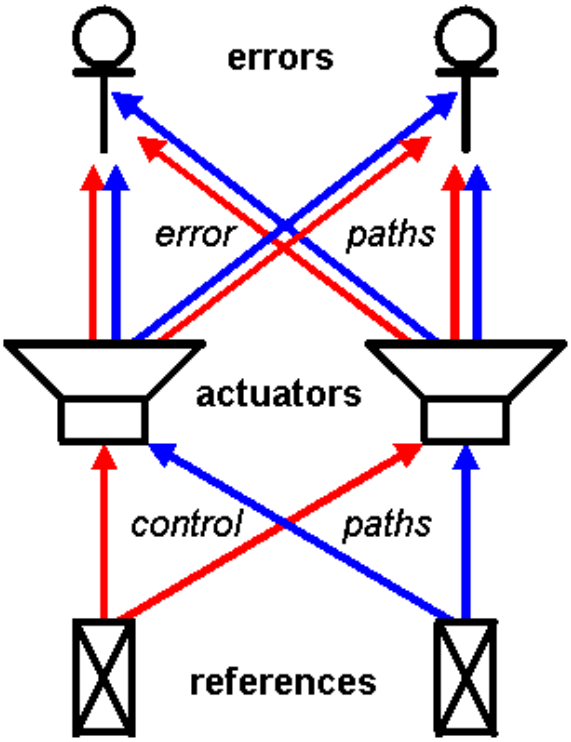

Figure 1.11: Schematic of a two channel filtered–x feed forward control.

$$\begin{Bmatrix} e_1 \\ e_2 \\ \vdots \\ e_L \end{Bmatrix} = \begin{Bmatrix} d_1 \\ d_2 \\ \vdots \\ d_L \end{Bmatrix} + \begin{bmatrix} C_{11} & C_{12} & \cdots & C_{1M} \\ C_{21} & C_{22} & & \vdots \\ \vdots & & \ddots & \vdots \\ C_{L1} & C_{L2} & \cdots & C_{LM} \end{bmatrix} \begin{Bmatrix} y_1 \\ y_2 \\ \vdots \\ y_M \end{Bmatrix} \tag{1.39}$$

The cost function, or error surface, is the $2M + 1$ dimension surface of error criteria versus real and imaginary parts of each of the M sources and is expressed as

$$J = \mathbf{e}^H \mathbf{e} \tag{1.40}$$

and substituting the error equation into the cost function gives

$$J = \mathbf{d}^H \mathbf{d} + \mathbf{d}^H \mathbf{G} \mathbf{u} + \mathbf{u}^H \mathbf{G}^H \mathbf{d} + \mathbf{u}^H \mathbf{G}^H \mathbf{G} \mathbf{u} \tag{1.41}$$

Minimization of the error is achieved by operating at the minimum point on the error surface. In the frequency domain, for $\mathbf{e} \rightarrow \mathbf{0}$, $\mathbf{u} = -\mathbf{G}^{-1}\mathbf{d}$ and the resulting vector of secondary error signals may be expressed as

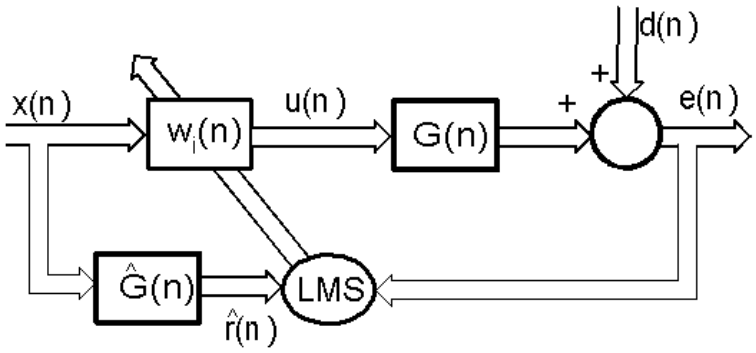

Figure 1.12: Multiple channel filtered–x feed forward control.

$$\mathbf{z} = \mathbf{GHx} \tag{1.42}$$

which may be expressed, for each error channel, as

$$Z_l(\omega) = \sum_{m=1}^{M} G_{lm}(j\omega) \sum_{k=1}^{K} H_{mk}(j\omega) X_k(\omega) \tag{1.43}$$

and rearranged to

$$Z_l(\omega) = \sum_{m=1}^{M} \sum_{k=1}^{K} G_{lm}(j\omega) H_{mk}(j\omega) X_k(\omega) \tag{1.44}$$

Pre–multiplying the reference signals, Y_k, by secondary path filters, G_{lm}, gives the filtered reference signals, R_{lmk}, allowing for the secondary error to be expressed as

$$Z_l(\omega) = \sum_{m=1}^{M} \sum_{k=1}^{K} G_{lm}(j\omega) R_{lmk}(j\omega) \tag{1.45}$$

and in matrix form

$$\mathbf{z} = \mathbf{Rh} \tag{1.46}$$

with

$$\mathbf{R} = \left(\mathbf{r}_1^T, \mathbf{r}_2^T, \ldots, \mathbf{r}_L^T\right)^T \tag{1.47}$$

The vectors, $\mathbf{r}_l$ and $\mathbf{h}$ are determined by

$$\mathbf{r}_l = \left[R_{l11}(\omega) \ldots R_{lM1}(\omega) \left| R_{l12}(\omega) \ldots R_{lM2}(\omega) \right| \ldots \left| R_{l1K}(\omega) \ldots R_{lMK}(\omega)\right]^T \right. \tag{1.48}$$

and

$$\mathbf{h} = \left[H_{l11}\left(\omega\right)\ldots H_{lM1}\left(\omega\right)\left|H_{l12}\left(\omega\right)\ldots H_{lM2}\left(\omega\right)\right|\ldots\left|H_{l1K}\left(\omega\right)\ldots H_{lMK}\left(\omega\right)\right]^T \tag{1.49}$$

Note that $\mathbf{r}_l$ and $\mathbf{h}$ each has K groupings with each of these groupings being M elements long resulting in vectors of length MK. The error equation is then

$$\mathbf{e} = \mathbf{d} + \mathbf{R}\mathbf{h} \tag{1.50}$$

and the cost function

$$J = E\left[\mathbf{e}^H\mathbf{e}\right] \tag{1.51}$$

In the time domain, however, the error must be represented using causal FIR filters. At time step n, the L^{th} order error vector may be written as [28]

$$\mathbf{e}(\mathbf{n}) = \mathbf{d}(\mathbf{n}) + \mathbf{R}(\mathbf{n})\mathbf{w} \tag{1.52}$$

where $\mathbf{w}$ is the vector of I control filter weights and $\mathbf{R}(n)$ the matrix of sampled reference signals of size (L,I). The rows of the matrix $\mathbf{R}(n)$ consist of the L reference signals from time step n through *n-I+1* so that the reference signal has a time history of *I-1* previous samples. Similar to representation in the frequency domain, the time domain representation of the filtered reference signals is

$$\mathbf{r}_l^T(n) = \left[r_{l11}\left(n\right)\ldots r_{lM1}\left(n\right)\left|r_{l12}\left(n\right)\ldots r_{lM2}\left(n\right)\right|\ldots\left|r_{l1K}\left(n\right)\ldots r_{lMK}\left(n\right)\right] \tag{1.53}$$

again of length MK and may be arranged in matrix form

$$\mathbf{R}(n) = \begin{bmatrix} \mathbf{r}_1^T(n)\mathbf{r}_1^T(n-1)\ldots\mathbf{r}_1^T(n-I+1) \\ \mathbf{r}_2^T(n)\mathbf{r}_2^T(n-1)\ldots\mathbf{r}_2^T(n-I+1) \\ \vdots \\ \mathbf{r}_L^T(n)\mathbf{r}_L^T(n-1)\ldots\mathbf{r}_L^T(n-I+1) \end{bmatrix} \tag{1.54}$$

and is of size (L,MKI). Filtered reference signals are determined by

$$r_{lmk} = x_k g_{lm} \tag{1.55}$$

where g_{lm} is the vector denoting the error path between error channel l and actuator m. The LM control filters, each having I tap weights may be expressed as

$$\mathbf{w} = \left[\mathbf{h}^T(0)\mathbf{h}^T(1)\ldots\mathbf{h}^T(I-1)\right]^T \tag{1.56}$$

where

$$\mathbf{h}^T(i) = \left[h_{11}\left(i\right)\ldots h_{M1}\left(i\right)\left|h_{12}\left(i\right)\ldots h_{M2}\left(i\right)\right|\ldots\left|h_{1K}\left(i\right)\ldots h_{MK}\left(i\right)\right]^T \tag{1.57}$$

and so $\mathbf{w}$ is of length MKI since there are I elements for each $\mathbf{h}$ of length MK and "$h_{mk}(i)$ is the i_{th} coefficient of the FIR control filter driving the m_{th} secondary source from the k_{th} reference signal"[28]. The cost function in the time domain is then

$$J = E\left[\mathbf{e}^T(n)\mathbf{e}(n)\right] \tag{1.58}$$

Control filters may be determined using one of several means of finding the minimum value of the cost function. Two of these methods are the *steepest descent* and the *stochastic gradient* algorithms. Expanding the cost function and taking its derivative with respect to the filter weights, the steepest descent algorithm gives

$$\frac{\partial J}{\partial \mathbf{w}} = 2E\left[\mathbf{R}^T(n)\mathbf{e}(n)\right] \tag{1.59}$$

This algorithm proves to be relatively time consuming since the statistical expectation would require time averaging of the slope after each iteration of the control filters. Instead, the stochastic gradient algorithm may be used to reduce computational overhead. Here, the gradient of the sum of squares of the instantaneous error is used.

$$\frac{\partial\left[\mathbf{e}^T\mathbf{e}\right]}{\partial \mathbf{w}} = 2\mathbf{R}^T(n)\mathbf{e}(n) \tag{1.60}$$

It can be shown that this approach leads to the following control filter update equation, or *Multiple Error LMS algorithm* which is the instantaneous equivalent of the method of steepest descent.

$$\mathbf{w}(n) = \mathbf{w}(n-1) - \alpha\mathbf{R}^T(n-1)\mathbf{e}(n-1) \tag{1.61}$$

where α is the convergence parameter. An important fact regarding the stochastic gradient algorithm is that "the update quantity is an instantaneous estimate of the true gradient, which is correct on average but at any one instant has a random or stochastic error associated with it [28]."

Decoupling of the controller may now be explored. Here, diagonalization will be explored in an attempt to reduce computational overhead of a square control system. For a square controller, K=M=L, or in other words, the number of reference, control, and error signals are equal. To reduce complexity, the square controller will be represented by S, therefore, the square control system will be said to have S references, S controllers, and S errors.

For a diagonalized controller of size $S \cdot S \cdot S$ or S^3, equation 1.53 is expressed as

$$\mathbf{r}_l^T(n) = [0 \ldots 0 r_{ll}(n) \, 0 \ldots 0] \tag{1.62}$$

which, by equation 1.47, gives the form

$$\mathbf{R}(n) = \begin{bmatrix} r_{111} & 0 & \dots & 0 \\ 0 & r_{222} & \dots & 0 \\ \vdots & & \ddots & \dots \\ 0 & \dots & 0 & r_{SSS} \end{bmatrix} \tag{1.63}$$

or simply

$$\mathbf{R}(n) = diag\,(r_{sss}) \tag{1.64}$$

where $1 \leq s \leq S$. Equation 1.57 then takes the form

$$\mathbf{h}^T(i) = [h_{11}(i)0\dots0|0h_{22}(i)0\dots0|\dots|0\dots0h_{SS}(i)]^T \tag{1.65}$$

which leads to

$$\begin{aligned} \mathbf{w} = \; & [h_{11}(0)\ 0\dots0|0\ h_{22}(0)\ 0\dots0|\dots|0\dots0\ h_{SS}(0)| \\ & h_{11}(1)\ 0\dots0|0\ h_{22}(1)\ 0\dots0|\dots|0\dots0\ h_{SS}(1)|\dots| \\ & h_{11}(I-1)\ 0\dots0|0\ h_{22}(I-1)\ 0\dots0|\dots|0\dots0\ h_{SS}(I-1)]^T \end{aligned} \tag{1.66}$$

Substituting expressions used for diagonalized control into the Multiple Error LMS algorithm gives the same expression as in equation 1.61 for MIMO control. Therefore, diagonalization does not reduce the number of computations required; off diagonal terms are simply zeroed and are still used in the computations. However, each control unit may be expressed as an independent control system. This would result in, assuming negligible cross–correlation between channels, S SISO units acting independent of each other. The LMS algorithm for multi–SISO control of an S by S by S controller then is composed of S equations of the following expression

$$\mathbf{w}_s(n) = \mathbf{w}_s(n-1) - \alpha\mathbf{R}_s^T(n-1)e_s(n-1) \tag{1.67}$$

where s is the channel number, $\mathbf{w}_s$ and $\mathbf{R}_s^T$ are both of length I, and the convergence coefficient may be determined by

$$0 < \alpha \leq \frac{1}{IE\,[f^2\,(n)]} \tag{1.68}$$

with $E\,[f^2\,(n)]$ being the mean square value of the reference sequence and I the number of coefficients of the control filter, $w\,(n-1)$. Note, too that mean square of the reference sequence is equal to the autocorrelation of the current reference sequence[28].

Comparison of various control strategies requires knowledge of computational overhead as well as control performance. Decoupling MIMO controllers generally reduces the control performance, and, as shown above, does not reduce the computational overhead.

However, use of multiple SISO control units would give the same control performance as fully decoupled or diagonalized MIMO control with significant reduction in computational overhead. A comparison of a MIMO, feed forward, filtered–x control system that is fully determined (same number of references, actuators, and errors) to that of a multiple SISO system having the same number of elements is shown with two comparisons made. First, the number of calculations required to update the control filters using each method were determined. Second, the number of calculations required for calculating the actuator outputs was determined. Since fully determined systems have an equal number of references, actuators, and errors, the number of each is denoted here as S where $1 \leq s \leq S$.

Observation of equation 1.67, suggests that the SISO version of the feed forward, filtered–x algorithm requires I operations to transpose $\mathbf{R}_s$, one operation to calculate αe_s, I operations to calculate $\alpha e_s \mathbf{R}_s$, and another I operations to calculate $w_s - \alpha e_s \mathbf{R}_s$. This results in $3I+1$ calculations per actuator or $S(3I+1)$ for all S SISO units. In comparison, equation 1.61, for the MIMO case, requires IS^3 operations to transpose $\mathbf{R}(n-1)$, S operations to determine $\alpha\mathbf{e}(n-1)$, IS^4 operations to determine $\alpha\mathbf{R}(n-1)\mathbf{e}(n-1)$, and IS^2 operations to determine $\mathbf{w}(n-1)\alpha\mathbf{R}(n-1)\mathbf{e}(n-1)$, and IS^2 giving a total of $S + I(S^4 + S^3 + S^2)$ operations.

Knowing the control filters, the actuator signals may then be determined. Observation of equation 1.52, suggests that multiple SISO requires $I(I-1)$ operations per channel for a total of $SI(I-1)$ operations to determine the necessary actuator signals at each time step; for MIMO, I^2S^5 operations are required. For $I = 100$ coefficients, the number of operations versus controller size required to determine the control filters is shown in Figure 1.13 and Figure 1.14 presents the number of operations required to then calculate the actuator signals.

Therefore, for multiple SISO architectures, a doubling of the channel count results in a doubling of the number of calculations required to determine the control filters and the control signals. For a MIMO architecture, the number of calculations required to determine the control signals increases by a factor of thirty–two for each doubling of the channel count. And, for determining the control filters, a doubling of the channel count results in an increase proportional to the first four powers of S; for a channel count of four, $336I + 4$ computations would be required, whereas, $4672I + 8$ computations would be required for a channel count of eight. This is approximately an increase of a factor of fourteen.

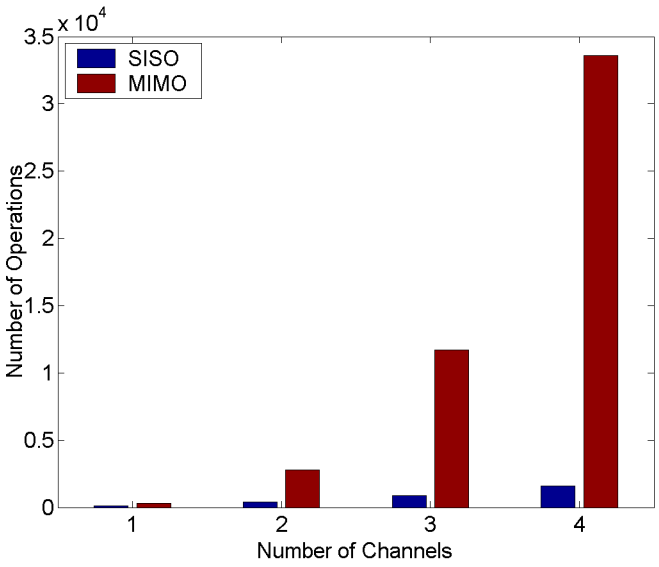

Figure 1.13: Number of calculations required to determine the feed forward, filtered–x control filter having 100 coefficients.

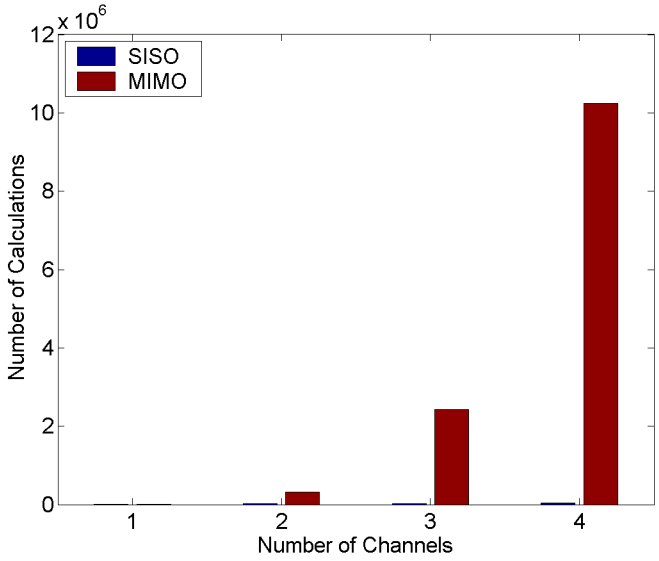

Figure 1.14: Number of calculations required to determine the control signals of a feed forward, filtered–x controller using a control filter with 100 coefficients.

1.5 Active Noise Control

Active control involves the real–time measurement of some variable which is then acted upon either in a direct or indirect manner to manipulate its value. The variable of interest is typically chosen such that controlling its value will allow for the minimization of sound pressure at some point in the acoustic field, sound intensity (acoustic power flow) across some defined surface, or some other variable related to the acoustic response. These variables may be controlled directly by sensing them with microphones or intensity probes or they may be estimated by measuring structure vibration. Although several active techniques exist for noise control they may all be grouped into two different categories: Active Structural Acoustic Control and Active Noise Cancellation.

Active Structural Acoustic Control (ASAC) involves sensing and manipulation of the vibration of a radiating structure. Proper vibration control of the radiating structure results in an attenuated noise field. According to Bies and Hansen [5], "active control of noise is the process of reducing existing noise by the introduction of additional noise by means of one or more secondary (or control) noise sources." Bies and Hansen then describe the three mechanisms by which noise reduction occurs. The first involves the theory of sound field cancellation. Here, the secondary noise field is introduced out of phase with the primary field thus cancelling sound. However, the zones of silence created by cancelling noise tends to be very localized and "is always balanced by other areas of reinforcement where the sound level is increased". A second method involves changing the radiation impedance of the radiating structure such that it is unable to radiate noise. The structure vibration need not be reduced. Proper selection of the structure radiation impedance, such that it is reactive with a negligible real component, results in the inability for the vibration to radiate an appreciable amount of noise. To prevent the structure from radiating noise, the secondary sources must be "large enough and located in such a way that they are capable of presenting the required impedance [5]". Bies and Hansen then mention that these requirements are easily achieved in one–dimensional wave guides but, for three–dimensional space "the control source will need to be close to the primary source [and] be of similar size with a similar volume velocity."

Absorption of the primary noise field using secondary actuators is another means of active noise control. In this method, the energy of the primary noise, typically with additional electrical input to the secondary actuators, assists the secondary actuators to move. This method is useful primarily for the attenuation of plane waves. However, for non–plane wave radiation, it "is likely to result only in areas of reduced noise close to the control source."

Active Noise Cancellation (ANC) involves sensing and controlling a variable of the acoustic field. Paul Lueg was the first to suggest the possibility of active noise cancellation [28]. In his 1934 patent application, he described his theory for controlling acoustic plane waves in rigid ducts by introducing additional sound. A reproduction of his design is shown in Figure 1.15. His design used a microphone (M), placed in the duct, to detect the primary noise field. This signal was then input to a speaker (L) placed down stream via some electronic device (V). The electronic device was responsible for producing the necessary

delay and amplification of the microphone signal so that the speaker may generate the proper secondary wave. This difficulty with the realization of Lueg's design in the 1930s was that "V" could not be properly implemented. With the advent of computers, the control system may now be properly realized [5].

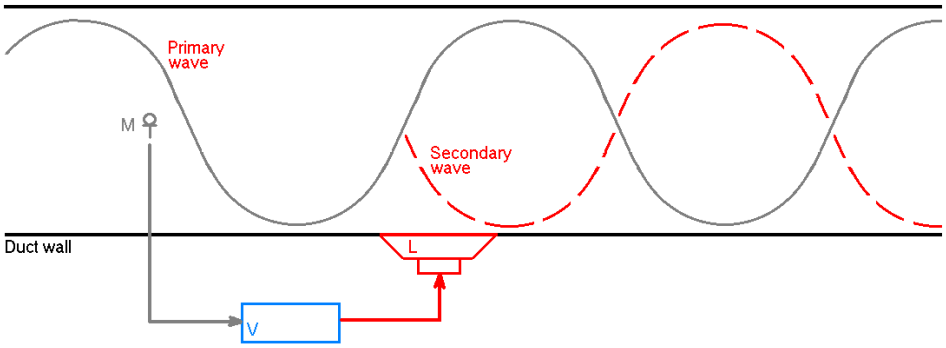

Figure 1.15: A reproduction of the part of Paul Lueg's patent application for controlling sound in a rigid duct by introducing additional sound. The diagram shows the primary wave (S_1), microphone (M), speaker (L), electronics (V), and resulting secondary wave (S_2).

Active Noise Cancellation (ANC) may be implemented using one of two control strategies—feed back control or feed forward control. In feed back control, "the error sensor signal is returned back through an amplifier with magnitude and phase response designed to produce cancellation at the sensor. The undesired sound can be reduced through the use of a very high loop gain [2]". The high feed back gain generally results in stability problems since "error in the controller phase response can change the desired negative feed back into unstable positive feed back." Feed forward control, however, is "generally more robust than feed back" particulary when "the feed forward system has a reference input isolated from the secondary source". In feed forward control, "the undesired signal [or reference signal] is sensed [and is used] to generate a signal which produces a secondary noise that is 180^o out of phase with the disturbance, thereby cancelling the unwanted noise.

Active Noise Control Using Virtual Microphones

In an attempt to better center the zone of quiet, or spatial area where noise reduction is desired—the area around a person's head—Rafaely et al [29] considered minimizing the sound pressure level at a point in space other than at a physical microphone for an active headrest noise control system. The idea was that if the transfer function between a physical and virtual microphone was known, then the sound pressure level at the virtual microphone—the center of the desired zone of quiet—could be predicted. This transfer function was determined by temporarily placing a physical microphone at the virtual microphone location and another physical microphone in the seat's headrest. The secondary noise sources (speakers) were

mounted in the head rest and were located 10 cm from the virtual microphone location or the entrance to the ear canal of the manikin used in the experiments. Placement of these secondary sources is critical since Joseph et al [30] had determined that the zone of quiet is dependent on the gradient of the pressure radiated from the secondary source. Therefore, the size of the zone of quiet and the amount of reduction within it are more easily achieved if the secondary source has a uniform sound pressure [29].

Experiments showed that control at the virtual microphone location, using the virtual microphone method, resulted in better performance than when compared to using just the single physical microphone mounted in the headrest. Two tests were conducted. The first, or forward test, determined the effect of moving the manikin head up to 7 cm forward from its natural seated position and for the second, or lateral, test the manikin head was moved as much as 6 cm closer to the secondary source and up to 6 cm further away from its natural seated position. For the forward test, the best performance at both the physical and virtual microphones was at the naturally seated position. Here, the physical microphone resulted in approximately 4 dB at the manikin's ear and approximately 9 dB using the virtual microphone method. At 6 cm, this performance dropped off considerably to approximately 2 dB and 5 dB, respectively. For the lateral test, the best performance when using the physical microphone was when the manikin's head was located close to the physical microphone. Here, approximately 11 dB of attenuation was achieved. This performance dropped to less than 3 dB when moved 12 cm away. For the virtual microphone method, the best performance was when the manikin's head was at approximately 1 cm from the naturally seated position. Here, a reduction of approximately 11 dB was achieved with the performance dropping to about 7.5 dB when moved 5 cm closer to the secondary source and to only 5 dB when moved 5 cm further away.

An improvement over active noise control using measured transfer functions was attempted by Kestell et al [31]. Here, the variables such as sound pressure level and sound pressure density were mathematically interpolated from values measured at physical microphones using a technique they described as *forward difference prediction*. Therefore, the predicted signals at the virtual microphones were then able to be updated as the system changed—a big advantage over the transfer function method. These predicted error signals at the virtual microphones were then minimized by the controller. For their early work regarding virtual microphones [31], four virtual microphone algorithms were studied. The first two involved the prediction of sound pressure at the virtual microphone and the other two techniques predicted the energy density. Experiments were performed using a long, narrow, rigid duct (0.205 m x 0.205 m x 4.800 m) with a speaker mounted on one end for generating a broad band primary noise source. Control sources were placed at 0.5 m and 1.0 m from the opposite end of the rigidly terminated duct. Experimental results were then compared to a finite element model.

Control was then performed using each of the two virtual sound pressure techniques. For the first virtual sound pressure technique, two physical microphones were used to predict the sound pressure at some point allowing for a first order virtual microphone. The second technique used three microphones to predict the virtual sound pressure. Having three known

sound pressures resulted in a second order virtual microphone algorithm. The third and fourth methods focussed on first order and second order virtual energy density sensors.

Theoretical and experimental studies for the undamped duct were first performed for on–resonance excitation with the virtual microphone location being at most 100 mm from the physical microphones. Using the first order method, analytical results were similar to control performance achieved when using a single, physical microphone for the error signal. However, experiments showed that this technique was not very effective since marginal control was attained. In addition, it was shown that the second order virtual microphone was "useless as an error sensor". Likewise, the experiment control performance results for the two virtual energy density techniques, were "no better than when a conventional remotely–located single microphone [was] used." Off–resonance experiments using sound reduction at a single microphone resulted in "an increase in modal spill over with a high level of very localized attenuation when compared to the resonance example" of 8 dB at the observer location. Control using the second order virtual microphone (8 dB) outperformed the single microphone but, the best performance was achieved using the first order technique which achieved 16 dB of reduction.

Kestell and Hansen [32] then applied forward difference prediction techniques both in a free space and inside an aircraft cabin. A 100 Hz tonal disturbance in free space was first controlled using a single, remotely placed error microphone. At the microphone a 40 dB reduction was attained but, at only 100 mm from the error microphone, that performance was limited to only 8 dB. At the same 100 mm separation distance, the first order forward difference technique resulted in a 22 dB reduction. For the second order technique no advantage over the single, remotely placed microphone was achieved. Forward difference prediction was then performed experimentally inside an aircraft cabin between 50–400 Hz with a single secondary source mounted in the head rest. Here, improvement over the single, remotely placed error microphone was achieved using both the first and second order virtual microphone technique with the first order technique proving best. At 100 mm from the physical microphones, 5 dB and 8 dB of attenuation was achieved using the remotely placed error microphone and the second order technique, respectively. However, a reduction of 20 dB was achieved for the same scenario using the first order method. The second order virtual energy density method was then studied. Here, similar performance to the first order virtual microphone technique was achieved. In addition, greater global control was achieved in comparison to control using the remote microphone. However, it was shown that this technique had no advantage over the control of energy density at the error microphone.

Active noise cancellation using intensity minimization

Placement of error sensors close to the radiating structure allows for several benefits. First, it removes the error sensors from the vicinity of the desired zone of silence, thereby reducing any interference with people. Second, placing error sensors closer to the radiating structure minimizes the acoustic path delay, thereby reducing the likelihood of controller instabilities due to time–varying errors [33]. Third, error sensors in the far field tend to result in noise

reduction in the direction of the error sensors but not necessarily in a global sense. Therefore, placing error sensors close to the radiating structure would be beneficial.

Attempts to remove error sensors from the desired zone of silence has led researchers to investigate the minimization of radiated sound intensity. The theory suggests that minimizing the sound intensity close to the radiating structure would also result in minimizing the sound intensity away from the structure in the desired zone of silence. Berry et al [33] investigated, analytically, the use of sound intensity minimization and compared it to the minimization of mean squared sound pressure and the minimization of sound power. For their analysis, a plate measuring 1.0 by 0.75 meters was modelled using a grid of 10 by 10 elements, mounted in an infinite baffle, and excited with a 100 Hz tone.

The analysis by Berry et al found that, although intensity minimization does have some benefits compared to sound pressure minimization, sound intensity minimization does not work well for distances less than approximately one–tenth the wavelength of the controlled frequency with best performance at a distance equal to 15% of a wavelength. For greater distances, minimization of either sound intensity or sound pressure gave similar results. "This is to be expected since the intensity becomes proportional to the squared pressure at large distances from the source, and the intensity minimization then becomes equivalent to squared pressure minimization. "Intensity minimization suffers from a rapid decrease of the control performance when the sensors are in the near field of the sources" and is due to "the signed nature of the cost function". In addition, "near field intensity minimization does not, in general, provide significant improvements as compared to near field squared pressure minimization, and may in some cases give smaller attenuations than pressure minimization".

Active Noise Control Using Volume Velocity

Volume velocity is the change in net volume displacement per unit time and is a function of the integral of surface velocity of a structure. Acoustic variables, such as pressure or radiated power, may be determined knowing only the structure vibration, and therefore, this technique may be used when it is desired to perform control at a point in space where transducers may not be permitted. In addition, the near field acoustic pressure may be related to the far field acoustic pressure using the same theory [34].

This technique attempts to decouple the structure vibration from the radiated noise field [35] and may be used to determine the sound power radiation in terms of a set of velocity distributions independent of other velocity distributions [34]. These independent radiators are referred to as radiation modes. Therefore, describing the radiated noise field in terms of radiation modes, an estimate may be made of the number of independent parameters required to describe the response. Further, reduction of the amplitude of a radiation mode guarantees reduction of the radiated noise field unlike the reduction of a radiating structural mode since power radiated by a structural mode is dependent on the response of other structural modes. Therefore, an increase in radiated sound power may occur even though the amplitude of a structural mode is reduced [36].

The radiation modes are calculated as the eigenvectors of an elemental radiation resistance matrix and the efficiencies of these radiation modes are proportional to their corresponding eigenvalues. In addition, the radiation modes may be expressed in terms of the velocities of the radiating surface over a discrete number of points. Shapes of these radiation modes may be used to determine sensor and actuator design and placement for effective control. And, further, the minimum number of sensors and actuators may be determined thus reducing controller complexity. It should be noted, however, that "radiation mode shapes are slowly varying functions of frequency". Johnson and Elliott then continue with "it is not possible to design a single fixed sensor which will accurately measure the amplitude of a given radiation mode over the entire frequency range. However, the shape of the first radiation mode remains reasonably constant [for a given frequency range]." For low frequencies, the fundamental radiation mode is usually the only radiation mode having significant influence on the radiated acoustic field and therefore is an approximation of the volume velocity. For a vibrating flat panel, the fundamental radiation mode has a uniform velocity distribution having an amplitude proportional to the volume velocity of the structure.

Johnson and Elliott [36] then applied the theory of radiation modes to simulate active cancellation of volume velocity. Control of the first radiation mode was targeted using a piezoelectric patch bonded to the center of the radiating panel. Control was successfully performed, annihilating the first radiation mode, however, control spillover resulted in an increase in radiated power by higher order modes—radiation modes five and six. Increasing the radiation power of modes five and six did not significantly influence the radiated sound field since their radiation efficiencies were very low relative to the first radiation mode which was accountable for 95% of the radiated sound power. Control spill over occurs when the actuator is not efficient at the frequencies at which it is driven or when several structural modes, all contributing to a particular radiation mode, are driven out of phase. The actuator effort then results in a battle between the structural modes and negligible attenuation of the radiation mode is achieved. There may also be large increases in both structural vibration and near field sound pressure while achieving far field reduction. These increases occur at frequencies where the secondary actuator is incapable of coupling into the first radiation mode. Another qualification of this technique was to compare the attenuation achieved using volume velocity minimization to that of the optimal control strategy of sound power minimization using a disturbance of 350 Hz. Here, minimization of the first radiation mode resulted in 11.3 dB of attenuation compared to 12.5 dB for the optimal control of sound power minimization. Although 1.2 dB of additional control was achieved for the latter method, the volume velocity method required only a single sensor compared to measuring "the sound power radiation from a vibrating panel [which] would potentially require large numbers of acoustic sensors".

1.6 Previous Developments in the Attenuation of TBL-Induced Interior Noise

"Under typical cruise conditions, the turbulent boundary layer pressure fluctuations imparted on the exterior fuselage shell of a streamlined aircraft constitute the most important source of cabin noise [37]." In super-sonic aircraft, "the levels of sound and vibration induced by the airflow are so high that they can threaten the integrity of many electronic and mechanical instruments [38]" and it should be noted that "flow induced noise increases more rapidly, with respect to vehicle velocity, than other noise sources [39]". The transmission of flow noise has been successfully attenuated using insulation placed between the fuselage and trim panel, however "their weight may be prohibitive for most applications" [40]. Further, for low-frequency disturbances, the "passive approach is not very effective [41]". Therefore, the use of active control for low-frequency, flow induced interior noise "is still the subject of current research [38]". In particular, "there is a lack of understanding [of] the detailed physics" of the "excitation due to TBL, the flow noise transmission through the structure, and the flow noise radiation inside a cavity [38]".

Maury et al [38] investigated flow induced sound radiation from a flexible panel. Their model was developed to predict the kinetic energy of and the sound radiated from a thin, simply supported, baffled panel excited by a turbulent flow up to frequencies of 1000 Hz. In their analysis, Maury et al showed that cancellation of either the first structural mode or the first radiation mode provided similar performance. However, for higher frequency attenuation of the radiated sound power "the cancellation of a limited number of the higher order radiation modes was more efficient than the cancellation of the same number of structural modes [38]". Given the use of six independent controllers, "The strategy could provide attenuation up to 13 dB [38]" however, this analysis assumed perfectly matched sensor/actuator pairs and did not account for spillover effects "which will always occur and degrade the results [38]".

Maury et al [37] further developed their model presented in [38] using a double panel system. This double panel system had a fuselage panel, excited by a TBL, with an interior trim panel. In between the two panels was a layer of fiberglass insulation similar to the configuration found in a commercial aircraft. In their work, Maury et al [37] showed that the majority of the noise radiated to the interior was due to the first fuselage panel mode. Since "the insulating material has little effect below this resonance" Maury et al investigated the use of various active control strategies to combat low frequency radiated noise. They showed that the "most efficient strategy is the suppression of the low-order skin panel structural modes" with theoretical performance of up to 16 dB. However, bonding of actuators to the fuselage panel may not be feasible since pressurization of the fuselage at altitude results in a tensioning of the panels [37]. However, "significant reductions in the sound power radiated can also be achieved by the active suppression of the low order structural modes of the trim panel" and therefore it "may be more feasible to control the vibration of the trim panel [37]". This approach was shown to have a theoretically achievable maximum performance of 12 dB controlling only the first structural mode.

Gibbs et al [42] used generalized predictive control and radiation filters to demonstrate

active control of turbulent boundary layer induced sound radiation from aircraft panels. The control system used three actuators and fifteen accelerometers to predict the radiated sound field. On-resonance performance from 10–20 dB was achieved with 5–10 dB attenuation achieved from 150–800 Hz. This effort was further advanced by Gibbs et al [43] to require only a single actuator and four accelerometer measurements to predict the radiated sound field.

Gibbs and Cabell [44] demonstrated the first known active control of TBL induced sound radiation on more than two bays of a tensioned aircraft fuselage section simultaneously. The 0.063" thick aluminum panel consisted of six bays each separated by aluminum frames and stringers. Each bay measured 20" by 10" and the panel was tensioned in the cross-flow direction to simulate hoop stress induced by cabin pressurization at 40,000 feet altitude. The panel assembly was mounted on the sidewall of a Mach 0.125 wind tunnel. Radiated sound power was estimated by performing a discrete Rayleigh integral of fifteen point measurements, made using accelerometers, across each panel.

In this effort, Gibbs and Cabell [44] investigated the feasibility of reducing broadband radiation using a single–input, single–output (SISO) feedback controller per bay and compared the technique to the use of a multiple–input, multiple–output (MIMO) feedback approach. Control was applied using a single rectangular piezoceramic actuator mounted at the center of each bay. The first radiation mode was estimated by summing the response of four accelerometers mounted on each bay and was then minimized by the controller. Six bay MIMO control reduced radiated sound power of the dominant 180 Hz mode by 9 dB with 4 db attenuation over the 150–800 Hz band. SISO control, applied to each of the six bays, achieved 4 dB at the 180 Hz mode with 2.5 dB from 15–800 Hz.

1.7 Smart Foam

Smart Foam is the term given to a novel, lightweight acoustic actuator, which is in essence, a loudspeaker. The concept of how Smart Foam works is presented below and is proceeded by a summary of previous Smart Foam research. Previous research includes development of the Smart Foam concept and its use in active noise control on simple structures and more complex systems such as an aircraft fuselage.

The Smart Foam concept

In porous materials, such as open cell foam, sound energy is absorbed thereby reducing sound pressure levels. Acoustic waves enter the interstices of the porous material dissipating energy, by means of viscous losses, into heat [45]. However, "The absorbtivity of such materials are functions of frequency, being relatively small at the lower frequencies and increasing with the thickness of the material [45]." Therefore, "porous liners are not very effective at achieving low frequency performance [5]". However, the use of an active material, placed within the foam, may be used to increase the effective thickness of the foam layer as described below following a brief overview of how active materials work.

Active materials are those materials showing a relationship between electrical charge and mechanical strain. This relationship is referred to as the piezoelectric effect and is found, typically, in certain crystalline materials. Materials having the piezoelectric effect may be deformed by applying an electric charge across the poling direction of the material, thus allowing them to be used as an actuator. The converse may also be achieved by mechanically deforming the piezoelectric material such that a charge is produced. In this configuration the transducer may be used as a sensor. [46]

Piezoelectric materials are generally described using rectilinear coordinates, each denoted from 1 through 3, as shown in Figure 1.16 where the "3" direction typically refers to the thickness.

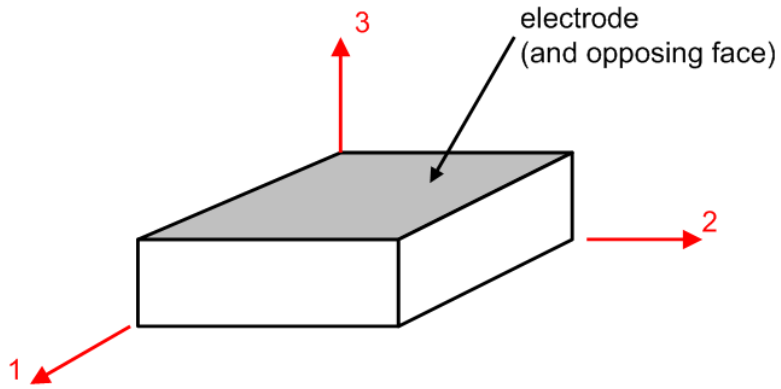

Figure 1.16: Description of the piezoelectric element and it's notation.

Piezoelectric materials, given a small electric field or small mechanical strain, may be described by the linear constitutive equations [46] as

$$\epsilon^i = S_{ij}^E \sigma_j + d_{mi} E_m \tag{1.69}$$

$$D_m = d_{mi} \sigma_i + \zeta_{ik} E_k \tag{1.70}$$

where $i, j = 1, 2, \ldots, 6$ and $m, k = 1, 2, 3$ refer to the three principal directions. ϵ is the strain, σ the stress, D the electrical displacement in units of charge per unit area, E the electric field in units of volts per unit length, S^E the elastic compliance, d the piezoelectric strain constant, and ζ the material permittivity.

Of particular interest are the strain constants d_{33}, d_{31}, and d_{32}. The first subscript refers to the direction of the charge and the second the direction of mechanical strain. For thin materials having negligible effect through the thickness and width, d_{31} may be best suited with the resultant stain along the "1" direction expressed as

$$\epsilon_{pe}^{1} = \frac{d_{31}V}{h_a} \tag{1.71}$$

where h_a is the material thickness.

Lower frequency attenuation may be achieved using active control to operate on a curved layer of active material within the foam. Such an active material, when strained using an applied voltage, will induce a volume velocity by means of a pumping action. This pumping action results due to the coupling between the predominant in-plane strain of the active material and its curvature as depicted in Figure 1.17. This pumping action, similar to the operation of an ordinary loud speaker, would then generate the required volume velocity to generate sound. To ensure maximum sound power is radiated from the curved active sheet a baffle (Figure 1.18), placed on each side, must be used such that a dipole will not be formed.

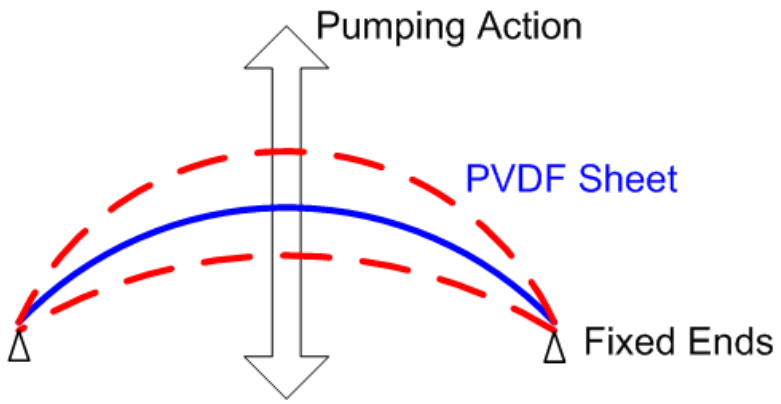

Figure 1.17: Curving a thin active material will result in a pumping action.

Smart Foam consists of a sheet of polyvinylidene difluoride (PVDF) sandwiched in between mating halves of a block of foam cut to the shape desired for the PVDF sheet. This research and other newer developments used a Smart Foam design having only one half-sine wave as depicted in Figure 1.19 whereas earlier works used several opposing curves to form the PVDF sheet as shown in Figures 1.20. For the half-sine design, the entire sheet of PVDF vibrates in phase and thus has a single electrode attached to each of the two opposing surfaces.

The older style Smart Foam design, taking the form of several opposing cylindrical shapes, has two wiring configurations—parallel and series-parallel as shown in Figures 1.20. The parallel design was proposed by Tibbets [47] and characterized in earlier Smart Foam research [48] to result in a non-linear response. However, the use of the series-parallel design, although requiring "about twice the voltage of the parallel actuator to control the same acoustic levels [48]", alleviates the non-linear response.

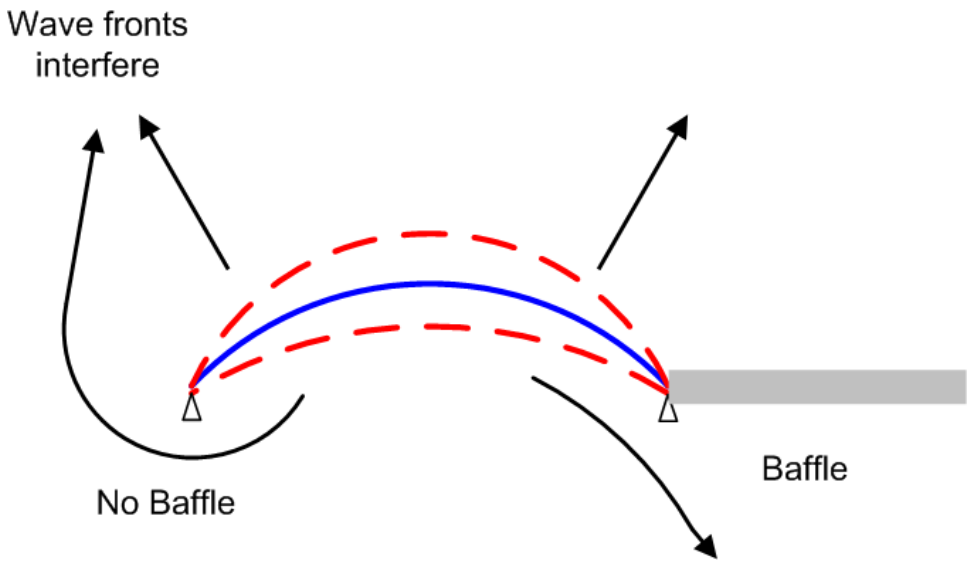

Figure 1.18: The sides of the active sheet must be baffled to maximize radiated sound power.

Early work with active foam and Smart Foam elements

Tibbets [47] patented the use of a piezo sheet for use as an acoustic source. As described in the patent "The transducer is characterized by an arrangement of the piezoelectric film into a series of elongate curved cylindrical segments of alternating sign of curvature, with the surface electrodes on the film being divided in selected locations between adjacent segments [47]". The piezo sheet was supported by a frame designed to allow the piezo sheet to take the multi-cylindrical form.

Tibbets' concept was later developed using acoustic foam in place of the frame. Green [49] and Bolton and Green [50] presented a theory regarding the application of an active foam

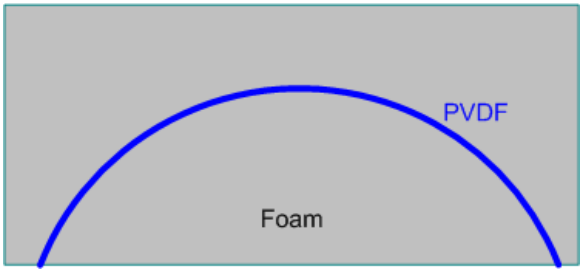

Figure 1.19: Smart Foam Half-Sine Design.

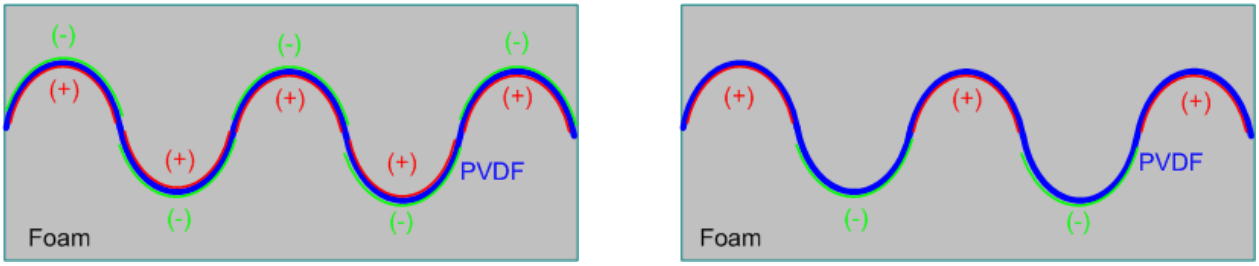

a) Parallel b) Series-Parallel

Figure 1.20: Early Smart Foam development investigated the use of two alternate wiring schemes.

for use in active sound absorption. Their theory provided values for the displacement and corresponding force of the foam face along with the required power to match the impedance of the foam to that of the incident wave. Their theory also described the mechanism for completely absorbing the energy of the impending acoustic wave. Active sound absorption has the effect in this case to make the physical foam layer seem thicker in terms of the acoustic effect it has.

Unlike Bolton and Green's work on active foam, past and present research on Smart Foam involves its use as a means of acoustic radiation control [51].

In an effort by Gentry et al [51], the actuator is driven such that sound radiating from a vibrating structure is reduced by lowering the resistive radiation impedance of the radiating structure [52]. In addition, reflections of sound waves off the Smart Foam's exposed surface may also be attenuated [51]. In their work, Gentry et al [51] mounted a circular Smart Foam element over a 0.3 m (1.0 ft) diameter metal piston. The piston was excited using discrete tones between 70–400 Hz. Adaptive, feed forward, filtered–x control was applied and the resulting sound field was determined to have up to 20 dB reduction. The same actuator was then used in a standing wave tube to determine its ability to reduce acoustic reflection. Sinusoidal tones from 100–1000 Hz were used as the disturbance. Performance was achieved at all frequencies with up to 55 dB attenuation at frequencies above 600 Hz. Between 150–300 Hz, the Smart Foam attenuated reflected waves by 10 dB.

Guigou et al [48] and Gentry et al [53] then further developed that of [51] by performing noise control of a random excitation. Here, the Smart Foam actuator was mounted near the surface of an oscillating piston driven with band limited noise from 0-1600 Hz. Feed forward control, using a LMS algorithm with one error microphone, placed either in the near field or the far field, and an ideal reference, was then used to attenuate the noise. This system achieved global attenuation of 10 dB using either error microphone location. In addition, transmission loss across the Smart Foam element was measured. Using either a microphone placed in the far field or an accelerometer mounted on the perturbing piston, transmission loss was increased by 10 dB between 150–650 Hz for a 0–800 Hz random disturbance.

An effort by Fuller et al [54] and Gentry et al [53] investigated the use of two different bonding agents used to adhere the PVDF layer to the foam halves. It was shown that using

a silicone bonding layer resulted in a non-linear response having higher order harmonics. The use of spray glue resulted in no harmonics. At an excitation voltage of 25 V_{rms}, both adhesives resulted in a sound pressure level of 19 dB at the 290 Hz drive frequency. However, at higher voltages, use of spray glue resulted in sound pressure levels 4 dB less than when using the silicone.

Guigou et al [55] then applied Smart Foam elements to a flat plate in an anechoic environment. The plate measured 170(6.7) by 50(2) by 1.5(0.06) mm(inches). Six Smart Foam elements were mounted on the plate covering its entire surface. Error signals consisting of a single microphone per Smart Foam element were placed close to its surface. Plate disturbance was caused by a piezoelectric patch bonded directly to the plate and a hemisphere of ten microphones was placed over the radiating plate to measure the resulting sound field. Although not directly stated, data in a figure presented in [55] suggested up to 9 dB of sound power attenuation near 600 Hz. Less control was attained at other frequencies. Note, though, that the control band was not stated for this work.

Noise control using Smart Foam elements on aircraft

Guigou and Fuller [56] then applied the Smart Foam treatment to the cockpit of a Cesna Citation VII aircraft. Four banks of Smart Foam elements, with each bank comprising of a single channel, were placed on the interior of the fuselage panel with a band limited random noise source directed at the same area from the exterior of the aircraft. For the LMS filtered–x control, error microphones were located inside the aircraft cabin with either an ideal reference or that of measured panel acceleration. For the 250-1050 Hz random disturbance and measured acceleration used for the reference, global attenuation was "2.5 dB for the 2 control channel system, while it [was] 8 dB for the 4 channel control system. These results demonstrate that increasing the number of channels from 2 to 4 greatly improve the global performance [56]".

In [57], Guigou and Fuller demonstrate the use of Smart Foam elements for the attenuation of broadband noise in the cockpit of a Cessna Citation III fuselage. Here, they employed multiple input, multiple output (MIMO), feed forward, filtered–x control to minimize interior noise levels measured with microphones located in the vicinity of both the pilot's ears and the pilot's shoulders. The noise source was a band–limited, random speaker excitation directed at the fuselage from about 25 mm (1″) from the surface. Four banks of Smart Foam elements were bonded to the interior surfaces of these corresponding fuselage panels with each bank treated as a single channel of control. Control over several frequency bands was observed for different reference sensors: the speaker disturbance signal, the acceleration of the fuselage panel at the disturbance speaker, and the interior sound pressure level up close to the fuselage panel. Using a control band of 250–1050 Hz, with the ideal speaker disturbance signal as the reference, a global sound pressure reduction of 2.8 dB over this band was attained using two channels of control whereas 8 dB was attained for the four channel case. In addition, global attenuation for the four channel case was reported to be more uniform than for the 2 channel test.

Using the same 250–1050 Hz control band with an ideal reference, a comparison of noise reduction at the pilot's ear level was made between two test cases. The first case had four error microphones located 7 inches from the radiating fuselage panels. Here, a global reduction of 8 dB was achieved. Moving the error microphones 4 inches closer to the fuselage panels (3 inches from the surface) resulted in only 6 dB of noise reduction. The control band was then changed to 500–700 Hz and used the same ideal reference with 4 error microphones placed 7 inches from the radiating panels. Using this narrower control band, an average noise reduction of 15 dB was achieved at the error microphones with 9 dB of attenuation in the vicinity of the pilot's ear level. Using an accelerometer reference, the attenuation at the error microphones was reported to be 6 dB at the pilot's ear level.

Control of TBL induced interior noise using Smart Foam elements

Use of Smart Foam to control turbulent boundary layer induced noise was first conducted by Griffin [58] and by Johnson et al [4]. In this research, Smart Foam was tested using wind tunnel excitation to simulate the effect of TBL induced interior noise of an airplane in flight. Feed forward, filtered–x control was used on each of three test scenarios. The first was performed on a low speed (Mach 0.2) wind tunnel at NASA Langley Research Center (LaRC) and the other two at Arnold Engineering Development Center (AEDC) at Mach 0.8 and Mach 2.5.

The NASA/LaRC test setup consisted of a 60" long T6 aluminum plate measuring 20" wide and 0.060" thick and was mounted in a steel frame which formed six equally sized bays. This is shown in Figure 1.21. Control was applied to only one bay using an arrangement of six Smart Foam elements configured for four channel control as shown in Figure 1.22. Each channel of control had a single accelerometer for providing the reference signal with four microphones, placed 20" from the plate, for the error signals. Note that the anechoic enclosure was used only on the one bay where control was applied (Figure 1.23).

For the Mach 0.2 flow case, a reduction of 2–5 dB_A over a control bandwidth of 400–1000 Hz was attained with an average attenuation of 2.5 dB_A across the control band and 0.7 between 0 and 2000 Hz. Passive attenuation, achieved by the presence of the foam, was 3.8 dB_A and 3.5 dB_A for the 400–1000 Hz and 0–2000 Hz bands, respectively. See Figure 1.24 for a reproduction of Griffin's results [58].

Similar to the NASA/LaRC setup, the test configuration at AEDC consisted of six bays each measuring 15" by 5-1/4". The anechoic enclosure was used with control applied to one bay using three Smart Foam actuators each using a single accelerometer for the reference signals and four microphones for the error signals. See Figure 1.25.

Increasing the flow to Mach 0.8 resulted in no change in mean square sound pressure between 0–2000 Hz and 3.5 dB_A averaged reduction between the 400–800 Hz control band with peak values of 10 dB_A. Passive attenuation, afforded by the foam layer, was 5.6 dB_A and 5.5 dB_A for the 0–2000 Hz and the 400–800 Hz bands, respectively. These results are reproduced in Figure 1.26. Testing was repeated on the AEDC wind tunnel at Mach 2.5. However, control was limited to a fraction of a decibel over both the control band of 400–

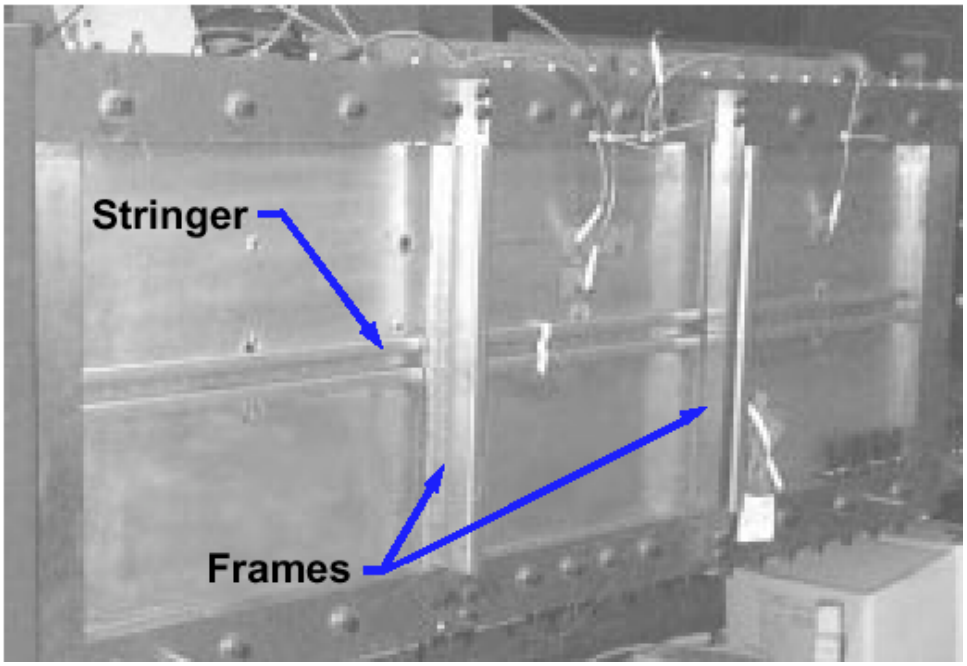

Figure 1.21: Griffin Test Setup at NASA/LaRC [58].

1000 Hz and from 0–2000 Hz. This negligible performance was due to "a poorly coherent reference signal and the lack of control authority due to the test chamber depressurization" [58].

Griffin's work was also applied to a lower speed wind (Mach 0.1) tunnel at Virginia Tech where the use of Smart Foam elements for controlling turbulent boundary layer induced interior noise was conducted in depth [58]. This test setup consisted of a 0.050" thick aluminum plate, mounted flush to the inner wall of the wind tunnel, measuring 20" in the flow direction by 10" wide. The plate had four Smart Foam elements mounted on its surface and radiated into the anechoic enclosure discussed previously. Reference signals were obtained using a single accelerometer mounted under each Smart Foam element. Error signals, provided by four microphones—one per channel, were located along with four additional observer microphones in a plane twenty inches from the radiating plate.

Here, four independent Smart Foam elements were used as the control actuators as shown in Figure 1.27. Each control channel had a single accelerometer mounted on the radiating plate directly below the corresponding Smart Foam element as shown in Figure 1.27. Furthermore, there was a single error microphone used per control channel. Therefore, the adaptive feed forward, filtered–x control system was of size 4x4x4 (actuator channels by reference channels by error channels), and its control algorithm was configured to be fully coupled.

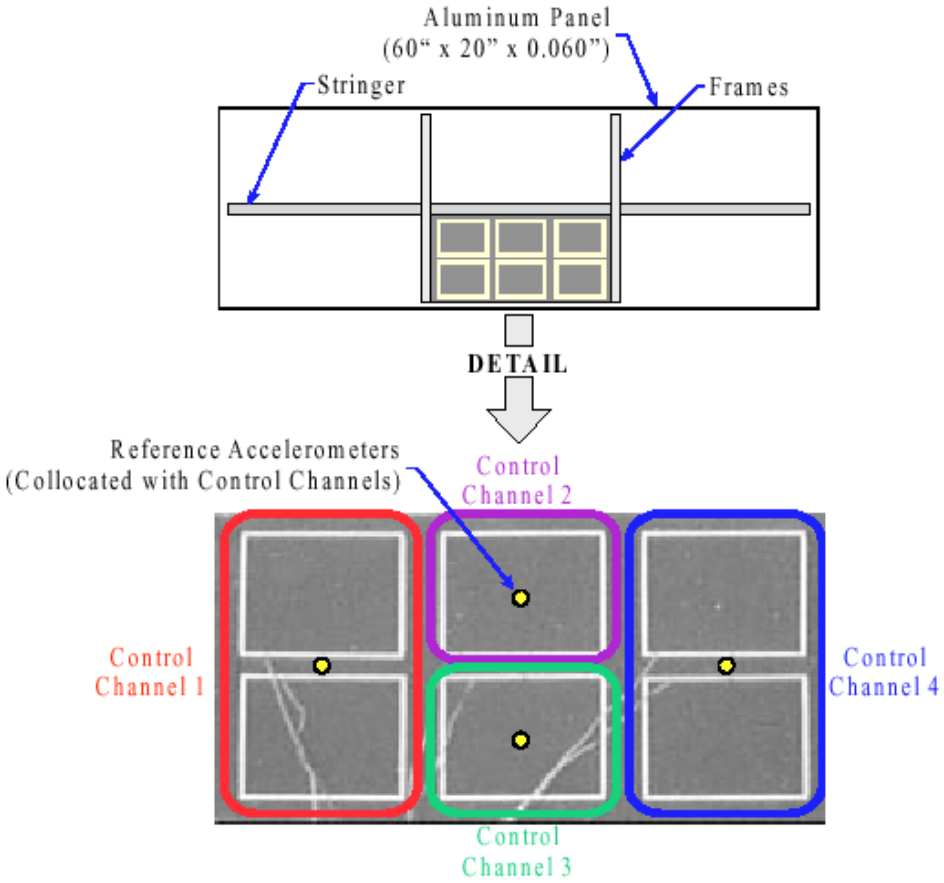

Figure 1.22: The Griffin test setup at NASA/LaRC used six Smart Foam elements configured for four channel control. [58].

The control bandwidth was set to be from 250 Hz to 630 Hz. Over this band, the average attenuation due to active control was 4.5 dB_A with 1.6 dB_A average attenuation from 0–2000 Hz. These results are reproduced in Figure 1.28. In addition, passive attenuation was 4.2 dB_A and 7.6 dB_A for the 250–630 Hz and 0–2000 Hz bands, respectively [58].

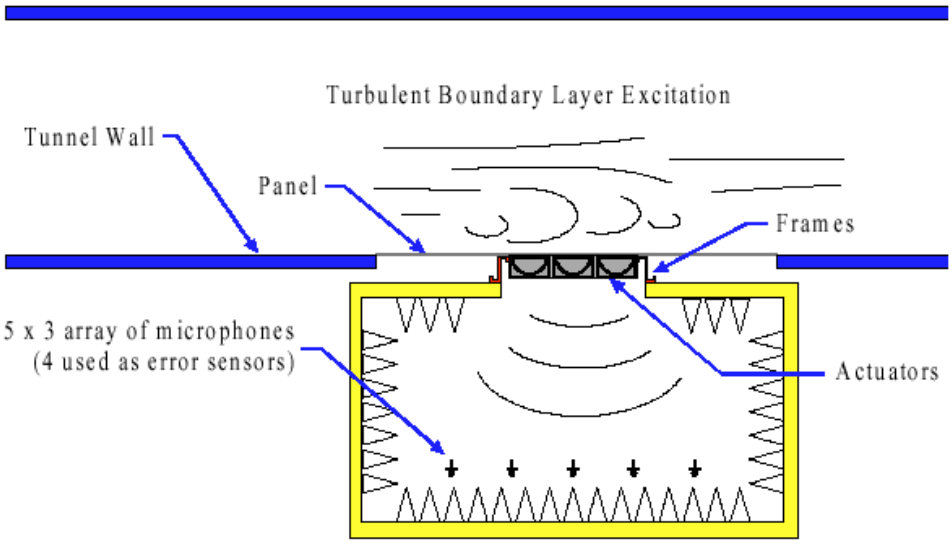

Figure 1.23: Anechoic enclosure placed around the one bay used for NASA/LaRC control experiments. [58].

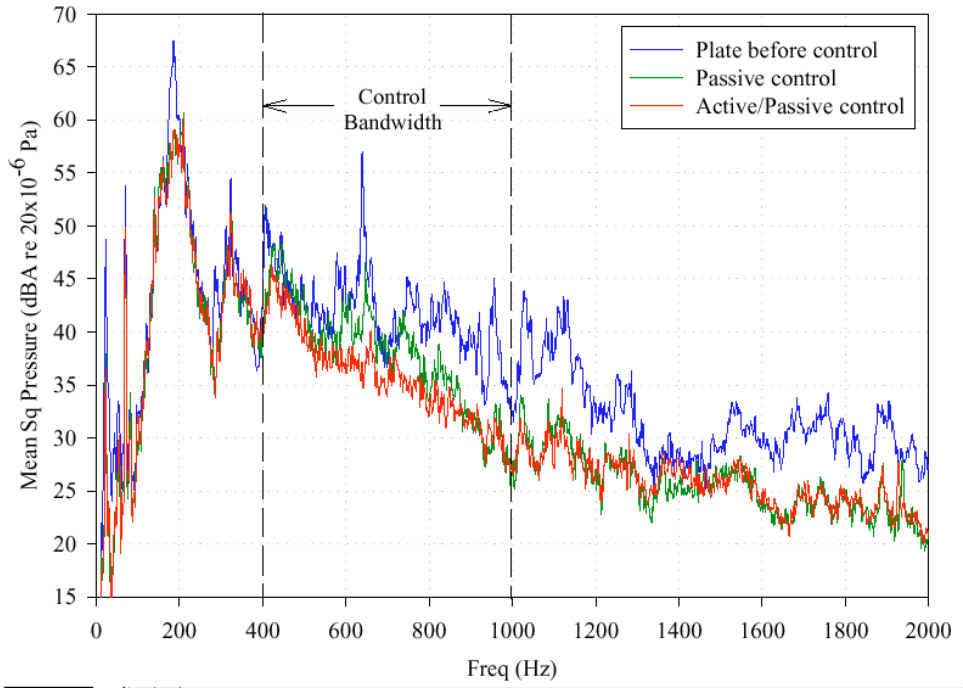

Figure 1.24: NASA/LaRC Test Results. [58].

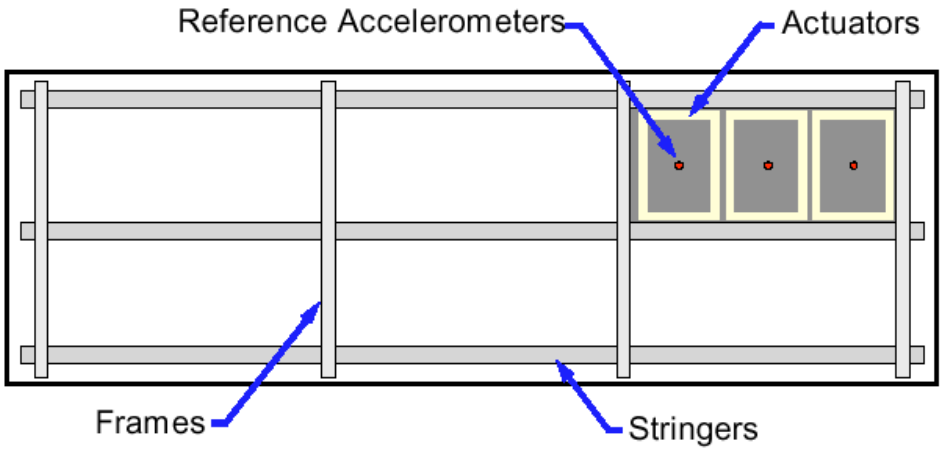

Figure 1.25: AEDC Test Configuration. [58].

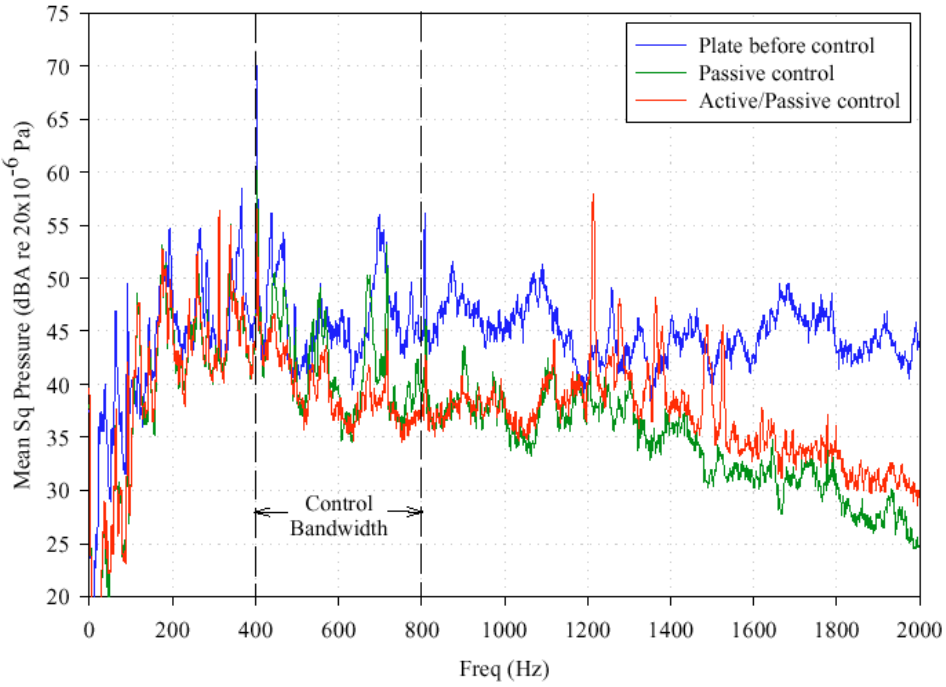

Figure 1.26: AEDC Results for Mach 0.8. [58].

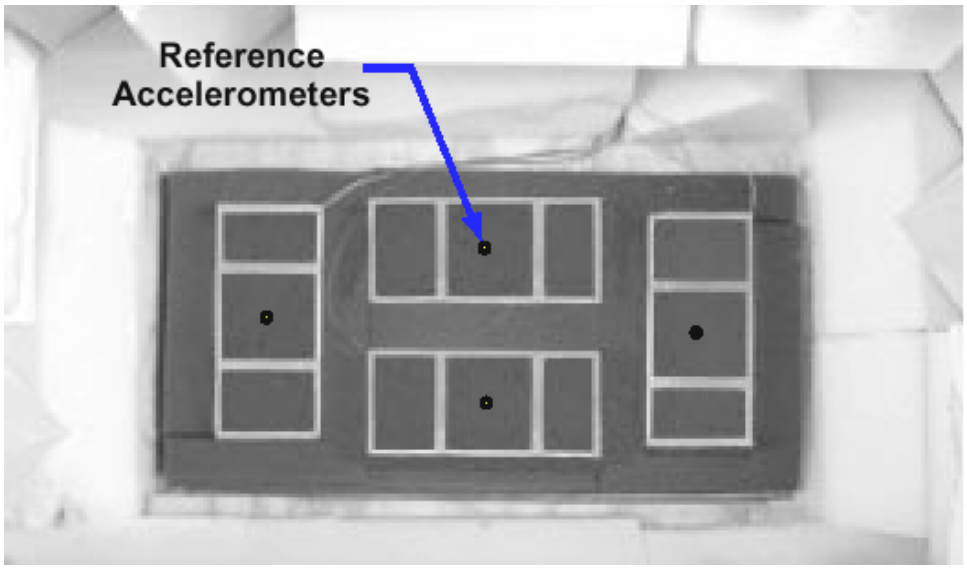

Figure 1.27: Griffin Test Setup at Virginia Tech [58].

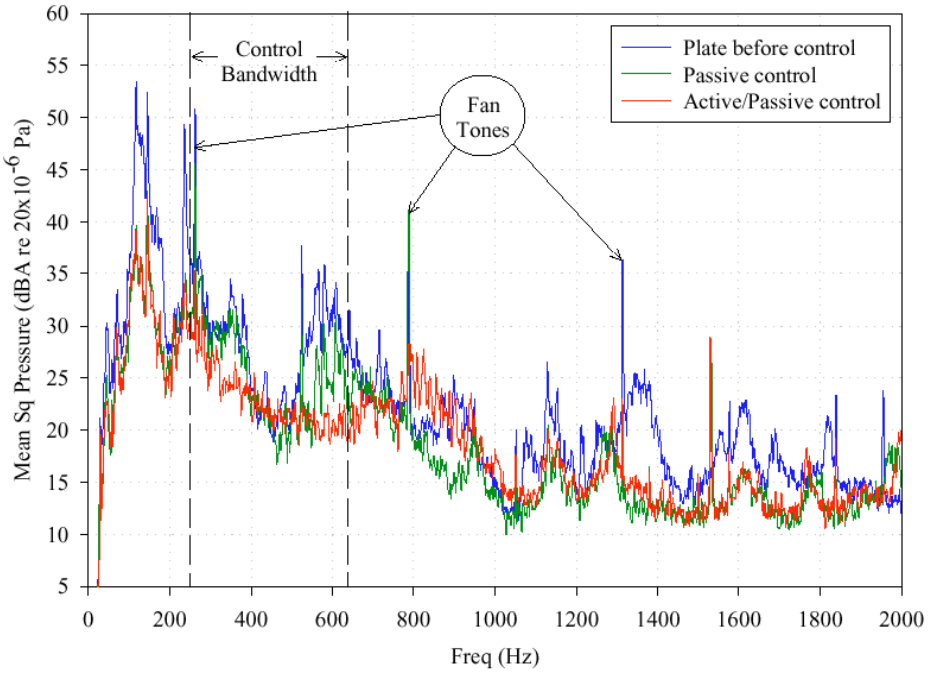

Figure 1.28: Griffin Test Setup at Virginia Tech [58].

1.8 Objectives and Contributions

The aim of this research was to develop Smart Foam such that it may be feasible for use in real–world applications having a turbulent boundary layer induced noise source. The error to be minimized by the control system is the resulting interior noise field in the vicinity of the crew and passengers. However, placement of error sensors in such a location would obstruct the interior. Therefore, error sensors must be placed remotely, close to the radiating plate. This then requires minimization in the near field such that far field mean square sound pressure may also be reduced.

To date, research in active TBL induced interior noise control required the use of many small control systems each coupled to the next. Further, due to the poor spatial correlation of TBL induced plate vibration, many vibration measurements, used for reference signals, must be obtained. The poor correlation also results in poor coherence between the plate vibration and the interior noise field. For a large system, the controller may become excessively complex and therefore may require a prohibitive number of actuators, sensors, and computations by a control system requiring an excessive number of channels. Therefore, for active control of TBL induced interior noise to be feasible, control system complexity must be reduced while maintaining sufficient performance. Although a simpler system may result in lesser performance than the more complex counterpart, such a simpler system may be desired should the trade–off in performance versus complexity be acceptable.

A practical control system would require the consideration of several aspects. First, error sensors must be developed such that they may sense close to the radiating structure without being inhibited by an excessive near field response which would jeopardize control performance. Second, reference sensing must be performed such that the coherence between the plate vibration and the interior noise field is increased. Third, the number of actuators required for sufficient control must be determined and fourth, trade-offs using an uncoupled control system must be identified for their ability to achieve sufficient performance while requiring significantly fewer computations by the control system.

Specific target aims of this research are as follows:

•Development of a multiple–SISO Smart Foam Treatment

–Develop an integrated, compact unit consisting of a Smart Foam element, reference sensor, error sensor, and controller

•Smart Foam Element

–Develop a Smart Foam element to have dimensions corresponding to the performance of the error and reference arrays

–Develop a Smart Foam element having sufficient control authority over the desired control band

•Reference Sensor Development

–Develop a reference sensor capable of increasing the coherence between plate vibration and the radiated interior noise field

•Error Sensor Development

–Develop an error sensor capable of rejecting the near field response

–Develop a directional error sensor capable of primarily sensing noise radiated in the vicinity of a corresponding actuator

•Control System Development

–Develop a control approach capable of significantly reducing the number of computations required to achieve control

•Improve Low Frequency Performance

–Use distributed vibration absorbers to improve low frequency performance of Smart Foam elements

–Achieve active performance at higher frequencies while simultaneously achieving low frequency performance

The multiple–SISO Smart Foam treatment required several aspects of development as noted in the above list. The integrated system required a single Smart Foam element along with an error sensor capable of sensing in the near field and a reference sensor capable of achieving sufficient coherence between the vibrating plate and the interior noise field. The control system required the reduction of coupling paths to reduce the number of computations. However, this then required that each error sensor be designed to be directional such that it would sense only that noise radiating from the vicinity of the corresponding Smart Foam element. In addition, being located in the near field, the error sensor had to be designed such that it would not sense near field components of the acoustic field generated by the vibrating plate.

Several reference sensor designs were explored. Various configurations were used consisting of either ordinary accelerometers or spatially distributed sensors. Each of these

reference measurements were used as reference inputs—one per actuator—hence the "**S**ingle **I**nput" of "multiple–**SI**SO" used to describe this research effort.

An error sensor array was developed that was directional towards the respective Smart Foam element and was also designed to reject near field response. A single error sensor array consisted of three microphones evenly spaced on a circular ring whose signals were summed. This summed signal would then be used as the one error signal for that particular control channel.

Each control channel also had a single Smart Foam element used to generate the secondary noise field. This is the **S**ingle **O**utput as referred to in "multiple–SI**SO**". Multiple instances of these integrated units were used simultaneously and thus referred to as a "**multiple**–SISO" control approach.

Smart Foam elements have relatively poor active performance at low frequencies ($<$ 400 Hz). To combat this problem, tuning masses were added to the tops of the Smart Foam elements to provide reactive control of structure vibration in the form of a Distributed Vibration Absorber (DVA). This technique was developed extensively [16] [17] [18] [19] [20] [21] [22] [23] and was presented earlier in this chapter.

1.9 Dissertation Structure

The body of this dissertation is arranged in eight chapters followed by three appendices. Following this introduction, Chapter 2—Correlation of Turbulent Flow and its Influence on Active Noise Control, defines the problem and introduces the experiment setup used. Reference sensing and error sensing techniques are then discussed, respectively, in Chapter 3—Reference Sensing and in Chapter 4—Error Sensing. In Chapter 5—Actuators, the development and performance of Smart Foam actuators is discussed. Chapter 6—Coherence and Causality Studies then discusses the importance of coherence and causality and their relation to active noise control with Chapter 7—Active Noise Control presenting the active noise control experiments and simulations. Conclusions and recommendations for future work are then presented in Chapter 8—Conclusions and Recommendations. Appendices are provided for the design and qualification of the wind tunnel, design and qualification of the summing amplifiers used for the error sensor arrays, and computer codes used for modelling, pre– and post–processing of control simulations and data reduction.

Chapter 2

Correlation of Turbulent Flow and its Influence on Active Noise Control

Since the acoustic field to be controlled is radiated by a plate subjected to a turbulent boundary layer, it is important to first understand the characteristics of such a flow. This chapter introduces the concept of turbulent flow and how it influences plate vibration. In addition, it presents experimentally determined data describing the characteristics of the turbulent flow acting on the plate. It is this plate which then radiates into the anechoic environment. The resulting acoustic pressure is minimized by the control system.

It will be shown herein that a turbulent flow is both temporally and spatially random or uncorrelated. In addition, it will be shown that the response of a baffled plate subjected to a tangentially acting turbulent flow also vibrates in an uncorrelated manner.

Knowledge of the spatial and temporal correlation of the plate vibration is important since it directly relates to the performance of the control system. The spatial correlation relates to the number of measurements required to accurately describe the response. Too few measurements would give an inaccurate estimation of the plate response since portions of the plate would vibrate in a manner uncorrelated with those measured. For this research effort, this directly relates to the number of reference sensors required to accurately describe the turbulent boundary layer induced plate vibration. Further, the temporal correlation describes the time span in which a signal, measured at a fixed point, is related to itself. This directly relates to the minimum sampling rate required by the control system to achieve sufficient control.

2.1 Theory

This section introduces the theory of turbulent flow, spatial and temporal correlation of such a flow, vibration of plates, and acoustic radiation resulting from a vibrating plate.

Theory of Turbulent Flow

Turbulent flow is a complex phenomenon described using advanced theories. Concepts described here are those pertaining to the influence of turbulent boundary layers on plate vibration and resulting radiated noise. The parameters discussed are the Reynold's number, boundary layer thickness, and the lengths of eddies and their aspect ratios within the turbulent boundary layer. These concepts are introduced first for a free stream impinging on a flat plate, as is the case for an aircraft in flight. However, this research effort examined a turbulent boundary layer induced plate vibration given an internal flow (the flow within the wind tunnel test section). Therefore, theories presented for flow over a flat plate are then expanded to describe internal flows. Further, temporal and spatial correlation of the flow within the turbulent boundary layer, and the determination of the frequency spectrum of a turbulent flow are presented.

"Turbulence is produced where the gradient of mean velocity [of the flow] is different from zero. Production is most vigorous in wakes and adjacent to walls, and since a wake owes its formation to separation from a solid body, a wall is seen to be essential, directly or indirectly, for the generation of turbulence [59]". The boundary layer is a "thin layer of retarded fluid whose forward motion is impeded by a drag exerted by the plate [59]", F_{shear}. Although this drag force impedes the boundary layer flow, the free stream convects linear momentum in the flow direction and a mass flow rate across the outer edge of the boundary layer thereby maintaining the turbulent flow [60]. This is shown in Figure 2.1 for a flow in the x direction having a velocity profile varying with distance from the wall .

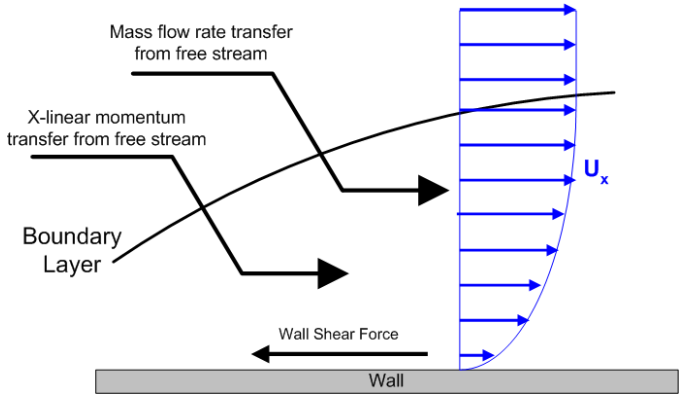

Figure 2.1: Representation of the nominal boundary layer.

The basic concept of a boundary layer is a velocity profile, starting from zero at some solid, stationary boundary, and increases to a velocity approaching that of the free stream. This basic concept, however, has been described using several arbitrary definitions when defining its *thickness*. Several definitions for boundary layer thickness exist, including: nominal thickness, displacement thickness, momentum thickness, and energy thickness.

Nominal thickness is the distance from the stationary boundary to that point in the flow having a velocity of $0.99U_0$ where U_0 is the free stream velocity. The displacement thickness concept regards the thickness of a layer in the free stream having a mass flow rate equal to the difference in mass flow rate between the boundary layer and a layer in the free stream having the same space. In effect, the displacement thickness concept represents the distance the streamlines of the free stream shifted due to the presence of the boundary layer. The momentum thickness and energy thickness are similar to the definition used for the displacement thickness concept. However, for momentum thickness, the governing metric is the difference in flow momentum between the freestream and boundary layer occupying the same space, and for the energy thickness method, it is the difference in flux of kinetic energy.

Characteristics of a turbulent flow are directly related to the thickness of the boundary layer. For this work, the sizes of the eddies existing in the boundary layer are most important. Eddies must be able to physically fit within the velocity profile of the boundary layer, and therefore, it is the nominal thickness of the boundary layer which must be considered. Figure 2.2 depicts this graphically.

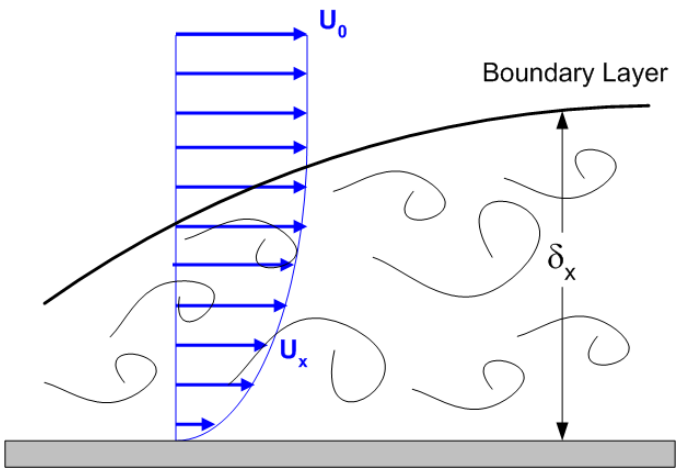

Figure 2.2: Representation of the nominal boundary layer for a turbulent flow.

Knowing the geometry of the flat plate, the flow medium, and its mean velocity, the ratio of inertia forces and viscous forces may be calculated. This ratio is referred to as the Reynold's number from which the boundary layer thickness may be estimated. The range of eddy lengths existing in the boundary layer may then be determined and it is these eddy lengths which relate to temporal and spatial flow correlation which in turn influences the temporal and spatial correlation of the plate vibration. The Reynold's number for flow across a flat plate may be expressed as

$$R_x = \frac{U_0 x}{\nu} \tag{2.1}$$

where x is the flow distance travelled from the leading edge, and ν the kinematic viscosity [61]. If the calculated Reynold's number is greater than the critical Reynold's number (R_{crit}) the flow will be turbulent. For a flat plate, $R_{crit} = 500,000$ is typically used [60].

Boundary layer flow may be either laminar or turbulent. Starting off as laminar, the flow will transition to turbulence at some point, as shown in Figure 2.3, where the critical Reynold's number is achieved. This point is referred to as the critical distance, x_{crit} and may be determined by equation 2.1 by setting $R_x = R_{crit}$.

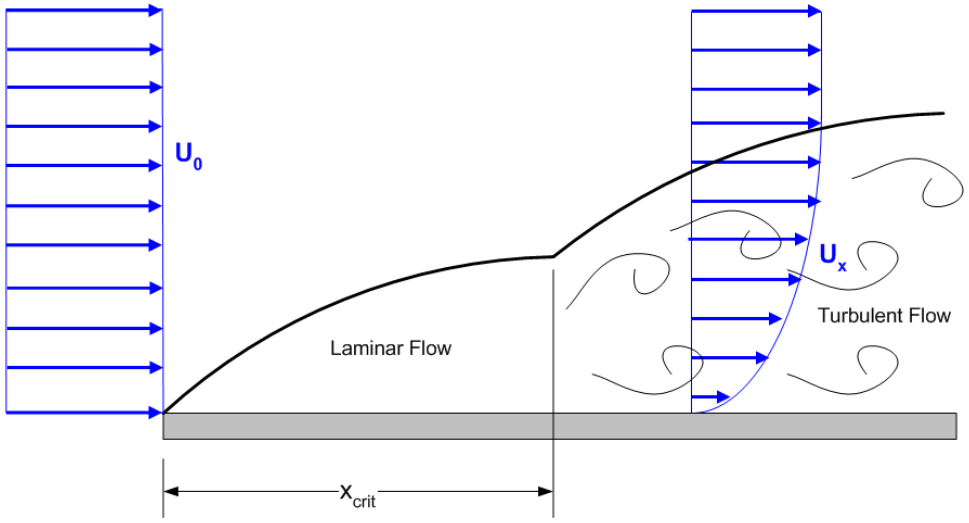

Figure 2.3: Laminar flow transitioning to a turbulent flow.

The boundary layer thickness for flow across a flat plate may then be determined by [61]

$$\delta = \frac{0.16x}{R_x^{1/7}} \tag{2.2}$$

and flow speed within the boundary layer at some distance y from the wall may then be estimated by [60]

$$U_x = \left(\frac{y}{\delta}\right) U_o \tag{2.3}$$

For flow within a circular duct the Reynold's number may be expressed as

$$R_D = \frac{U_0 D}{\nu} \tag{2.4}$$

where D is the inner diameter of the duct. The onset of turbulence is generally considered to occur for an internal flow when the duct Reynold's number is greater than the critical duct Reynold's number $R_{crit} > 2300$ [60]. However, "for the Reynold's number range between 2000 to 4000, the flow is unstable and this zone is called the *transition zone*[62]".

To determine the Reynold's number for a rectangular duct, the effective diameter of an imaginary circular duct must first be computed. This is referred to as the *hydraulic diameter* and is expressed as

$$D_H = \frac{4A_{flow}}{P_{flow}} \tag{2.5}$$

where A_{flow} is the cross–sectional area of the duct and P_{flow} the wetted perimeter of the flow within the duct. For a square duct having sides of length s, the hydraulic diameter is

$$D_H = \frac{4s^2}{4s} = s \tag{2.6}$$

Therefore, the hydraulic diameter of a square duct is simply the length of one side, $D_H = s$.

By equations 2.4 and 2.5, the duct Reynold's number is $R_D = 49$ m/s (0.305 m) / $1.5(10)^{-5} = 9.96(10)^5$. Since $9.96(10)^5 \gg 2300$ the internal flow is turbulent.

Analogous to the critical distance, x_{crit} for flow over a flat plate, the fully developed internal flow is shown in Figure 2.4 and occurs at the *entrance length* [63]. For a laminar flow, this would be estimated by

$$L_e \approx 0.06 D_H R_D \tag{2.7}$$

and for a turbulent internal flow the entrance length is estimated to be

$$L_e \approx 4.4 D_H R_D^{1/6} \tag{2.8}$$

The maximum ratio of entrance length to hydraulic diameter is defined to be [63]

$$\left(\frac{L_e}{D_H}\right)_{max} \approx 140 \tag{2.9}$$

Since the flow within the duct was determined to be turbulent, equation 2.8 is used giving $L_e \approx 4.4$ (0.305 m) $(9.96(10)^5)^{1/6} = 13.4$ m and $L_e/D_H = 43.9$ satisfying equation 2.9.

By equation 2.3, the boundary layer displacement thickness may be assumed to vary linearly starting at zero at the duct entrance [63]

$$\delta = \frac{x}{L_e}\frac{D_H}{2} \tag{2.10}$$

As stated in Appendix A—Wind Tunnel Setup and Qualification, the distance from the converging nozzle to the trailing edge of the flat plate mounted in the wind tunnel test section was four meters. Therefore, at the trailing edge of the plate used the boundary layer displacement thickness is estimated to be 45.5 mm or 1.8 inch. As shown in the next section, the order of the largest eddies is related to the displacement thickness.

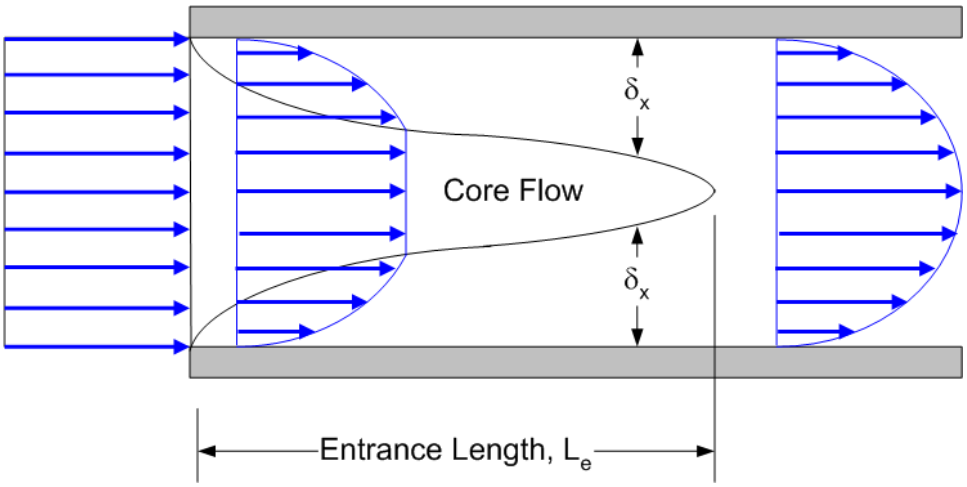

Figure 2.4: Boundary layer development of an internal flow.

Theory of Correlation

Correlation of the turbulent flow is most important since it is the random nature of the turbulent boundary layer that results in such highly uncorrelated plate vibration. Correlation of an output signal with a given input signal may be performed to estimate the relation between the two signals. Such an analysis may be performed between two signals at a given time when measured at two different locations and is referred to as *spatial correlation*. Further, *temporal correlation* refers to the correlation between two transient signals measured at the same location with one signal lagging in time relative to the other by time delay τ [64] [65].

The general form of correlation is the cross–correlation between two continuous signals x_1, x_2 where $x_1 \neq x_2$ and is referred to as autocorrelation for $x_1 = x_2$. Temporal cross–correlation is defined as [64]

$$R_{x_1x_2}(\tau) = \int_{-\infty}^{\infty}\int_{-\infty}^{\infty} x_1x_2p(x,y)\,\mathrm{d}x_1\,\mathrm{d}x_2 \tag{2.11}$$

where $x_1 = x_k(t)$, $x_2 = y_k(t+\tau)$, $k = 1, 2, 3, \ldots$ the signal index, and $p(x_1, x_2)$ the probability density function. The relation between the cross–correlation and the autocorrelations of the input and output signals is expressed in the cross–correlation inequality

$$|R_{xy}(\tau)|^2 \leq R_{xx}(0)R_{yy}(0) \tag{2.12}$$

Further, the cross–correlation function is required to be a non–negative, definite function such that reversing the order of the two signals, x, y produces the same result [64]

$$R_{xy}(\tau) = R_{yx}(-\tau) \tag{2.13}$$

Note, for $x = y$ the autocorrelation is symmetric about $\tau = 0$ where it has a maximum value. "This result is consistent with the notion that a signal matches perfectly with itself at zero shift [27]".

The probability density function requires [64]

$$p(x) \geq 0 \tag{2.14}$$

and

$$\int_{-\infty}^{\infty} p(x)\,\mathrm{d}x = 1 \tag{2.15}$$

Over some interval $a \leq x \leq b$ a uniform probability function is expressed as $p(x) = \frac{1}{b-a}$ [64]. Therefore, given a uniform probability function for transient signals x_1, x_2 of duration T starting at time zero, the cross–correlation may be expressed as [64]

$$R_{x_ky_k}(\tau) = \frac{1}{T}\int_0^T \int_0^T x_k(t)y_k(t+\tau)\,\mathrm{d}x_k\,\mathrm{d}y_k \tag{2.16}$$

Likewise, the preceding may be expressed for spatial correlation. In place of time delay, τ, is used spatial lag, δ where $0 \leq \delta \leq L$. L equals the spatial distance between the locations of two measured transient signals taken at a common time. The spatial cross–correlation may then be expressed as [64] [65]

$$R_{x_k y_k}(\delta) = \frac{1}{L} \int_0^L \int_0^L x_k(l) y_k(l+\delta) \, \mathrm{d}x_k \, \mathrm{d}y_k \tag{2.17}$$

Analyzing digitized signals, as obtained by a data acquisition system, requires the use of the discrete correlation function. The general expression for discrete correlation, $r_{x_k y_k}(l)$, given an infinite sample size is

$$r_{x_k y_k}(l) = \sum_{n=-\infty}^{\infty} x_k(n) y_k(n-l) \tag{2.18}$$

where l is the time shift Δt or spatial lag Δx. As for the continuous correlation function, the discrete correlation function satisfies $r_{xy}(l) = r_{yx}(-l)$.

The general expression for the discrete correlation function of two causal signals over a finite sample given some time delay or spatial lag at sample m may be expressed as

$$r_{x_k y_k}(m) = \sum_{n=m}^{N-1} x_k(n) y_k(n-m) \tag{2.19}$$

where $0 \leq m \leq N-1$ for x_k, y_k of length N producing $r_{x_k y_k}(m)$ of length $2N-1$ with zero lag at sample N.

Correlation of a Turbulent Flow

Two points within the boundary layer may be related in terms of their spatial and temporal correlation. Two common methods of correlating turbulent flow are the Eulerian autocorrelation and the Lagrangian correlation techniques. "Eulerian autocorrelation and Lagrangian correlation can be used to define length and time scales of turbulence. Eulerian autocorrelation is used for isotropic turbulence. Lagrangian correlation is formed from two components of the fluctuation of velocity of a given element of fluid at different times and is used in studies of diffusion and dispersion of fluid borne matter in turbulent flows.[66]" Small eddies are the product of the breakdown of larger ones losing energy in the form of heat. Lagrangian methods, since they deal primarily with diffusion and dispersion of turbulent flows, are better suited for these larger eddies. The Eulerian approach, being the correlation of the flow at two points, is better suited for smaller eddies. Since this research is for relatively low frequencies, smaller eddies were the dominant characteristic of the turbulent flow. Therefore, the Eulerian approach to correlation of turbulent flow was investigated.

Given two points, A and B, separated by some distance r, their components of velocity fluctuation in Eulerian terms may be represented as in Figure 2.5 [59].

Correlation coefficients, or correlation normalized by the square of the Lagrangian standard deviation of velocity, is the form often used in describing turbulent flow. Describing

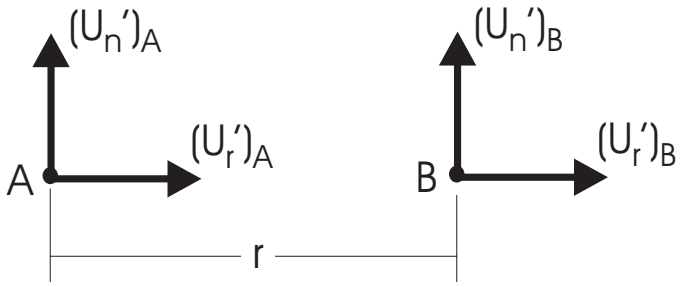

Figure 2.5: Components of a turbulent flow at two points.

the relation of the flow between points A and B may be expressed as

$$\begin{aligned} f(r) &= \frac{\overline{(u'_r)_A\,(u'_r)_B}}{u^{*2}} \\ g(r) &= \frac{\overline{(u'_n)_A\,(u'_n)_B}}{u^{*2}} \end{aligned} \tag{2.20}$$

where $u'_r = \overline{u} - u$, the difference between the mean and instantaneous velocities at a point. Turbulence microscales, an indication of the length of shorter eddies, may then be determined by

$$\begin{aligned} \lambda_f &= \frac{r}{\sqrt{1 - f(r)}} \\ \lambda_g &= \frac{r}{\sqrt{1 - g(r)}} \end{aligned} \tag{2.21}$$

Note that λ_f is the correlation length in the flow direction, $\overline{AB}$, and λ_g is the correlation length normal to $\overline{AB}$. These two correlation lengths are related by

$$g(r) = f(r) + \frac{r}{2}\frac{\partial}{\partial r} f(r) \tag{2.22}$$

and their corresponding microscale lengths are related by

$$\lambda_f = \sqrt{2}\lambda_g \tag{2.23}$$

Therefore, the aspect ratio of smaller eddies, on the order of turbulent microscales, is $\sqrt{2}$. This is emphasized further in Figure 2.1a.

Turbulence macroscales for eddy lengths may then be determined by integrating the correlation coefficients (equations 2.20) over all spacings

$$\begin{aligned} \Lambda_f &= \int_0^\infty f(r)\,\mathrm{d}r \\ \Lambda_g &= \int_0^\infty g(r)\,\mathrm{d}r \end{aligned} \tag{2.24}$$

Note that the macroscales for length, Λ_f and Λ_g, are related by

$$g(r) = f(r) + \frac{r}{2}\frac{\partial}{\partial r} f(r) \tag{2.25}$$

which leads to the following relation for the aspect ratio of macroscales

$$\Lambda_f = 2\Lambda_g \tag{2.26}$$

As calculated previously in this chapter, the boundary layer thickness at the trailing edge of the vibrating plate is 45.5 mm or 1.8 inch. By the relation presented in Figure 2.1b, the macroscale, or length of the biggest eddy in the flow, would be twice that value—91 mm or 3.6 inch.

Knowing the macroscales, the temporal correlations may be determined by

$$T = \frac{\Lambda_f}{u^*} \tag{2.27}$$

where u^* is the Lagrangian standard deviation of velocity. Note that since there is no mean flow in the cross–flow direction, the notion of a temporal correlation in this direction would be meaningless. Temporal correlation for microscales is not discussed since larger (macroscale) eddies dominate the character of the turbulent flow. Regarding the character of eddies within the flow, "Large eddies are on the order of the boundary layer thickness [and] near the wall, [the flow] has most energy in low wave numbers [59]." In addition, "the dissipation is weighted by the factor k^2 and is clearly more effective at large wave numbers. We deduce that [net] dissipation occurs in the small eddies [59]." These concepts were especially important in regards to this research effort since the control band of the TBL induced noise was for low frequencies (< 1200 Hz). Therefore, it was only necessary to consider the effects of the larger eddies (those at lower wave numbers).

Eddies at a given wave number have a corresponding spin rate and length. Each component i of the wave number may be expressed as

$$k_i = \frac{2\pi}{\lambda_i} = \frac{2\pi n_i}{\overline{u}_i} \tag{2.28}$$

where λ is the length of the eddy with spin rate n (Hz) having a mean velocity component of $\overline{u_i}$. Knowing this relation and the flow direction macroscale, the wavenumber in the flow direction for the largest eddy is then $2\pi/\Lambda_f$ giving 0.054 m^{-1}. By the same relation, the corresponding spin rate is then $u_i/\Lambda_f = 49$ m/s / 0.116 m = 422 Hz.

Regarding the difficulty of theoretically determining the nature of a turbulent flow, Cebici and Smith [66] stated, in reference to their theories presented on the general behavior

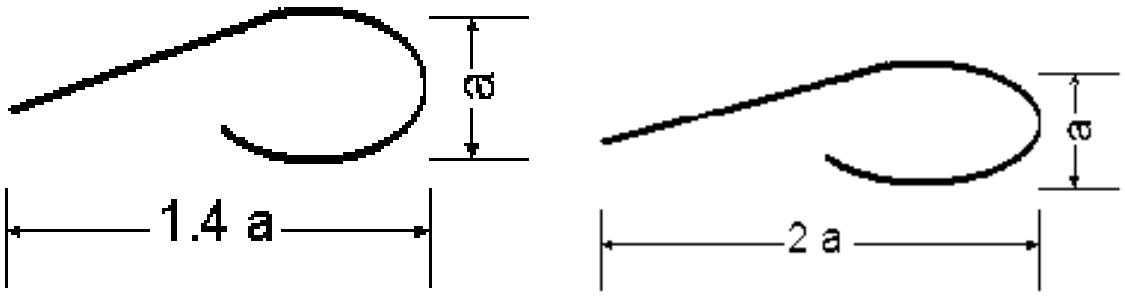

a) Microscale aspect ratio.

b) Macroscale aspect ratio.

Figure 2.6: Eddy aspect ratios. a) Eddy microscales have aspect ratios on the order of $\sqrt{2}$ b) The largest eddies are restricted in size by the boundary layer thickness. In–flow and cross–flow macroscales have an aspect ratio on the order of 2.

of turbulent boundary layers, "it should be noted that the actual behavior of turbulent flow differs appreciably from that suggested to the formulas." This difficulty occurs because "the fluctuating velocity is *at least* one order of magnitude smaller than the free stream velocity, and the mixing length is *comparable* in thickness to the size of the boundary layer." They go on to say "when an eddy moves a distance l in the transverse direction, it will travel a rather long distance in the downstream direction in the same length of time. At the end of its travel, the eddy will find itself in a location where the conditions are very different from those at its origin." Therefore, to best determine the effect of the turbulent flow and its influence on plate vibration, fluctuations in surface pressure at the wall must be determined experimentally. From this experiment, the forcing function acting on the plate may be inferred knowing the spatial and temporal correlation between the measurement points. Spatial and temporal correlation, determined by experiment, is discussed later in this chapter.

Theory of Acoustic Radiation from a Vibrating Plate

The amount of acoustic energy radiated by an finite plate is a function of the structural wavenumber, the acoustic wavenumber, and the boundary conditions [67]. However, considering an infinitely long plate, acoustic radiation is dependent only on the relation between the structural and acoustic wavenumbers; boundary conditions do not exist. Acoustic radiation of a finite plate is then an extension of the infinite case. Therefore, acoustic radiation from an infinitely long, one–dimensional plate due to transverse vibration is first considered followed by the finite case.

Transverse displacement of the one–dimensional, infinitely long plate may be expressed as

$$\eta\left(x,t\right)=\tilde{\eta}e^{j\left(\omega t-\kappa x\right)} \tag{2.29}$$

where $\eta(x,t)$ is the plate transverse displacement at point x and time t, $2\pi/\kappa$ is a structure wavelength, and ω/κ is the structure phase speed, c_{ph} as shown in Figure 2.7.

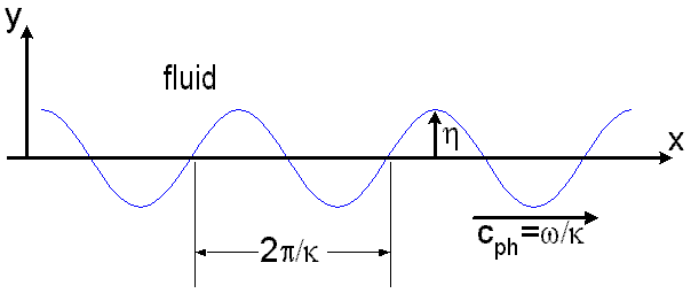

Figure 2.7: Transverse wave in an infinitely long plate in contact with a fluid.

Knowing the solution of the two–dimensional wave equation along with the fluid momentum equation at the plate–fluid interface, the acoustic field may be determined. This leads to the expression relating the acoustic and structural wavenumber components

$$k_y = \pm\left(k^2 - \kappa^2\right)^{1/2} \tag{2.30}$$

where $k = \omega/c$. Note that the acoustic wavenumber component parallel to the structure surface, k_x, must equal the acoustic wavenumber κ for this relation to be satisfied. The value of k_y describes how well the infinite plate radiates. The three cases include

a) $\kappa < k$. The speed of sound in the fluid is less than the wave phase speed in the plate. Therefore, sound radiates and does so at an angle of

$$\cos\phi = k_y/k = \left(1 - \frac{\kappa}{k}\right)^2 \tag{2.31}$$

and the real, positive wave impedance at the fluid–structure interface is

$$\frac{\tilde{p}}{\tilde{v}}_{y=0} = \frac{\rho_0 c}{\sqrt{k^2 - \kappa^2}} \tag{2.32}$$

b) $\kappa > k$. The speed of sound in the fluid is greater than the wave phase speed in the plate. Since $\kappa > k$, k_y is imaginary, $k_y = -j\sqrt{\kappa^2 - k^2}$, and so the disturbance of the fluid decays exponentially with increasing distance from the plate surface. The wave impedance is then imaginary and positive and does not exert any work on the fluid

$$\frac{\tilde{p}}{\tilde{v}}_{y=0} = \frac{j\rho_0 c}{\sqrt{\frac{\kappa^2}{k^2} - 1}} \tag{2.33}$$

Therefore, the plate does not radiate.

c) $\kappa = k$. The speed of sound in the fluid and the wave phase speed in the plate are equal giving $k_y = 0$ and the wave impedance is

$$\left(\frac{\tilde{p}}{\tilde{v}}\right)_{y=0} \rightarrow \infty \tag{2.34}$$

Since a finite plate vibration produces an infinite sound pressure, this scenario may not be realized physically. Therefore, on an infinite structure, acoustic radiation will occur only at structural wavenumbers which are less than the acoustic wavenumber. However, for real, finite systems, this is not true; some degree of acoustic radiation will occur at all wavenumbers.

The equation of motion of a thin, flat, isotropic plate having uniformly distributed properties may be expressed as [68]

$$EI\left(\frac{\partial^4 w}{\partial x^4} + 2\frac{\partial^4 v}{\partial x^2 \partial z^2} + \frac{\partial^4 v}{\partial z^4}\right) + \rho h \frac{\partial^2 v}{\partial t^2} = -P(x,z)e^{j\omega t} \tag{2.35}$$

where the moment of inertia per unit width is

$$I = \frac{h^3}{12(1-\nu^2)} \tag{2.36}$$

and E is the modulus of elasticity, h the plate thickness, ν Poisson's ratio, ρ the mass density, x, z the coordinates of the plate, and w the plate transverse displacement. The applied pressure load P is set to zero for the case of free vibration. Equation 2.35 neglects rotational inertia and assumes the response is small with respect to thickness. This formulation is then limited to low frequencies [69].

For the simply supported, baffled, finite length plate of infinite width, as shown in Figure 2.8, the transverse velocity distribution for mode p is

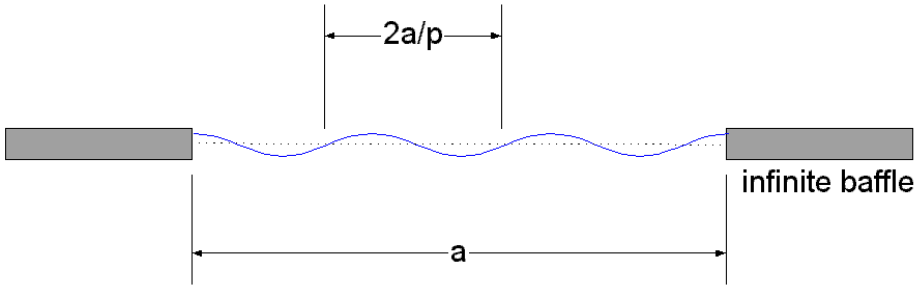

Figure 2.8: Modal vibration of a simply supported, baffled beam of infinite width.

$$v_n(x,t) = \tilde{v_p} \sin\left(\frac{p\pi x}{z}\right) e^{j\omega t}\ , \quad 0 < x < a \tag{2.37}$$

and equals zero for all other values of x. The wavenumber transform takes the form

$$\tilde{V}\left(k_x\right) = \tilde{v_p}\frac{\left(p\pi/a\right)\left[\left(-1\right)^p e^{-jk_x a} - 1\right]}{k_x^2 - \left(p\pi/a\right)^2} \tag{2.38}$$

The wavenumber transform of the surface pressure can be shown to take the form [67]

$$\bar{P} = \frac{1}{4\pi} Re\left\{\int_{-\infty}^{\infty} \frac{\pm\omega\rho_0 \left|\tilde{V}\left(k_x\right)\right|^2}{\sqrt{k^2 - k_x^2}}\,\mathrm{d}k_x\right\} \tag{2.39}$$

and since only wavenumbers contributing to the real part of the integral radiate, the wavenumber transform of the surface pressure may be simplified to

$$\bar{P} = \frac{\rho_0 ck}{4\pi}\int_{-k}^{k} \frac{\left|\tilde{V}\left(k_x\right)\right|^2}{\sqrt{k^2 - k_x^2}}\,\mathrm{d}k_x \tag{2.40}$$

and so, to determine the power radiated by mode (p, q), $\left|\tilde{V}\left(k_x\right)\right|^2$ must be evaluated and may be calculated using equation 2.41.

$$\left|\tilde{V}_{p,q}\left(k_x\right)\right|^2 = \left[\frac{2\pi p/a}{k_x^2 - \left(p\pi/a\right)^2}\right]^2 \sin^2\left(\frac{k_x a - p\pi}{2}\right) \tag{2.41}$$

The spectrum peaks at the structural wavelength, $\lambda = 2a/p$ or, for the corresponding wavenumber, $k_x = 2\pi/\lambda$ and has a value of $\left|\tilde{v_p}\right|^2 a^2/4$.

Knowing how an infinitely long plate radiates, the theory may be expanded to describe the finite plate. A flexural wave travelling through the plate at some angle α to the x-axis may be expressed in terms of the x, z wavenumber components as

$$k_f^2 = k_x^2 + k_z^2 \tag{2.42}$$

where each component may be expressed as

$$k_x = k_f \cos(\alpha) \tag{2.43}$$

and

$$k_z = k_f \sin(\alpha) \tag{2.44}$$

The general free response of a finite plate may then be expressed

$$v(x, z, t) = Ae^{-j(k_x x + k_z z)}e^{j\omega t} \tag{2.45}$$

or, on resonance for mode (p, q) as

$$v_{p,q}(x, z, t) = V_{p,q}\sin(k_x, px)\sin(k_z, qz)e^{j\omega t} \tag{2.46}$$

where $V_{p,q}$ is the modal amplitude of mode (p, q) with each coordinate direction having wavenumber eigenvalues

$$k_{x,p} = p\pi/a; p = 1, 2, 3, \ldots \tag{2.47}$$

$$k_{z,q} = q\pi/b; q = 1, 2, 3, \ldots \tag{2.48}$$

The response of equation 2.46 is shown in Figure 2.9 for select low order modes having resonant angular frequencies

$$\omega_{p,q} = \sqrt{\frac{EI}{\rho h}} \left[\left(\frac{p\pi}{a} \right)^2 + \left(\frac{q\pi}{b} \right)^2 \right] \tag{2.49}$$

or in terms of equations 2.47 and 2.48

$$\omega_{p,q} = \sqrt{\frac{EI}{\rho h}} \left[k_{x,p}^2 + k_{z,q}^2 \right] \tag{2.50}$$

The plate total response is then the summation of all modal responses given by equation 2.46 as

$$V(x, z, t) = \sum_{p=1}^{\infty} \sum_{q=1}^{\infty} v_{p,q}(x, z, t) \tag{2.51}$$

The plate forced response for each mode is determined by substituting the assumed free response of equation 2.46 into equation 2.35

$$V_{p,q} = \frac{4}{\rho h a b(\omega^2 - \omega_{p,q}^2)} \int_0^a \int_0^b P(x, z) \sin(k_{x,p} x) \sin(k_{z,q} z) \, \mathrm{d}x \, \mathrm{d}z \tag{2.52}$$

Notice that the undamped forced response goes to infinity at each resonance, $\omega = \omega_{p,q}$.

Knowing k_f, its components and the plate geometry, the wavevector diagram may be drawn as shown in Figure 2.10. Plate modes are depicted as the intersections of the grid lines with acoustic wavenumber $(k = \omega/c)$ superimposed.
The radii, k, k_f may be related by

$$k_f^2 = \sqrt{\frac{k^2 c^2 \rho h}{EI}} \tag{2.53}$$

or

$$\frac{k_f}{k} = c \left(\frac{\rho h}{EI} \right)^{1/4} \left(\frac{1}{\omega} \right)^{1/2} \tag{2.54}$$

Setting $k_f/k = 1$ gives an expression for the critical frequency, ω_c

$$\omega = c^2 \sqrt{\frac{\rho h}{EI}} = \omega_c \tag{2.55}$$

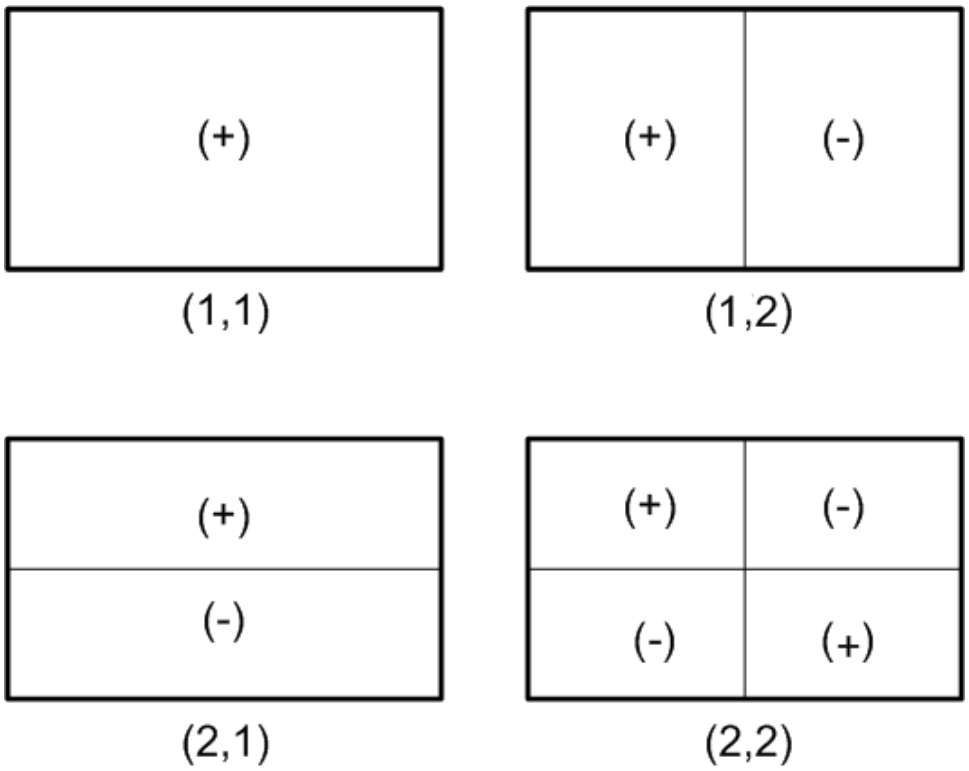

Figure 2.9: Modal responses of a plate for select low order modes.

thus allowing equation 2.54 to be expressed as

$$\frac{k_f}{k} = \sqrt{\frac{\omega_c}{\omega}} \tag{2.56}$$

Expressing equation 2.49 in terms of k_f

$$\omega = \sqrt{\frac{EI}{\rho h}} k_f^2 \tag{2.57}$$

Comparison of the dispersion relation (equation 2.57) for the finite plate to the acoustic wave relation, the critical frequency is represented as the intersection of the two curves as shown in Figure 2.11. For $\omega < \omega_c$, $k < k_f$ and the plate does not radiate well. Alternatively, above the critical frequency where $k > k_f$ such wavenumbers are considered *supersonic* and the plate radiates well [68].

To demonstrate the cut–on of a finite plate, the wavenumber spectra components must first be determined. By equation 2.41, the radiated power in the x direction due to mode (p, q) may be computed with the z component taking the same form. Equation 2.41 is restated here

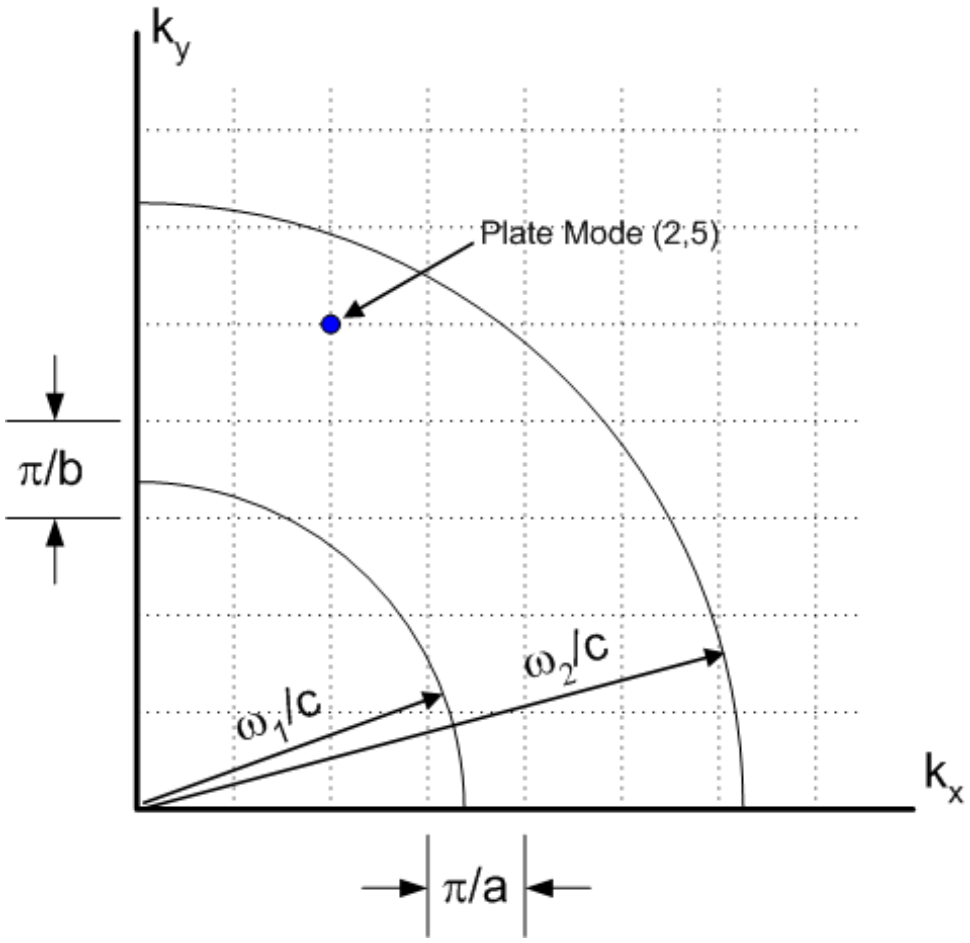

Figure 2.10: Wavevector diagram showing acoustic and bending wavenumbers.

$$\left|\tilde{V}_{p,q}\left(k_x\right)\right|^2 = \left[\frac{2\pi p/a}{k_x^2 - \left(p\pi/a\right)^2}\right]^2 \sin^2\left(\frac{k_x a - p\pi}{2}\right) \tag{2.58}$$

as well as in z

$$\left|\tilde{V}_{p,q}\left(k_z\right)\right|^2 = \left[\frac{2\pi q/b}{k_z^2 - \left(q\pi/b\right)^2}\right]^2 \sin^2\left(\frac{k_z b - q\pi}{2}\right) \tag{2.59}$$

Plotting these two equations as in Figures 2.12, the radiated power may be determined. Any combination of k_x, k_z where $k > k_x^2 + k_z^2$ results in achieving cut–on and the plate radiates well.

Sound generated by positive and negative plate vibration cancels and therefore does not radiate. However, for Figures 2.12–a,b, a net acoustic radiation occurs at the edges of

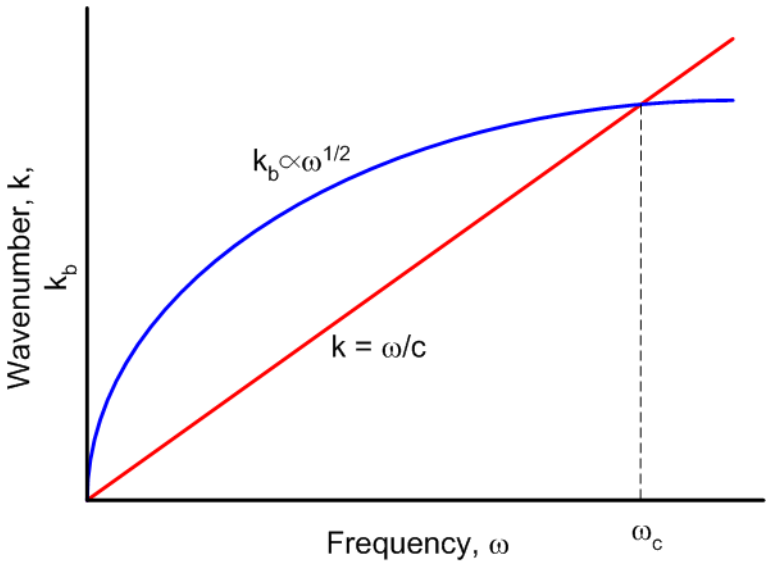

Figure 2.11: Dispersion relation. The intersection of the two curves depicts the critical frequency, ω_c.

the plate as shown in Figures 2.13. This is referred to as *edge modes* whereas for Figure 2.12–c, the plate radiates only at the corners and is thus referred to as a *corner mode*. The corner mode is shown in Figure 2.14.

Noise control experiments were conducted up to 800 Hz using a radiating aluminum plate measuring 0.248 m by 0.510 m. At 800 Hz, the acoustic wavenumber is k_0=14.6 m^{-1}. By the wavevector diagram in Figure 2.15, it is observed that wavenumbers corresponding to $m = 1, 2$ and $n = 1$ modes are less than the acoustic wavenumber at 800 Hz and therefore are cut–on. Modes having m, n indices outside this boundary are not cut–on at 800 Hz.

The (1,1) mode is spatially in phase at all points and therefore radiates from the entire vibrating surface. However, the cut–on (2,1) mode radiates as an edge mode satisfying $k > m\pi/a$ and $k > n\pi/b$. Modes of order $(m, 1)\forall m$ satisfying $k < m\pi/a$ and $k > n\pi/b$ radiate as corner modes. Further, modes of order $(1, n)\forall n$ and $(2, n)\forall n$ satisfying the conditions $k > m\pi/a$ and $k < n\pi/b$ also radiate as corner modes.

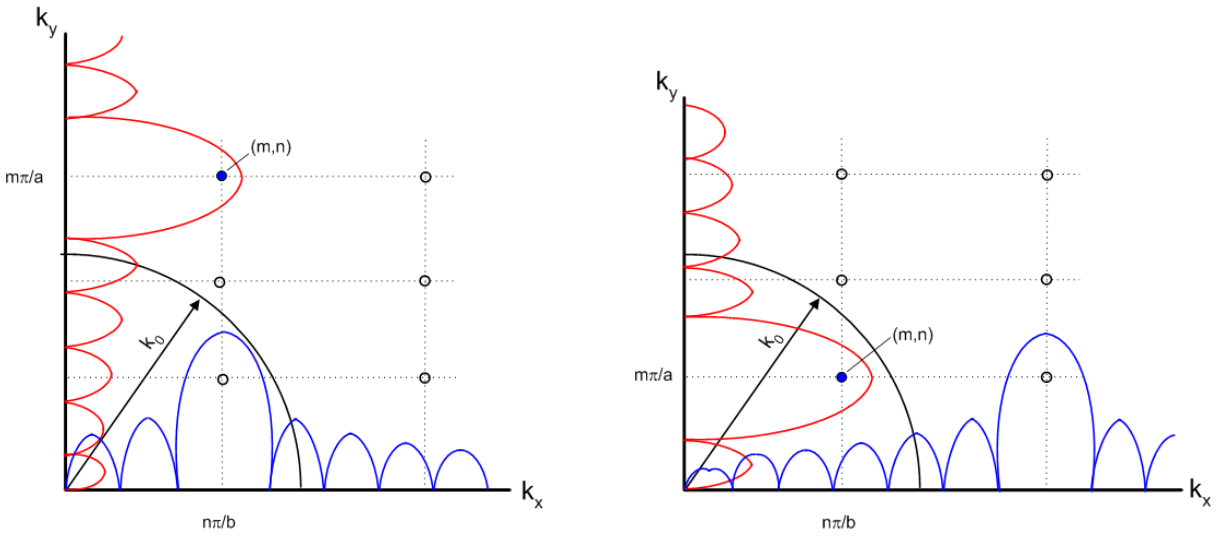

a) $k > m\pi/a$; $k < n\pi/b$

b) $k < m\pi/a$; $k > n\pi/b$

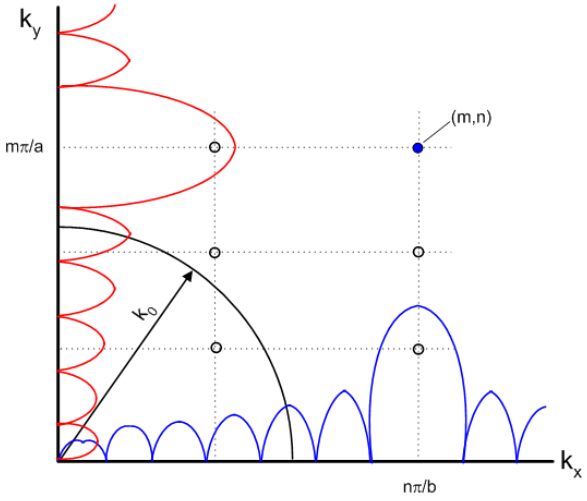

c) $k < m\pi/a$; $k < n\pi/b$

Figure 2.12: Wavenumber spectrae of finite plates. a) $k > m\pi/a$; $k < n\pi/b$, b) $k < m\pi/a$; $k > n\pi/b$, c) $k < m\pi/a$; $k < n\pi/b$

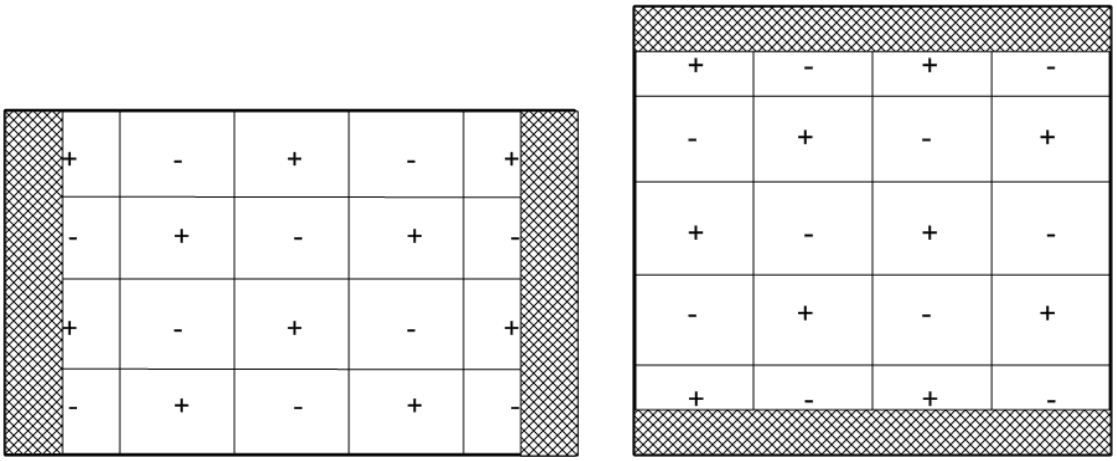

a)Net acoustic radiation from the sides

b)Net acoustic radiation from the top and bottom

Figure 2.13: Plate acoustic edge modes.

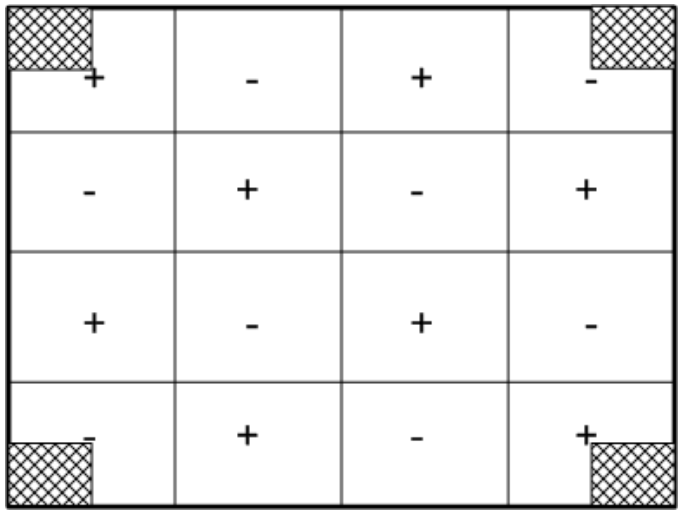

Figure 2.14: Plate acoustic corner mode.

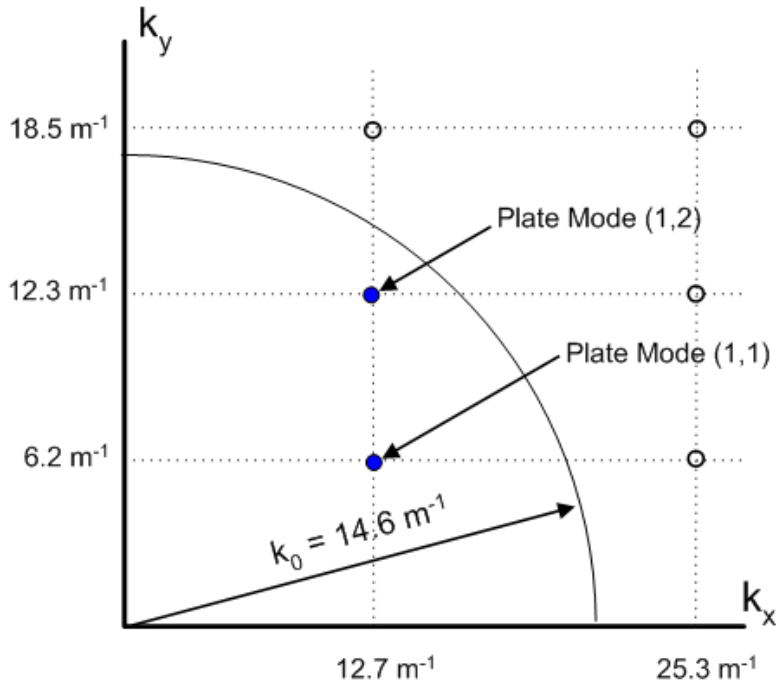

Figure 2.15: Plate vibration modes which are cut–on below 800 Hz.

2.2 Experiment Setup

The test setup consists of an aluminum plate mounted on a wall of a subsonic wind tunnel. The wind tunnel used reportedly had a flow speed of approximately Mach 0.1 and the plate measured 0.51 m (20″) along the flow, 0.248 m (9–3/4″) in width, with a thickness 1.6 mm (0.063″). An anechoic enclosure was placed over the plate in an effort to reduce the effect of background noise. An array of sixteen accelerometers was placed on the mid–line of the plate along the flow direction. These locations were spaced 25 mm (1″) apart and 64 mm (2–1/2″) from the plate ends. See Figures 2.16—2.19. Note that this study was performed prior to the rebuild described in Appendix A—Wind Tunnel Setup.

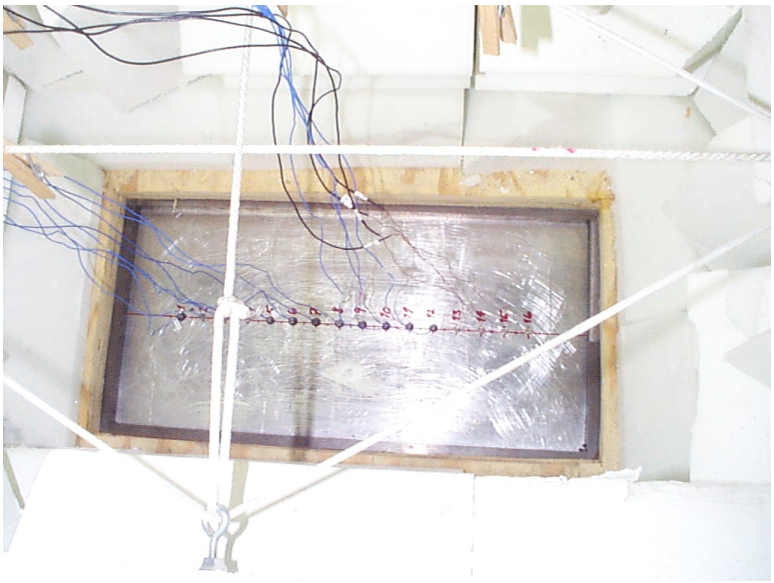

Figure 2.16: Sixteen accelerometers were mounted on the centerline of the plate in the flow direction to determine the correlation of the vibration due to the turbulent flow.

Sixteen microphones were then placed through the sidewall of the wind tunnel located along the length of the aluminum plate as shown in Figure 2.18. Microphone placements were in–line with their respectively numbered accelerometers and were mounted flush to the inside wall as shown in Figure 2.17 and Figure 2.18. This line array of sixteen microphones was centered between the duct ceiling and floor with 25 mm (1″) spacings. Measurements were also performed using a vertical microphone orientation as shown in Figure 2.19. Due to geometric limitations, the microphone spacing for the vertical measurements was reduced to 10 mm (5/8″).

The data acquisition system consisted of a Pentium®166 laptop computer with a 16 channel National Instruments data acquisition board. Acquired data were AC coupled and the sampling rate was set to 5000 Hz giving a maximum analysis frequency of 5000/2.56 =

Figure 2.17: Sixteen microphones were mounted along the centerline of the tunnel side wall to determine the correlation of the turbulent flow.

1953.1 Hz. Data were acquired in the time domain in 5.0 second blocks. Anti-aliasing filters were set to the maximum analysis frequency.

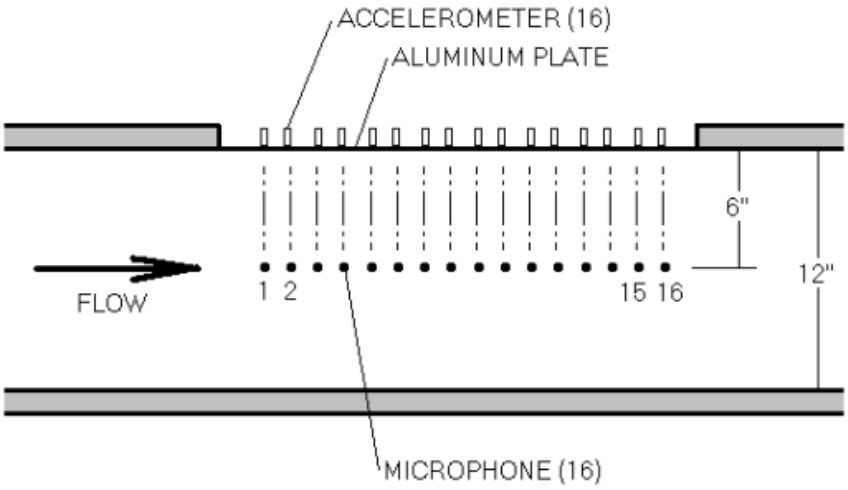

Figure 2.18: Sixteen microphones mounted with 25 mm spacings for flow–direction correlation measurements.

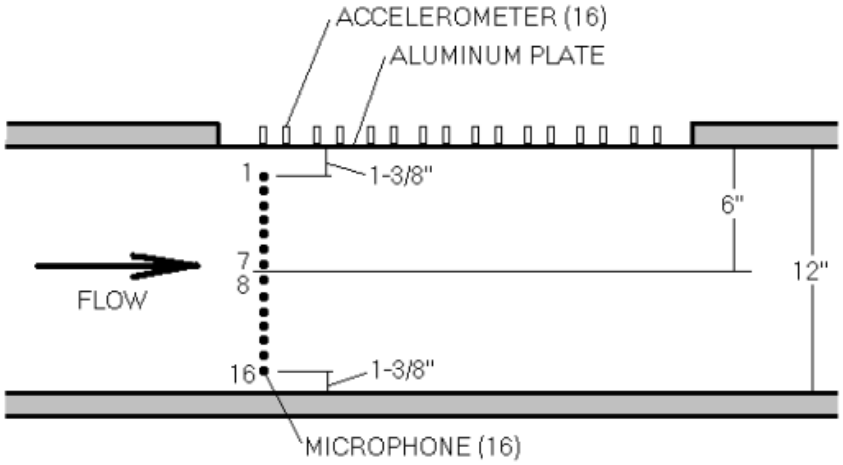

Figure 2.19: Sixteen microphones mounted with 25 mm spacings for flow–direction correlation measurements.

2.3 Results and Discussion

Flow and plate correlation studies were performed in an attempt to better understand the character of the disturbance. Knowing the character of the disturbance, it was assumed, may lead to a more effective control strategy.

Experimental Correlation of the Turbulent Flow

This section presents experimental results for the cross–correlation of the turbulent flow both in the flow and cross–flow directions

Cross–correlation of the turbulent flow measured using the flow–direction array of sixteen microphones is presented in Figure 2.20 as per the configuration described in Figures 2.17 and 2.18. Both temporal, τ, and spatial, δ, shifts are shown. The time delay represents how well correlated the data is at a single transducer to itself over time. Spatial shift refers to how well the data at a particular point in space correlates to data at another point in space at the same point in time. Spatial cross–correlation was -3 dB at a distance of 30 mm. For the temporal cross–correlation, a value of -3 dB occurred for a delay of 0.4 ms.

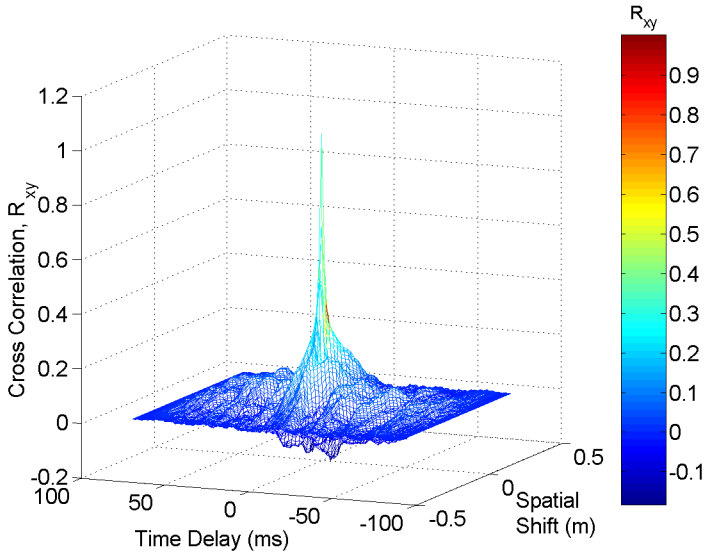

Figure 2.20: Surface plot of microphone cross-correlation, $R_{xy}(\tau, \delta)$, in the flow direction.

Data from Figure 2.20 was reprinted in Figure 2.21 in two dimensions. Notice that the graph in Figure 2.21, primarily at the main peak centered at $\tau = 0$ and $\delta = 0$, is not symmetric. Its skew is due to the fact that the sound field is affected by the flow in the duct.

To identify the frequency content of the signals, the Fourier transform of the time response of a microphone placed at the center of the microphone array was calculated. The

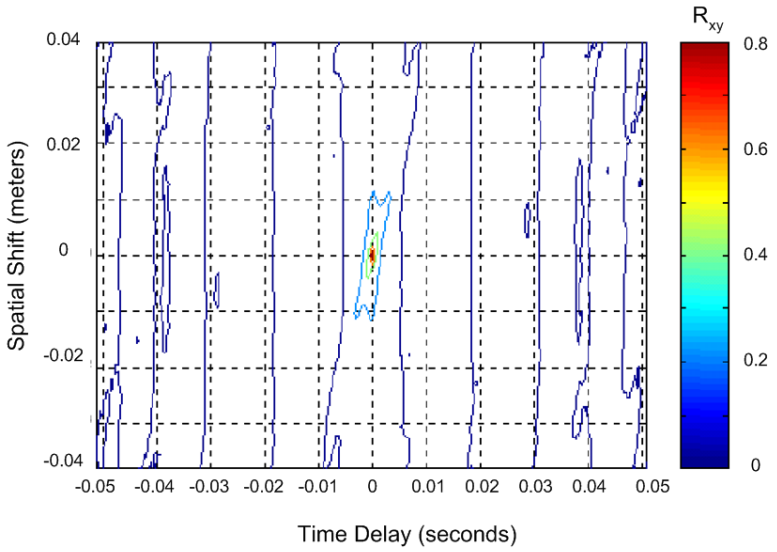

Figure 2.21: Contour plot of microphone cross-correlation in the flow direction.

resulting frequency response is shown in Figure 2.22. Note in Figure 2.22 that the (1,1) mode of the plate, as determined in Appendix A[1], resulted in the dominant correlation. This response was due to the turbulent flow exciting the plate (1,1) mode radiating into the enclosure. Note although the (1,2) mode, occurring at 165 Hz, was cut-on below 800 Hz it did not radiate as is apparent in Figure 2.22. This may be due in part to the mode vibrating as a dipole and further may indicate that the flow does not well excite this mode.

Cross–correlation of the pressure in the duct was then calculated in the vertical, or cross–flow, direction of the duct with results shown in Figure 2.23. Observation of the figure suggested that the flow was less correlated in both space and time when compared to measurements performed along the flow direction. Further, by Figure 2.24 the cross–flow data was determined to be symmetric with respect to both zero time delay and zero spatial shift. This should be expected since it may be assumed that the average cross–flow velocity would be zero.

Similar to flow correlation, cross–flow correlation quickly diminished with increasing temporal and spatial shifts. By equation 2.23, -3 dB spatial cross–correlation occurred at 25 mm. For temporal cross–correlation, a value of -3 dB resulted given a delay of 1.2 ms.

The Fourier transform of the time response of a microphone placed at the center of the microphone array was calculated. The resulting frequency response is shown in Figure 2.25. Notice, by comparing Figure 2.22 and Figure 2.25 that the noise radiated into the duct due to the plate (1,1) mode was significantly less for the cross–flow test case. For the test

[1]Note, the (1,1) plate response was computed to be 130 Hz prior to rebuilding the wind tunnel test section. After the rebuild, the (1,1) resonant response shifted to 119 Hz.

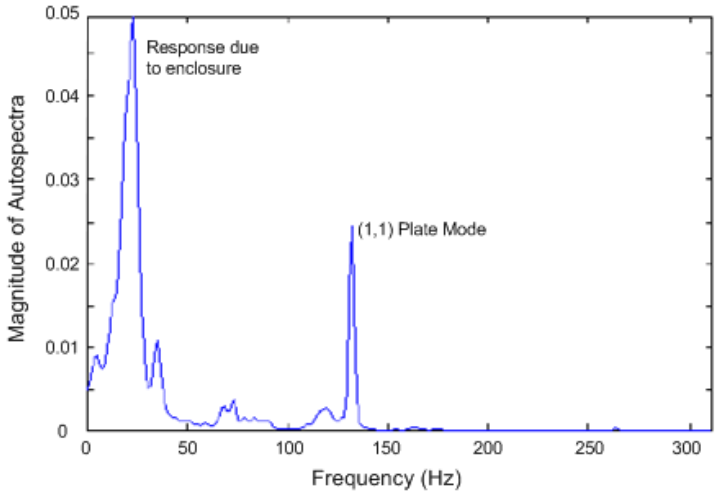

Figure 2.22: Plot of microphone autospectrum of a single microphone signal obtained at the center of the flow direction microphone array.

case utilizing microphones in–line with the flow the magnitude of the cross–spectrum at the (1,1) plate mode was approximately -16 dB whereas for the cross–flow test it was only about -20 dB. Further, as was shown for the flow parallel to the plate, the (1,2) mode again does not radiate.

The flow spectrum was then determined by measuring the frequency response of a single microphone in the flow. See Figure 2.26 for the experimentally determined, time averaged autospectrum of the flow from zero to 2000 Hz.

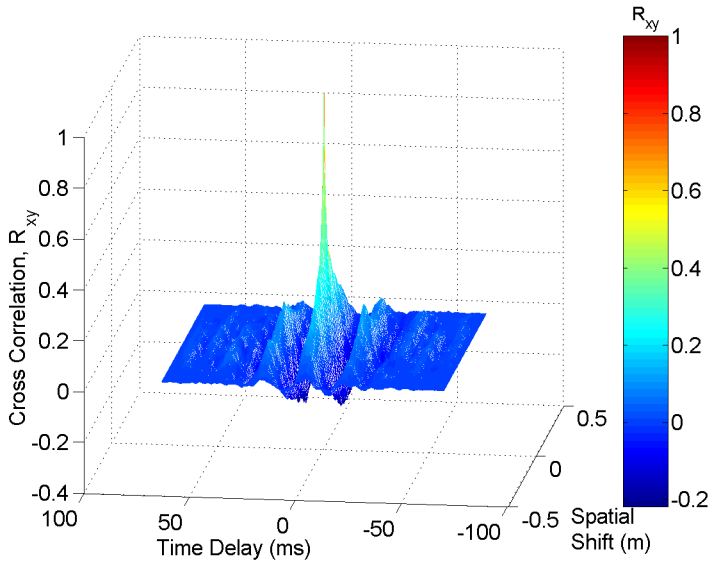

Figure 2.23: Plot of microphone cross-correlation in the cross–flow direction.

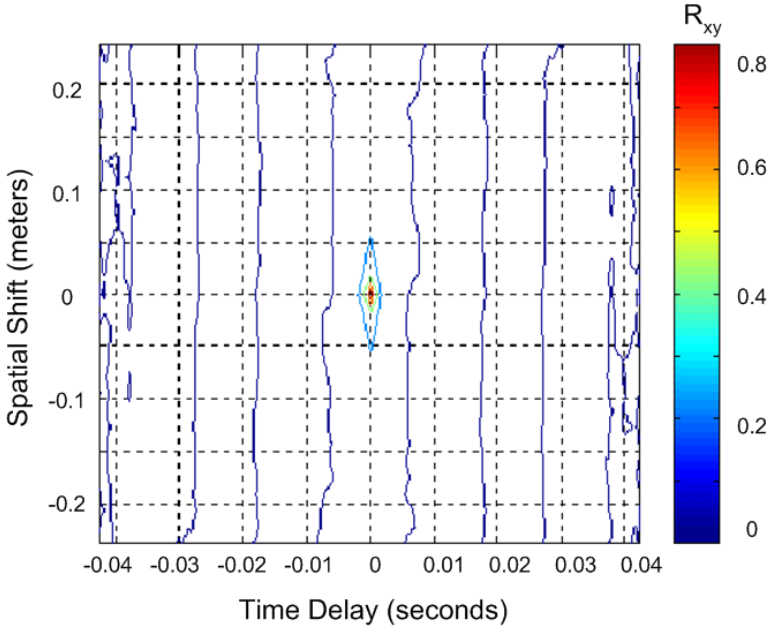

Figure 2.24: Contour plot of microphone cross-correlation in the cross–flow direction.

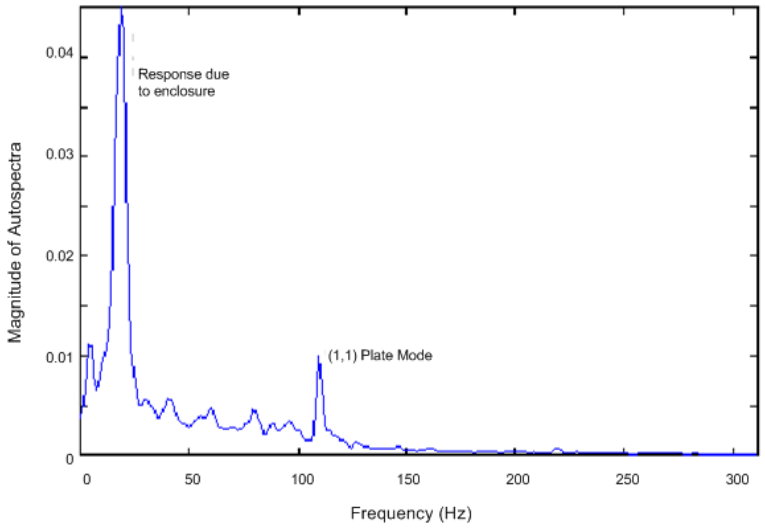

Figure 2.25: Plot of microphone cross–spectrum in the cross–flow direction.

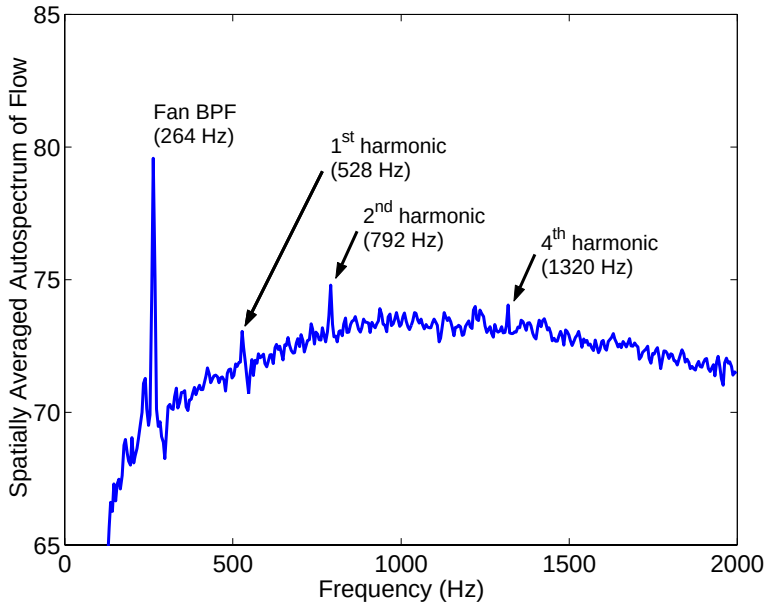

Figure 2.26: Spatially averaged autospectrum of the turbulent flow in the flow direction (Virginia Tech tunnel at M=0.14).

Experimental Correlation of the Flow–Induced Plate Vibration

The cross-correlation of the accelerometer signals measured on the aluminum plate was calculated and is presented in Figure 2.27. Comparison of the accelerometer data in Figure 2.27 with that of microphone data for measurements performed along the duct axis showed that the plate vibration had a greater correlation in both time and space than either flow component. In Figure 2.28, the contour plot is presented and indicates the spatial correlation at a particular instance in time.

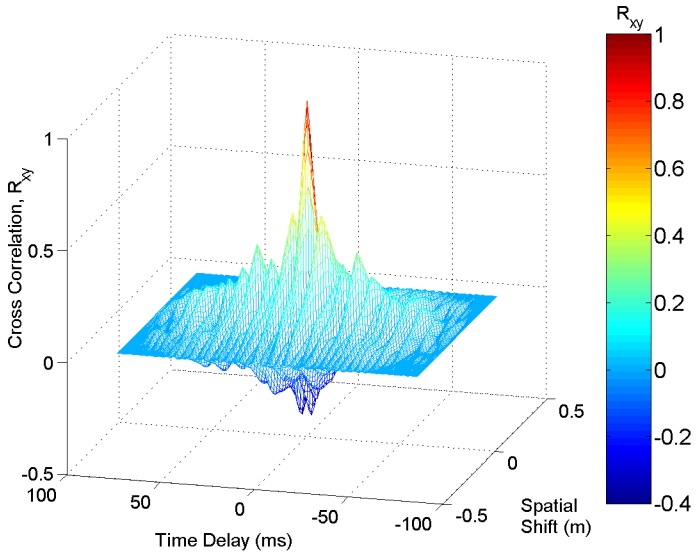

Figure 2.27: Plot of accelerometer cross–correlation.

The plate had a spatial cross–correlation of -3 dB between two points separated by 75 mm. A -3 dB temporal cross–correlation occurred at 0.8 ms. Note that the spatial cross–correlation of the plate vibration is the greatest of the three cases observed. This is due to the modal filtering of the plate vibration. Temporal cross–correlation of -3 dB for the plate vibration had a delay (0.8 ms) twice as long as that of the turbulent flow in the flow direction (0.4 ms). When comparing the delay associated with temporal cross–correlation for the cross–flow direction to that of the plate vibration, it is observed that the cross–flow delay is fifty percent longer than for the plate vibration. Note, however, that the plate vibration is due to variations along the flow direction, and therefore, it is more appropriate to compare cross–correlation of the plate vibration to that of the turbulent flow in the *flow* direction. These results are presented in Table 2.1.

The Fourier transform of one accelerometer signal was then calculated. See Figure 2.29, below. Comparing the cross–spectrum for the two microphone test cases (Figure 2.22 and Figure 2.25) to that for the plate acceleration data it was shown that the best correlation

Table 2.1: Comparison of Temporal and Spatial Correlation of a Turbulent Flow and Resulting Plate Vibration.

Configuration	**-3 dB Cross–correlation**	
	Temporal (ms)	*Spatial (mm)*
Plate Vibration	0.8	75
Flow Direction	0.4	30
Cross–flow Direction	1.2	25

was attained using the latter—that of plate vibration. For the plate acceleration data the cross–spectrum measured at the fundamental plate resonance was -11 dB compared to -16 dB for flow along the duct axis. This emphasizes the fact that, given a turbulent flow, the structure acts to increase spatial correlation.

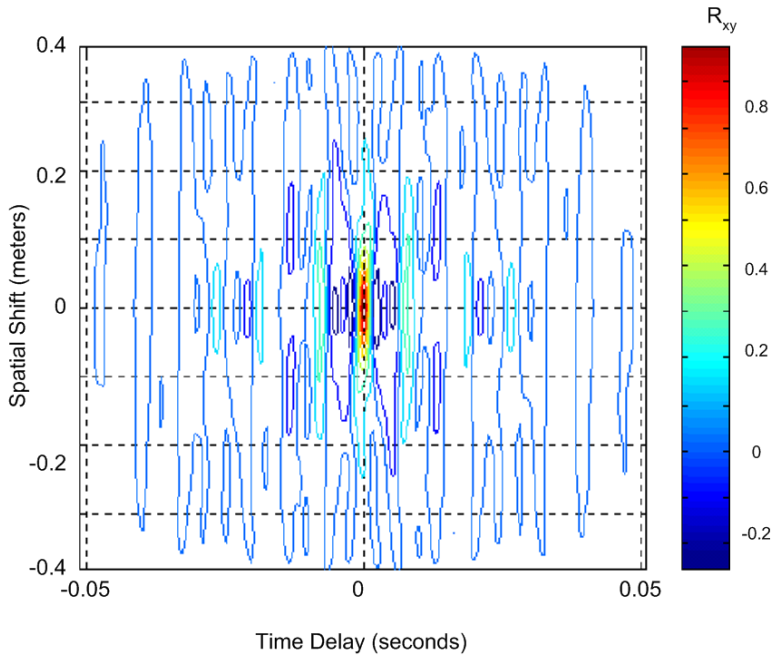

Figure 2.28: Contour plot of accelerometer cross–correlation.

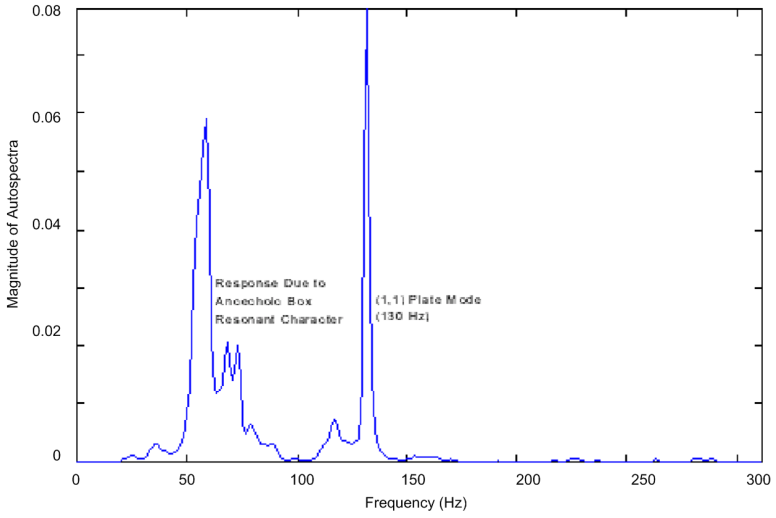

Figure 2.29: Plot of accelerometer autospectrum.

2.4 Summary

It can be concluded that below the maximum frequency of interest of 800 Hz, only two modes are cut-on. These are the (1,1) and (1,2) plate modes at 119 Hz and 165 Hz, respectively.

Temporal and spatial correlation was observed for three cases: flow in the direction parallel to the plate, flow in the cross-flow direction, and plate vibration in the flow direction. For the flow parallel to the plate, the temporal and spatial correlations at -3 dB were 0.4 ms and 30 mm, respectively. The spatial correlation for the cross-flow was approximately the same at 25 mm at -3 dB as that for the flow in the direction parallel to the flow. However, given a value of 1.2 ms at -3 dB, the temporal correlation was three times that of the flow in the parallel direction. Spatial correlation was the greatest for the plate vibration at 75 mm at -3 dB. Temporal correlation of the plate vibration was twice that of the flow in the direction parallel to the plate at 0.8 ms at -3 dB. This increase in temporal and spatial correlation relative to the correlation of the flow parallel to the plate is indicative of the modal filtering effect of the plate vibration.

The spectra of mean squared pressure of the interior field was shown to be due more so by the tangential flow than by the cross-flow. The (1,1) response due to the tangential flow was greater by 4 dB. This suggests that the interior noise field is due, primarily, to a turbulent boundary layer and not due to a normal component of the flow impinging on the plate. Further, no interior noise field was observed due to the (1,2) plate mode thus suggesting this mode acts either as a dipole with negligible edge radiation or it is not sufficiently excited by the turbulent flow.

Chapter 3

Reference Sensing

This chapter presents the need for a vibration sensor capable of obtaining the reference signal used for feed forward control. Proper sensing of the reference signal is important since it is this signal which is used by the controller to generate the secondary noise field. In addition, the sensed plate vibration must be coherent with the radiated primary acoustic field such that the generated secondary acoustic field may cancel the primary acoustic field. Therefore, the reference sensor must be capable of sensing such plate vibration, within the desired control band and coherent with the interior acoustic field, in order to obtain sufficient control.

The four reference sensing methods studied were: 1) the use of a single point acceleration measurement per actuator, 2) the use of multiple, independent point acceleration measurements per actuator, 3) the use of one discrete reference sensor array used per actuator, and 4) the use of a single, distributed PVDF spatial sensor per actuator.

In addition to the development of the reference sensors, studies were performed to estimate the number of control channels that would be required. To do so, singular value decomposition was performed on the cross–spectrum of a TBL induced plate acceleration measured at several points. The number of large singular values would estimate the number of independent reference signals required. Allowing one reference signal[1] per actuator, the number of actuators required could then be estimated.

3.1 Number of Control Channels Required

Control of interior noise due to TBL induced plate vibration is difficult since the plate vibration is not well correlated spatially. To determine the required number of references, a grid pattern of sixteen accelerometers was placed on the plate, as shown in Figure 3.1, and subjected to a turbulent boundary layer flow. The accelerometers were evenly spaced over the plate having a 50 mm by 100 mm (2" by 4") spacing. All channels were acquired simultaneously using a 4000 Hz sample rate, anti–aliasing filters set to 1200 Hz, and gains set

[1] Or one *group* of independent reference signals for the case where multiple independent point acceleration measurements are used for the reference signals.

appropriately to ensure sufficient signal–to–gain. The singular value decomposition (SVD) was performed on the cross–spectrum matrix, generated using thirty averages, at each spectral line.

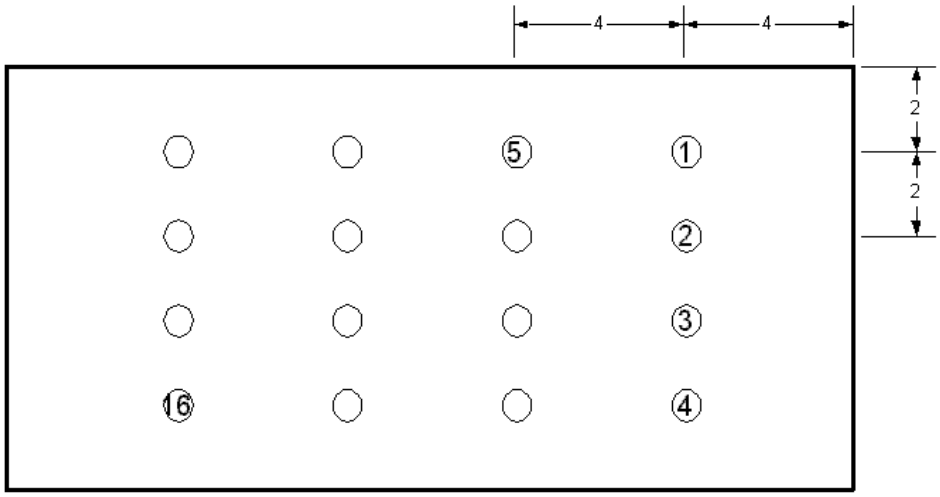

Figure 3.1: Sixteen accelerometers were arranged in a 4 by 4 grid across the plate having a spacing of 50 mm by 100 mm (2″ by 4″).

The cross–spectrum of these resulting acceleration signals may then be calculated and arranged in matrix form—one matrix per spectral line. Performing SVD on each matrix would indicate the rank of each matrix of cross–spectra [70]. The number of independent reference signals required at a particular frequency may then be estimated knowing the rank of the respective cross–spectrum matrix. Knowing the number of reference accelerometers required, effective control may be achieved using the minimum number of channels.

The cross–spectrum between two time signals x_i, x_j may be expressed as

$$G_{x_i x_j}(\omega) = \frac{S_i(\omega)}{S_j^*(\omega)} \tag{3.1}$$

where $i = 1, 2, 3, ..., n$ and $j = 1, 2, 3, ..., n$, given n input signals. S_i is the linear Fourier transform of time signal x_i and S^* denotes the complex conjugate of S. Note, for $i = j$, $G_{ij}(\omega) = G_{ii}(\omega)$—the autospectrum of the response of accelerometer i.

By performing an SVD of the cross–spectrum matrix at some frequency, ω, G may be expressed as [70]

$$G_{ij}(\omega) = U \Sigma V^T \tag{3.2}$$

which may be rearranged to express the singular values as

$$\Sigma = U^T G_{ij}(\omega) V \tag{3.3}$$

where

$$\Sigma = \begin{bmatrix} S & 0 \\ 0 & 0 \end{bmatrix} \tag{3.4}$$

and $S = diag(\sigma_1, \sigma_2, ..., \sigma_n)$ where $\sigma_1 \leq \sigma_2 \leq ... \leq \sigma_n$ are the eigenvalues of G. The columns of U and the rows of V are referred to as the left and right singular vectors of G, respectively [70].

The value at which a singular value may be considered large enough such that it relates to an independent signal is subjective. To determine which singular values were sufficiently large, they were first normalized to the largest singular value, σ_1. Gains of σ_2/σ_1 and σ_{16}/σ_1 were then plotted in Figure 3.2. Note that curves of singular values not shown (σ_3/σ_1 through σ_{15}/σ_1) each had similar trends and all lay between σ_2/σ_1 and σ_{16}/σ_1.

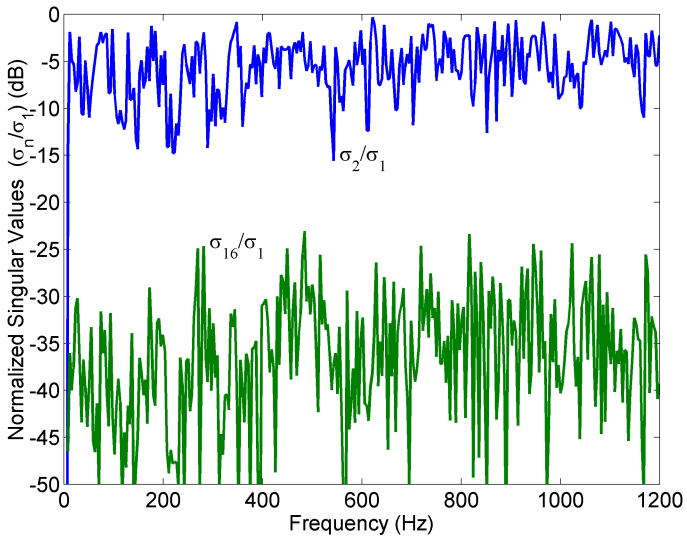

Figure 3.2: Normalized singular values versus frequency for σ_2/σ_1 and σ_{16}/σ_1. The remaining (not shown) singular values curves each had similar trends and all lay between σ_2/σ_1 and σ_{16}/σ_1.

The number of independent reference signals depends on the chosen gain threshold, or the minimum gain required to be considered pertinent, of the singular values. Decreasing the value of this threshold increases the required number of independent signals. In Figure 3.3, two threshold gains were chosen for the analysis: -10 dB and -20 dB. Normalized singular values, for a given frequency, having a gain, relative to σ_1, greater than the threshold gain are considered to be independent and thus contribute to the rank of the matrix. For the

-10 dB case, it was determined that five independent references (i.e. rank of 5) were identified for most frequencies. Decreasing the threshold gain to -20 dB, the number of independent references increased to twelve for most frequencies and to as much as fifteen for some. Figure 3.3 then suggests, for either the -10 dB or -20 dB gain thresholds, that for frequencies above 400 Hz the rank of the cross–correlation increases. This suggests, then, that more independent reference signals are required for control at higher frequencies. Choosing the more demanding configuration—the -20 dB gain threshold—it is estimated that between eight and twelve reference channels would be required to achieve sufficient control in the target bandwidth of 400–800 Hz.

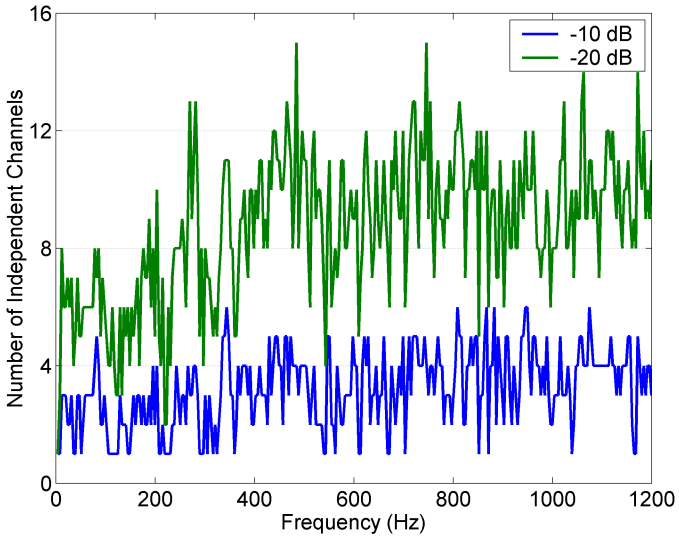

Figure 3.3: The number of independent reference signals depends on the chosen cut–off gain of the singular values. Increasing this gain increases the number of independent signals independent.

3.2 Reference Sensing Methods

This section presents the four methods of reference sensing explored. The theory used for analyzing the spatial response of the reference sensors is presented first. This is then followed by descriptions of each reference sensing method along with corresponding analytical results. Frequency dependent gain and phase, determined by experiment, are then presented for the discrete reference sensor array and the distributed PVDF spatial sensor.

The spatial response of an ideal accelerometer may be modelled as a delta function located at the center of the accelerometer. The one dimensional spatial Fourier transform of a general function, $s(x)$ is

$$S(k) = \int_{-\infty}^{\infty} s(x) e^{-j2\pi kx} \, \mathrm{d}x \tag{3.5}$$

where x is the spatial variable and k the wavenumber. For the delta function located at some position x_0, the spatial Fourier transform is then [27]

$$S(k) = \int_{-\infty}^{\infty} \delta(x - x_0) \, e^{-j2\pi kx} \, \mathrm{d}x = e^{-j2\pi kx_0} \tag{3.6}$$

where x is the spatial variable and $S(k)$ the wavenumber domain sensitivity. By the Euler identity

$$e^{-j2\pi kx_0} = \cos(2\pi kx_0) - \sin(2\pi kx_0) \tag{3.7}$$

having a magnitude of

$$\sqrt{\cos^2(2\pi kx_0) + \sin^2(2\pi kx_0)} = 1 \tag{3.8}$$

and phase

$$\phi = \tan^{-1}(2\pi kx_0) \tag{3.9}$$

Note, that for zero spatial delay ($x_0 = 0$) the spatial Fourier transform of an impulse therefore has a unit frequency response and zero phase for all wavenumbers. Non-zero spatial delay maintains a unit frequency response magnitude but introduces wavenumber dependent phase.

The sifting property is a useful feature of the dirac delta function and may be expressed as [27]

$$S(k) = \int_{-\infty}^{\infty} f(x) \delta(x - x_0) \, e^{-j2\pi kx} \, \mathrm{d}x = f(x_0) \tag{3.10}$$

where $f(x_0)$ is some function of x evaluated at x_0.

To determine the wavenumber response of the two dimensional array, the two dimensional spatial Fourier transform is computed. Similar to the one dimensional case (equation 3.6), for a single delta function located in 2-space the two dimensional spatial Fourier transform may be expressed as in equation 3.11 [68]

$$S(k) = \int_{-\infty}^{\infty}\int_{-\infty}^{\infty} \delta(x - x_0, y - y_0)\, e^{-j2\pi k_x x} e^{-j2\pi k_y y}\, \mathrm{d}x\, \mathrm{d}y = e^{-j2\pi(k_x x_0 + k_y y_0)} \tag{3.11}$$

and so by Euler's identity the two-dimensional spatial Fourier transform of a delta dirac function is unity for all wavenumber pairs, k_x, k_y with phase $\phi = \tan^{-1}\{2\pi(k_x x_0 + k_y y_0)\}$.

The discrete form analog to the Dirac delta function is the Kronecker delta which has the two-dimensional spatial response

$$X(k_m, k_n) = \sum_{m=-\infty}^{\infty}\sum_{n=-\infty}^{\infty} \delta(m - m_0, n - n_0) e^{-i2\pi k_m m} e^{-i2\pi k_n n} = e^{-i2\pi(k_m m_0 + k_n n_0)} \tag{3.12}$$

where for $m_0 = n_0 = 0$, $X(k_m, k_n) = 1$ with zero phase for all k_m, k_n. However, for m_0, n_0 not both equal to zero the response has unit magnitude with phase

$$\phi = \tan^{-1}(2\pi(k_m m_0 + k_n n_0)) \tag{3.13}$$

Similar to equation 3.12 but for finite limits, the discrete Fourier transform of the Kronecker delta function is

$$X(k_m, k_n) = \frac{1}{MN}\sum_{m=0}^{M}\sum_{n=0}^{N} \delta(m - m_0, n - n_0) e^{-i2\pi k_m m} e^{-i2\pi k_n n} \tag{3.14}$$

$$X(k_m, k_n) = \frac{1}{MN} e^{-i2\pi(k_m m_0 + k_n n_0)} \tag{3.15}$$

By the Euler identity of equation 3.7, the magnitude of equation 3.15 is $1/MN$ with phase of

$$\phi = \tan^{-1}\left(2\pi\left(\frac{k_m m_0}{M} + \frac{k_n n_0}{N}\right)\right) \tag{3.16}$$

A point reference sensor is theoretically capable of sensing an infinite bandwidth of wavenumbers since its planform area would be zero [27]. However, real accelerometers do not have zero planform area, but rather a distributed circular planform, and therefore do not have infinite bandwidth.

The wavenumber response of a continuous system must be analyzed by first knowing the spatial sensitivity to a travelling wave. This spatial sensitivity response may then be transformed to the wavenumber domain using the spatial Fourier transform. For a disk of radius a having a radial sensitivity $S(R)$, the sensitivity of the disk to sense a travelling wave is determined by integrating over the area of the sensor in contact with the vibrating structure (equation 3.17). Note, that such a disk sensor is symmetric and therefore the analysis sets the x-axis to be collinear with the direction of wave propagation as shown in Figure 3.4.

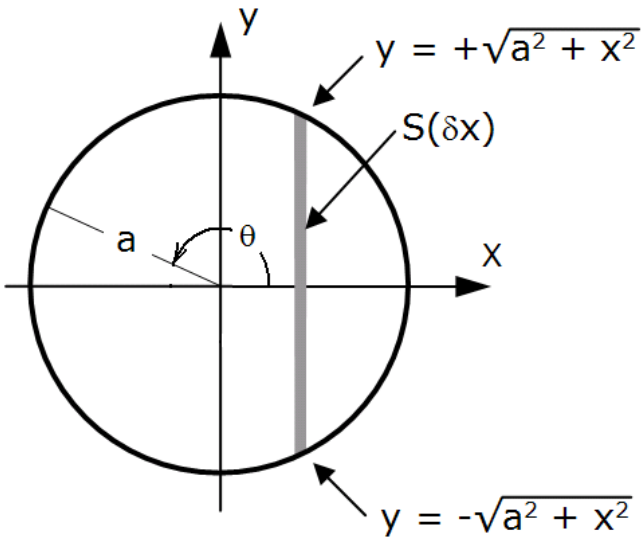

Figure 3.4: Integration limits for determining the sensitivity of a disk sensor.

$$S\left(x\right) = \int_{y=-\sqrt{a^2-x^2}}^{\sqrt{a^2-x^2}} S(r)\,\mathrm{d}y \tag{3.17}$$

and by the equation of a circle, $x^2 + (y/2)^2 = a^2$ or $y/2 = \sqrt{a^2 - x^2}$. Assuming S(r) is independent of radial position and has unit magnitude, equation 3.17 may be simplified to

$$S\left(x\right) = \int_{y=-\sqrt{a^2-x^2}}^{\sqrt{a^2-x^2}} \mathrm{d}y \tag{3.18}$$

or further to

$$S\left(x\right) = 2\int_{y=0}^{\sqrt{a^2-x^2}} \mathrm{d}y \tag{3.19}$$

resulting in a disk spatial sensitivity of $S(x) = 2\sqrt{a^2 - x^2}$.

The spatial Fourier transform of $S(x)$ may then be taken for $x \leq a$ as

$$S\left(k\right) = \int_{x=-a}^{a} S(x)e^{-jkx}\,\mathrm{d}x \tag{3.20}$$

or

$$S\left(k\right) = 2\int_{x=-a}^{a} \sqrt{a^2 - x^2}e^{-jkx}\,\mathrm{d}x \tag{3.21}$$

and by Figure 3.4, $x = a\sin\theta$ giving

$$S(k) = 2a^2 \int_{x=-\pi}^{\pi} \cos\theta \sqrt{1 - \sin^2\theta} e^{-jka\sin\theta} \, \mathrm{d}\theta \tag{3.22}$$

and by the Pythagorean theorem, $1 - \sin^2\theta = \cos^2\theta$ such that

$$S(k) = 2a^2 \int_{x=-\pi}^{\pi} \cos^2\theta e^{-} jka\sin\theta \, \mathrm{d}\theta \tag{3.23}$$

which evaluates to [71]

$$S(k) = \frac{2\pi a^2 J_1(ka)}{ka} \tag{3.24}$$

where J_1 the first order Bessel function of the first kind having the first null point at [72]

$$k_0 = \frac{3.8317}{a} \tag{3.25}$$

The wavenumber response for an accelerometer having a circular planform may be determined using equation 3.24. Regarding control, the maximum wavenumber of interest is that wavenumber corresponding to the maximum frequency of interest of the radiated acoustic field. Given that the band of interest for active control was 400–800 Hz for this research effort, the maximum wavenumber of interest would be at 800 Hz given the material and geometry of the radiating plate. The relation between wavenumber and angular frequency, $\omega = 2\pi f$, may be expressed [5]

$$k = \omega^{1/2} \left(\frac{12\rho(1-\nu^2)}{Eh^2} \right)^{1/4} \tag{3.26}$$

For the 1.5 mm thick aluminum plate used, the resulting cut–off wavenumber was estimated to be 49 m^{-1} given $\nu = 0.3$, $\rho = 2710$ kg/m^3, and $E = 70$ GPa.

Single and Multiple Point Reference Sensing

The simplest form of reference sensing used for this research effort used a single accelerometer placed on the vibrating plate at the center of each actuator. The accelerometers used throughout this research effort were PCB model 352A10 which have a base radius of 2.8 mm. The first null point, by equation 3.25 is then calculated to be 1380 m^{-1}. In addition, by equation 3.24, the -3 dB down point was determined to be 790 m^{-1}. Note then that the use of a simple accelerometer as a reference sensor has the potential to measure wavenumbers well outside the desired cut–off wavenumber of 49 m^{-1}.

The correlation study presented in Chapter 2 showed that the spatial correlation between two points on the vibrating structure, separated by a distance of 30 mm, decreased by 3 dB. Further, accelerometers spaced at even greater distances had reduced spatial correlation.

By increasing the number of accelerometers placed in an area over which the spatial correlation decreased, the multiple coherence of the primary path would, in theory, *increase*

since each reference would give more information about the noise source. Therefore, the multiple coherence of the primary path between references and a point in the interior acoustic field would be greater using multiple, well–separated accelerometers for each actuator as opposed to using only a single reference per actuator.

Since the signals from each accelerometer are considered separately, the spatial response of each is simply the spatial response of a single accelerometer of a given radius. The accelerometers in the multiple point reference sensing method were the same as those used in the single point reference sensing method. Therefore, the wavenumber response of each accelerometer used in the multiple point reference sensing configuration then also had a theoretical first null point at 1380 m^{-1} and a 3 dB down point at 790 m^{-1}.

The increased theoretical maximum performance using this technique relative to other reference sensing methods studied in this research effort is shown in Chapter 6—Coherence and Causality Studies. Control simulation results are presented in Chapter 7—Active Noise Control using both MIMO and decoupled control. Decoupled control using a single reference per actuator is referred to as multiple–SISO (mSISO) control whereas decoupled control using more than one reference per actuator is referred to as multiple–MISO (mMISO). However, mMISO could not be performed due to limitations with the control simulation software. Therefore, simulations having more than one reference per actuator was limited to MIMO control.

Further, the multiple references per actuator concept was developed after the wind tunnel had been dismantled and proceeded the single reference per actuator control simulations discussed in Chapter 7—Active Noise Control. Therefore, multiple reference simulations could only be performed using existing data. MIMO control simulations using multiple references per actuator then used, for a particular actuator, the one accelerometer mounted beneath it along with an additional accelerometer located under a neighboring Smart Foam element. A list of accelerometers used for each actuator in the multiple reference MIMO control simulation is listed in Table 3.1. Figure 3.5 shows the accelerometer placement across the plate with the two references associated with actuator #1 identified. This configuration uses the encircled accelerometers at locations #1 and #2 for the two independent reference signals used for actuator #1.

Discrete Reference Sensor Arrays

Given that the goal of this research effort was to perform active control between 400–800 Hz, it would be useful to design a reference sensor which would be capable of filtering out higher frequency vibration. This would then allow the controller to operate only on those frequencies of interest without the need to low–pass the measured signal. Using array theory, such a sensor may be designed such that it has a cut–off frequency at the 49 m^{-1} wavenumber corresponding to an 800 Hz structural wave in the 1.5 mm aluminum plate used and described above.

The concept of the discrete reference sensor array uses four accelerometers arranged such that the combination of their signals, when properly weighted and summed, results in

Table 3.1: List of accelerometer measurements used for Multi–MISO control simulations. Reference also Figure 3.5 for accelerometer locations.

Actuator	**Accelerometer Locations**	
	1 Ref/Actuator	2 Refs/Actuator
1	1	1,2
2	2	2,4
3	3	3,1
4	4	4,3
5	5	5,6
6	6	6,4
7	7	7,5
8	8	8,6

a reference signal having a cut–off at the maximum wavenumber of interest for control—49 m^{-1}. Since the cut–off wavenumber of the accelerometers is almost a factor of thirty greater than the maximum wavenumber of interest, the accelerometers may be modelled as point measurements. Therefore, the discrete reference array may be modelled using one delta function to represent the spatial response of each accelerometer.

The array was designed using a total of four accelerometers; three accelerometers were arranged at the corners of an equilateral/equiangular triangle with a fourth placed at the center. Each of the four accelerometers were modelled as delta functions. The three delta functions modelling the accelerometers at the corners had unity gain with the one at the center having a gain of two. This model is depicted in Figure 3.6.

By equation 3.15, the wavenumber response magnitude of the center accelerometer, centered at $x = y = 0$ with 2x gain, is

$$|X_0(k_m, k_n)| = \frac{1}{MN} \sum_{m=0}^{M} \sum_{n=0}^{N} \delta(m-0, n-0) e^{-i2\pi k_m 0} e^{-i2\pi k_n 0} = \frac{2}{MN} \tag{3.27}$$

having zero phase. The response magnitude of the remaining three accelerometers having 1x gain and appropriate values of (m_0, n_0) would then be

$$|X_a(k_m, k_n)| = \frac{1}{MN}; \forall a = 1, 2, 3 \tag{3.28}$$

each having respective phase of

$$\phi_a = \tan^{-1}\left(2\pi\left(\frac{k_m m_0}{M} + \frac{k_n n_0}{N}\right)\right); \forall a = 1, 2, 3 \tag{3.29}$$

Summing the wavenumber domain responses of the four delta functions results in the response of the discrete reference array. In rectilinear coordinates, plotting the response

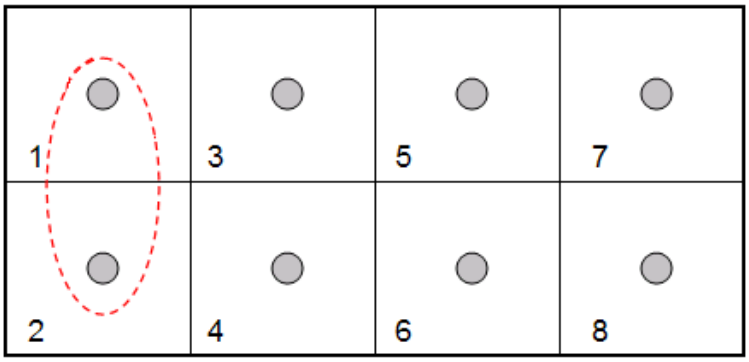

Figure 3.5: Multiple reference per actuator MIMO control simulations used reference signals from neighboring actuator locations. References corresponding to actuator #1 are shown.

versus the wavenumber components, k_x and k_y, results in a circular pattern centered at $k_x = k_y = 0$. When the radius of this pattern results in a cut–off wavenumber, $k_0 = \sqrt{k_x^2 + k_y^2}$, equaling the acoustic wavenumber, k_a, the sensor measures only those vibrations resulting in a radiated acoustic field. Likewise, the sensor may also be designed to sense only that vibration radiating within a desired wavenumber band. Therefore, as used in this research, the spatial sensors may be designed to roll–off at the wavenumber corresponding to the maximum control wavenumber. This would allow for proper filtering of the disturbance signals resulting in more effective control.

Figure 3.7 shows a plot of the ratio of the radiated power below the desired sensor cut–off wavenumber (49 m^{-1}) to the total radiated sound power. Maximum performance was achieved using an accelerometer radial spacing of 5.9 cm (2.3″). However, the spacing may be reduced to 4 cm (1.6″) with minimal performance reduction. A photograph of the discrete reference sensor array is shown in Figure 3.8.

The transfer function between a random excitation and the response of the reference array was then determined by experiment. The excitation was produced by a speaker mounted in the wind tunnel duct approximately 25 mm (1″) below the plate. It was driven with a random signal that was AC coupled and low–passed at 2500 Hz. Results using the reference array were compared to those using a single, centered accelerometer to observe the filtering effect of the array and presented in Figure 3.9. At frequencies greater than 800 Hz, the frequency response function (FRF) of the reference array attenuated the reference signals by approximately 5 dB and up to nearly 10 dB was achieved at narrow bands. However, within the pass band, reductions up to 2 dB were present and outside the pass band gains up to 4 dB occurred within certain frequency ranges.

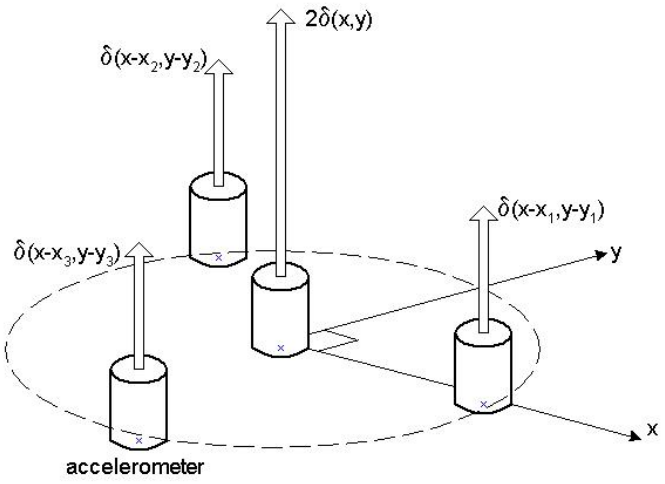

Figure 3.6: The accelerometer array was modelled using delta functions at each accelerometer location. The center delta function had a value of two and the others a value of unity.

Distributed PVDF Spatial Sensors

The fourth and last means of reference sensing explored is the use of a continuous, distributed PVDF reference sensor. This spatial sensor consists of a single sheet of circular PVDF bonded to the vibrating structure.

Distributed PVDF reference sensors were first investigated by Miller et al [73]. In Miller's work, one–dimensional spatial filters were designed as low pass wavenumber domain filters able to sense structural waves on a long, slender beam. Kidner and Johnson [74] expanded this topic to two–dimensional wavenumber domain filters using concentric rings of etched PVDF. This method allowed for low passed and band passed filters.

For research performed in this effort, the distributed reference sensor design was based on work performed by [74]. However, there was one difference. In [74], the cut–off frequency was chosen to be at the first null point, or lowest frequency where the response goes to zero, of the sensor response. It was argued that the response for wavenumbers smaller than this value would all be in phase and therefore would not threaten stability when using feed back control. For this research, though, it was best to design the cut–off frequency to occur at the -3 dB down point (half power point) in the more traditional manner of specifying the pass band of a filter. In addition, to reduce complexity of the experiment and to eliminate the effect of spatial aliasing present with the concentric rings approach, the sensors were designed to be of a single, etched disk. The response of a thin disk mounted on an infinite plate in the wavenumber domain is given by equation 3.24 and the first null point occurs at a wavenumber, k_0 according to equation 3.25.

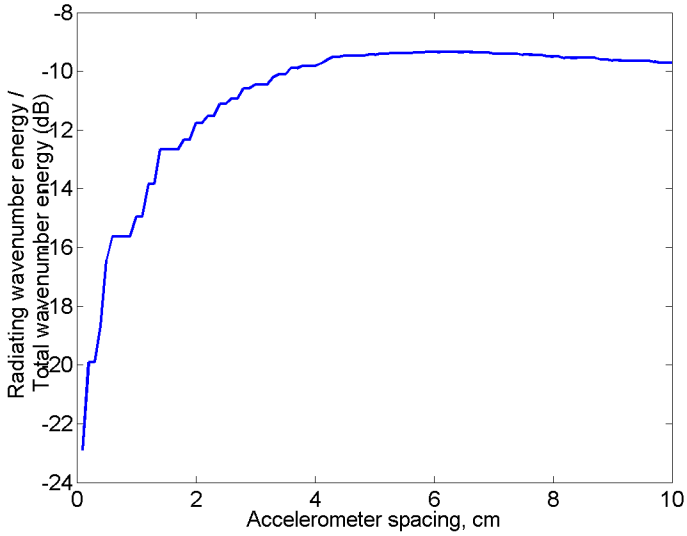

Figure 3.7: The ratio of measured radiated sound power within the cut-off wavenumber versus total radiated power was used to determine the proper accelerometer spacing of the discrete reference sensor arrays.

For the distributed reference sensor, equation 3.24 was first used to identify the performance of a sensor having the maximum allowable radius. The maximum allowable radius was governed by the planform area of the actuators used (see the eight channel configuration in Chapter 5—Actuators) of 62 mm. By equation 3.24, this design resulted in a cut–off wavenumber of 37 m^{-1}. The radius was then iteratively reduced and the gain determined at the desired cut–off wavenumber of 45 m^{-1}. As the sensor radius was decreased the sensor bandwidth increased. The required sensor radius was determined when the sensor gain equaled -3 dB at the desired cut–off wavenumber. The desired cut–off frequency was 800 Hz. By equation 3.26, the required cut–off wavenumber was therefore 45 m^{-1} giving a sensor radius of 49 mm. Figure 3.10 shows a plot of theoretical performance calculated by equation 3.24 and plotted in dB, of a distributed spatial filter in the wavenumber domain. Note, that the sensor wavenumber response had a first null at 78 m^{-1}.

The distributed PVDF spatial reference sensor was then qualified experimentally. This test was performed similar to that performed for qualifying the discrete array. Placed at the center of the distributed PVDF spatial sensor was an accelerometer whose signal was used as the baseline for estimating the PVDF sensor gain. The response of the spatial filter, with respect to the response of the accelerometer, is plotted in Figure 3.11. Although the response was not as flat as for the discrete reference array, there was noticeable attenuation above the 800 Hz (49 m^{-1}) cut–off. Reductions outside the pass band were as great as 10 dB with much of the response being attenuated more than 5 dB. However, within the pass band,

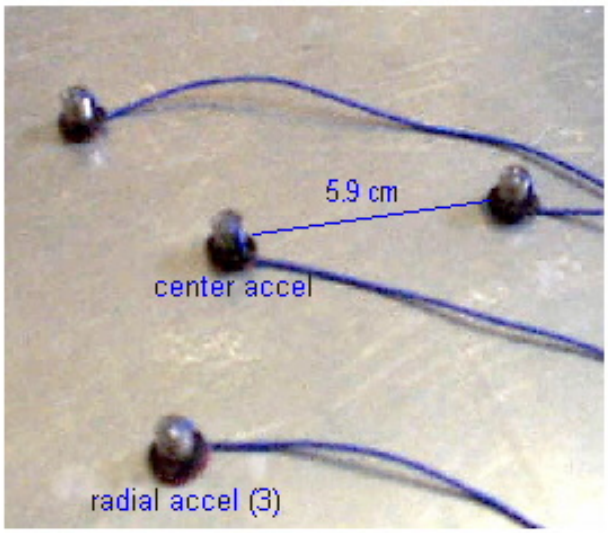

Figure 3.8: The accelerometer array consists of three radial accelerometers placed in a triangular pattern with a fourth at its center. The radial spacing was 5.9 cm or 2.3″. The sum of these four signals was used as the reference signal.

a 10 dB notch appears at approximately 285 Hz and frequencies below 40 Hz suffered from excessive amplification. In addition, outside the pass band, at 840 Hz and 1030 Hz, the response was relatively high. A photograph of the eight reference sensors mounted to the plate is shown in Figure 3.12.

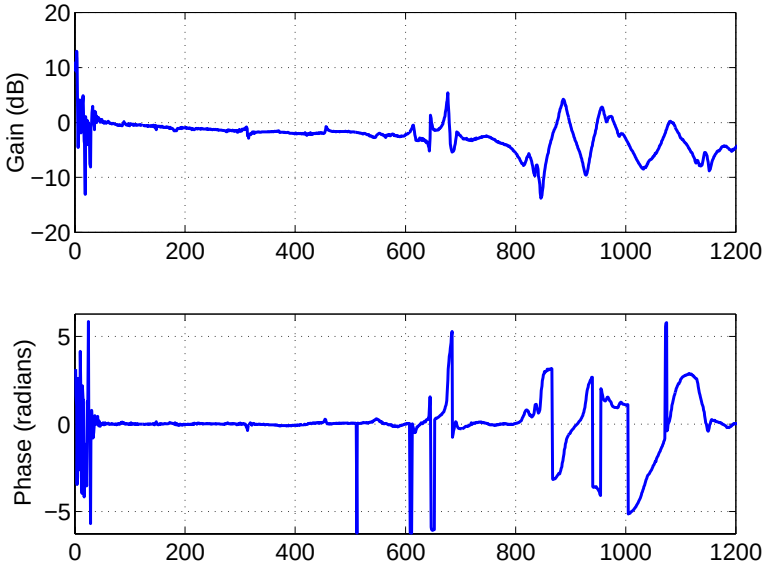

Figure 3.9: Frequency response magnitude and phase of a reference array.

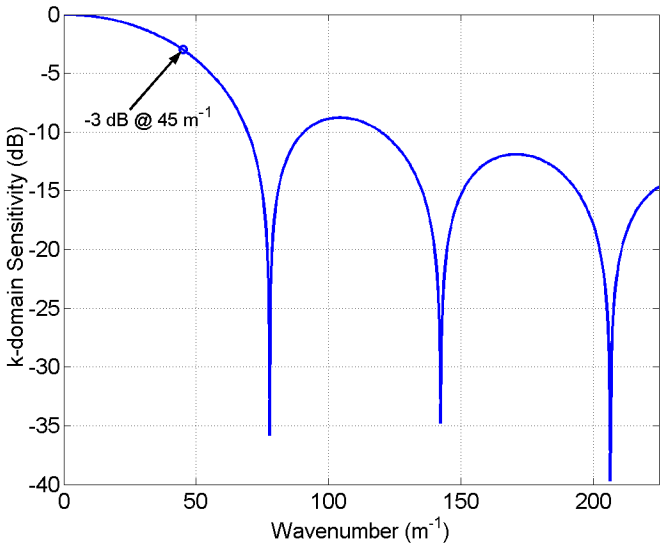

Figure 3.10: The shaped PVDF spatial filters were designed to have a low–pass roll–off at 45 m^{-1} corresponding to 800 Hz for the plate used.

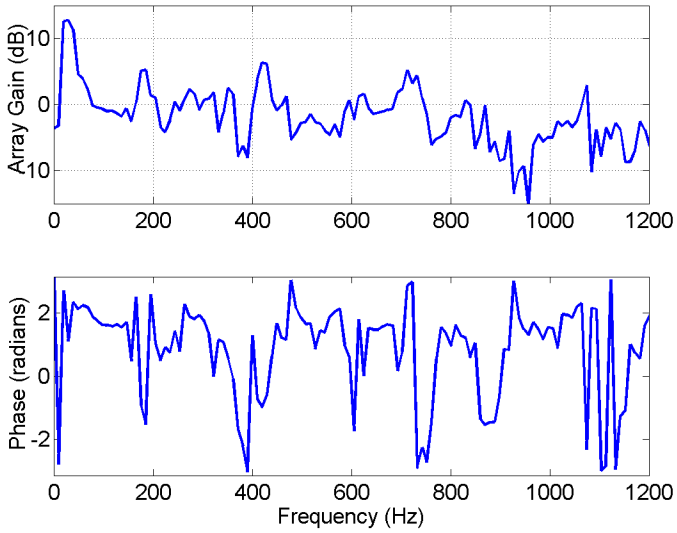

Figure 3.11: The FRF magnitude and phase of a distributed reference array.

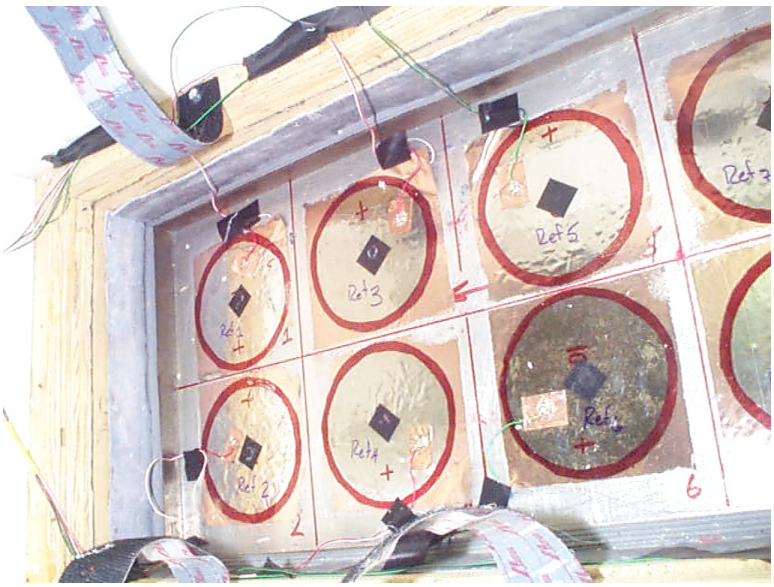

Figure 3.12: The shaped PVDF spatial reference sensors were bonded to the vibrating plate and were designed to have a low–pass cut–off frequency of 800 Hz.

3.3 Summary

Four reference sensing techniques were presented: 1) the use of a single point acceleration measurement per actuator, 2) the use of multiple, independent point acceleration measurements per actuator, 3) the use of one discrete reference sensor array used per actuator, and 4) the use of a single, distributed PVDF spatial sensor per actuator.

The scope of this research required the use of a single reference per actuator. However, the use of multiple references per actuator was also studied to determine if the added complexity would benefit control performance. The chapter outlined the use of such a reference sensing technique.

Spatial sensors were designed to sense only those vibrations in the desired control band. For a cut–off of 800 Hz, the plate used had a corresponding cut–off wavenumber of 45 m^{-1} For the discrete arrays, attenuation outside the pass band was approximately 5 dB with up to 10 dB in narrow bands. However, the response would be amplified by as much as 5 dB. And, in addition, within the pass band, there was as much as 2 dB of attenuation.

The distributed spatial sensor was shown to have a roll–off at the desired cut–off frequency of 800 Hz. Much of the stop band was attenuated by 5 dB with reductions peaking at 10 dB. However, within the pass band, a 10 dB notch occurred at 285 Hz.

Studies performed in this chapter suggested that a minimum of eight control channels would be required to achieve sufficient control performance within the required 400–800 Hz control band. Although the study performed considered a maximum of fourteen control channels, it was shown that increasing the channel count from eight to fourteen would offer little advantage while further increasing complexity.

Chapter 4

Error Sensing

This chapter presents the need for an acoustic sensor capable of obtaining the error signal used for feed forward control experiments and simulations performed in Chapter 7. Proper sensing of the error signal is important since it is this signal which is minimized by the controller. The error sensor must therefore be capable of sensing the desired noise to be minimized while filtering out extraneous noises. In this research effort, the mean square pressure radiated from the turbulent flow induced plate vibration was to be minimized.

Chapter 1 outlined how decoupling of control paths significantly reduces control system computational overhead. However, since the influence of measured noise from paths which are not modelled may result in an unstable control system, it would be desirable to measure only those paths which are indeed modelled. Therefore, a further requirement of the error sensor was that it must be able to sense noise which radiates primarily from the vicinity of its corresponding actuator. Doing so would physically decouple each control channel thus allowing for more effective decoupled control.

The means by which error sensor array requirements are accomplished are presented below. A discussion regarding acoustic fields is presented followed by the modelling of error sensor arrays. Modelling begins by determining the required error sensor array diameter and the number of microphones required for sufficient directionality in the far field at the maximum control frequency. Further analysis characterizes the directionality of the array in the near field and its ability to filter out near field acoustic waves.

4.1 Acoustic Fields

The acoustic field consists of three regions in which acoustic waves perform differently. These three regions, in order of increasing distance from the source, are the hydrodynamic near field, the geometric (Fresnel) near field, and the far field.

The hydrodynamic near field is "considered to be that region immediately adjacent to the vibrating surface of the source, extending outward a distance much less than one wavelength [5]". Within this region exists both propagating and non-propagating (evanescent) waves. Evanescent waves decay with increasing distance from the source, and therefore

neither propagate to the geometric near field nor to the far field. The hydrodynamic near field "is characterized by fluid motion which is not directly associated with sound propagation [5]". If the acoustic wavelength is long compared to the separation distance of the two sources, "local differences in phase and displacement of adjacent parts of a vibrating surface will result in fluid motion tangential to the surface [and] the acoustic pressure will be out of phase with the local particle velocity."

Between the hydrodynamic near field and the far field exists the geometric near field. Here, "acoustic pressure and particle velocity [of a particular acoustic wave] are in phase", as with the far field, however the "sound pressure levels do not drop off at the rate of 6 dB for each doubling of the distance from the source" due to "interference between waves from various parts of the source" and so "relative maxima and minima are to be expected". This suggests that two waves in the geometric near field will, in general, have a phase difference in pressures and a phase difference in particle velocities. In the far field, however, two interfering waves will have no mismatch of phase for either their pressures or their particle velocities. "Sound propagation to the far field is associated with the in–phase components of pressure and particle velocity" suggesting that "measurements of the acoustic pressure amplitude in the near field give no indication of the sound power radiated by the source." Criteria for the far field include

$$\begin{aligned} r &\gg \frac{\lambda}{2\pi} \\ r &\gg l \\ r &\gg \frac{\pi l^2}{2\lambda} \end{aligned} \tag{4.1}$$

where r is the distance from the source, λ the wavelength of radiated sound, and l the characteristic source dimension. See Figure 4.1 for a graphical representation of the acoustic regions in relation to the interior height of the enclosure. Note that the far field is present within the enclosure only from 100 Hz to 500 Hz with much of the remaining spectrum in the geometric near field.

4.2 Development of Error Sensor Arrays

A control system, in general, will provide better control performance if all cross-coupling paths are properly modelled. However, the computational overhead of such a controller may be excessive and perhaps even impossible to implement given hardware limitations. Therefore, the reduced computational overhead of a decoupled controller, given lesser control performance, may be an acceptable trade–off. Further, minimizing mean squared pressure requires microphones be placed within the interior. Such an approach may not be realizable and would therefore require the sensors be placed in locations remote to the volume in which control is desired. An error sensor capable of achieving these two needs was required for this research.

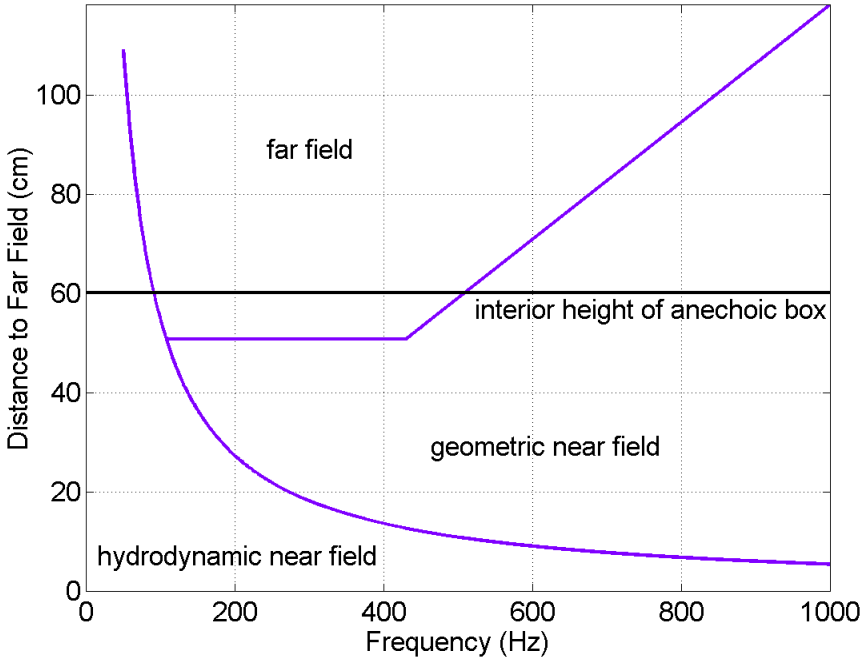

Figure 4.1: The acoustic field within the enclosure. Note that the far field exists only over the 91–471 Hz band.

Although cross–coupling may simply be ignored in the control system, the measured acoustic pressure would still consist of pressure components due to waves radiating from other vicinities. It therefore would be of benefit if each error sensor was capable of measuring acoustic waves radiating primarily from the vicinity of its respective actuator while filtering out those waves radiating from neighboring areas.

Error sensors were thus required to be placed as close to the radiating plate as possible. However, sensing of the radiating acoustic waves using sensors placed close to the vibrating structure resulted in sensing in the hydrodynamic near field. Since the error to be minimized by the control system was the radiating component of the acoustic field, sensors capable of filtering out the near field component were therefore necessary. Error sensor arrays were therefore developed to sense the radiating component of acoustic waves originating in the vicinity of their respective actuator.

The design of the error sensor arrays consisted of three microphones, whose outputs are summed, evenly spaced on a ring of some radius with the directionality resulting due to constructive and destructive interference of waves reaching the three microphones. Should two waves of similar phase meet, constructive interference would occur thereby resulting in a wave of greater magnitude. Conversely, two waves of opposing phase would destructively

interfere thus resulting in a wave of lesser magnitude than either of the two original waves. Wave interference is demonstrated in Figures 4.2a,b. In Figure 4.2a, two in-phase waves, one of unit amplitude and the other of amplitude 0.9, are in phase and therefore interfere constructively producing a wave of amplitude 1.9. Figure 4.2b also depicts two waves—the first of unit amplitude and the other of amplitude 0.98 but of opposing phase. These two waves therefore interfere destructively producing a wave of amplitude 0.02. Had these waves been of equal amplitude their interference would have resulted in a wave of zero amplitude.

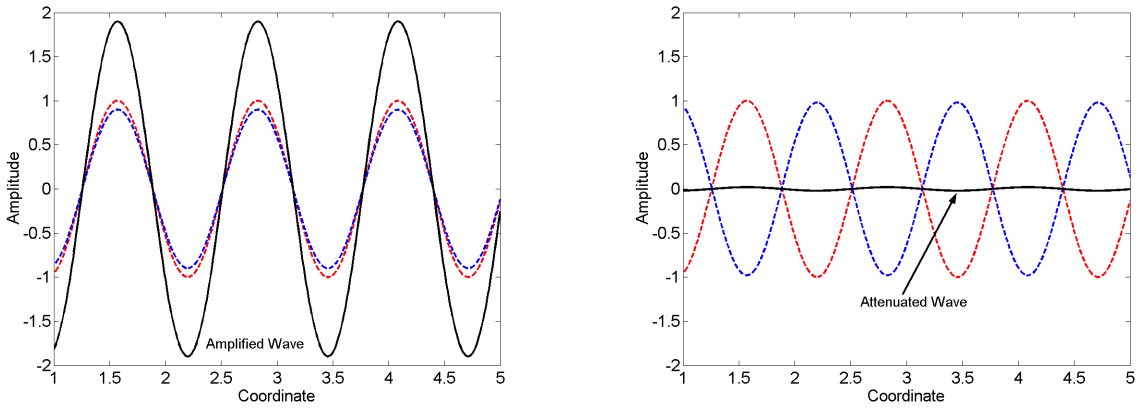

a) Amplification of two in-phase waves

b) Attenuation of two out-of-phase waves

Figure 4.2: Two waves magnify (a) in amplitude at points where their phase are of the same. At points of opposing phase, the resulting wave (b) is reduced in amplitude.

For a given frequency, correct sizing of the radius would create an error array capable of sufficiently rejecting sound waves radiating to it from noise sources at locations other than those desired. See Figure 4.3 for a picture of a typical error array. Error arrays were centered directly over each respective Smart Foam element such that the array would sense primary and secondary noise radiated from the vicinity of the actuator.

Three analyses were required for the development of the discrete error sensor arrays. The first analysis was used to determine the proper sizing of the error sensor array. This analysis was performed given an error sensor array placed in the far field, free of any near field effects, to determine the array free field (far field) directivity. This analysis was then extended to determine the error sensor array directivity in the near field. The third analysis investigated the ability of the error sensor array to reject near field acoustic waves from being sensed. Therefore, the three analyses each had their own goals; The first study determined the diameter and number of error sensors required, the second determined the ability of the error sensor array to decouple error paths from the vicinity of other Smart Foam elements, and the third determined the ability of the error sensor array to reject the near field component of the sensed acoustic field.

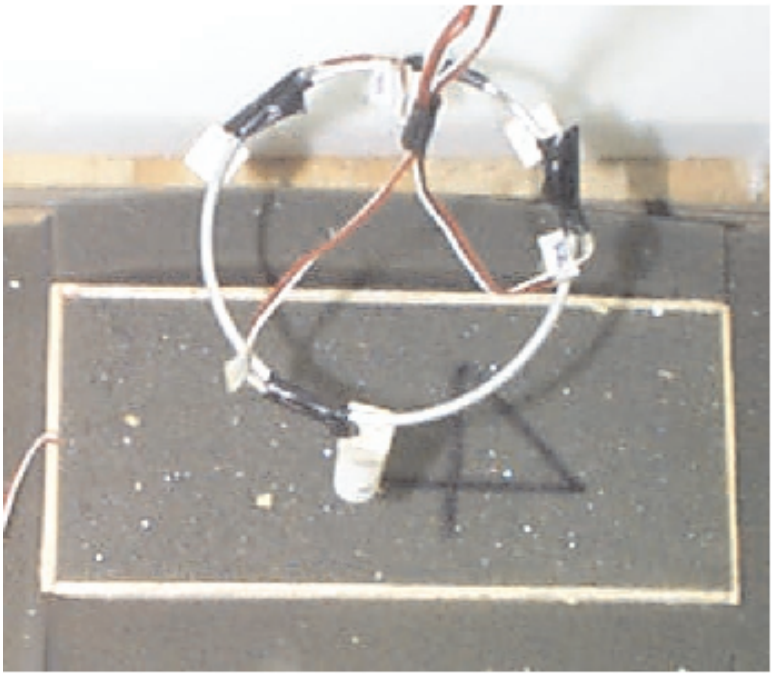

Figure 4.3: The error array is focussed directly over its respective actuator.

Sensor Array Far Field Analysis

Computer simulations were performed to determine the radius required of the error array. This analysis considered the error array response in the far field at 800 Hz—the control band maximum frequency used for control experiments and simulations. Assuming a linear system where both the source and each microphone are omnidirectional, the simulation may make use of acoustic reciprocity. Each of the three microphones were then represented as monopole sources and the resulting sound pressure on some imaginary spherical surface of one meter radius, centered at the error ring origin, could be calculated. The sound pressure due to the three monopole sources represented the directionality of the error array. The cost function used for tuning the microphone ring to the desired angular frequency, ω for this simulation was

$$P_{obs} = \sum_i P_i \tag{4.2}$$

where

$$P_i = \sum_j A_j \frac{e^{-j\omega c r_j}}{r_j} \tag{4.3}$$

with r_j equal to the distance to the imaginary spherical surface from microphone i to element

j, c the acoustic phase speed in air (343 m/s), and A_i the acoustic amplitude. Code for this simulation, **M***icrophone* **A***rray* **D***esigner (MAD.m)* may be found in Appendix C—Matlab Scripts.

Geometry used for this analysis is defined in Figure 4.4. The three microphones used in the error array were labelled *mic 1*, *mic 2*, and *mic 3* and arranged on an imaginary circle of radius, r_{array}. Note, mic 1 lies on the Y–axis at a distance of r_{array}. The in–plane (relative to the error array plane) sweep angle, θ, swept from zero to 2π in the XY–plane originating at the mic 1. The normal–to–the–plane sweep angle, ϕ, swept from zero to 2π in the YZ–plane also originating at mic 1.

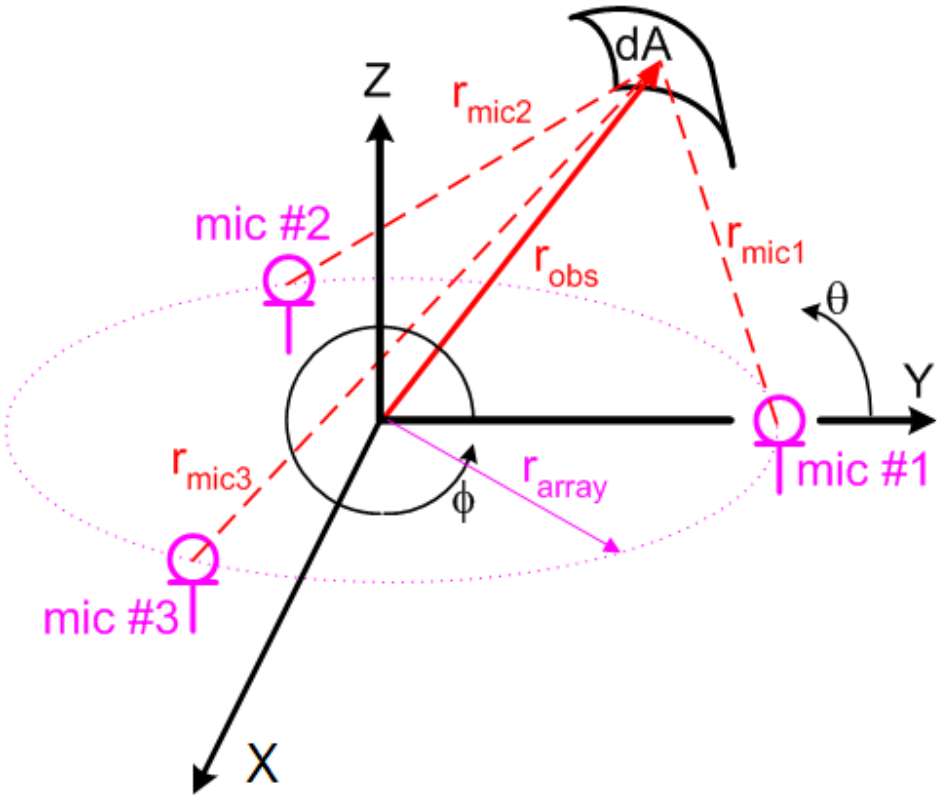

Figure 4.4: Dimensions used for the simulation of error sensor array performance.

The resulting pressure at an observation point of area dA on an imaginary spherical surface of r_{obs} was then determined knowing the radial distance between the observation point and the three monopole sources. Equation 4.2 could then be evaluated to determine the resulting acoustic pressure distribution over the imaginary spherical surface. Combining equations 4.2 and 4.3 with appropriate substitutions for r_1, r_2, and r_3 gives

$$P_{obs} = \frac{e^{-j\omega c r_1}}{r_1} + \frac{e^{-j\omega c r_2}}{r_2} + \frac{e^{-j\omega c r_3}}{r_3} \tag{4.4}$$

where the distance to mic 1 from the origin was determined by

$$r_1 = \sqrt{\left(X_{obs} - X_{mic1}\right)^2 + \left(Y_{obs} - Y_{mic1}\right)^2 + Z_{obs}^2} \tag{4.5}$$

and similarly for mic 2 and mic 3. X_{obs}, Y_{obs}, and Z_{obs} were the coordinates of the observation point and determined by

$$\begin{aligned} X_{obs} &= r_{obs}\cos(\phi)\cos(\theta) \\ Y_{obs} &= r_{obs}\cos(\phi)\sin(\theta) \\ Z_{obs} &= r_{obs}\sin(\phi) \end{aligned} \tag{4.6}$$

and the coordinates of the three point sources may be expressed as

$$\begin{aligned} X_{mic,n} &= r_{array}\cos\left(\frac{2\pi(n-1)}{3}\right) \\ Y_{mic,n} &= r_{array}\sin\left(\frac{2\pi(n-1)}{3}\right) \\ Z_{mic,n} &= 0\ , \quad \forall n \end{aligned} \tag{4.7}$$

with the microphone index being n=1,2,3.

As stated previously, the intent of the error sensor array was to sense acoustic radiation from the vicinity of its corresponding actuator. Properly designed, the error sensor array would measure, primarily, only noise radiated from this localized area with no influence from other waves in the acoustic field. Given the radius of the error sensor array, the characteristic dimension of the actuator, and the distance between the actuator and the error sensor array, the noise radiating from this target area may be used to determine the required directivity of the array. The directivity of the ideal array would sense only the noise radiated within a cone of angle 2ψ, where

$$\psi = \tan^{-1}\left(\frac{D_{source}}{2h}\right) \tag{4.8}$$

as shown in Figure 4.5. However, for reasons discussed in Chapter 3, such an ideal sensor is not achievable since the impulse response of the spatial filter will be influenced by the character of the stop band. The array must therefore be designed such that the ratio of the acoustic pressure due to sound waves within the cone of angle 2ψ (Figure 4.5) to that of the measured acoustic pressure is sufficiently great. The gain of the error sensor array, E_{array}^{sphere}, may be defined as

$$E_{array}^{sphere} = 10log_{10}\left(\frac{W_{total}^{sphere}}{W_{total}^{sphere} - W_{cone}}\right) \tag{4.9}$$

where W_{cone} is the acoustic power within the cone and W_{total}^{sphere} the total power measured by the error sensor array. This ratio expresses the gain of the measured signal, from within W_{total}^{sphere}, to the magnitude of the undesired signal content present outside the cone. The gain ratio may be expressed in terms of the angular design frequency, ω, the sweep angles, ϕ and θ, and the cone half angle, ψ

$$E_{array}^{sphere} = 10log_{10}\left\{\frac{\int_{\theta=0}^{2\pi}\int_{\phi=0}^{2\pi} P_{obs}\left(\theta,\phi,r_{obs}\right)^2 r_{obs}^2 \sin(\mathrm{d}\theta)\sin(\mathrm{d}\phi)\,\mathrm{d}\phi\,\mathrm{d}\theta}{\int_{\theta=0}^{2\pi}\int_{\phi=\psi}^{\psi+\frac{\pi}{2}} P_{obs}\left(\theta,\phi,r_{obs}\right)^2 r_{obs}^2 \sin(\mathrm{d}\theta)\sin(\mathrm{d}\phi)\,\mathrm{d}\phi\,\mathrm{d}\theta}\right\} \tag{4.10}$$

and since r_{obs}, $\mathrm{d}\theta$, and $\mathrm{d}\phi$ are constant, the expression may be simplified to

$$E_{array}^{sphere} = 10log_{10}\left\{\frac{\int_{\theta=0}^{2\pi}\int_{\phi=0}^{2\pi} P_{obs}\left(\theta,\phi\right)^2\,\mathrm{d}\phi\,\mathrm{d}\theta}{\int_{\theta=0}^{2\pi}\int_{\phi=\psi}^{\psi+\frac{\pi}{2}} P_{obs}\left(\theta,\phi\right)^2\,\mathrm{d}\phi\,\mathrm{d}\theta}\right\} \tag{4.11}$$

Substitution for P_{obs} is then made using equation 4.4 giving

$$E_{array}^{sphere} = 10log_{10}\left\{\frac{\int_{\theta=0}^{2\pi}\int_{\phi=0}^{2\pi}\left(\frac{e^{-j\omega cr_1}}{r_1}+\frac{e^{-j\omega cr_2}}{r_2}+\frac{e^{-j\omega cr_3}}{r_3}\right)^2\mathrm{d}\phi\,\mathrm{d}\theta}{\int_{\theta=0}^{2\pi}\int_{\phi=\psi}^{\psi+\frac{\pi}{2}}\left(\frac{e^{-j\omega cr_1}}{r_1}+\frac{e^{-j\omega cr_2}}{r_2}+\frac{e^{-j\omega cr_3}}{r_3}\right)^2\mathrm{d}\phi\,\mathrm{d}\theta}\right\} \tag{4.12}$$

Since the array focus was designed to point toward an actuator, the cone angle is limited to $2\psi \leq \pi$. Therefore, due to symmetry about the XZ–plane, at most, only half of the sound power measured by the error sensor array could come from the direction of its corresponding actuator. Therefore, the error sensor array gain would be, at most, 3 dB. However, if the assumption of a free field may be made, then the error sensor gain would only include the hemisphere existing in negative Y, $0 \leq \phi \leq \pi$, and therefore, the error array may be expressed as

$$E_{array}^{hemisphere} = 10log_{10}\left(\frac{W_{total}^{hemisphere}}{W_{total}^{hemisphere} - W_{cone}}\right) \tag{4.13}$$

where $W_{total}^{hemisphere}$ is the total power within the hemisphere of negative Y. Referring to equation 4.12 for the spherical case, the hemispherical gain for a continuous system may be determined by

$$E_{array}^{hemisphere} = 10log_{10}\left\{\frac{\int_{\theta=0}^{2\pi}\int_{\phi=0}^{\pi}\left(\frac{e^{-j\omega cr_1}}{r_1}+\frac{e^{-j\omega cr_2}}{r_2}+\frac{e^{-j\omega cr_3}}{r_3}\right)^2\mathrm{d}\phi\,\mathrm{d}\theta}{\int_{\theta=0}^{2\pi}\int_{\phi=\psi-\frac{\pi}{2}}^{\psi+\frac{\pi}{2}}\left(\frac{e^{-j\omega cr_1}}{r_1}+\frac{e^{-j\omega cr_2}}{r_2}+\frac{e^{-j\omega cr_3}}{r_3}\right)^2\mathrm{d}\phi\,\mathrm{d}\theta}\right\} \tag{4.14}$$

Since the error sensor arrays were placed in an anechoic environment for this research, they were modelled using the hemisphere approach. Far field gain was determined based on a 75 mm source target at a distance of 100 mm. The source diameter is the typical width of a Smart Foam element used in this research effort and the distance was experimentally

determined as shown in Chapter 7—Active Noise Control. Figure 4.6 shows the response of the array at 800 Hz for four different error array diameters: 25 mm (1″), 76mm (3″), 152 mm (6″), and 356 mm (14″).

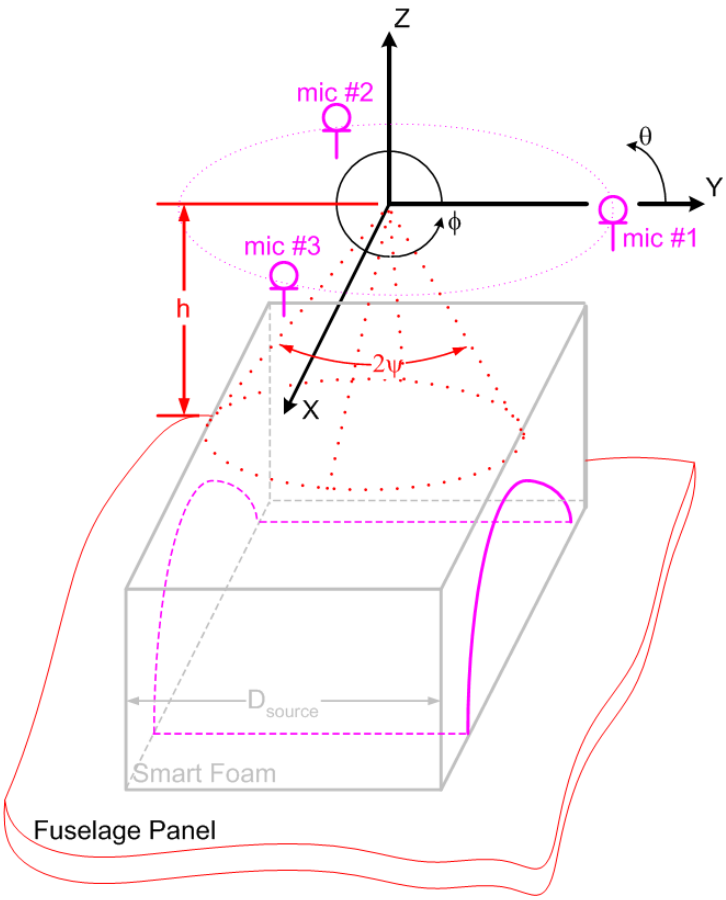

Figure 4.5: The error sensor arrays were designed to sense noise radiated from the vicinity of its corresponding actuator. The directionality of the actuator was defined to be the ratio of measured acoustic power to the acoustic power outside the cone of angle 2ψ.

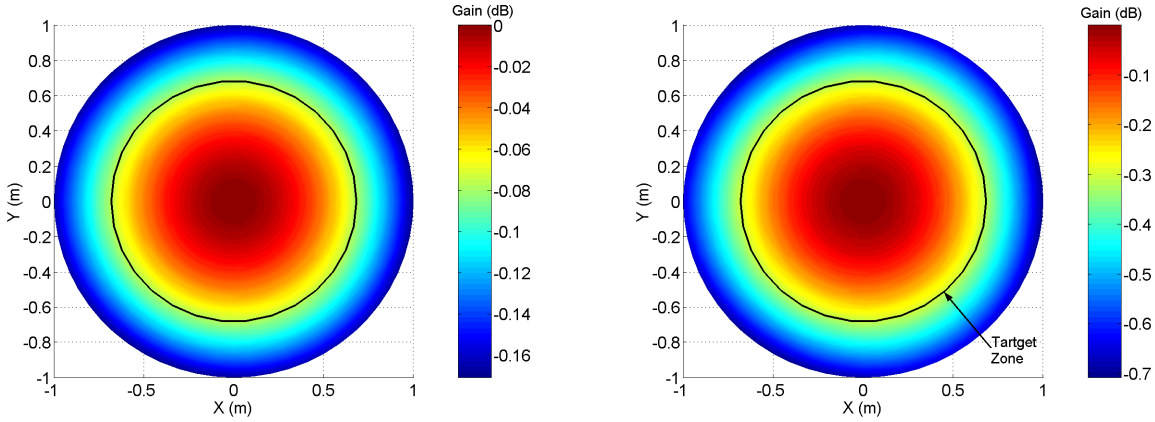

a) Gain at 800 Hz using a 3 cm array diameter

b) Gain at 800 Hz using a 8 cm array diameter

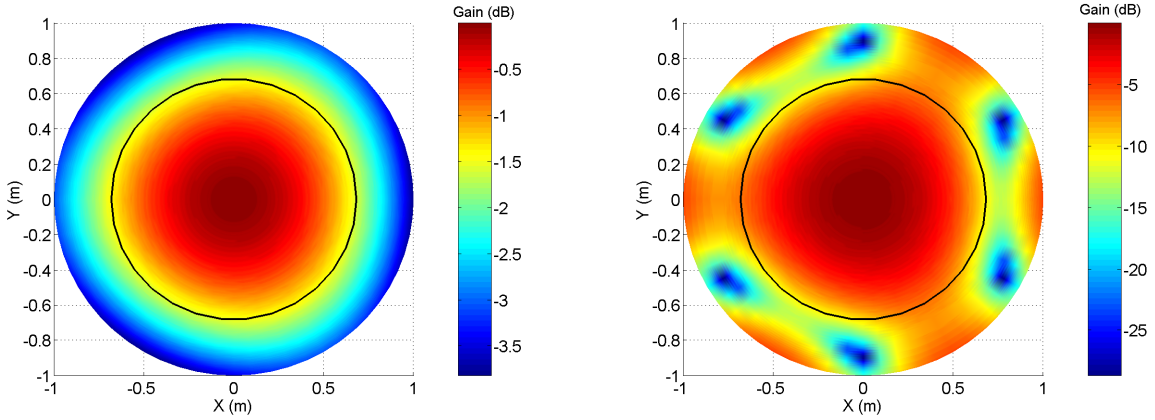

c) Gain at 800 Hz using a 15 cm array diameter

d) Gain at 800 Hz using a 38 cm array diameter

Figure 4.6: Error sensor array gains depend on the array diameter. The cone of directivity intersects the surface of summed pressures.

Figure 4.7 is a plot of hemispherical array gain versus array diameter at 800 Hz. Maximum gain was 3.7 dB and was achieved using a 360 cm (14″) diameter array. Note, that the use of a 2 m (78–1/2″) diameter array gave a zero gain at 800 Hz and for larger diameters the array gain asymptotically approached a value close to 1.2 dB. The sensor array radius was chosen to be 38 mm (1.5″). This dimension was chosen as a sufficient tradeoff between physical sensor size (with respect to actuator dimensions) and array gain.

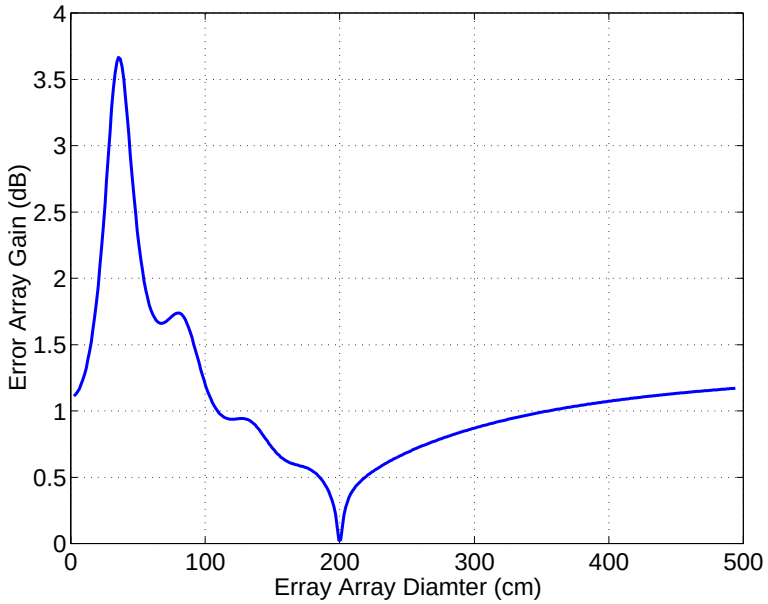

Figure 4.7: Error sensor gain versus array diameter. Maximum gain occurred using a diameter of 360 cm (14″). Using a diameter of 2 m, the array gain went to zero, and for larger diameters the array gain was asymptotical to approximately 1 dB.

The sensor array was then quantified experimentally by sweeping the source through two arcs—the azimuthal and elevation angles—relative to the array as shown in Figure 4.8 and compared to analytical data from Figure 4.9b. For the azimuthal configuration, microphone #1 is placed on the vertical line of geometric symmetry. Therefore, the directionality from 0^o to 90^o should be the mirror image of that from 90^o to 180^o. However, for the elevation angle, the trajectory of the disturbance did not cross any lines of geometric symmetry. Experimental and analytical values of azimuthal and elevation directionality decreased as the disturbance was moved off axis, therefore suggesting directionality in this plane. Between 30^o and 150^o the experimental data correlated well with the analytically determined response. However, there were discrepancies in the correlation at extremes of angles as shown in Figures 4.9. These discrepancies suggested that the actual performance of the error sensor array was more directional than that computed.

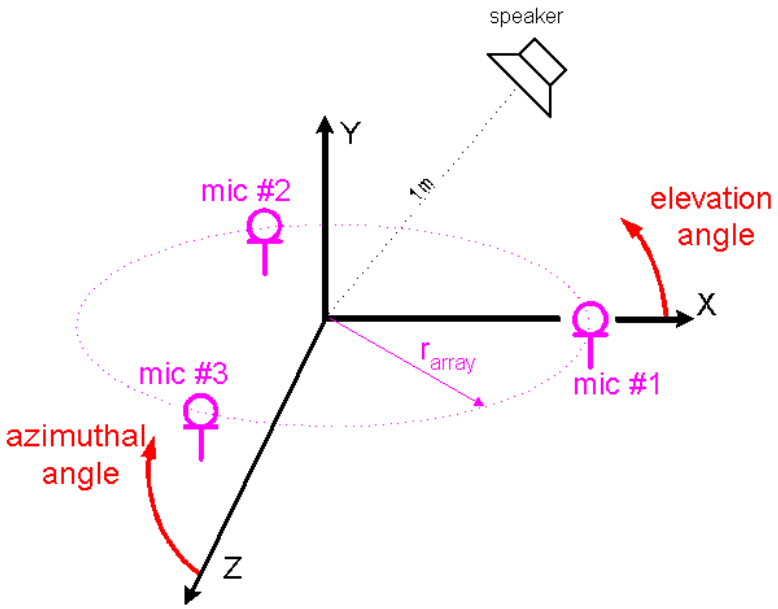

Figure 4.8: Far field directionality of the error sensor arrays was determined by placing a source and an array in an anechoic environment. They were spaced sufficiently such that measurements would be only of far field acoustics. The array was held stationary while the 800 Hz source was indexed in 15^o increments at a distance of 1 m.

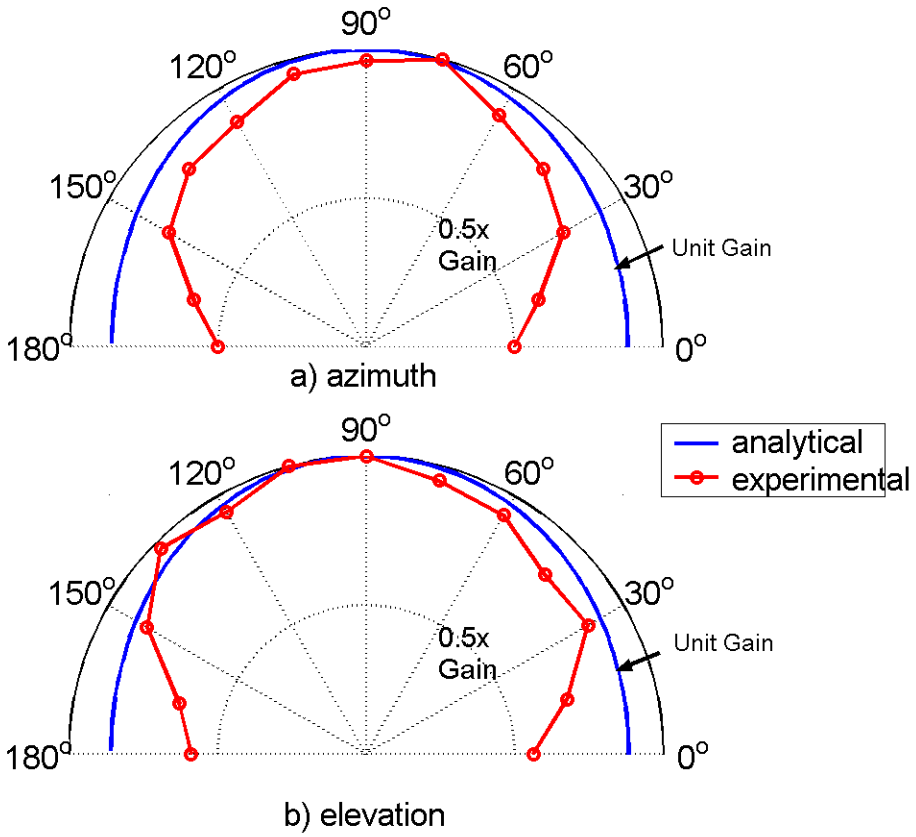

Figure 4.9: Results of error array directionality experiment. (a)Azimuthal angle directionality (b)Elevation angle directionality.

Sensor Array Near Field Analyses

Knowing the radius of the sensor array required for sufficient far field directionality, near field characteristics could then be estimated. Such characteristics of interest were the near field directivity and the ability of the array to reject near field waves (near field rejection) from being sensed. For this study, the sound pressure measured at the sensor array was compared to that measured by a single microphone as previously considered. However, the source used for this model was a 25 cm by 51 cm [1] array of small pistons mounted in an infinite baffle. Using this array, near field analyses were studied using five different source spatial patterns. For each of these patterns, the elements within the array were phased such that the array would radiate either uniformly, as a monopole, as a dipole, as a quadrapole or with random phase. Sensor array response was computed at two geometric locations relative to the piston array–at one corner of the piston array, and on one side. These placements represent locations used during control experiments and control simulations and were denoted Type I Placement and Type II Placement, respectively.

Presented below are theories regarding sensor near field rejection analysis and near field directivity. Analytical results follow for each of the two array placements and each of the five piston array spatial patterns for a total of ten observed events per analysis.

Theory—Near Field Directivity and Near Field Rejection

Theories regarding the near field analyses—near field directivity and near field rejection—performed to characterize the error sensor arrays are presented here.

Near field directivity refers to how well the error sensor array rejects acoustic energy originating outside the desired target area. This analysis demonstrates the ability of the error sensor array to physically decouple its respective channel from neighboring channels given both the near field and far field components of the acoustic field.

Near field rejection refers to the ability of the error sensor array to reject the near field component of the acoustic field. A high near field rejection gain refers to an array capable of rejecting much of the near field component. Such an array would then primarily sense only the radiating component of the generated acoustic field.

Equation 4.3 used in the previous analysis only considered far field effects. To also represent the near field component, the equation may be expressed as

$$P_i = A_i \frac{e^{-j\omega c r_i}}{r_i} \frac{jk}{1 + jka} \tag{4.15}$$

And, similar to equation 4.2, the acoustic pressure observed by the sensor array would be

$$P_{obs} = \sum_k A_k \frac{e^{-j\omega c r_k}}{r_k} \tag{4.16}$$

[1] This geometry was chosen based on the geometry of the radiating plate used in the wind tunnel control experiments and simulations.

with r_k equal to the distance between microphone i and each j element of the rectangular piston array.

The gain equation used for this study involved normalizing the measured error sensor array signals to that of a single microphone placed at the center of the array. This was done for measured signals due to noise radiated from the entire plate and for noise measured if it were only radiated from the target zone (i.e. the vicinity of the actuator). This expression is

$$E_{array}^{NF} = 10log_{10}\left\{\frac{\frac{P_{array}}{P_{1mic}}}{\frac{P_{array}}{P_{1mic}} - \frac{P_{target,array}}{P_{target,1mic}}}\right\} \tag{4.17}$$

where P_{1mic} is the pressure measured at a single microphone located at the center of the array, P_{array} the sum of pressures measured by the array, $P_{target,1mic}$ the pressure measured at the centered microphone due to noise radiated from the target zone, and $P_{target,array}$ the sum of pressures measured by the array due to noise radiated from the target zone. This expression may be rearranged to

$$E_{array}^{NF} = 10log_{10}\left\{\frac{1}{1 - \frac{P_{target,array}}{P_{target,1mic}}\frac{P_{1mic}}{P_{array}}}\right\} \tag{4.18}$$

Note, $P_{target,array} \leq P_{array}$ and $P_{target,1mic} \leq P_{1mic}$.

To determine the sensor gain in the presence of near field effects the following equation was formulated.

$$E_{array}^{NFRejection} = 10log_{10}\left\{\frac{\left(\frac{P_{1mic}}{P_{1mic}^{FF}}\right)}{\left(\frac{P_{Array}}{P_{Array}^{FF}}\right)}\right\} \tag{4.19}$$

where P_{1mic}^{FF} and P_{Array}^{FF} are the single microphone pressure and the sum of pressures at the sensor array given only far field waves. Equation 4.19 may be simplified to

$$E_{array}^{NFRejection} = 10log_{10}\left\{\frac{P_{1mic}}{P_{1mic}^{FF}}\frac{P_{Array}^{FF}}{P_{Array}}\right\} \tag{4.20}$$

Response at Type I and Type II Placements was observed for each of the five piston array configurations. Type I Placement refers to an error array used with actuators mounted at the corners of the plate. Type II Placement refers to actuators mounted along one edge of the radiating plate—the four actuators in the center. These two scenarios are shown in Figure 4.10.

Results—Sensor Near Field Rejection Analysis

Results for the near field error sensor gain and the near field error sensor rejection gain are presented. Results are arranged relative to the spatial phase of the piston array used in

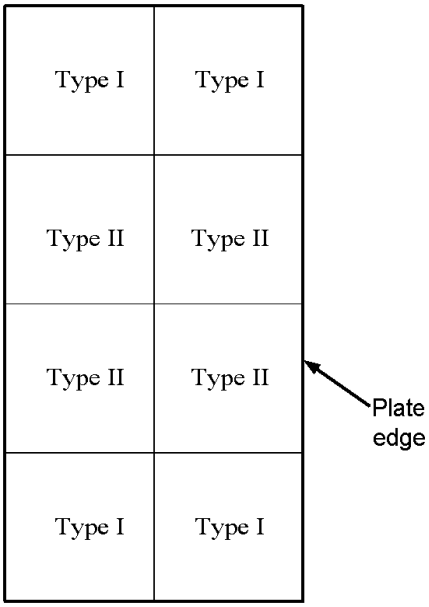

Figure 4.10: Error array placement was performed using two different scenarios—Type I Placement and Type II Placement. Type I Placement occurred at the plate corners and Type II Placement at the plate edges.

the following order: uniform phase, monopole piston array, dipole piston array, quadrapole piston array, and random phase piston array. Within each of these five categories, results are presented for both Type I and Type II Placements. These results are then summarized in Table 4.1 below.

The piston array consisted of a grid of many small pistons. This array was placed in an infinite baffle therefore radiating into a half space without reflections. The phase configurations of the radiating piston array are shown graphically in Figure 4.11. Here, the uniform, monopole, dipole, and quadrapole arrangements are shown. For the random phase piston array, each small piston has random phase.

The uniform phase piston array consisted of a number of small piston sources (monopole sources) arranged on a grid and mounted in an infinite baffle. Piston sources (elements) were all in phase and each had the same magnitude. Grid spacing decreased until gains converged requiring 15 elements per side for a total of 225 elements.

Figure 4.12 presents results for the Type I Placement of sensor arrays given the uniform phase piston array. For this configuration, the sensor array gain and near field rejection gain were 10.8 dB and 4.8 dB, respectively.

Figure 4.13 presents results for the Type II Placement of sensor arrays using the uniform phase piston array. For this configuration, the near field sensor array gain and near field rejection gain were 13.8 dB and 4.8 dB, respectively. Placement of the sensor array

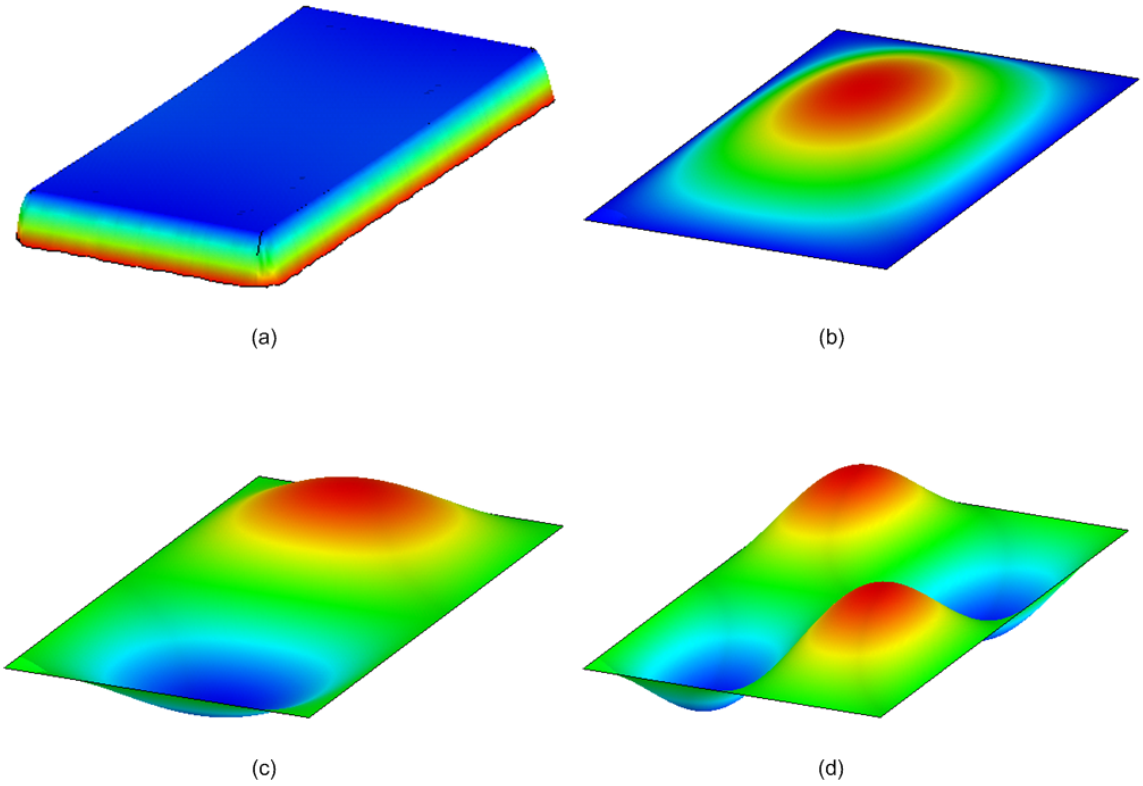

Figure 4.11: Spatial phase using the 0.248 m by 0.508 m (9-3/4″ by 20″) piston array. (a) uniform, (b) monopole, (c) dipole and (d) quadrapole. A fourth spatial phase distribution, random, was also used but is not shown.

at the edge of the plate increases sensor gain by 3.0 dB with respect to Type I Placement. With all other factors equal, this would suggest that control performed at Type II Placement locations, given a uniform source, should achieve better performance than control performed at Type I Placement.

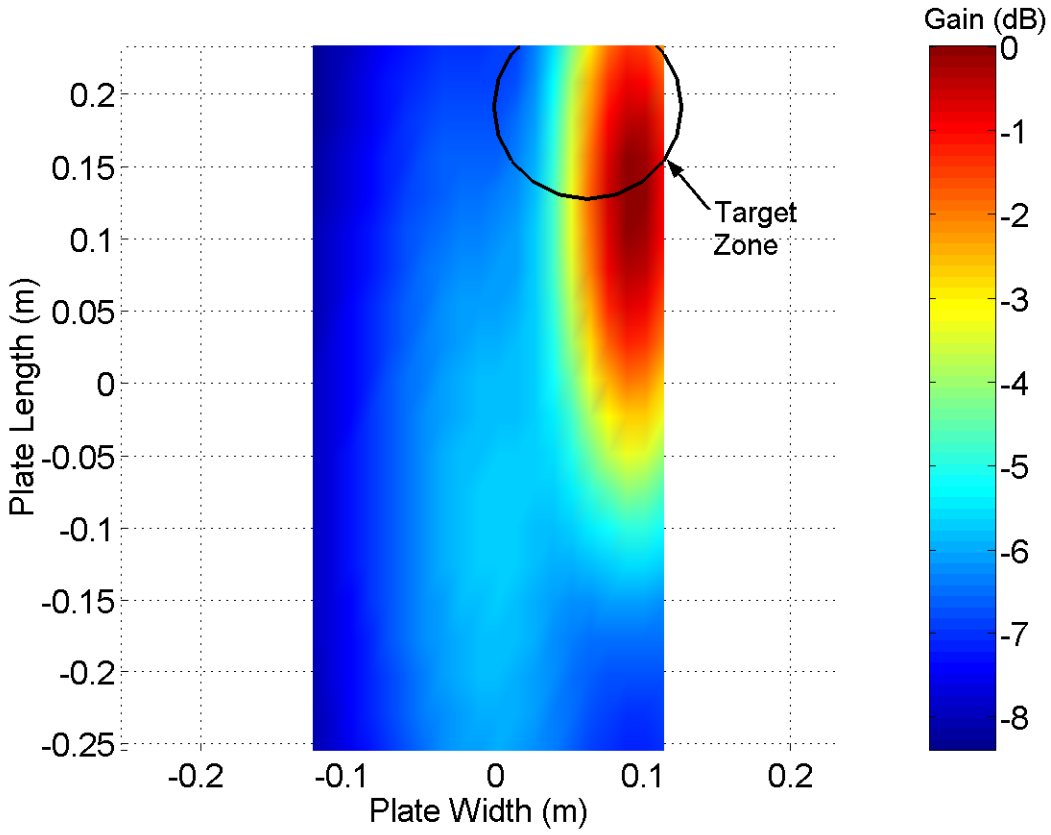

Figure 4.12: Error array gain at Type I placement (at plate corner) over the 0.248 m by 0.508 m (9-3/4″ by 20″) uniform phase piston array.

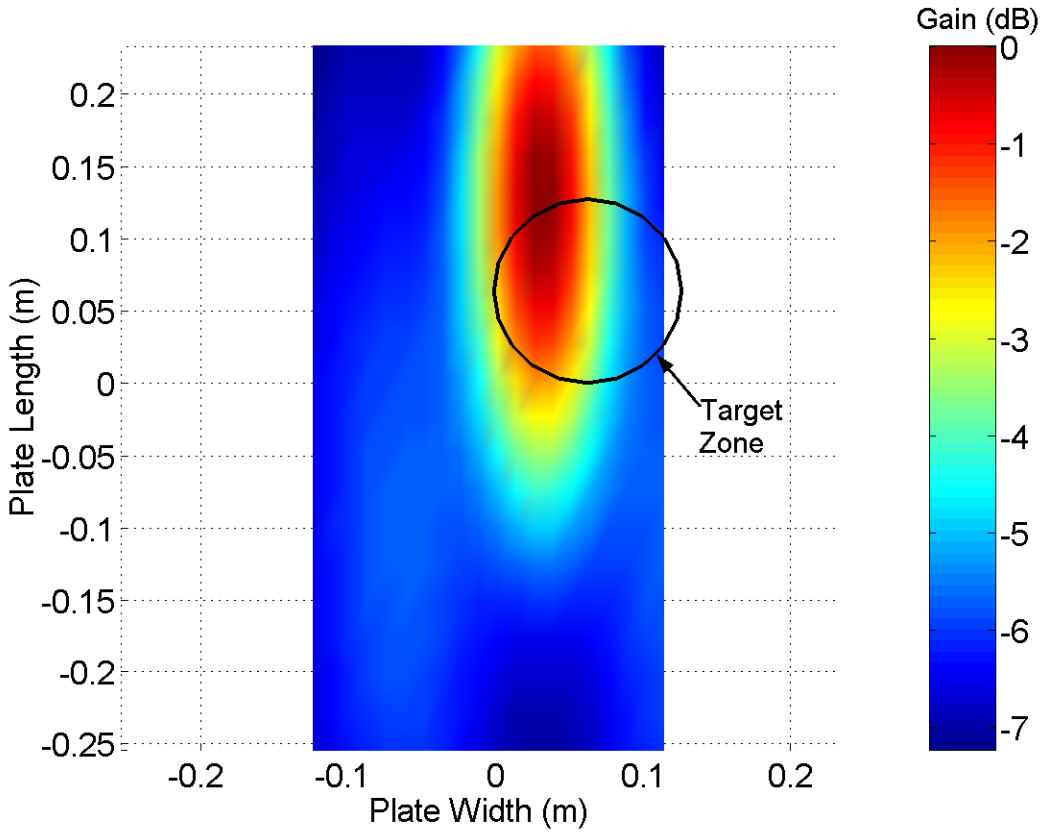

Figure 4.13: Error array gain at Type II placement (at plate edge) over the 0.248 m by 0.508 m (9-3/4″ by 20″) uniform phase piston array.

For the monopole phase piston array, the piston sources were all in phase having a magnitude which varied with respect to a half-wave sinusoid in each direction from zero along the edges to unity at the center of the array as shown in Figure 4.11b and Figure 4.14. Grid spacing was decreased until gains converged requiring 30 elements per side for a total of 900 elements. Note that all sources are in phase having a magnitude ranging from zero at the plate edges to unity at the center.

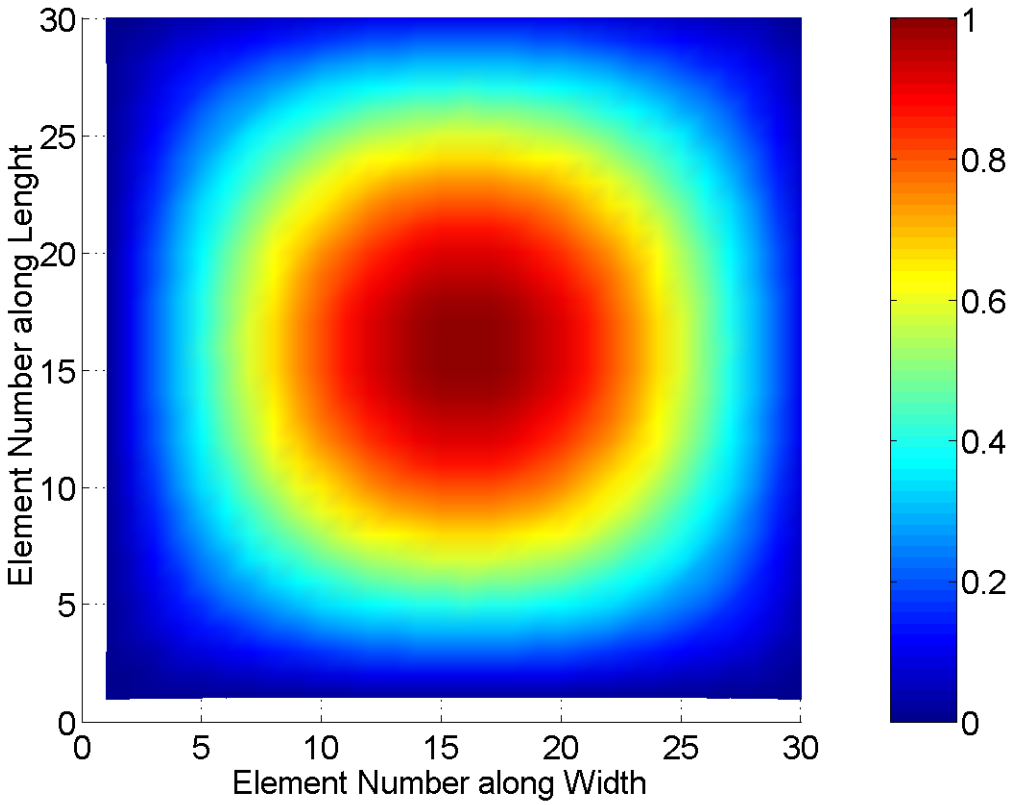

Figure 4.14: Monopole piston array phase distribution.

Figure 4.15 presents results for the Type I Placement of sensor arrays given the monopole piston array. For this configuration, the sensor array gain and near field rejection gain were 13.1 dB and 4.8 dB, respectively.

Figure 4.16 presents results for the Type II Placement of sensor arrays using the monopole piston array. For this configuration, the near field sensor array gain and near field rejection gain were 16.5 dB and 4.8 dB, respectively. Placement of the sensor array at the edge of the plate decreases sensor gain by 6.5 dB with respect to Type I Placement given a monopole source. With all other factors equal, this would suggest that control performed

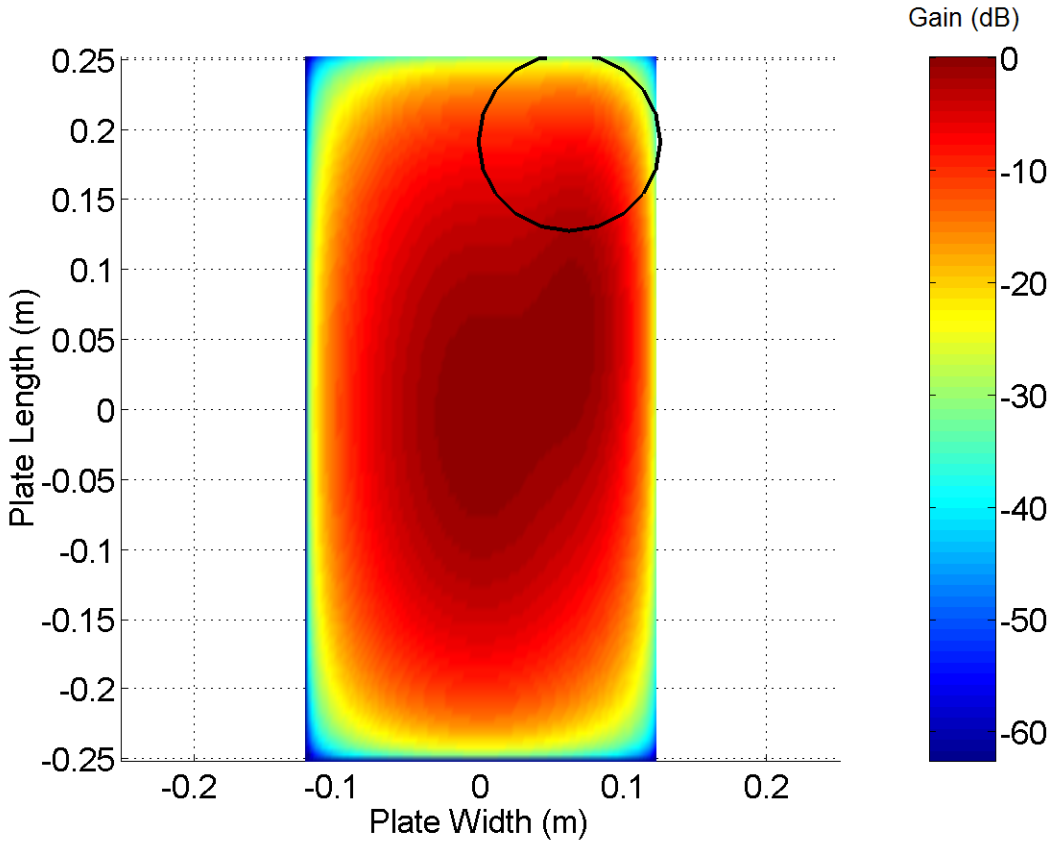

Figure 4.15: Error array gain at Type I placement (at plate corner) over the 0.248 m by 0.508 m (9-3/4″ by 20″) monopole piston array.

at Type I Placement locations, given a monopole source, should achieve better performance than control performed at Type II Placement locations.

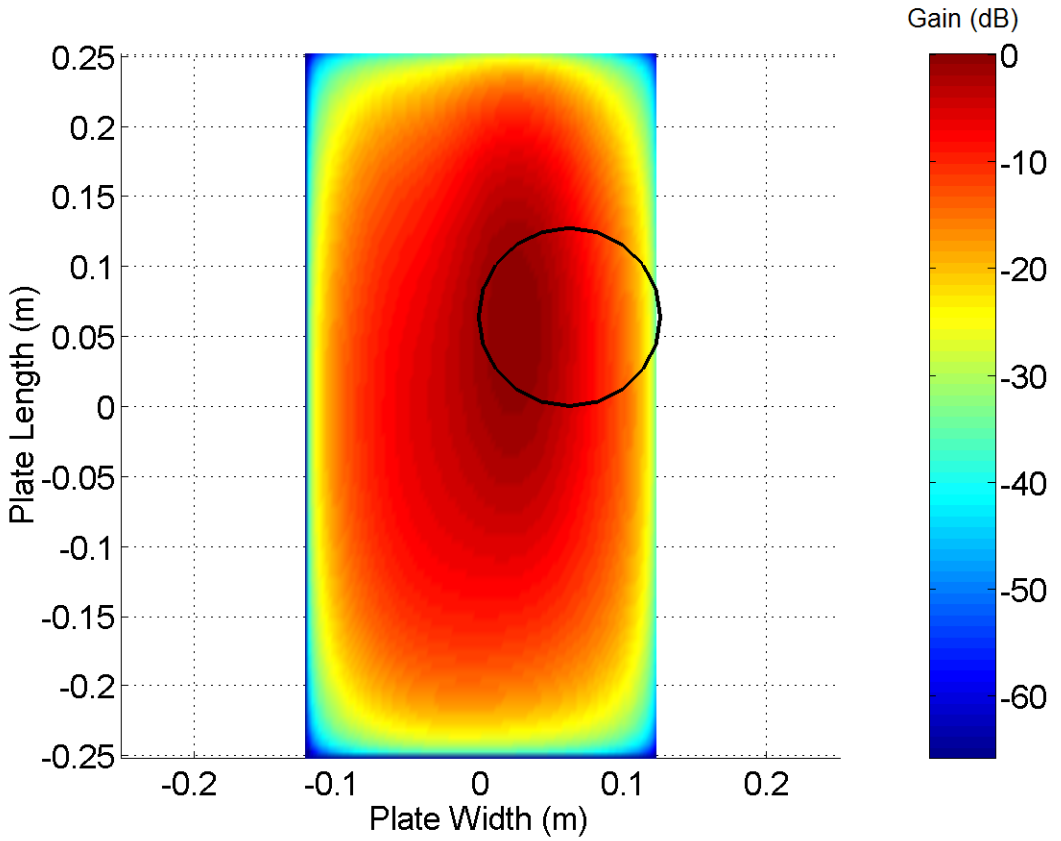

Figure 4.16: Error array gain at Type II placement (at plate corner) over the 0.248 m by 0.508 m (9-3/4″ by 20″) monopole piston array.

For the piston array configured as a dipole, the piston sources were phased having a magnitude which varied with respect to one full-wave sinusoid along the length of the piston array. Along the piston array width, the piston sources were phased having a magnitude which varied with respect to one half-wave sinusoid. This configuration resulted in zero magnitude at the piston array boundaries and along the line bisecting the array into two equal square areas as shown in Figure 4.11c and Figure 4.17. Note that each half-space is out of phase with respect to each other. Grid spacing was decreased until gains converged requiring 200 elements per side for a total of 40,000 elements in the piston array.

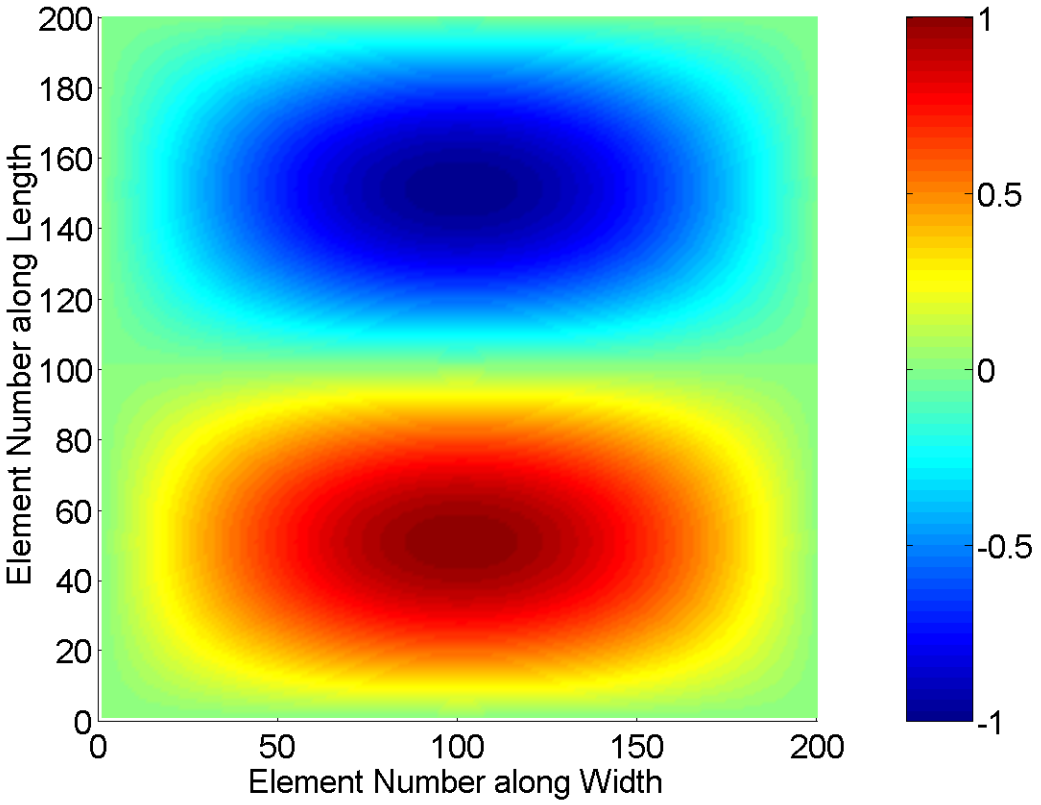

Figure 4.17: Dipole piston array phase distribution.

Figure 4.18 presents results for the Type I Placement of sensor arrays given the dipole piston array. For this configuration, the sensor array gain and near field rejection gain were 13.5 dB and 4.8 dB, respectively.

Figure 4.19 presents results for the Type II Placement of sensor arrays using the dipole piston array. For this configuration, the near field sensor array gain and near field rejection gain were 14.7 dB and 4.8 dB, respectively. Placement of the sensor array at the

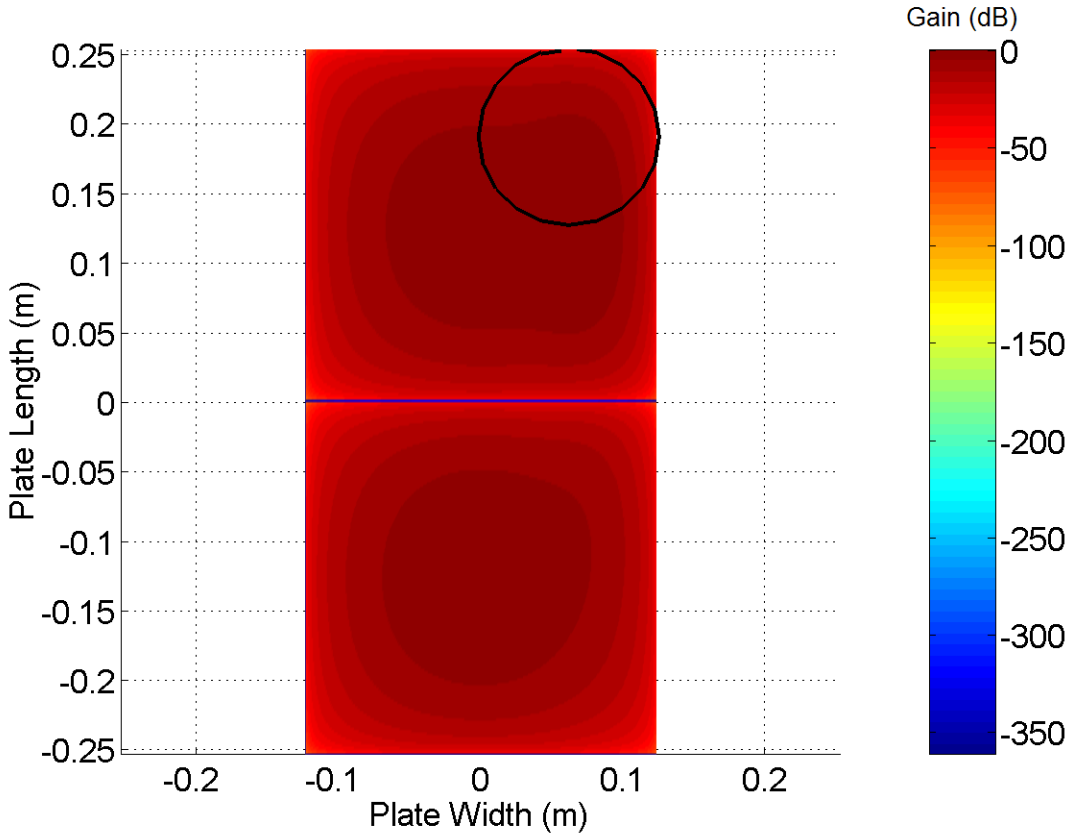

Figure 4.18: Error array gain at Type I placement (at plate corner) over the 0.248 m by 0.508 m (9-3/4″ by 20″) dipole piston array.

edge of the plate increases sensor gain by 1.2 dB with respect to Type I Placement given a dipole source. With all other factors equal, this would suggest that control performed at Type II Placement, given a dipole source, should achieve better performance than control performed at Type I Placement.

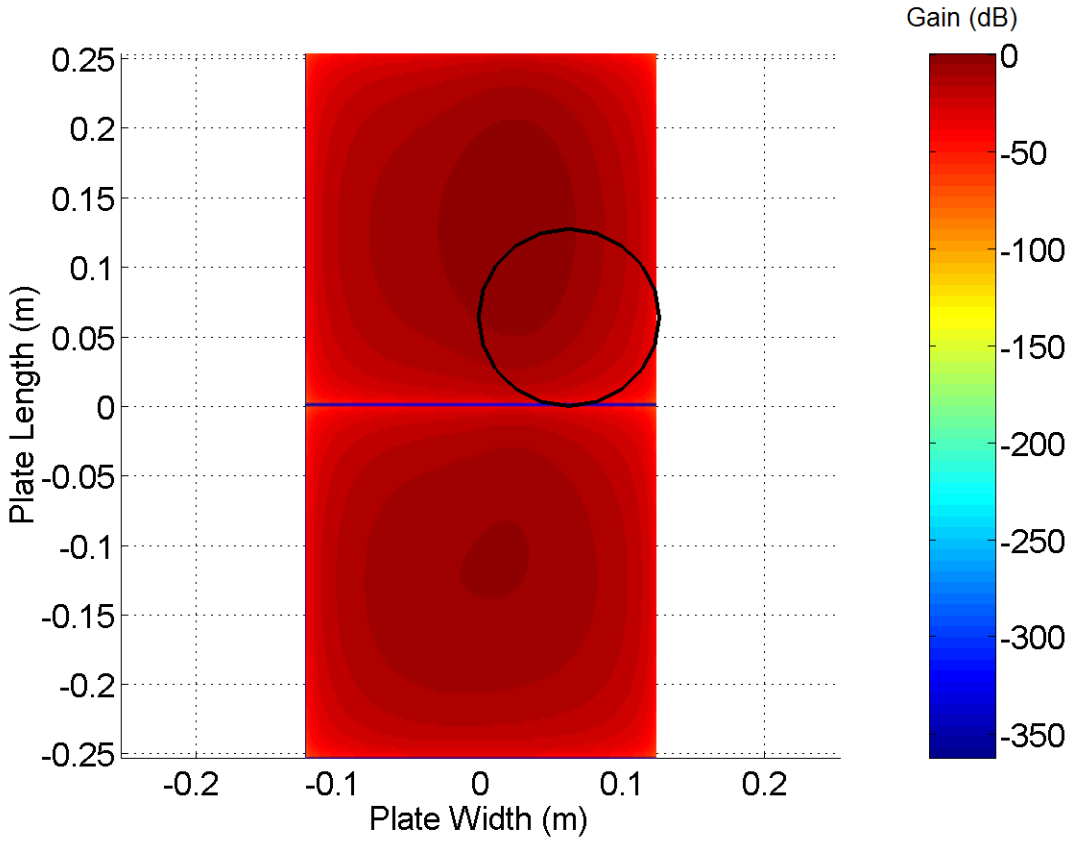

Figure 4.19: Error array gain at Type II placement (at plate corner) over the 0.248 m by 0.508 m (9-3/4″ by 20″) dipole piston array.

For the piston array configured as a quadrapole, the piston sources were phased having a magnitude which varied with respect to one full-wave sinusoid along both the length and the width of the piston array. This configuration resulted in zero magnitude at the piston array boundaries and along two orthogonal lines dividing the array into four equal rectangular areas. The magnitude of the quadrapole piston array is shown in Figure 4.11d and Figure 4.20. Grid spacing was decreased until gains converged requiring 500 elements per side for a total of 250,000 elements in the piston array.

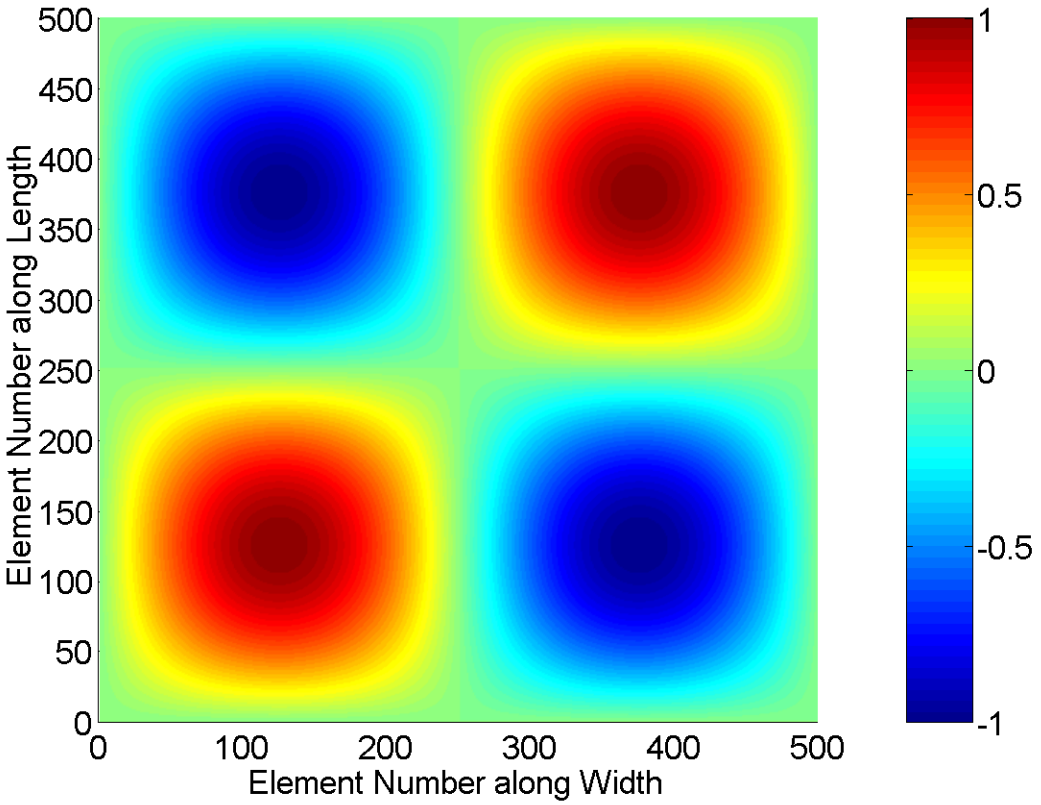

Figure 4.20: Quadrapole piston array phase distribution.

Figure 4.21 presents results for the Type I Placement of sensor arrays given the rectangular quadrapole piston source array. For this configuration, the sensor array gain and near field rejection gain were 14.6 dB and 4.8 dB, respectively.

Figure 4.22 presents results for the Type II Placement of sensor arrays using the quadrapole piston array. For this configuration, the near field sensor array gain and near field rejection gain were 9.5 dB and 4.8 dB, respectively. Placement of the sensor array at the edge of the plate decreases sensor gain by 5.1 dB with respect to Type I Placement given

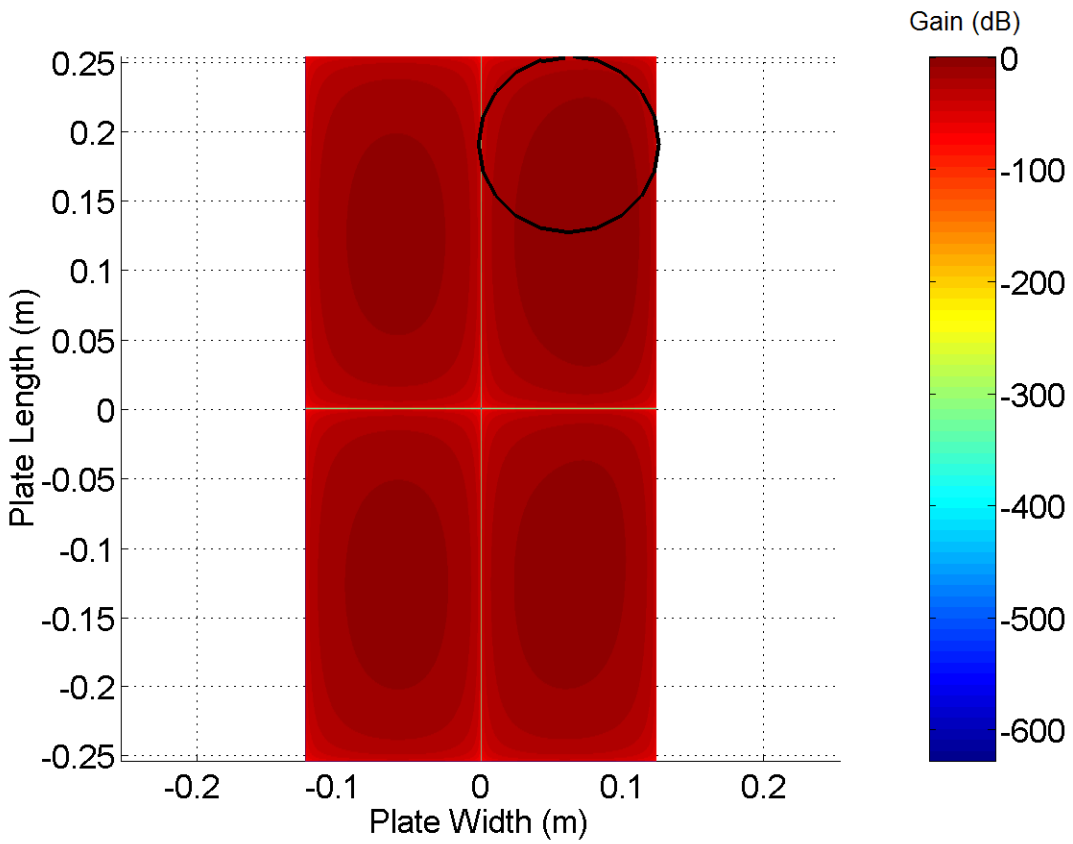

Figure 4.21: Error array gain at Type I placement (at plate corner) over the 0.248 m by 0.508 m (9-3/4″ by 20″) quadrapole piston array.

a quadrapole source. With all other factors equal, this would suggest that control performed at Type I Placement, given a quadrapole source, should achieve better performance than control performed at Type II Placement.

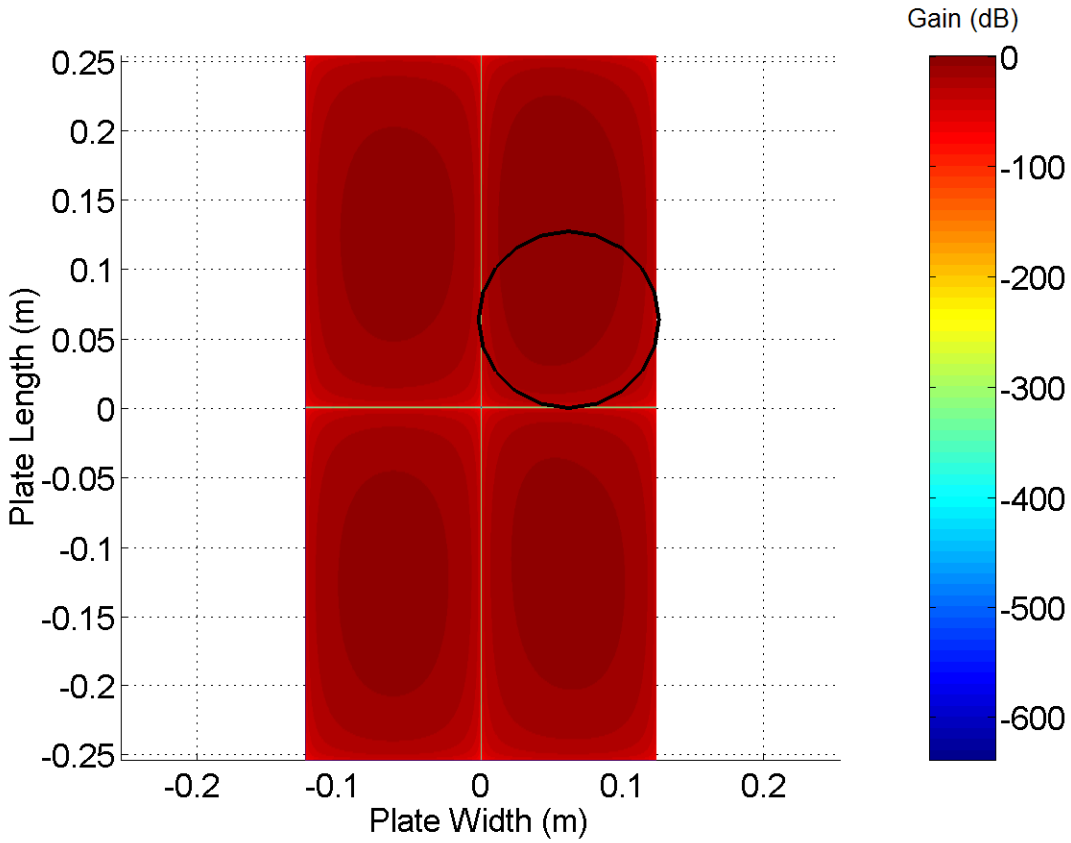

Figure 4.22: Error array gain at Type II placement (at plate corner) over the 0.248 m by 0.508 m (9-3/4″ by 20″) quadrapole piston array.

For the piston array in the random phase configuration, the piston sources were phased having random magnitude. Grid spacing was decreased until gains converged requiring 600 elements per side for a total of 360,000 elements in the piston array. The magnitude of the piston array for this configuration is shown in Figure 4.23.

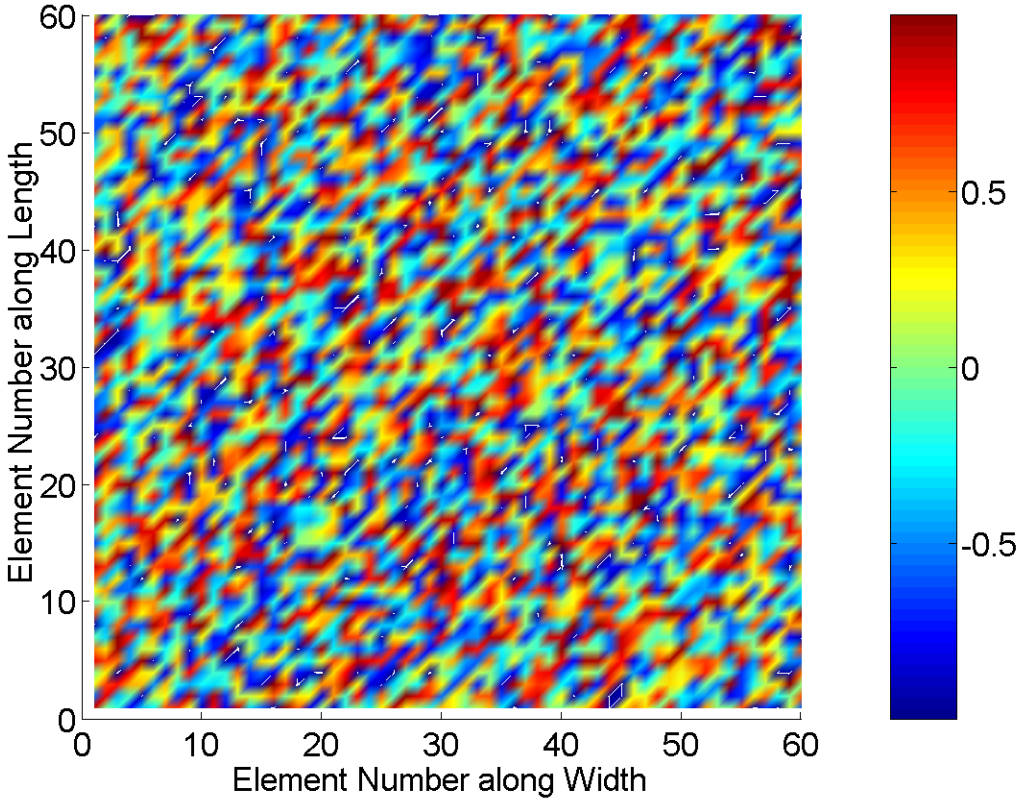

Figure 4.23: Random piston array phase distribution.

Figure 4.24 presents results for the Type I Placement of sensor arrays given the random phase piston source array. For this configuration, the sensor array gain and near field rejection gain were 6.5 dB and 4.8 dB, respectively.

Figure 4.25 presents results for the Type II Placement of sensor arrays using the random phase piston source array. For this configuration, the near field sensor array gain and near field rejection gain were 14.3 dB and 4.8 dB, respectively. Placement of the sensor array at the edge of the plate increases sensor gain by 7.8 dB with respect to Type I Placement given a random phase source. With all other factors equal, this would suggest that control performed at Type II Placement, given a random phase source, should achieve better performance than control performed at Type I Placement.

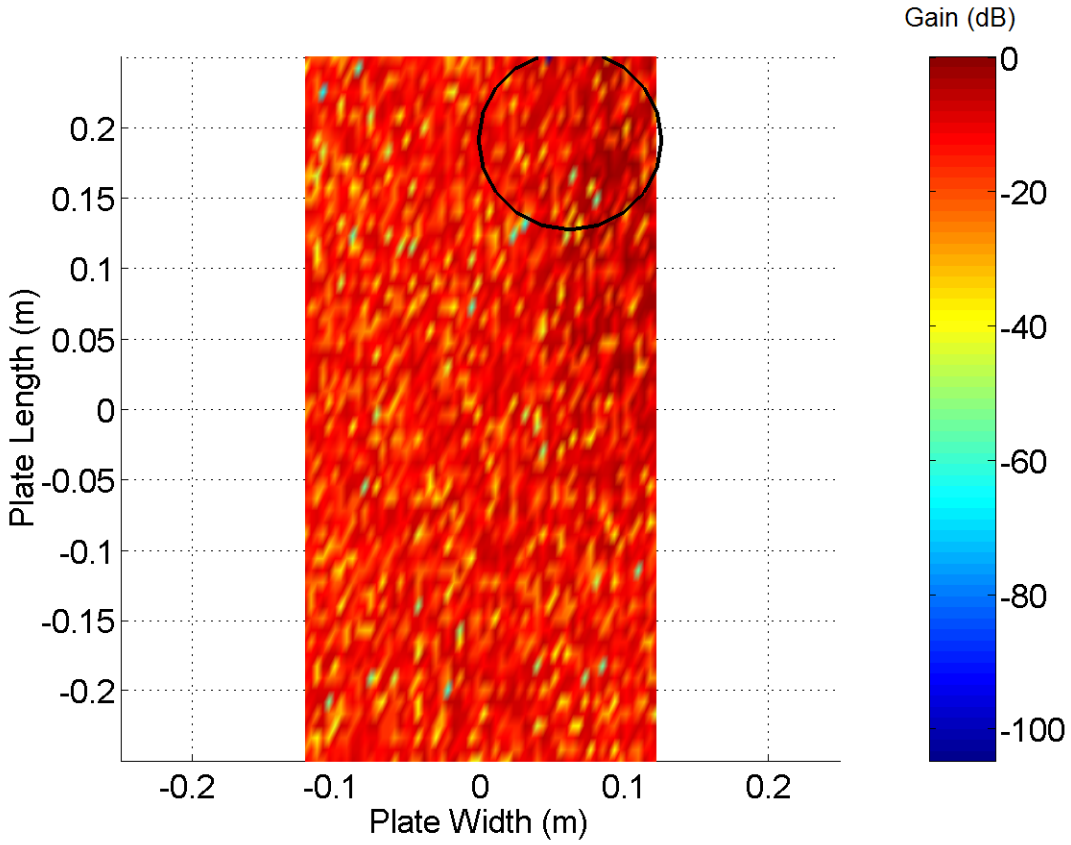

Figure 4.24: Error array gain at Type I placement (at plate corner) over the 0.248 m by 0.508 m (9-3/4″ by 20″) random phase piston array.

Table 4.1: Summary of results for near field error gain analysis using the 0.248 m x 0.508 m piston array.

Piston Array Configuration	**Near Field Gains** Sensor Gain E^{NF}_{array}, Rejection Gain $E^{NFRejection}_{array}$
	Type I	*Type II*
Uniform	10.8 dB, 4.8 dB	13.8 dB, 4.8 dB
Monopole	13.1 dB, 4.8 dB	16.5 dB, 4.8 dB
Dipole	13.5 dB, 4.8 dB	14.7 dB, 4.8 dB
Quadrapole	14.6 dB, 4.8 dB	9.5 dB, 4.8 dB
Random	6.5 dB, 4.8 dB	14.3 dB, 4.8 dB

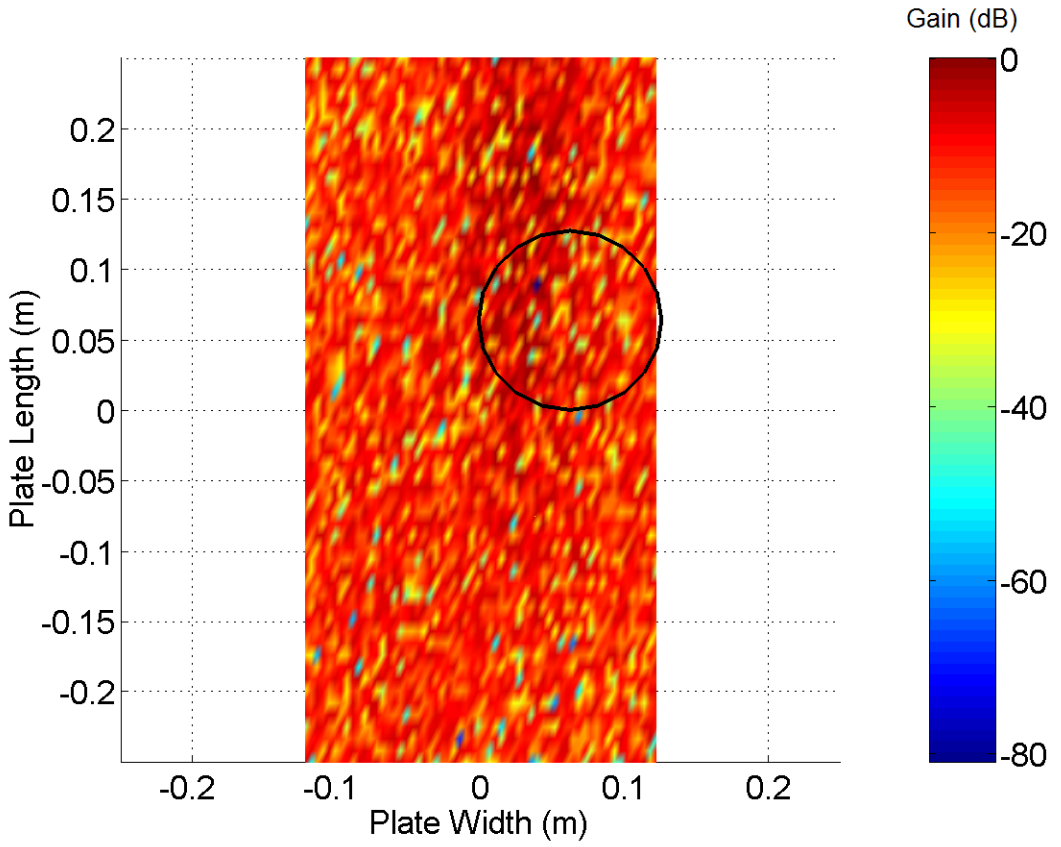

Figure 4.25: Error array gain at Type II placement (at plate corner) over the 0.248 m by 0.508 m (9-3/4″ by 20″) random piston array.

4.3 Summary

Three analyses were performed to characterize the error sensor arrays: far field directivity, near field directivity, and near field rejection. The sensor array was first developed in the far field to identify the radius required and the sensitivity of the array to changes in its radius.

Given geometric limitations, the design of the error sensor array resulted in poor far field directivity. However, considerable performance was achieved for near field directivity and near field rejection. Since the arrays were intended for use in the near field the poor far field performance was not considered to be a detriment to this research effort.

Error sensor directionality was developed with respect to far field acoustics at a design frequency of 800 Hz. The analysis suggested that a maximum far field sensor gain of 3.7 dB could be achieved but would require an array radius of 190 mm. This would be prohibitively large given the geometry of the enclosure and the required number and resulting size of the actuators. For a 38 mm radius array, simulation suggested directionality would only be approximately 1.5 dB. However, experiment showed the error array was 3 dB more sensitive on axis than at 90^o to the axis.

Simulations were then performed to investigate error array performance in the near field. Error array directionality and the ability to reject near field components was considered. These analyses were performed using an array of small piston sources acting over an area equal to the area of the radiating plate used in control experiments and control simulations.

Error array performance was considered at the two locations used in the control experiments and the control simulations. These locations, Type I Placement and Type II Placement, refer to those control channels located at the corners and edges of the radiating plate, respectively. For each placement, five phase configurations of the piston array were observed: uniform phase piston array, monopole piston array, dipole piston array, quadrapole piston array, and random phase piston array. The first four cases had near field rejection gains from 9.5 dB to 16.5 dB. Performance varied with placement by up to 3 dB for a given source with Type II Placement having greater gain for all but the quadrapole case.

The random phase piston source configuration had a near field rejection gain of 6.5 dB at Type I Placement and 14.3 dB at Type II Placement. This configuration best approximates control experiment and control simulation conditions given the random nature of the turbulent boundary layer induced interior noise.

Near field directivity was estimated to be 4.8 dB for all cases. Therefore, error array performance was determined to be independent of the noise source and placement relative to it.

Chapter 5

Actuators

Smart Foam actuators were used to generate the secondary acoustic field used to cancel interior noise due to the radiating plate. Previous research conducted using Smart Foam was presented in Chapter 1—Introduction. This chapter presents the fabrication and qualification of the Smart Foam configurations used for this research effort.

5.1 Fabrication of Smart Foam Elements

Smart Foam elements consist of three key elements. They are the upper and lower foam pieces and the polyvinylidene diflouride (PVDF) sheet sandwiched between them. The foam used in the actuators shown here is Polydamp® Acoustical Foam (PAF) and is manufactured by Polymer Technologies, Inc. PAF is an acoustical grade, open cell, flexible, ether based urethane foam having a mass density of 29 kg/m^3 and porosity of 28 cells/cm (70 cells/inch). Components of a typical Smart Foam element, and its placement on a structure, is shown in Figure 5.1 and Figure 5.2, respectively. Although the Smart Foam element is shown mounted on the radiating structure, it may be mounted away from it as well as the secondary source in active noise cancellation applications.

The steps required for making a Smart Foam element are outlined below. Note, though, that Smart Foam elements are typically baffled so that they radiate in a more monopolistic manner. For clarity, baffles are not shown since details of the Smart Foam components would be hidden.

Since there was no rigid mount to attach the ends of the PVDF sheet, balsa rails were incorporated into the design. These rails provided a stiff boundary condition to the PVDF sheet allowing for a significantly greater authority than if the actuator were allowed free–free end conditions. In addition to providing the clamped–clamped boundary condition, the balsa rails provided a surface to which double–sided tape could be used for mounting the Smart Foam elements to the vibrating plate. Further, their design doubled as a convenient handle during the mounting process.

Presented is the process used to construct the 18 cm long, 8 cm wide, 9 cm tall Smart Foam element used in the four channel control experiments. The process is the same for

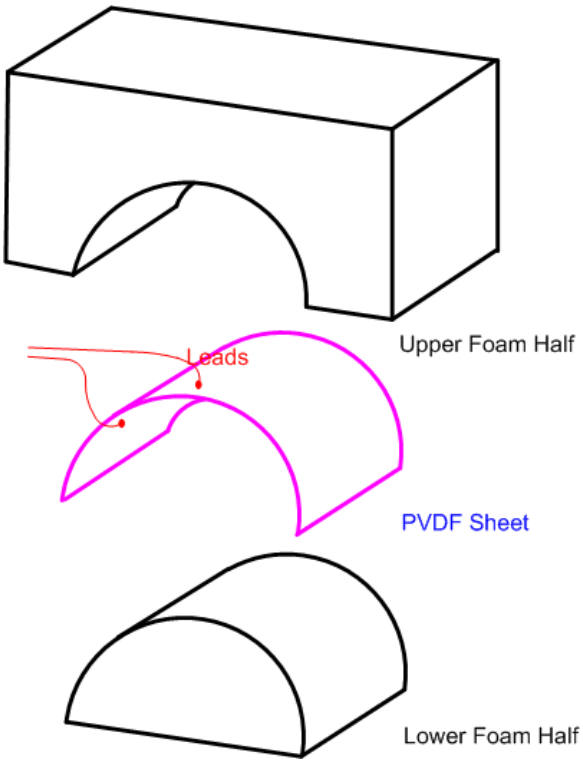

Figure 5.1: Smart Foam elements consists of two foam pieces sandwiching a PVDF layer. Elements may be placed on or near a radiating structure as a means a of secondary source in noise cancellation applications.

constructing Smart Foam elements of other sizes, however the dimensions must be changed appropriately.

The first step in making the elements is to cut the foam in an arc measuring 83 mm (3-1/4″) in radius (Figure 5.3). Two additional cuts were then made on the lower piece allowing for placement of the balsa rails.

Double–sided tape is then applied to the balsa rails—on the hypotenuse and on one other side. The tape on the hypotenuse is used to adhere the rails to the foam at the 10 mm (3/8″) x 45^o cuts (Figure 5.4) and the other piece is used later to adhere the PVDF. The rails used are 45^o angles measuring 10 mm (3/8″) in width and 8 cm (3″) in length.

After cutting the foam, the PVDF sheet is then cut to size and etched. The etching is required in order to prevent short–circuiting across the actuator electrodes. Etching is performed using acetone or etchant solution (nail polish remover works well and is readily available) applied with a small swab or cloth. Both sides of the PVDF must be done in order to determine that the electrodes have been properly etched. This allows removal of the electrode on each opposing surface of the PVDF sheet exposing the clear active material within. Visual inspection will identify remaining electrode material having the potential to

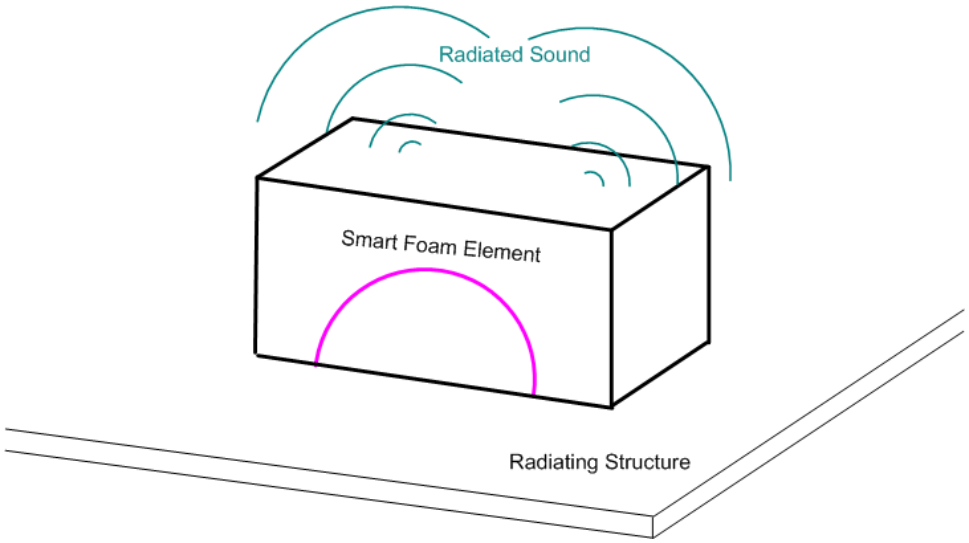

Figure 5.2: Smart Foam may be placed on or near a radiating structure as a means a of secondary source in noise cancellation applications.

cause an electrical short. After inspection, a continuity test producing infinite resistance across the two silver ink electrodes may be performed to ensure proper etching.

Leads are then attached to the electrodes. First, leads are soldered to 25 mm (1″) long strips of 12 mm (1/2″) wide copper tape. After soldering, the tape is adhered to the PVDF. It should be noted that heat from directly soldering leads to the electrodes results in localized shrinking or even melting of the PVDF. The wiring used is either 26 or 30 AWG depending on availability. It is recommended that thinner (higher gauge) wiring be used so as to not affect the dynamics of the smart cell. However, thin wire breaks easily with use and must be handled with care. Using an excess of length for the leads allows the wire to be trimmed and stripped fresh for each application thus ensuring a high quality electrical connection. See Figure 5.5 for a completed PVDF sheet with attached leads.

The PVDF actuator is then placed on the lower foam half. First, a light coating of spray glue is applied to the lower foam piece. Then, one end of the PVDF is adhered to one rail. The PVDF is tensioned slightly as shown in Figure 5.4 in order to preload the foam ensuring contact. The free end is then adhered to the other rail. Finally, the foam top is trimmed approximately 3 mm (1/8″) so that it does not contact the vibrating plate. It is then sprayed with a light coating of spray glue and adhered to the lower portion of the Smart Foam element. See Figure 5.6 for a photograph of the completed Smart Foam element.

The Smart Foam element is now ready to be mounted to the vibrating plate. Double–sided tape is again used by placing a strip on each exposed rail surface. Although the Smart Foam elements were designed to always remain in contact with the vibrating surface by using only the double-sided tape on the rails, a light coat of spray glue was applied as well to the

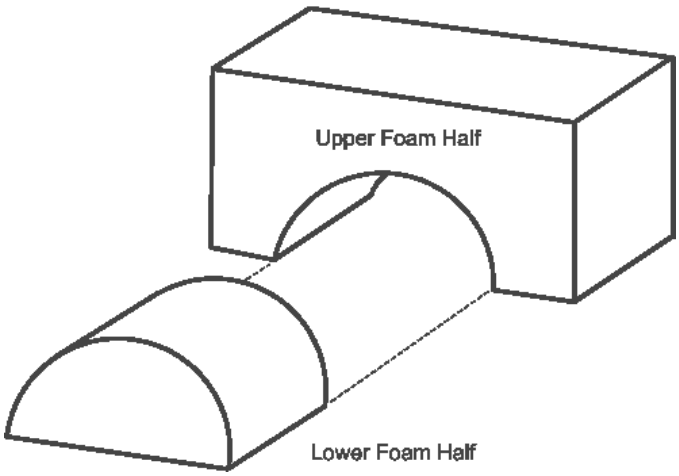

Figure 5.3: Foam block cut into two pieces allowing placement of the PVDF sheet. Lower edges of the lower block are cut to allow mounting of the balsa rails.

element bottoms before application.

5.2 Smart Foam Configurations

The two configurations of Smart Foam used during this research effort included a four channel configuration, using the previously mentioned Smart Foam elements, and an eight channel configuration. The first of these consisted of four Smart Foam elements each measuring 18 cm (7″) by 8 cm (3″) by 9 cm high. These elements were described earlier in the first section of this chapter entitled Fabrication of Smart Foam Elements.

Some experiments used tuning masses applied to each element of the four channel Smart Foam configuration in an attempt to increase low frequency performance. These tuning masses were sized to tune the Smart Foam elements to the (1,1) plate mode in an attempt to attenuate the dominant plate response. Such tuning would attenuate the plate vibration in a reactive manner thereby reducing low frequency interior noise outside the active bandwidth of the Smart Foam elements. This topic is further discussed in Chapter 7—Active Noise Control.

The eight channel configuration used four smaller Smart Foam elements each measuring 13 cm (5″) long by 12 cm (4-7/8″) wide and were 8 cm (3″) thick. For this configuration, the PVDF had a radius of 5 cm (2″).

A photograph of the four channel configuration is shown in Figure 5.7 with Figure 5.8 and Figure 5.9 depicting the geometry. The length of foam was 25 cm for elements placed along the width of the plate (elements #1 and #3) and 30 cm for those placed along the length (elements #2 and #4) as shown in Figure 5.9. These dimensions were chosen simply to

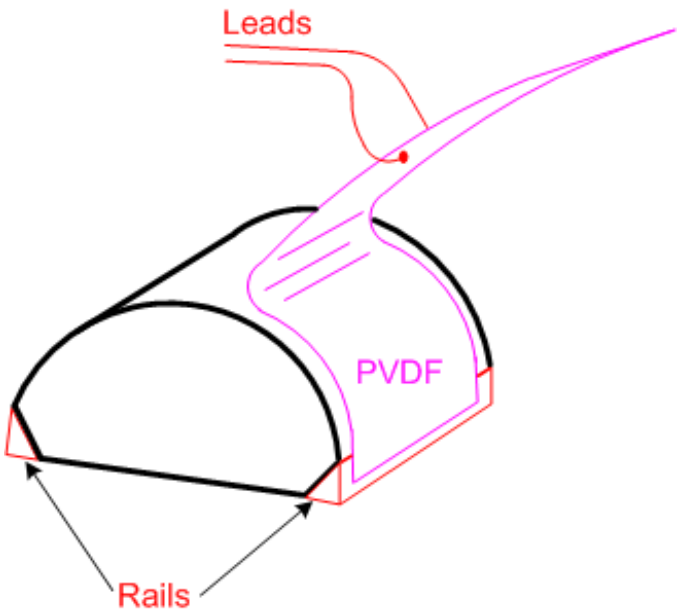

Figure 5.4: Foam lower half with balsa rails mounted.

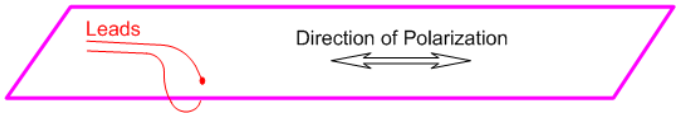

Figure 5.5: Leads attached to the PVDF sheet using conductive tape.

allow for complete coverage of the plate with a minimum number of foam pieces. The PVDF was formed to have as large of a radius as possible to increase low frequency performance. Therefore, given the foam geometry, the PVDF was designed to take the form of a semicircle of 75 mm radius.

Figure 5.10 shows the four channel Smart Foam configuration with tuning masses attached. For reactive control tests, 1.6 mm (0.063″) thick aluminum plates were adhered to the top of each Smart Foam element of the four element configuration using a thin coat of spray glue. For channels 1 and 3, the plates measured 76 mm by 178 mm and for channels 2 and 4 they measured 76 mm by 165 mm.

The eight channel configuration is shown in Figure 5.11 with a diagram in Figure 5.12 depicting the channel numbers. Respective element geometry is shown in Figure 5.13. Here, eight Smart Foam elements, measuring 8 cm (3″) in thickness, were arranged in a 2 by 4 grid with each actuator measuring 12 cm (4-7/8″) by 13 cm (5″). This arrangement allowed

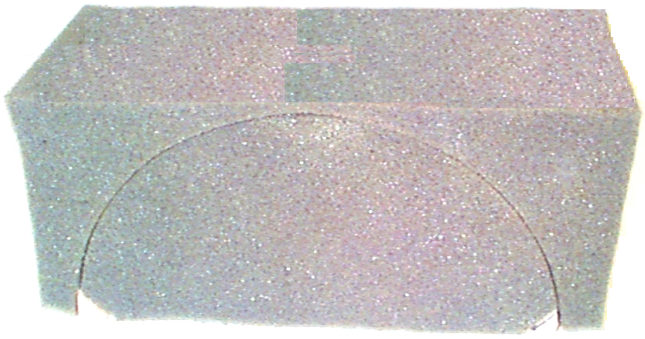

Figure 5.6: Completed Smart Foam element. Baffles omitted for clarity.

for complete coverage of the radiating plate.

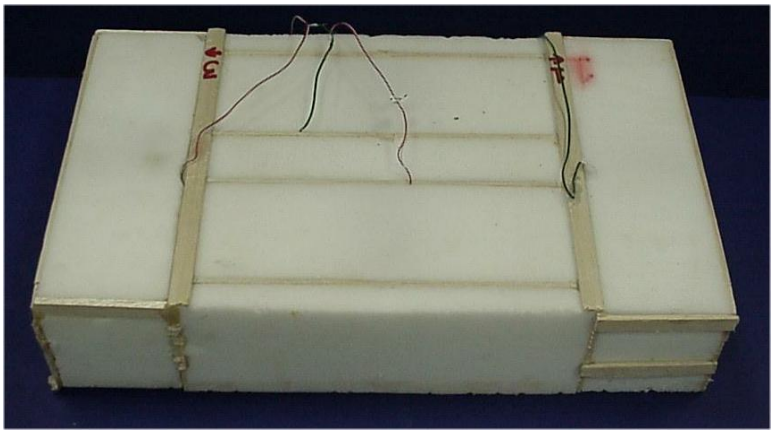

Figure 5.7: The four channel Smart Foam configuration.

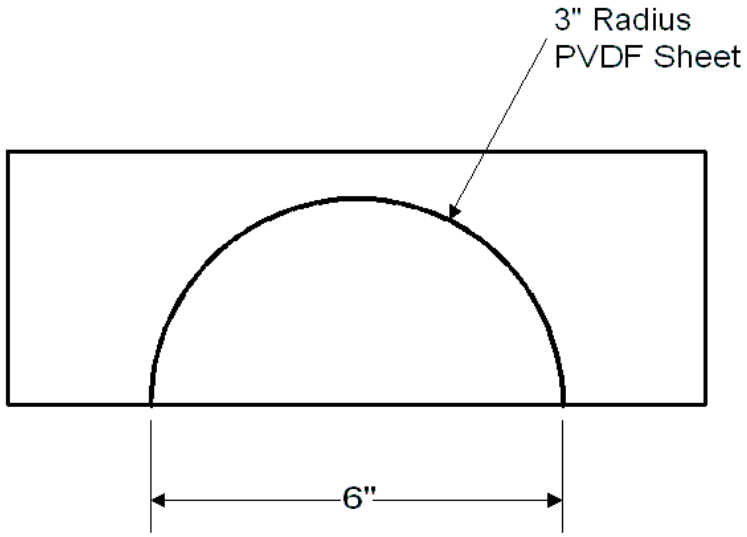

Figure 5.8: Geometry of the four channel Smart Foam configuration. Note, the length of foam was 25 cm for elements placed along the width of the plate (elements #1 and #3) and 30 cm for those placed along the length (elements #2 and #4).

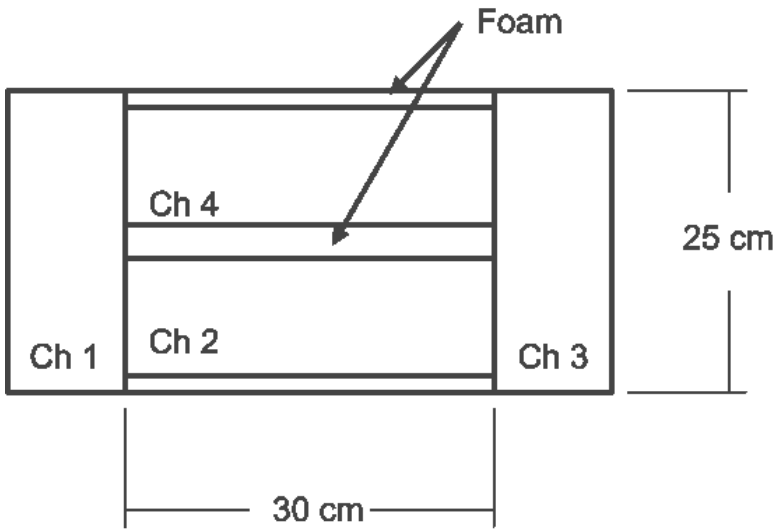

Figure 5.9: Channels 1 and 3 were placed at the far ends of the plate with channels 2 and 4 located in the middle.

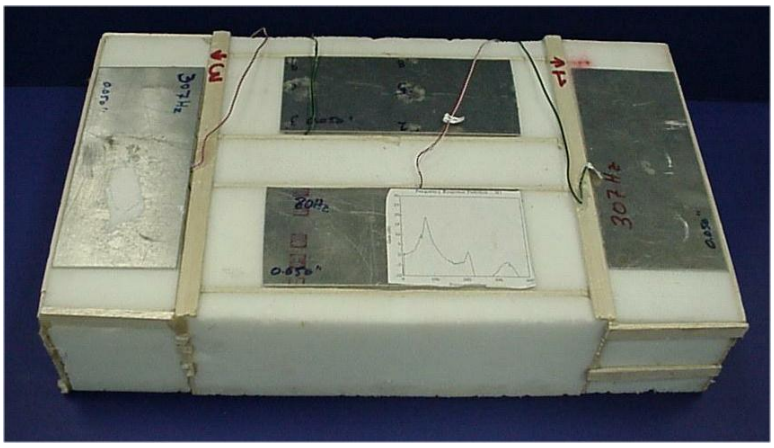

Figure 5.10: The four channel Smart Foam configuration with tuning masses (tuned to plate (1,1) mode).

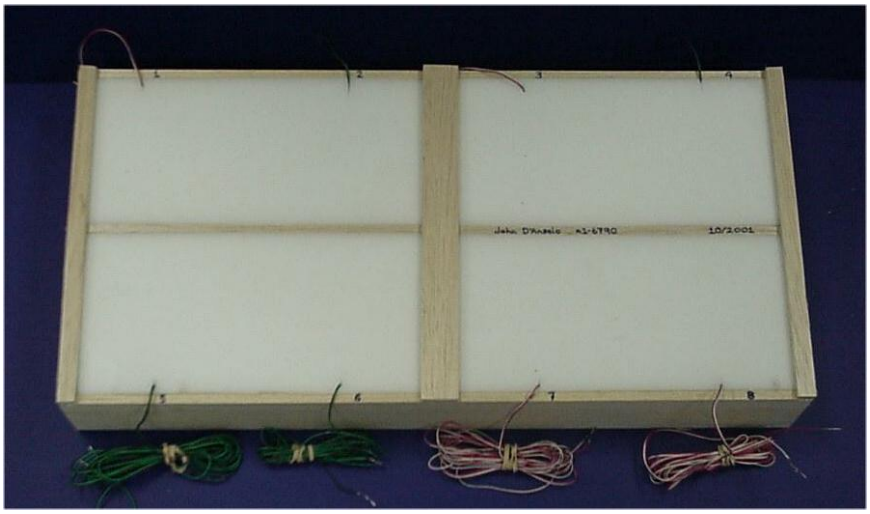

Figure 5.11: The eight channel Smart Foam configuration arranged in a 2 by 4 pattern. This configuration provided for a square planform which allowed for optimal design of the distributed reference sensors.

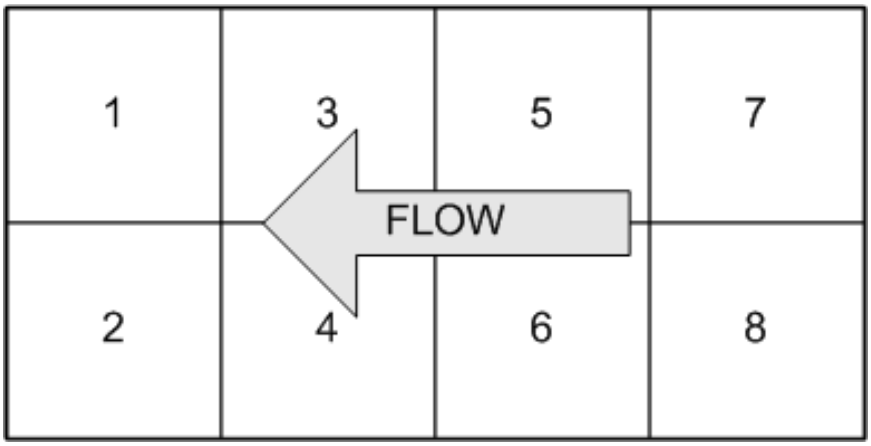

Figure 5.12: Diagram of the eight channel Smart Foam configuration.

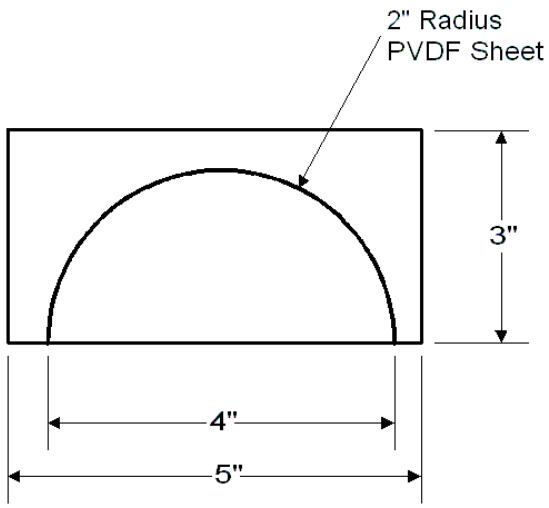

Figure 5.13: Geometry of the eight channel Smart Foam configuration.

5.3 Qualification of Smart Foam Elements

The two Smart Foam configurations were qualified to determine their controller authority. To determine the frequencies at which the two Smart Foam element designs were effective, the transfer functions between a random input and the mean sum of squares at the observer microphones was measured. The input was a random excitation generated by a random signal generator and input to a voltage amplifier. The output of the voltage amplifier was connected to the actuator and the resulting sound pressures at the observer microphones was acquired. In addition, the excitation signal was also acquired, however, the "out over 20" amplifier output was used rather than the full voltage output. This minimized signal–to–noise problems with the data acquisition system. This was required to ensure proper use of dynamic range for the microphone signals. Therefore, the gain of the transfer functions of mean squared sound pressure to excitation voltage required a 20x (or 26 dB) increase. Plots of these transfer functions are shown in Figure 5.14.

The response of the narrower (8 cm x 18 cm) elements, which were used in the four element configuration, cut on at 400 Hz. Elements used in the eight element configuration (12 cm x 13 cm) were designed having a square planform. This square planform, and the need to have twice as many actuators as the four element configuration, resulted in a smaller arc radius for the PVDF sheet. Therefore, the elements were not capable of cutting on until 600 Hz. Between 600–1100 Hz, elements for each of the two configurations performed with similar performance. Above 1100 Hz, the smaller elements used for the eight element configuration remained flat whereas performance decreased for the elements used in the four element configuration. Therefore, the smaller elements of the eight channel configuration were best suited to higher frequency applications.

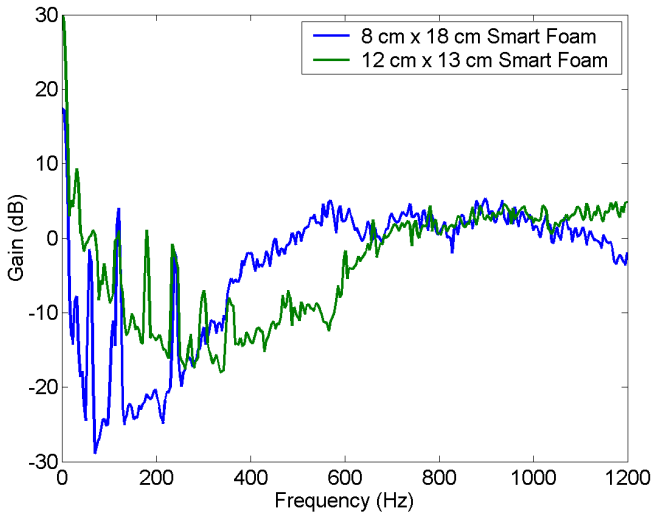

Figure 5.14: Transfer function of Smart Foam elements. The 8 cm x 18 cm Smart Foam elements are effective at frequencies greater than 400 Hz whereas the smaller, 12 cm x 13 cm elements only work at frequencies greater than 600 Hz.

5.4 Summary

Smart Foam elements were used as the control source for active control experiments and simulations performed during this research effort. Both a four channel and an eight channel configuration was used. The four channel configuration was used for control experiments and, for some tests, used tuning masses to increase the low frequency response. The eight channel configuration was used for control simulations.

Elements used in the four channel configuration measured 18 cm long by 8 cm wide and were 9 cm thick. For the eight channel configuration, Smart Foam elements measured 12 cm by 13 cm and were 8 cm thick. Observation of transfer functions between input voltage and mean square acoustic pressure measured in the observer plane was the same for each actuator from 650–1100 Hz. Elements used in the four channel configuration cut–on at 400 Hz whereas the eight channel design did not cut–on until 600 Hz. However, the eight channel design performed better at frequencies above 1100 Hz. Therefore, the smaller elements of the eight channel configuration was best suited to higher frequency applications.

Chapter 6

Coherence and Causality Studies

Effective control depends on several factors in a feed forward control system: control authority, control system causality, and coherence of the primary and secondary paths of the control system. Control authority refers to the controller's ability to provide sufficient input to the variable desired to be controlled. This information was presented in Chapter 5—Actuators.

Coherence is a measure of how well an output may be linearly related to an input [64]. For active noise cancellation to be effective, the secondary noise field must be sufficiently coherent with the primary noise field. Assuming sufficient control authority and causality, unit coherence would allow a generated secondary noise field to eliminate *all* of the primary noise field whereas a coherence of zero suggests no performance may be achieved. For coherence between zero and unity, control performance increases logarithmically [64].

As shown in the feed forward control theory presented in Chapter 1, the primary paths (transfer functions between the reference and error signals) and the secondary paths (transfer functions between actuator and error signals) each influence control performance. Therefore, the coherence for the primary and secondary paths must be sufficiently high to achieve sufficient control performance.

Causality is a constraint which refers to "the condition under which the delay in the acoustical path is greater than the electronic path such that the resulting controller is causal and hence implementable [75]." This means then that the filter representing the controller has zero value for all time prior to the occurrence of the input and thus may be represented fully in the time domain.

To therefore achieve maximum control of a random process, the control system must have sufficient control authority, unit coherence and be causal. Results from this chapter were used to identify how best to approach active noise experiments and simulations presented in Chapter 7—Active Noise Control.

6.1 Theory

This section presents theories regarding the concepts of both coherence and causality. Coherence concepts discussed here include, but are not limited to, ordinary coherence, partial co-

herence, and multiple coherence as well as how coherence relates to the theoretical maximum attenuation. Causality and its importance in feed forward control of random disturbances are then discussed.

Theories of Coherence

Coherence is defined by Bendat and Piersol [64] as the "measure [of] the extent to which [the output] may be related to the [input] by an optimum, linear, least squares relationship". It is expressed as

$$\gamma^2(f) = \frac{G_{xy}^2(f)}{G_{xx}(f)G_{yy}(f)} \tag{6.1}$$

where $G_{xx}(f)$ is the power spectrum of the input signal, $G_{yy}(f)$ the power spectrum of the output signal, and $G_{xy}(f)$ the cross–power spectrum with f denoting frequency. Note that $0 \leq \gamma^2(f) \leq 1$ holds true always with unit coherence suggesting the output is entirely related, in a linear fashion, to the input. However, "a high coherence value does not [necessarily] indicate a causal relationship." Reasons for poor coherence include the following: extraneous noise in the measurements, the system relating the input and output is non–linear, or the output may be due to more than one input [64].

Although a high coherence may be measured, it does not necessarily mean that there is high coherence between the input and output signals. Considering a system having two inputs, x_1 and x_2, and one output, y. If $\gamma_{x_1y}^2$ equals unity, then it would suggest that y is related entirely to x_1. However, if x_1 and x_2 are highly coherent, $\gamma_{x_1x_2}^2 \rightarrow 1$, the high coherence of γ_{x1y}^2 may simply reflect a highly coherent relation between x_1 and x_2 and that y is actually only coherent with x_2 rather than with x_1. This situation calls for another form of coherence—partial coherence—to best determine the relationships.

Partial coherence has the ability to distinguish how coherent each input is to the output thereby eliminating erroneously high coherence values between poorly coherent signals. In order to determine partial coherence, the inputs and outputs must first be *conditioned* such that each input is independent from the next and each output is independent from the next. Partial coherence is defined as

$$\gamma_{2y\cdot1}^2(f) = \frac{G_{2y\cdot1(f)}^2}{G_{22\cdot1}(f)G_{yy\cdot1}(f)} \tag{6.2}$$

where $x_{2\cdot1}$, the conditioned record, represents that part of x_2 not due to x_1 and may be determined by

$$x_{2\cdot1} = x_2 - x_{2:1} \tag{6.3}$$

where $x_{2:1}$ is that part of x_2 which is entirely related to x_1. Figure 6.1 presents these concepts in block diagram form and the following mathematical relation

$$x_{2:1} = L_{12}(f)x_1 \tag{6.4}$$

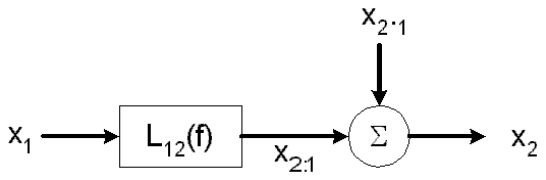

Figure 6.1: Decomposition of x_2 from x_1 for use in partial coherence calculations.

where L_{12} is the transfer function between input x_1 and output x_2. Then, $x_{2\cdot1}$ may be calculated using

$$x_{2\cdot1} = x_2 - L_{12}(f)x_1 \tag{6.5}$$

and other conditioned records may be calculated similarly. Knowing the conditioned records, the partial coherence input and output spectra may be calculated leading to the expression of partial coherence as was given in equation 6.2.

For systems having several inputs each relating to several outputs the concept of multiple coherence may be employed. "The multiple coherence function is a direct extension of the ordinary coherence function" [64]. Mathematically, it may be expressed as

$$\Gamma^2_{y:x}(f) = \frac{G_{vv}(f)}{G_{yy}(f)} \tag{6.6}$$

where subtracting the output noise, n, from the measured output, y, results in the actual output signal such that $G_{vv}(f) = G_{yy}(f) - G_{nn}(f)$. Multiple coherence may also be expressed by first determining the ideal output spectrum, $G_{vv}(f)$, in terms of the ordinary coherence between the output and each input as

$$G_{vv}(f) = \left[\gamma^2_{1y} + \gamma^2_{2y} + \ldots\right] G_{yy}(f) \tag{6.7}$$

which then leads to

$$\Gamma^2_{y:x} = \gamma^2_{1y} + \gamma^2_{2y} + \ldots \tag{6.8}$$

Therefore, "for uncorrelated inputs, the multiple coherence function is the sum of the ordinary coherence functions between each input and [one] output" [64]. For correlated inputs, multiple coherence may be determined by summing the conditioned ordinary coherence, or partial coherence, functions as follows

$$\Gamma^2_{y:x} = 1 - \left[1 - \gamma^2_{1y}\right]\left[1 - \gamma^2_{2y}\right]\ldots \tag{6.9}$$

In matrix form, multiple coherence may be calculated by [28]

$$\mathbf{\Gamma}_{xy}^2 = \frac{\mathbf{S}_{xy}^H \mathbf{S}_{xx}^{-1} \mathbf{S}_{xy}}{S_{yy}} \tag{6.10}$$

The theoretical maximum value of control may be determined knowing coherence by

$$C_{max} = -10 \log_{10} \left(1 - \gamma^2\right) \tag{6.11}$$

Figure 6.2 is a plot of equation 6.11. Note that for $\gamma^2 = 0.9$ the maximum achievable attenuation is 10 dB and for $\gamma^2 = 0.99$ it would be 20 dB. Given sufficient control authority, unit coherence would thus allow absolute attenuation of the disturbance.

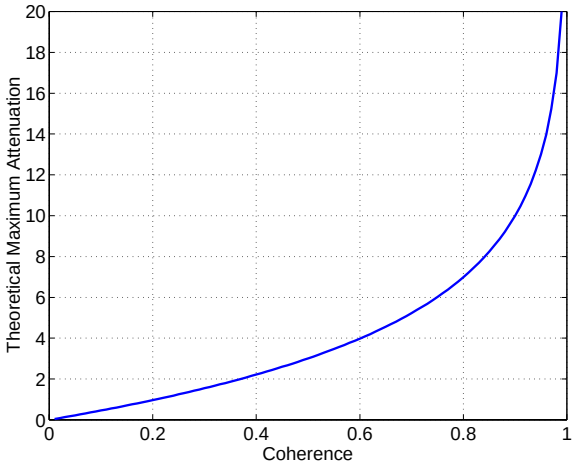

Figure 6.2: Theoretical maximum achievable attenuation may be determined knowing coherence. For $\gamma^2 = 0.9$, 10 dB of control may be achieved and for $\gamma^2 = 0.99$ it would be 20 dB. Unity coherence allows for absolute control.

Theory of Causality

Causality was introduced during the discussion on z–transforms in Chapter 1—Introduction. The concept is further discussed here in the context of the control filter used for active control.

Control path delay is due to anti–aliasing and smoothing filters, control system sampling processes, filter length, computation time, and the physical system [75] [76]. For a controller to be causal the delay in the acoustic path must be equal to or greater than the electronic path thus allowing the controller to be physically realizable in the time domain. Should the delay in the acoustic path be less than that through the electronic path, the controller representation would require a filter having some response at a time prior to an input. Such a system is referred to as *acausal* [75]. Filters representing a causal and an acausal system are shown in Figure 6.3. For the causal filter, note that the response is zero for all time prior to an input applied at $t \geq 0$ whereas an acausal filter has some non–zero response prior to the input. In other words an acausal filter "has an output that depends not only on present and past inputs but also on future inputs [27]."

The filter must also have a sufficient number of coefficients to accurately describe the input/output relation. As described in Chapter 1—Introduction, a FIR filter, such as the filtered–x, LMS control filter, has a finite duration response. Further, the FIR filter is stable provided its coefficients are bounded. Such a filter converges to zero and is described as being Bounded Input Bounded Output (BIBO) stable [27].

Note that causality does not imply stability and neither does stability imply causality [27]. Figures 6.3 both describe stable filters but only Figure 6.3a is both stable *and* causal. In contrast, the two filters shown in Figures 6.4 are improperly modelled and therefore do not capture the dynamics of the system. The filter shown in Figure 6.4a is causal but has too short a filter length to accurately describe the system whereas Figure 6.4b also has too short a filter length and is acausal. Improperly modelled control and system identification filters may lead to an unstable control system since the necessary information is not conveyed to the controller.

"Causality is usually not a problem for periodic problems so long as the controller has a long enough impulse response to produce the properly phased cancellation filter [75]." However, for active control systems dealing with broadband random noise "delay becomes crucial especially for applications that involve relatively large bandwidth [75]."

The delay of an acausal controller may be minimized by increasing the length of the acoustic path. Such an effort would increase the acoustic propagation time thereby reducing the delay between the acoustic and electronic paths. Sutton, et al [77] therefore recommend placing the reference sensors close to the disturbance and placing the error sensors close to the actuators. Though physical restraints may not make this option feasible control of an acausal system subjected to a non–deterministic disturbance is still achievable.

Although delay may be present, some control is still achievable for an acausal controller with performance decreasing as the delay through the control path increases. Burdisso et al [76] state that "performance degradation due to delay in the control path can be offset by increasing the compensator filter size." The following theory supports their argument.

Minimum mean square error may be expressed as

$$\sigma_{min}^2 = \sigma_i^2 - \mathbf{H}_r^T \mathbf{R}^{-1} \mathbf{H}_r \tag{6.12}$$

where σ_i^2 is the mean square error due only to the primary disturbance, expressed as

$$\sigma_i^2 = \frac{1}{2\pi} \int_{-\omega_{Ny}}^{\omega_{Ny}} \left| T_{i\epsilon} \left(e^{-j\omega t_s} \right) \right|^2 \Phi_0 \, \mathrm{d}\omega \tag{6.13}$$

with

$$R\left(r\right) = \frac{1}{2\pi} \int_{-\omega_{Ny}}^{\omega_{Ny}} \left| T_{c\epsilon} \left(e^{-j\omega t_s} \right) \right|^2 e^{j\omega r t_s} \Phi_0 \, \mathrm{d}\omega \tag{6.14}$$

where Φ_0 is the power spectral density function of the error signal due to the primary disturbance, $T_{i\epsilon}$ the transfer function between the disturbance and the error output, and $T_{c\epsilon}$ the transfer function between the control input and the error output. The autocorrelation matrix, $\mathbf{R}$ takes the form

$$\mathbf{R}_{ij} = \begin{cases} R(r) & : \quad i < j \\ R(r) & : \quad i = j \\ R(-r) & : \quad i > j \end{cases} \tag{6.15}$$

and

$$H\left(r\right) = \frac{1}{2\pi} \int_{-\omega_{Ny}}^{\omega_{Ny}} T_{i\epsilon} \left(e^{-j\omega t_s} \right) T_{c\epsilon} \left(e^{-j\omega \epsilon_s} \right) e^{-j\omega(d+r)t_s} \Phi_0 \, \mathrm{d}\omega \tag{6.16}$$

and the matrix expression of $\mathbf{H}$ takes the form

$$\mathbf{H} = \left\{ H(0), H(1), \ldots, H(L) \right\}^T \tag{6.17}$$

The control system effectiveness (in dB), given either a causal or acausal system, may then be determined by

$$\eta = 10 log_{10} \left(1 - \frac{\mathbf{H}_r^T \mathbf{R}^{-1} \mathbf{H}_r}{\sigma_i^2} \right) \tag{6.18}$$

Note that the autocorrelation matrix $\mathbf{R}$ is real, symmetric, and in general positive–semidefinite thus allowing for the determination of $\mathbf{R}^{-1}$. Therefore, all eigenvalues of $\mathbf{R}$ would be real and non–negative. As presented in [76], for a system of M sinusoidal inputs, the rank of $\mathbf{R}$ would equal $2M$ and its dimension would equal the number of filter weights, I_c. Therefore, to allow $\mathbf{R}^{-1}$, $2M \geq I_c$ is required. From equation 6.18 and the case where $2M > I_c$

$$\mathbf{H}_r^T \mathbf{R}^{-1} \mathbf{H}_r > 0 \tag{6.19}$$

which then implies some degree of control performance may be achieved regardless of the control path delay. In addition, it may be shown that equation 6.19 is a monotonically increasing function such that

$$\left(\mathbf{H}_r^T \mathbf{R}^{-1} \mathbf{H}_r\right)_{I_c+1} \geq \left(\mathbf{H}_r^T \mathbf{R}^{-1} \mathbf{H}_r\right)_{I_c} \tag{6.20}$$

suggesting then the poor performance of an acausal system may be offset partially by increasing the length of the control filters.

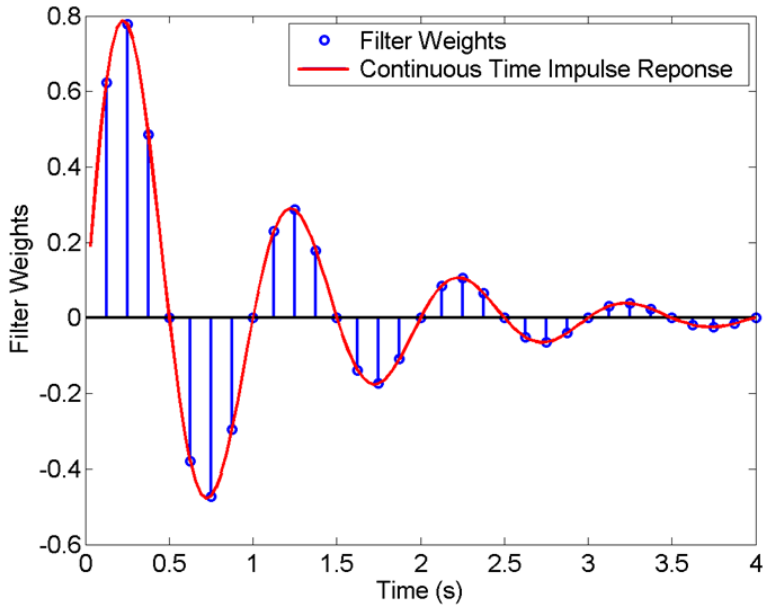

a) Causal Filter

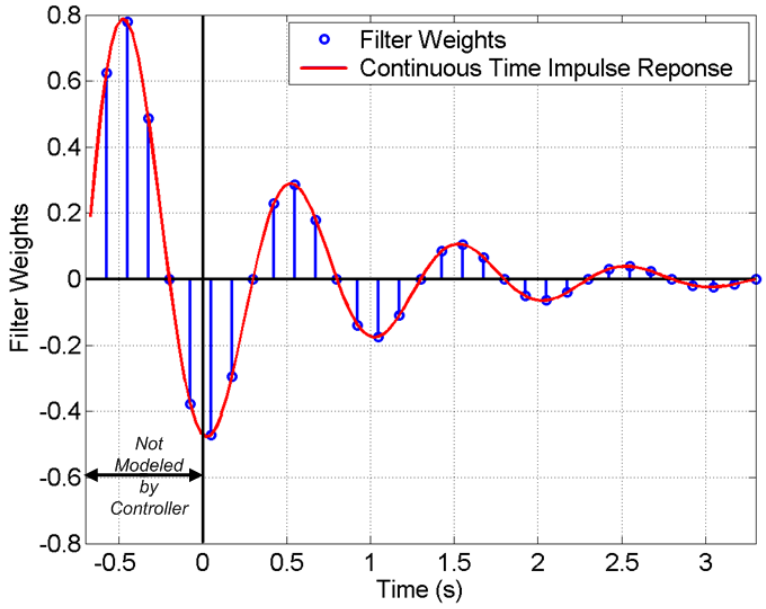

b) Acausal Filter

Figure 6.3: Causal and acausal filter representations (a) Causal filter (b) Acausal filter.

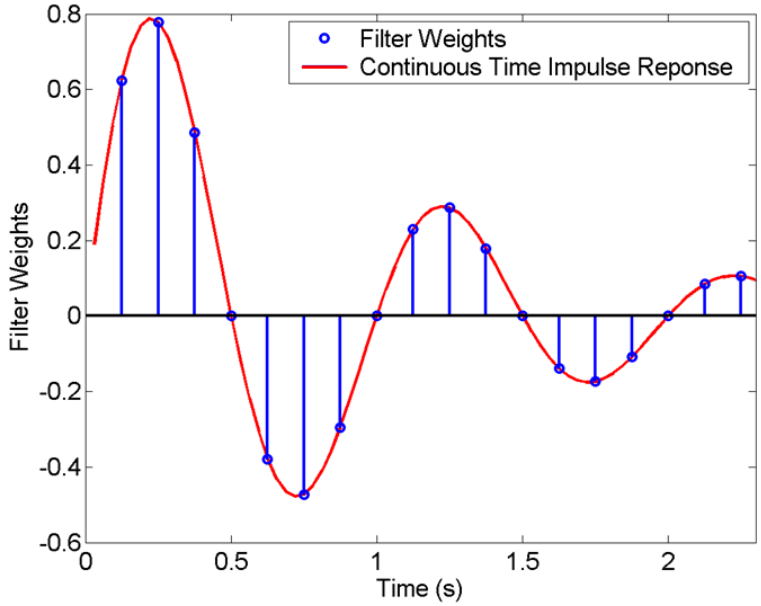

a) Unstable, causal Filter

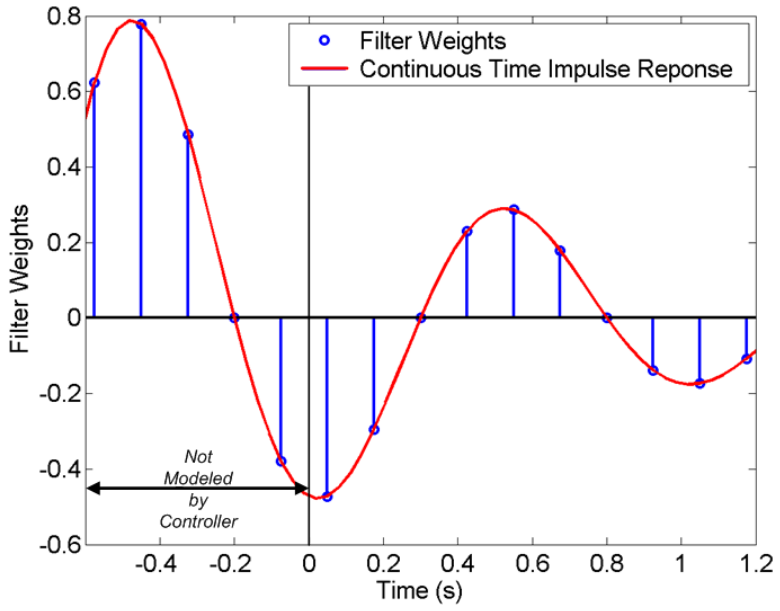

b) Unstable, acausal Filter

Figure 6.4: Improperly modelled filters do not have a sufficient number of coefficients to accurately describe the system (a) Causal filter with too few coefficients (b) Acausal filter with too few coefficients.

6.2 Experiment Setups

Experiment configurations for the coherence and causality studies are presented in this section. Results for experiments performed using these test configurations are presented in the following section.

Coherence Experiment Setups

The two coherence studies, those for the primary and secondary paths, were each conducted using similar test setups. Each setup had microphones in the noise field used as error sensors.

Primary path identification consisted of four methods of reference sensing. Each of these four means of reference sensing was observed in control experiments and/or simulations. The reference sensors were mounted to the radiating plate on the interior side (side radiating into the anechoic enclosure). The four reference sensors were 1) a single accelerometer mounted at the center of each actuator, 2) a discrete reference sensor array, consisting of four accelerometers whose signals were weighted and summed, centered under each actuator, 3) the use of one spatially distributed reference sensor made from shaped PVDF[1] centered under each actuator, and 4) the use of up to three independent (not summed) accelerometers. To determine the coherence of the secondary paths, the input voltage to each Smart Foam element was used as the reference signal with error signals consisting of the error sensor array and observer microphone signals.

Figure 6.5 shows the general experiment setup for determining the primary path coherence. Figure 6.6 shows reference sensors used for the first two cases—the use of a single accelerometer centered under each actuator and the use of the PVDF spatial sensors. Figure 6.7 shows the use of the discrete reference array developed in Chapter 3—Reference Sensing. The use of multiple references per actuator uses the same configuration as shown in Figure 6.6 and was discussed in detail in Chapter 3.

The eight Smart Foam actuators are shown in Figure 6.8 representing control test conditions. Error arrays were placed 100 mm from the tops of the Smart Foam elements and observer microphones were placed in the observer plane. The wind tunnel was then turned on generating a turbulent flow which perturbed the plate. The plate vibration then resulted in the interior primary acoustic field.

The secondary paths were determined similarly, but the tunnel was not turned on. Instead, each actuator was independently subjected to a random input by the Smart Foam using the configuration shown in Figure 6.9. This random input resulted in an interior secondary noise field[2]. Coherence could then be determined for the secondary paths between the actuated Smart Foam element and the error sensor arrays and observer microphones.

All coherence studies were performed using a 4000 Hz sample rate with anti–aliasing filters set to 1200 Hz. Thirty averages were performed and gains were set accordingly to

[1]Development of discrete and spatially distributed reference arrays were presented in Chapter 3

[2]Note that the primary noise field was not present for this test. In addition, only one Smart Foam element was actuated at a time.

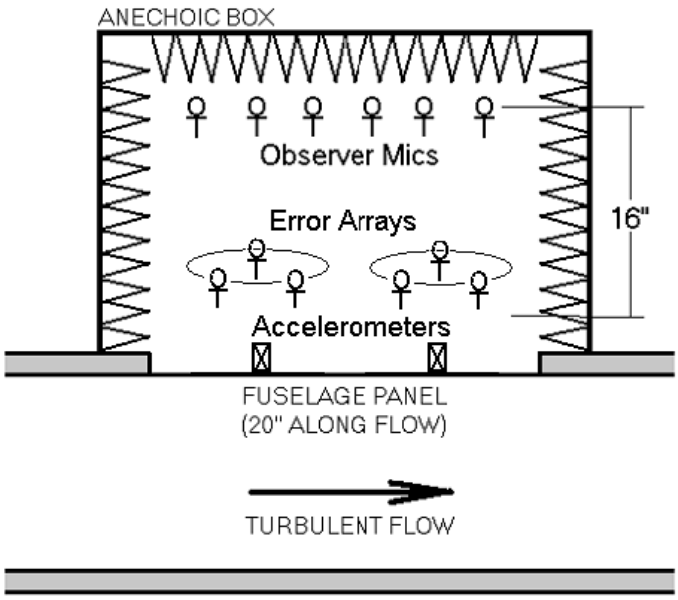

Figure 6.5: Experiment setup for primary path coherence studies.

maximize the signal-to-noise ratio.

Causality Experiment Setups

To determine the time delay, control was run using a speaker disturbance and an ideal (internal to the dsp algorithm) reference signal as shown in Figure 6.10. The ideal reference was input to the controller as would be done using an external reference and would therefore be subjected to delays in the control system. However, the ideal reference may be artificially delayed further thus affecting the control performance.

By choosing a deterministic reference signal, delaying the reference signal further such that the combined delay was some integer number of wavelengths, would result in a causal system. Note, though, that the control system is then input a reference signal which would then lag by some integer number of wavelengths. However, assuming a time-invariant reference signal such a reference signal would appear to the control system to be perfectly causal. This apparently causal system would then provide the maximum control performance.

The speaker[3] was placed in the duct of the test section about 3 cm (1″) below the plate. Four Smart Foam elements were mounted to the plate on the interior with the two centered elements wired in parallel allowing for three channels of control. A microphone array was

[3]Note, that the flow was not on for this experiment.

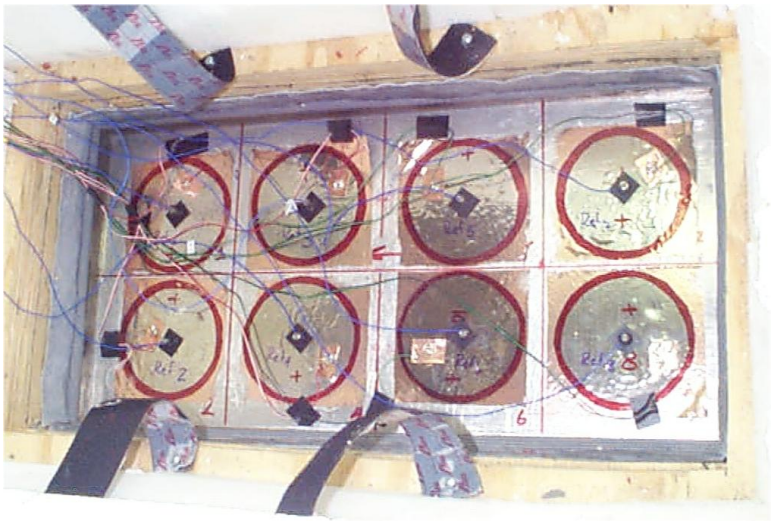

Figure 6.6: Experiment setup showing independent accelerometers and shaped PVDF reference sensors used for coherence studies.

then centered over each of the three actuators at 10 cm (4″). Reference transducers were not mounted since an ideal reference signal, internal to the controller, was used for this analysis.

The three channel array of four 8 cm by 18 cm (3″ by 7″) Smart Foam actuators was placed on the vibrating plate. Actuator #1 was used for control channel #1, actuator #3 for control channel #3, and actuators #2 and #4 were paired in phase for control channel #2. Error arrays were located three inches above the actuators. Error arrays #1 and #3 were located over the centers of their respective actuators and error array #2 was located at the center of the plate between the paired actuators used for control channel #2. The plate was excited by a speaker placed in the wind tunnel test section centered approximately 25 mm (1″) below the plate. This Smart Foam configuration is shown in Figure 6.11 and further detailed in Chapter 5—Actuators.

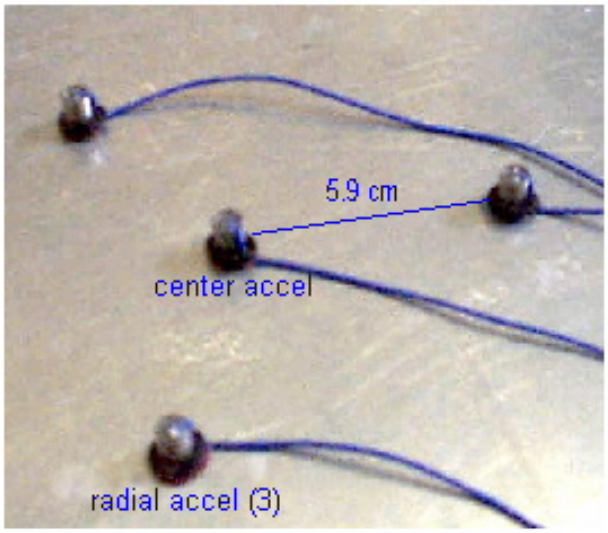

Figure 6.7: Discrete reference array. Each accelerometer signal was weighted appropriately and summed producing a single reference signal per control channel.

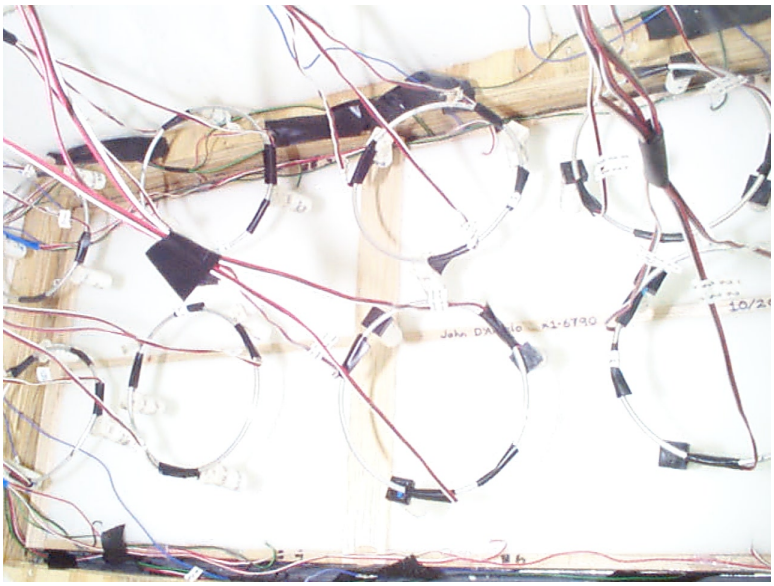

Figure 6.8: Experiment setup showing Smart Foam actuators and error array sensors used for coherence studies.

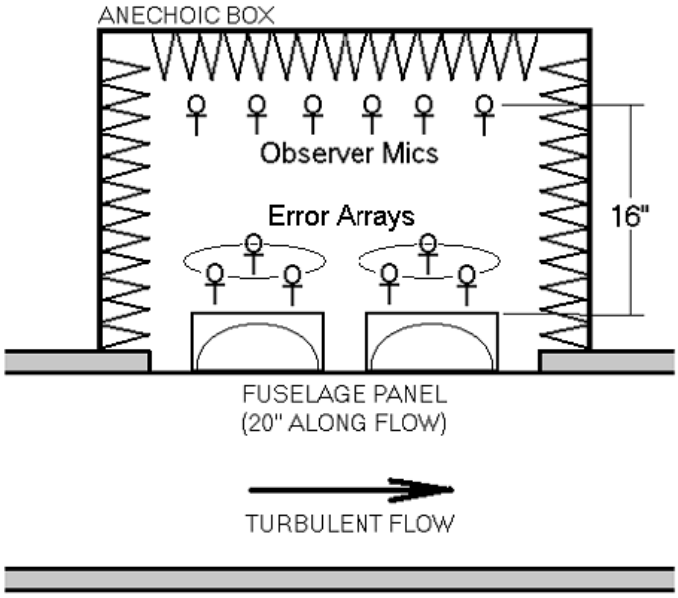

Figure 6.9: Experiment setup for secondary path coherence studies.

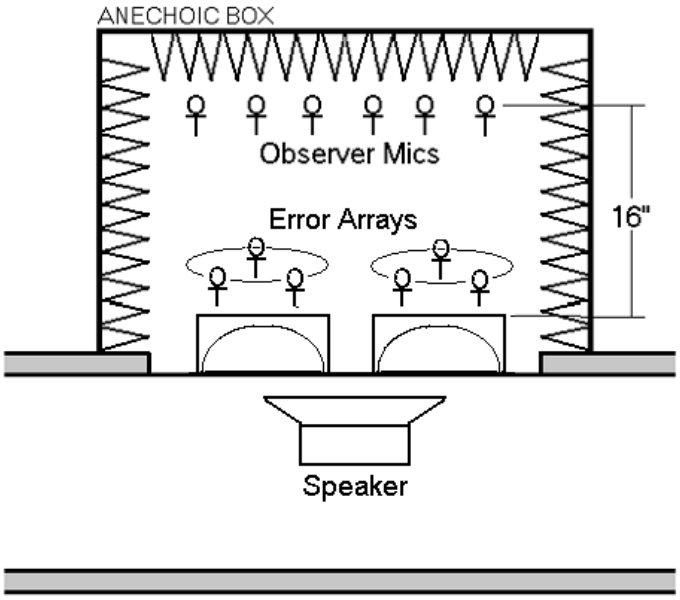

Figure 6.10: Experiment setup for causality study.

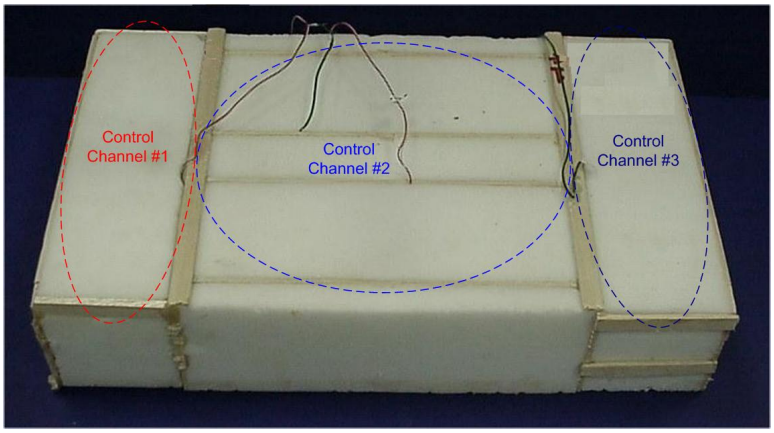

Figure 6.11: The four channel Smart Foam configuration used for the causality study. Note, the two centered Smart Foam elements were wired in parallel and acted as a single actuator.

6.3 Results and Discussion

Results from coherence and causality experiments are discussed in this section. Primary path coherence tests are presented first, followed by experiments performed to estimate secondary path coherence. Finally, control experiments used to determine the causality of the controller are presented.

Primary Path Multiple Coherence Study

As discussed previously, this research effort explored the use of four reference techniques. They are 1) a single accelerometer mounted at the center of each actuator, 2) a discrete reference sensor array consisting of four weighted and summed acceleration measurements, 3) a single distributed PVDF spatial filter per actuator, and 4) multiple independent reference signals per actuator. Further, as discussed in Chapter 5—Actuators, both four and eight element Smart Foam configurations were used. However, not all reference techniques were used with both Smart Foam configurations. The four element configuration used only single, point references and the discrete reference sensor arrays. The eight element configuration used both the single and multiple accelerometer measurements as well as the PVDF spatial filters for acquiring the reference signals. The eight element configuration did not use the discrete reference sensor arrays. Coherence tests were performed using the eight element Smart Foam configuration for all but the discrete reference sensor array experiments which were performed using the four element configuration.

For both the four and eight element Smart Foam configurations, primary path coherence was determined between the reference signal(s) and all error signals. Error sensor arrays were placed 100 mm from the actuators with six additional microphones placed in the observer plane. Only a single representative case is shown for each configuration. The reference(s) were located at location #1 (the location associated with Actuator #1) as depicted for the eight channel configuration shown in Chapter 5, in Figures 5.11 and 5.12.

Figure 6.12 shows the coherence and theoretical maximum achievable control between a single point reference and the eight error sensor arrays. It is shown here that the coherence between the reference and each error signal varies significantly as would be expected due to the directionality of the error sensor array and the increasing distance between the reference measurement point and neighboring error sensor arrays. For the 400–800 Hz band, coherence between the single point reference and the error sensor array was 9.4 dB. Coherence to the next two closest error sensor arrays, those at actuators #2 and #3, respectively, decreased to 5.8 dB and 5.2 dB. Coherence was approximately 2 dB at other error array locations. These values are summarized in Table 6.1.

Using the same configuration, the coherence between the single point reference and the observer microphones was considered. Results are presented in Figure 6.13 and further summarized in Table 6.1. Here, it is again shown that the coherence is greatest between the single point reference and the closest observer microphone. For the 400–800 Hz band, the resulting theoretical maximum achievable attenuation was 10.3 dB with the next highest

being 7.9 dB. Other values of theoretical maximum achievable control were 5 dB or less.

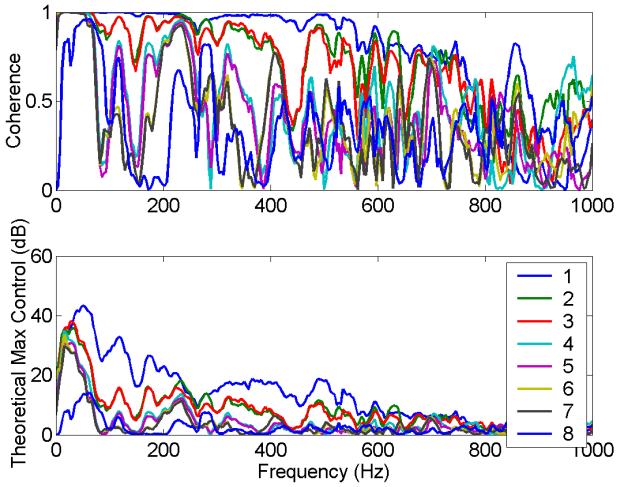

Figure 6.12: Coherence between fuselage plate vibration using a single reference sensor and error microphone arrays centered 100 cm above Actuator #1.

In an attempt to increase the primary path coherence, multiple coherence was computed using either two or three independent point references per actuator. Each of these references was obtained using an ordinary accelerometer. Error signals were obtained using error arrays and the observer microphones.

Multiple coherence and resulting theoretical maximum achievable control between two independent point reference signals and the error sensor arrays are presented in Figure 6.14 and for the observer microphones in Figure 6.15. At the error sensor arrays, the theoretical maximum achievable control decreased relative to the single point reference case at error array #1. However, it was increased at error array #2 to be on par with that of error array #1 thus resulting, potentially, in a more global attenuation. This would be expected since the two point references used for this case, as mentioned in the experiment setup section, were at locations #1 and #2. Theoretical maximum achievable control at the other error and observer locations was between 2.4–3.9 dB—on par with the single point reference configuration. Multiple coherence and theoretical maximum achievable control between the two point references and the observer microphones increased to 13.4 dB from 10.3 dB at observer microphone location #1.

The use of three independent point reference signals was then considered. For this case, the point references were located at locations #1, #2, and #3. For this case, the theoretical maximum achievable control, using independent point references, was greatest at all error sensor arrays given the three reference case. At error sensor array #1 and #2, 16.8 dB and 11.4 dB theoretical maximum achievable control was computed. At the

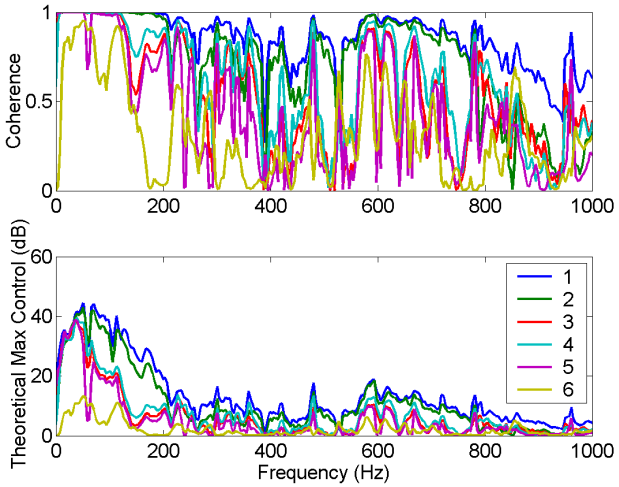

Figure 6.13: Coherence between fuselage plate vibration using a single reference sensor and observer microphones.

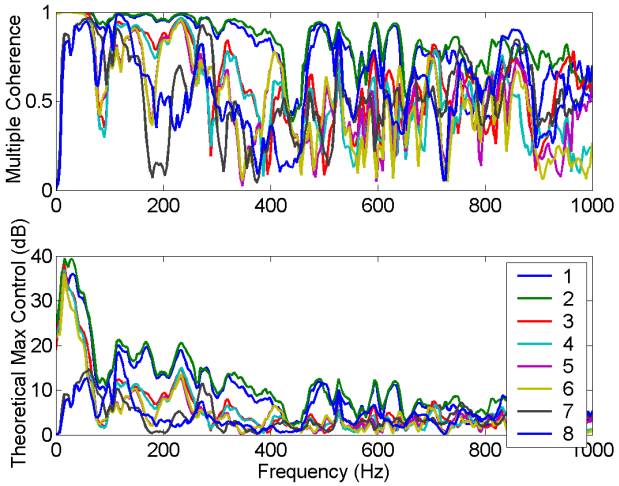

Figure 6.14: Multiple coherence between fuselage plate vibration using two independent point reference sensors and error microphone arrays centered 100 cm above Actuator #1.

remaining locations these values were between 5.4–7.7 dB and are presented in Table 6.1.

Although, relative to the use of one or two references per channel, the performance using three independent point references decreased at observer microphone #1. However, theoretical maximum achievable control at the first three observer microphone locations was most uniform—6.8–9.1 dB. This is shown in Figure 6.17 and Table 6.1.

Results given one, two and three point references per actuator, using the eight Smart Foam element configuration, are summarized in Table 6.1. These results are presented for the 400–800 Hz band corresponding to Figures 6.12 through 6.17, above. Although performance dropped for some reference/error combinations, in general increasing the number of references per actuator increases the multiple coherence. This effect is seen both at the error arrays and at the observer microphones. By equation 6.11 the theoretical maximum attenuation should therefore increase using the added references.

The eight distributed PVDF spatial sensors were then bonded to the vibrating plate at each actuator location. Sensors were mounted at the center of each respective actuator. Ordinary coherence was measured from each PVDF reference signal to each error array and between each PVDF reference signal to each observer microphone. Error arrays were placed at 100 mm and observer microphones were placed in the observer plane as with the previously described primary path coherence tests.

As was presented for the multiple point references primary path coherence studies, results for only a single PVDF reference sensor will be shown. Coherence and resulting theoretical maximum achievable control between PVDF spatial sensor #1 and the error sensor arrays is shown in Figure 6.18 and between the same reference signal and the observer microphones shown in Figure 6.19. Results for theoretical maximum achievable control are summarized in Table 6.2 for the 400–800 Hz band. Results using PVDF spatial sensors at other locations are not presented since their performance was similar to that achieved using the reference sensor located at location #1.

Coherence and corresponding theoretical maximum control were observed to decrease with further distance from the location of the reference sensor used. Coherence to the error sensor at location #1 was close to unity at lower frequencies with values dropping close to zero at the furthest error sensor, #8, across the entire band. For reference-to-error array paths having relatively high coherence at lower frequencies, all channels dropped in coherence at frequencies above 550 Hz until reaching a coherence no greater than 0.5 at 800 Hz. By Table 6.2, theoretical maximum achievable performance between the PVDF spatial sensor reference signal and its corresponding error sensor array at location #1 was 8.9 dB for the 400–800 Hz band. At error sensor arrays located at locations #2 and #3 the theoretical maximum achievable control was 5.2 dB and 4.6 dB, respectively, with performance at other paths being between 0.3–1.9 dB.

Results for observer microphones are shown in Figure 6.19 and summarized in Table 6.2. As shown for the PVDF spatial sensor–to–error array coherence above, coherence to the observer microphones closest to the reference was also close to unity at lower frequencies and over a narrow band between 600–700 Hz. However, coherence dropped between 220–580 Hz. Similar to the performance of the error sensor arrays, coherence at high frequencies rolled-off

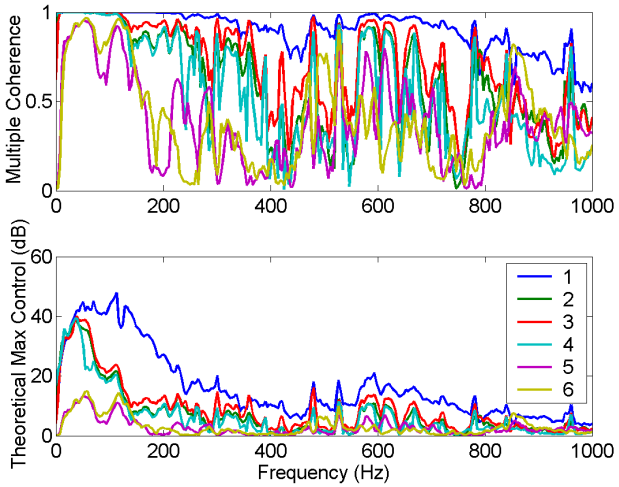

Figure 6.15: Multiple coherence between fuselage plate vibration using two independent point reference sensors and observer microphones.

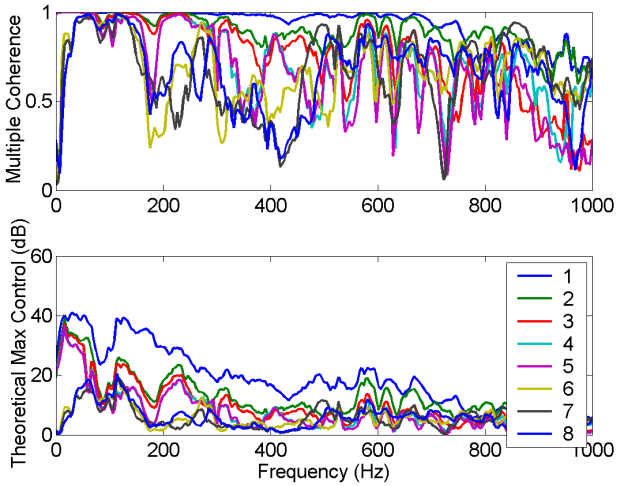

Figure 6.16: Multiple coherence between fuselage plate vibration using three independent point reference sensors and error microphone arrays centered 100 cm above Actuator #1.

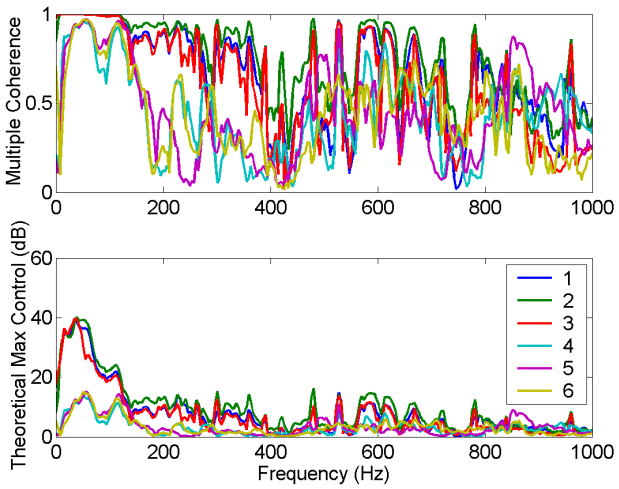

Figure 6.17: Coherence between fuselage plate vibration using three independent point reference sensors and observer microphones.

Table 6.1: Primary path multiple coherence using one, two or three point references per actuator.

Error Signal	**Theoretical Maximum Attenuation (dB)** 400–800 Hz		
	1 Reference	*2 References*	*3 References*
Error Sensor Arrays			
1	9.4	6.5	16.8
2	5.8	7.2	11.4
3	5.2	2.8	7.7
4	2.2	2.4	5.8
5	1.6	2.9	5.4
6	2.1	2.9	5.4
7	2.1	3.4	5.4
8	1.5	3.9	6.1
Observer Microphones			
1	10.3	13.4	7.7
2	7.9	7.0	9.1
3	3.6	8.3	6.8
4	5.0	5.9	2.2
5	3.4	1.7	2.1
6	1.4	1.7	3.1

significantly for all channels. For the 400–800 Hz band, the two microphones closest to the PVDF reference sensor had values of theoretical maximum achievable control of 8.8 dB and 8.5 dB. Values of theoretical maximum achievable control for the remaining four observer microphones was 2.7–6.3 dB.

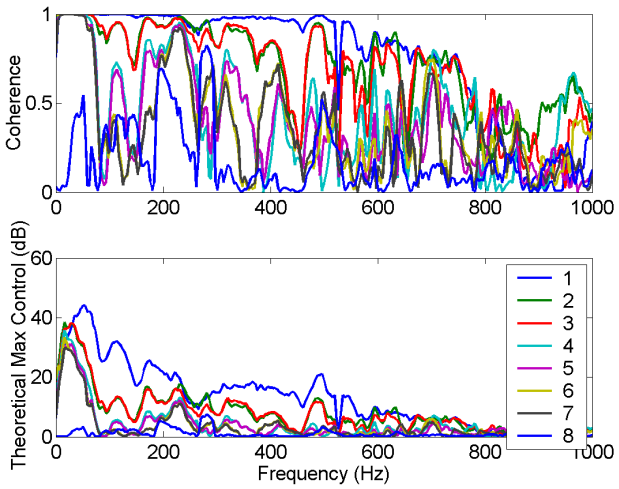

Figure 6.18: Multiple coherence between fuselage plate vibration using a distributed PVDF reference sensor and eight error microphone arrays.

Coherence was then measured using discrete reference sensor arrays to obtain the reference signals. Four discrete reference sensor arrays were arranged in the four Smart Foam element configuration. Coherence and resulting theoretical maximum achievable control between a discrete reference array, placed at location #1, and the error sensor arrays are shown in Figure 6.20. Figure 6.21 shows results using four observer microphones with results for both cases summarized in Table 6.3 for the 400–800 Hz band.

Observation of Figure 6.20 shows, as with previous reference sensing techniques, relatively high coherence at lower frequencies. Above 300 Hz, coherence decreased with the greatest decreases occurring at error sensor arrays other than that at location #1. However, coherence between the discrete reference sensor array and the error sensor array at location #1 decreased at frequencies greater than 650 Hz. In the 400–800 Hz band, the theoretical maximum achievable control was 4.4 dB at error sensor array #1. At the remaining error sensor arrays, values of 0.7–4.0 dB was achieved.

Performance at the observer microphones was similar with a significant roll-off starting at approximately 800 Hz. At observer microphone #1 4.2 dB was achieved with up to 3.5 dB theoretical maximum control computed for the other observer microphones.

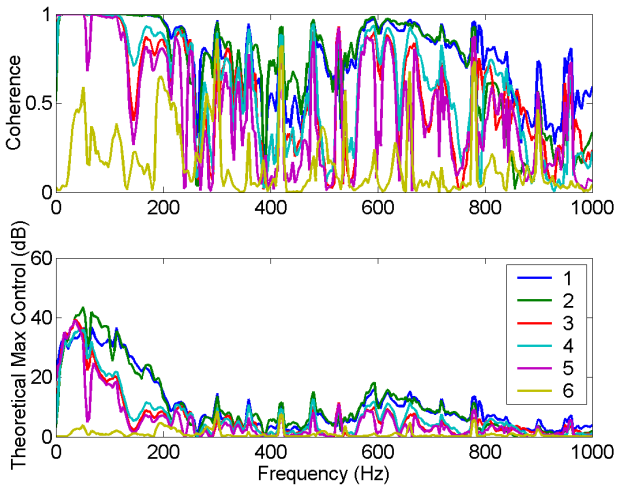

Figure 6.19: Multiple coherence between fuselage plate vibration using distributed PVDF reference sensors and observer microphones.

Table 6.2: Primary path multiple coherence using a PVDF Spatial Sensor at location #1.

Error Signal	**Theoretical Maximum Attenuation (dB)** 400–800 Hz
Error Sensor Arrays	
1	8.9
2	5.2
3	4.6
4	1.9
5	1.4
6	1.6
7	1.4
8	0.3
Observer Microphones	
1	8.8
2	8.5
3	6.3
4	6.7
5	5.1
6	2.7

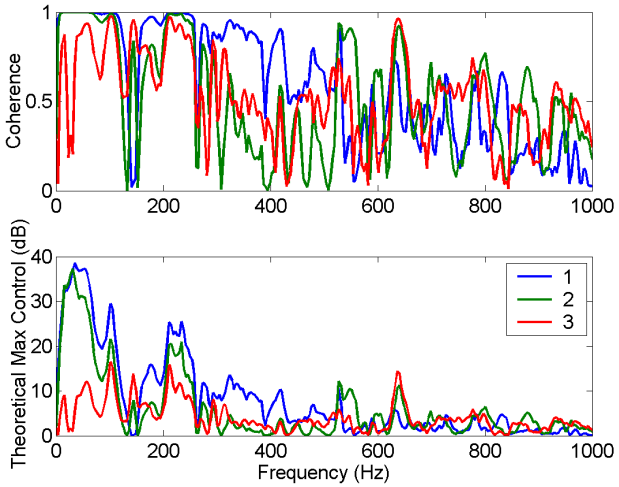

Figure 6.20: Coherence between fuselage plate vibration using a discrete reference sensor array and eight error microphone arrays.

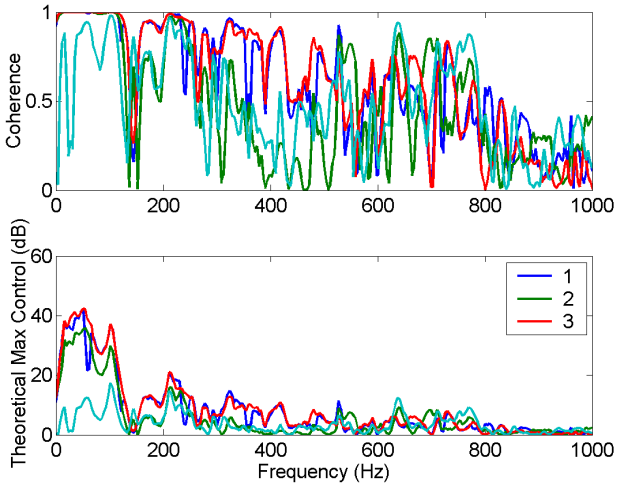

Figure 6.21: Coherence between fuselage plate vibration using a discrete reference sensor array and observer microphones.

Table 6.3: Primary path coherence using a Discrete Reference Sensor Array at location #1.

Error Signal	**Theoretical Maximum Attenuation (dB)** 400–800 Hz
Error Sensor Arrays	
1	4.4
2	4.0
3	2.5
4	2.3
5	1.5
6	1.1
7	1.1
8	0.7
Observer Microphones	
1	4.2
2	3.5
3	3.0
4	1.8
5	1.7
6	0.5

Secondary Path Multiple Coherence Study

Multiple coherence of the secondary paths was then determined using the eight Smart Foam element configuration. Each actuator produced similar coherence values to those shown in Figure 6.22. By the figure, the actuators do not have sufficient coherence below 350 Hz with improving performance at higher frequencies. Dips in coherence occurred at 60 Hz harmonics due to line noise in the microphone signals. At frequencies greater than 400 Hz, coherence was greater than 0.8 at all microphones. Above 500 Hz, coherence was between 0.9 and unity and above 600 Hz the coherence was unity at all microphones.

The test was then repeated using the error sensor arrays centered at 100 cm above each Smart Foam element. These results are shown in Figure 6.23. Here, it is observed that coherence is significantly different between each microphone and is highest at the error sensor array centered over the driven Smart Foam element. This should be expected since the error sensor arrays are designed to be directional thereby minimizing physical coupling between control channels. This decoupling therefore results in a reduction in coherence.

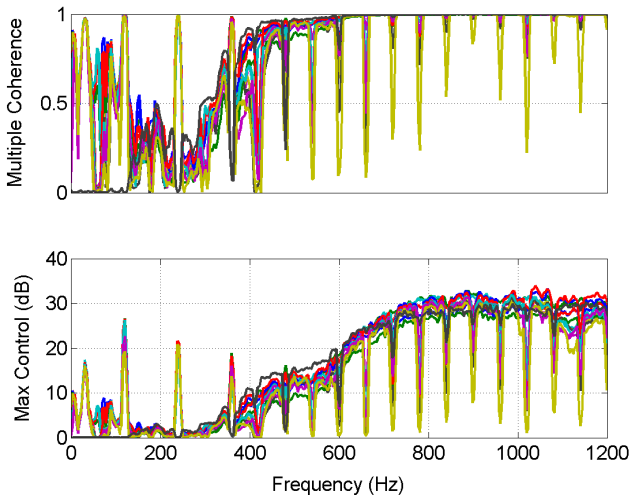

Figure 6.22: Multiple coherence between a single Smart Foam element and microphones in the observer plane.

Causality Study

If a control system is said to be causal, the delay time through the controller—the electrical path from the reference sensors to the actuators—must be less than the time of propagation of waves within the primary noise field from the source to the error sensors. From the actuators, waves from both the primary and secondary fields would then propagate to the error sensors.

For this research effort, the primary noise field is generated by the flow induced plate vibration. Therefore, the time of propagation from the vibrating plate to the PVDF actuator within the Smart Foam is the time of propagation of the primary noise field to the actuator. If the delay time through the controller is greater than the time of propagation of the primary noise field to the actuator then the system is said to be acausal. An acausal system means, then, that the controller will not be able to generate a secondary field capable of entirely cancelling the primary field. However, as mentioned previously, Burdisso et al stated that some degree of control is still attainable for acausal systems [76].

For Smart Foam elements used in this research, the tops of the curved PVDF sheets were 75 mm (3″) from the plate. The propagation time of the primary field to the actuator may then be determined by

$$T_p = d/c \tag{6.21}$$

where T_p is the time of propagation in seconds, c the wave speed (343 m/s, 1100 ft/s) and d the distance of propagation. Substituting for d in equation 6.21 as 75 mm we get a propagation time of 0.22 ms. Therefore, with the Smart Foam elements mounted on the plate, the control system would be causal only if the delay through the control system was less than 0.22 ms. The first factor that must be considered is the sampling rate of the controller. For this propagation time the minimum sampling rate, assuming no time delays due to other analog or digital circuitry, would need to be

$$F_{controller,min} = 1/T_p \tag{6.22}$$

and so with $T_p = 0.22$ ms, $F_{controller,min} = 4550$ Hz. Therefore, any sampling rate less than 4550 Hz is guaranteed to make the controller acausal. However, filters, amplifiers, and circuitry within the controller or in the signal conditioners, may also introduce additional time delay.

For the four channel[4] Spectrum C–40 controller, the maximum number of control filter coefficients given several combinations of the number of references, the number of actuators, and the sampling rate are listed in Table 6.4. For the controller used, then, it is shown that to sample at the minimum rate of 4550 Hz, a four-by-four control system would allow a maximum of 75 control coefficients per filter. In Chapter 7, it will be shown that this would not be enough coefficients to achieve sufficient control.

Tests were performed to determine the affect of causality. Control experiments were then performed using an ideal reference with three actuators and three summed error signals. Using an ideal reference signal, delay may be added to the primary disturbance so that the delays across the primary paths and the secondary paths are equal, thereby resulting in a causal system.

Data from this test are summarized in Table 6.5 and plotted in Figure 6.24. The trend for the error microphones suggested that 4 samples of delay at 2500 Hz allowed for

[4]The maximum channel count for control experiments was four. All eight channel control was performed as control simulations utilizing experimentally acquired data.

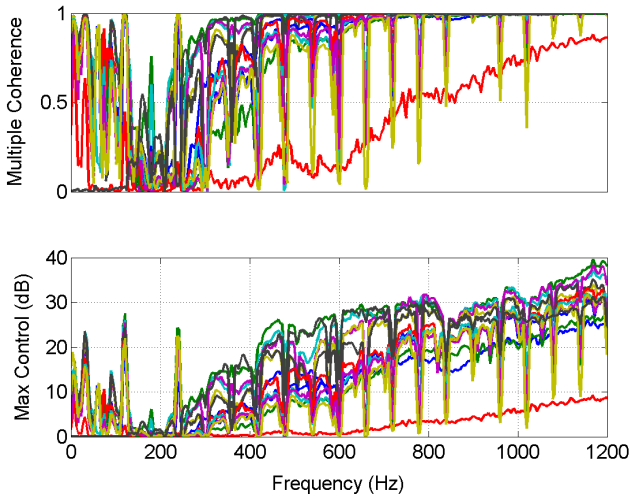

Figure 6.23: Multiple coherence between one Smart Foam element and microphone sensor arrays centered at 100 cm above actuators.

Table 6.4: Maximum Number of Controller Coefficients for the Four Channel C40 Controller

Sampling Rate (Hz)	Number of References	Number of Actuators	Maximum Number of Controller Coefficients
2500	2	2	255
2500	4	2	255
2500	4	4	255
4500	2	2	255
4500	4	2	75
4500	4	4	75
5000	2	2	210
5000	4	2	20
5000	4	4	20

the best control performance. Of the cases considered, the 4 sample delay case achieved the best control performance therefore suggesting the control system delay was 4/2500 Hz = 0.0016 s or 1.6 ms. Since the time of acoustic propagation from the source (vibrating plate) to the actuators was only 0.22 ms, it can be concluded that the controller was acausal for this research effort.

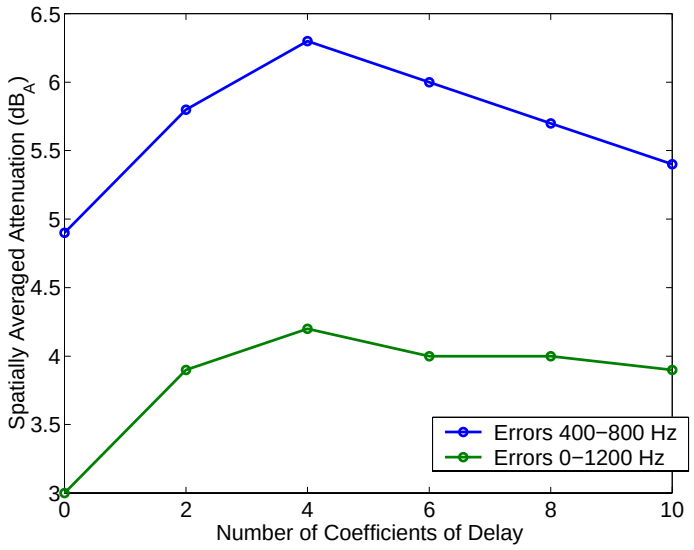

Figure 6.24: Comparison of ideal control performance.

Figure 6.25 plots the results for three channel (using the four element Smart Foam configuration) control using an ideal reference and four samples of delay at 2500 Hz (1.6 ms) using a control band of 400–800 Hz. This configuration had a 6.3 dB$_A$ attenuation at the error microphones and 2.4 dB$_A$ at the observer microphones. In addition, the overall attenuation at the error microphones across the observed band (0 – 1200 Hz) was 2.4 dB$_A$ at the error microphones and 1.2 dB$_A$ at the observers. This is attributed to control spill–over due to filter roll–off.

Table 6.5: Effect of Delay on Ideal Control Performance

Delay (#samples) @ 2500 Hz	Attenuation (dB_A) at error (observer) mics 400–800 Hz	0–1200 Hz
0	4.9(2.7)	3.0(1.2)
2	5.8(2.4)	3.9(1.3)
4	6.3(2.4)	4.2(1.2)
6	6.0(2.4)	4.0(1.2)
8	5.7(2.4)	4.0(1.2)
10	5.4(2.3)	3.9(1.2)

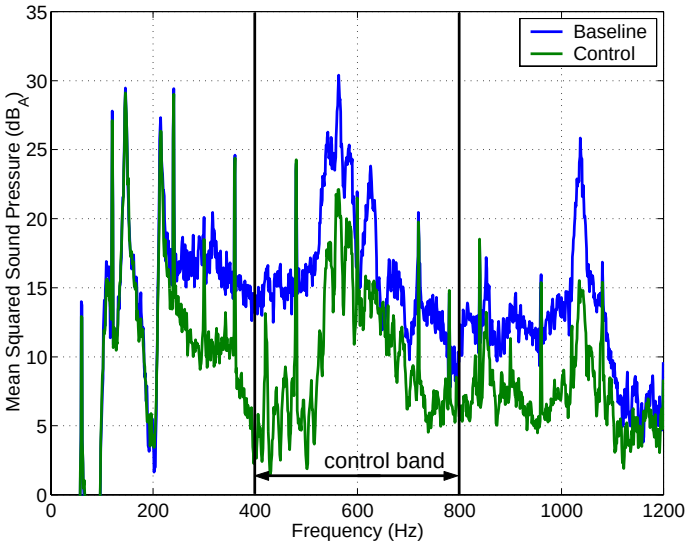

Figure 6.25: Comparison of ideal control performance using the four element Smart Foam configuration.

6.4 Summary

The coherence and resulting theoretical maximum achievable control using the four methods of reference sensing explored in this research effort were studied. It was shown that the use of independent point reference measurements benefited by using multiple references per actuator. For the 400–800 Hz band, it was shown that the use of one, two, or three independent point references gave theoretical maximum achievable control of 9.4 dB, 6.5 dB, and 16.8 dB, respectively. Although the theoretical performance of the two reference case was computed to be less than that of the one reference case, the resulting control was shown to be higher at immediately adjacent error sensor arrays. This then suggests the two reference case results in more global control. At the observer microphones, performance at the observer microphones varied given the number of and distance to the point reference sensor(s) but had a peak value of 13.4 dB for the two reference case compared to 10.3 dB using a single reference.

Using the discrete reference sensor array located at location #1, 4.4 dB and 4.0 dB theoretical maximum achievable control was obtained at the error sensor arrays at locations #1 and #2. Performance at other error sensor arrays was from 0.7 dB to 2.5 dB. The theoretical maximum achievable control was 4.2 dB at the closest observer microphone with performance between 0.5 dB to 3.5 dB at other locations.

The use of the distributed PVDF spatial sensor at location #1 for obtaining the reference signals was shown to have a theoretical maximum achievable control as high as 8.9 dB at the error sensor array at location #1. This dropped to 5.2 dB and 4.6 dB at the two next closest error arrays. Performance at the remaining error sensor arrays was from 0.3 dB to 1.9 dB. The two observer microphones closest to the PVDF reference sensor had 8.8 dB and 8.5 dB theoretical maximum achievable control. Performance at the remaining observer microphones was from 2.7 dB to 6.3 dB.

Comparing values of theoretical maximum achievable control using the four reference sensing techniques, it was observed that the use of three independent reference sensors per actuator theoretically performed best. Limiting the number of reference signals to only one per actuator, the use of a single point reference measurement per channel resulted in the greatest theoretical maximum achievable control. The use of the PVDF spatial sensor to obtain reference signals resulted in theoretical maximum achievable control on par with the single point reference approach. The use of discrete reference sensor arrays resulted in the lowest theoretical maximum achievable control. It is concluded that the use of the two spatial sensors observed will not improve active control performance relative to the use of a single accelerometer per actuator.

Comparing results at the observer microphones, peak performance was attained using *two* point references per actuator Restricting the number of references to only one per actuator, theoretical maximum achievable control at the observer microphones was highest (10.3 dB) using the single point reference measurement.

Secondary path coherence showed that the Smart Foam actuators used for the eight channel configuration had coherence greater than 0.8 at frequencies above 350 Hz with near–

unity coherence at frequencies greater than 600 Hz. Note, however, that coherence was very poor at lower frequencies.

Assuming delay within the control system occurred only from the sampling rate, it was shown that the minimum sampling rate required to achieve a causal system was 4550 Hz. At this sample rate the number of coefficients would be limited thus limiting performance. Since an acausal control system may benefit by the use of longer filters, it is recommended that the sample rate be set based on the band of control (400–800 Hz) thus allowing longer filter lengths to offset the effects of causality.

Real control systems require time for computations and may have added delay due to signal conditioning processes. Therefore, the actual delay time of a controller will be greater than that due only to the sampling rate. Control experiments performed using an ideal reference (generated by the controller) allowed future values of the reference to be read by the control system. Increasing the number of samples of delay allowed an estimate of the controller delay when the performance was at a maximum. This was determined to be 1.6 ms. Given a wave propagation time of 0.22 ms from the actuators to the error arrays, the system used for this research effort was shown to have a 1.48 ms delay between the reference and error input signals. The control system used for experiments presented in Chapter 7—Active Control was confirmed to be acausal. Knowing this information, control simulations could then be run with the proper delay thereby mimicking the performance of a real controller.

Chapter 7

Active Noise Control

This chapter presents the results of the active noise control experiments and simulations performed for this research effort. Theory of noise cancellation using sound pressure minimization was presented in Chapter 1 along with the governing theory of the feed forward, filtered reference, LMS control algorithm used for experiments and simulations presented below. Chapter 2 identified the spatial and temporal correlation of the turbulent flow and the resulting plate vibration. Reference and error sensing was presented in Chapter 3 and Chapter 4, respectively with the development and performance of Smart Foam elements presented in Chapter 5. Issues of coherence and causality were presented in Chapter 6.

Control experiments were performed using a four channel configuration with a single reference per actuator using a control band of 400–800 Hz. Tuning masses were added to the tops of the four Smart Foam elements to increase low frequency performance by reactively suppressing the plate structure response. Active control was then performed with the tuning masses in place to determine if the presence of the reactive treatment influenced the active performance.

The control system was limited to a maximum of four references. Therefore, for the eight channel configuration, control simulations were required. Simulations were performed using eight actuators with one error and one reference per actuator with a 400–800 Hz control band. The estimated delay of the controller used for the four channel configuration was incorporated into the simulation runs. Further, additional runs were performed using only one sample of delay. This then would identify the control performance given then best possible causality of a digital control system.

7.1 Experiment Setups

Test setups for control experiments and simulations are presented in this section. These tests were performed using the wind tunnel presented in Appendix A.

The boundary layer flow was obtained using a wind tunnel having a flat plate mounted flush to the test section inner wall as shown in Figure 7.1. Reference sensors were placed on the plate which radiated into the enclosure. Smart Foam elements were placed on the

radiating plate over the reference sensors and affixed with a light coat of ordinary spray glue. Depending on the test configuration, either single error microphones or error microphone arrays were centered over the Smart Foam elements at varying distances as noted and the observer microphones were placed within the enclosure 61 cm from the radiating plate. Observer microphone placement was the same for all test cases and is referred to as the observer plane.

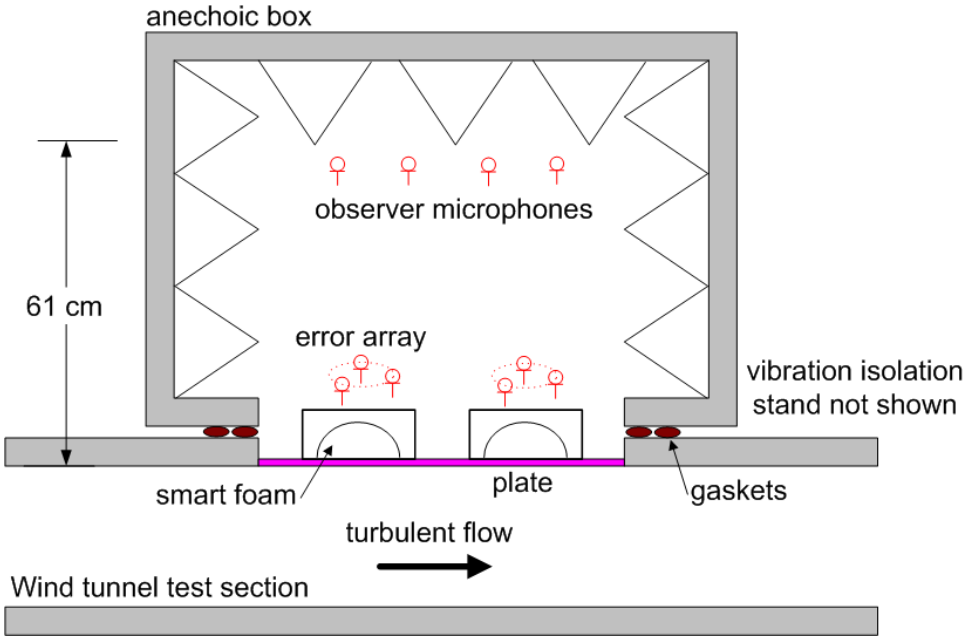

Figure 7.1: Setup for active control tests. Reference sensors mounted under Smart Foam (not shown).

The experiment setups for wind tunnel tests involved five main components. These consisted of reference sensors and Smart Foam elements mounted to the vibrating plate, error sensors placed in the near field, observer microphones placed in the far field, and the control system. Four methods of reference sensing were explored along with two error sensing methods. Further, three Smart Foam configurations were used for the actuators.

Reference sensing was discussed in Chapter 3—Reference Sensing and consisted of both point reference measurements using accelerometers and the use of two distributed sensor array designs. To restate briefly the reference sensing methods used, the first involved the use of a single PCB model 352A10 accelerometer per actuator.

The second reference sensing method, a spatial sensor referred to as the discrete reference sensor array, involved the use of four accelerometers. Three accelerometers of the discrete array were arranged in a triangular pattern under each actuator and had unity gain. A fourth accelerometer having 2x gain was placed at the center. The four signals were summed producing a single reference signal per actuator. The accelerometer pattern was

sized such that only wavenumbers within the desired control bandwidth would be sensed.

The third reference sensing method, referred to as the distributed reference sensor, involved the development of a distributed spatial sensor consisting only of a single PVDF disk. The disk was sized such that only wavenumbers within the desired control bandwidth would be sensed.

The fourth reference sensing method again used ordinary accelerometers. However, an additional reference is used with each actuator. Although this approach was beyond the scope of this research effort, it was performed to emphasize the benefits of such a reference sensing strategy since it does increase control performance both at the error sensors and in the observer plane. The use of two references per actuator results in greater coherence between the references and errors thereby resulting in greater control performance. Note, however that due to limitations in the control simulation software, this configuration could only be explored using a MIMO control scheme. Further, it was only performed for the single sample of delay case.

Error sensing was conducted primarily in the near field using error sensor arrays as discussed in Chapter 4—Error Sensing, although near field and far field error sensing was also performed using a single microphone per actuator as noted below. Error sensor arrays consisted of three microphones arranged on a circular ring. Each microphone had unity gain and was summed providing a single error signal per actuator. Microphones were also placed in the far field (observer microphones) to monitor the global attenuation achieved. Point and array measurements were conducted using PCB Acousticel microphones.

The first of the three Smart Foam actuator configurations consisted of four Smart Foam elements with spaces between them filled with open cell foam. The second configuration added tuning masses to increase low frequency performance by providing a means of reactively attenuating structure vibration thereby reducing the radiated noise field. The third configuration, consisting of eight Smart Foam elements, was developed as a result of control experiments performed using the four element Smart Foam configuration and the coherence studies conducted in Chapter 3–Reference Sensing.

Control was provided using either control experiments or control simulations. Four channel control, involving only a single reference per actuator and a single error per actuator, was conducted by experiment. However, due to channel limitations of the available control system, eight channel studies had to be simulated off–line. However, these simulations were conducted using measured data and the control algorithm was identical to that used in the control experiments. Therefore, control simulations and control experiments would provide similar results given similar conditions.

Configurations used for control experiments and simulations are presented in Table 7.1. Each configuration is discussed in detail below.

Table 7.1: List of control experiments and control simulations.

Number of Actuators	Reference Sensor	Error Sensors	Description
Control Experiments			
4	Accelerometer	Single Microphones	Near field and far field error sensing
4	Accelerometer	Error Arrays	Near field error sensing
4	Accelerometer	Error Arrays	Near field error sensing with tuning masses for reactive/active/passive control
4	Discrete Array	Error Arrays	Near field error sensing
4	n/a	n/a	Tuning masses for reactive/passive control
Control Simulations			
8	Accelerometer	Error Array	Near field error sensing
8	2 Accels/actuator	Error Array	Near field error sensing
8	PVDF Sensor	Error Array	Near field error sensing

Setup for Four Channel Control Experiments Using Single Point References

Control experiments were conducted using an arrangement of four Smart Foam elements as depicted in Figure 7.2. As discussed in Chapter 5—Actuators, each Smart Foam element measured 8 cm by 18 cm (3″ by 7″). Tests were also conducted using plates added to the tops of each Smart Foam element. The mass of these plates tuned each Smart Foam element to have a bounce mode equal in frequency to the (1,1) plate mode as discussed in Chapter 5. This configuration is shown in Figure 7.3.

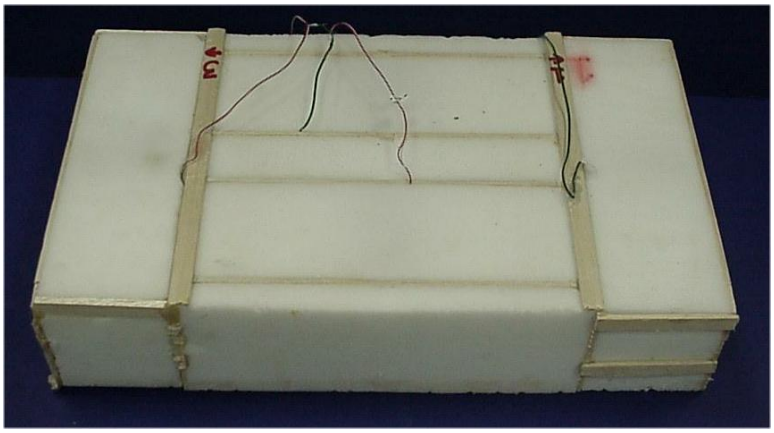

Figure 7.2: The four channel Smart Foam configuration.

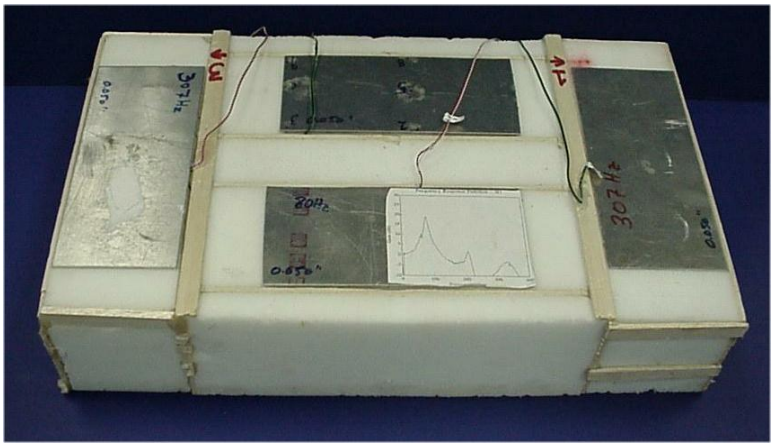

Figure 7.3: The four channel Smart Foam configuration with tuning masses (tuned to plate (1,1) mode).

The observer microphones were placed 61 cm from the fuselage panel for all experiments. Error sensors were either a single microphone placed in the observer plane or at a height of 100 mm above the actuators in an array of three microphones, equally spaced on a 75 mm diameter ring. Microphones in each error array were matched for similar sensitivities allowing for proper array directionality. Refer to Figure 7.4 and Chapter 4—Error Sensing for details.

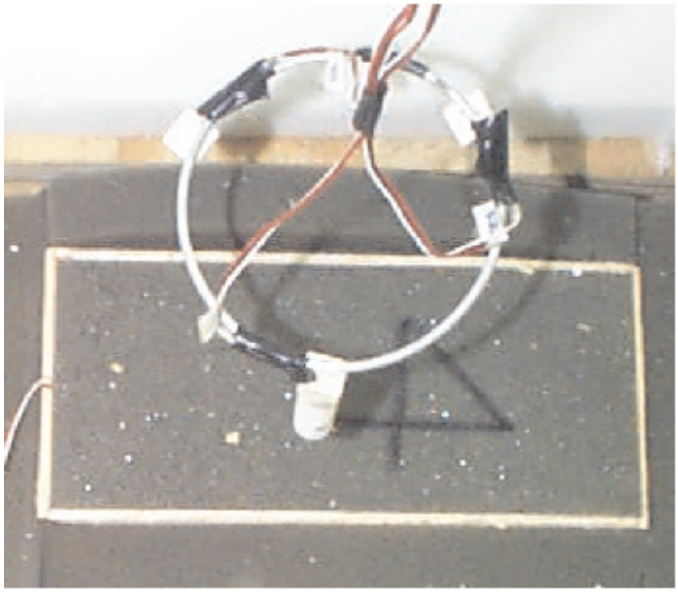

Figure 7.4: The error array is focussed directly over its respective actuator.

Smart Foam elements were placed on the vibrating plate and adhered using a light coat of ordinary spray glue. Reference sensing was performed using a single accelerometer per actuator mounted on the vibrating plate. Reference accelerometers were located at the center of its respective actuator using beeswax. A small piece of foam was cut from the underside of each Smart Foam element to facilitate the placement of the accelerometers.

The wiring diagram used for the data acquisition and control systems is shown in Figure 7.5. Data acquisition was performed using a custom written LabView interface with National Instruments SCXI hardware including analog anti–aliasing filters. The sampling rate was 4000 Hz with anti-aliasing filters set to 2000 Hz. Observer and summed error array signals were first appropriately conditioned and then acquired without additional filtering. These signals, acquired before and after control, allowed determination of control performance at error locations and within the observer plane.

The control system used was a Spectrum C–40 Dynamic Signal Processing (DSP) board programmed with an adaptive, feed forward, filtered–x, least mean square (LMS) control algorithm. The C–40 controller had one master processor with four slave processors.

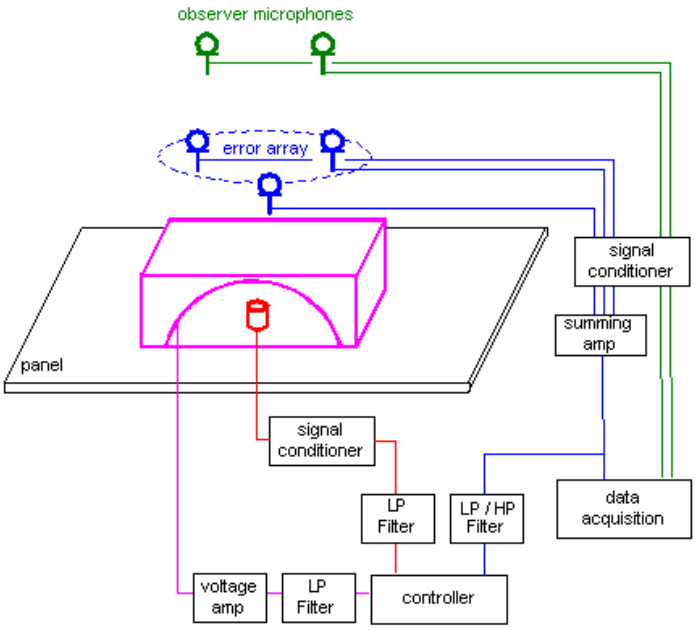

Figure 7.5: Wiring configuration for the four channel active control experiments using accelerometer references.

This configuration allowed for a maximum of four reference channels, eight actuator channels, and twelve error channels.

The conditioned error channels were band passed using Ithaco 4302 analog filters before inputting the signal to the controller. Reference signals were conditioned to output a voltage signal and low–pass filtered at the upper control band frequency (800 Hz). Actuator signals, output from the controller, were low–pass filtered to minimize signal noise and amplified using a voltage amplifier prior to driving the Smart Foam elements.

Setup for Four Channel Control Experiments Using Discrete Reference Sensor Arrays

This section discusses the experiment setup used for control experiments conducted using discrete reference sensor arrays. Development of discrete reference sensor arrays was presented in Chapter 3—Reference Sensing.

Discrete reference sensor arrays consisted of three accelerometers placed in a triangular pattern with a third at the center as shown in Figure 7.6. The conditioned output from each accelerometer was appropriately amplified and summed using the analog summing circuit presented in Appendix B—Summing Amplifier Design.

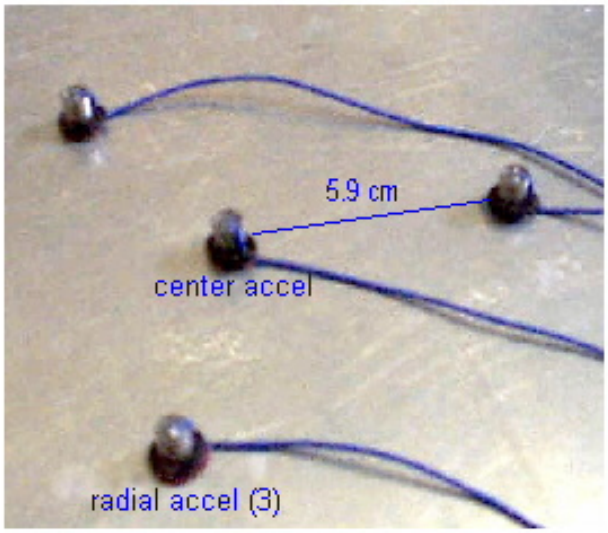

Figure 7.6: Discrete reference sensor array. The array consists of three radial accelerometers of unity gain placed in a triangular pattern with a fourth of 2x gain at its center. The radial spacing was 5.9 cm or 2.3″. The sum of these four signals was used as the reference signal.

Accelerometers used for the arrays were mounted on the vibrating plate using beeswax at the center of the respective actuator. A small piece of foam was cut from the underside of each Smart Foam element to facilitate the placement of each accelerometer.

Error signals were obtained using error sensor arrays placed in the near field located 100 mm from the tops of the Smart Foam elements. Observer microphones were placed in the far field in the observer plane.

The wiring diagram used for the data acquisition and control systems is shown in Figure 7.7. Data acquisition was performed using a custom written LabView interface with National Instruments SCXI hardware including analog anti–aliasing filters. The sampling rate was 4000 Hz with anti-aliasing filters set to 2000 Hz. Observer and summed error

array signals were first appropriately conditioned and then acquired without additional filtering. These signals, acquired before and after control, allowed determination of control performance at error locations and within the observer plane.

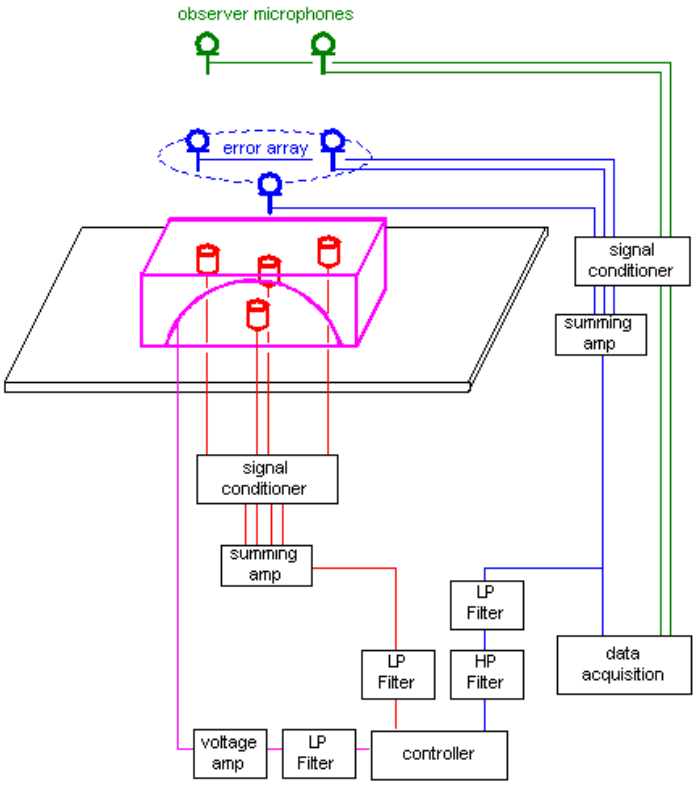

Figure 7.7: Wiring configuration for the four channel active control experiments using discrete reference arrays.

The control system used was a Spectrum C–40 Dynamic Signal Processing (DSP) board programmed with an adaptive, feed forward, filtered–x, least means squared (LMS) control algorithm. The conditioned error channels were band passed using Ithaco 4302 analog filters before inputting the signal to the controller. Reference signals were conditioned to output a voltage signal and low–pass filtered to the upper control band frequency (800 Hz). Actuator signals, output from the controller, were low–pass filtered to minimize signal noise and amplified using a voltage amplifier prior to driving the Smart Foam elements.

Setup for Eight Channel Control Simulations Using Accelerometer References

Eight channel control was performed off–line using control simulations. These simulations used measured reference, error, and observer time histories as well as measured system identification paths. The eight elements shown in Figure 7.8 were arranged in a two by four pattern with each element measuring approximately 13 cm square. These actuators were designed according to the study performed in Chapter 3—Reference Sensing.

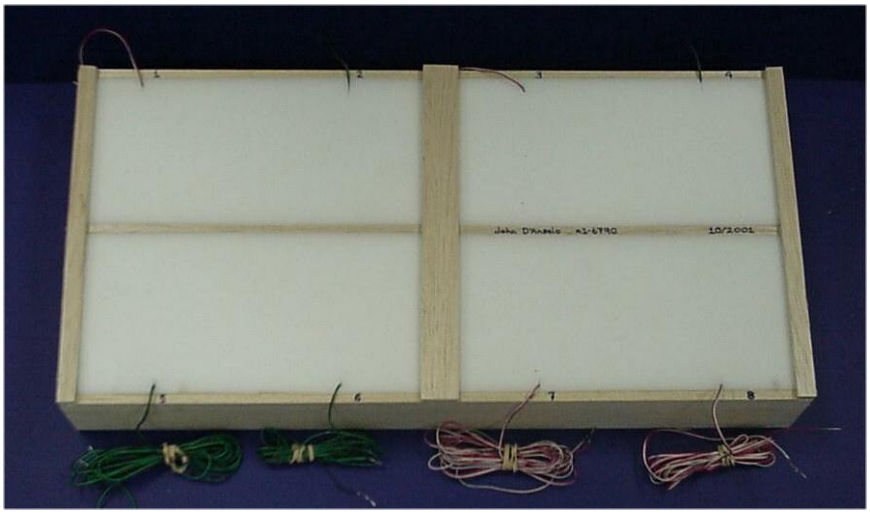

Figure 7.8: The eight channel Smart Foam configuration arranged in a 2 by 4 pattern. This configuration provided for a square planform which allowed for optimal design of the distributed reference sensors.

Computer simulations for the eight channel configuration required experimentally determined time histories of the reference, error and observer signals. Figure 7.9 depicts the setup used to obtain the time histories—turbulent flow induced plate vibration and resulting error and observer pressure fields. Plate vibration was induced by the turbulent flow to best represent actual testing conditions.

This configuration used a single accelerometer per actuator to acquire reference signals. Accelerometers were placed at the center of the respective actuator with a small piece of foam removed from the Smart Foam element to facilitate placement. Error sensing was conducted using error sensor arrays (Figure 7.4) in the near field. Signals from each error sensor were conditioned and summed using the analog summing circuits developed in Appendix B. Observer microphones were placed in the far field to monitor global performance.

As opposed to four channel control experiments, reference and error signals were not conditioned using analog filters. Instead, acquired time histories were filtered digitally prior to each control simulation. This required fewer experiments to be conducted and resulted in

more flexibility during the analysis allowing the control band to be modified as desired.

Data acquisition was performed using a custom written LabView interface with National Instruments SCXI hardware including analog anti–aliasing filters. The sampling rate was 4000 Hz with anti–aliasing filters set to 2000 Hz. Reference, error, and observer signals were appropriately conditioned and acquired simultaneously without filtering. These time histories were used in the control simulations.

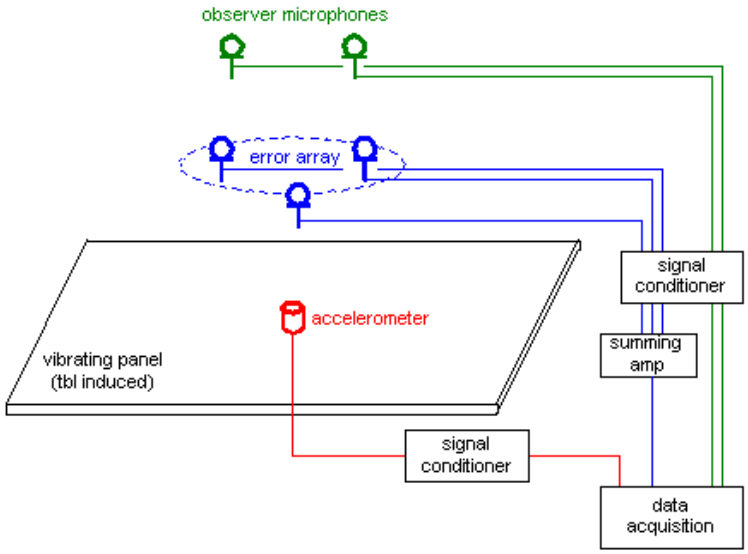

Figure 7.9: Primary paths were determined for the eight channel control configuration for use in the control simulation. The reference sensor used for this case was a single accelerometer per channel.

The secondary, or system identification, path—actuator input to interior noise field—was determined by exciting the actuators, one at a time, with a random disturbance. This excitation was measured along with the resulting interior noise field at the observer and error microphones. The excitation voltage was low–passed filtered at 1000 Hz and amplified using a voltage amplifier prior to actuating the Smart Foam element. Data was acquired using a 4000 Hz sampling rate with anti–aliasing filters set to 2000 Hz. The wiring diagram is shown in Figure 7.10.

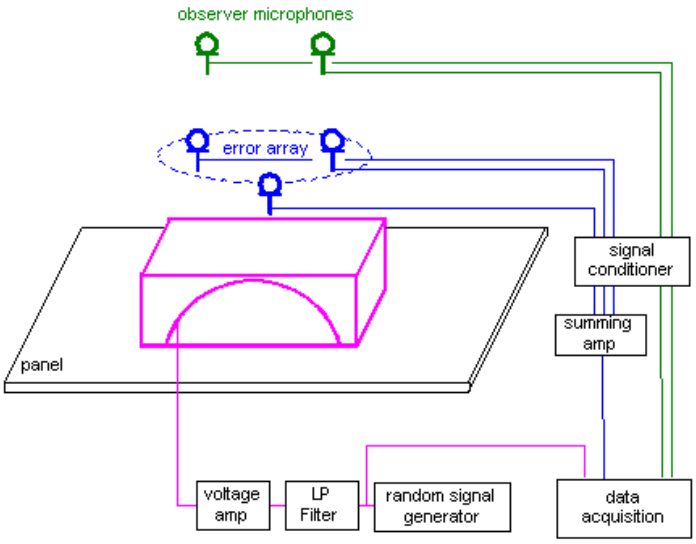

Figure 7.10: Secondary paths were determined for the eight channel control configuration for use in the control simulation.

Setup for Eight Channel Control Simulations Using Distributed PVDF Reference Sensors

The use of shaped PVDF spatial sensors for obtaining reference signals were used only in control simulations. These sensors were developed in Chapter 3 and are shown mounted on the plate in Figure 7.11.

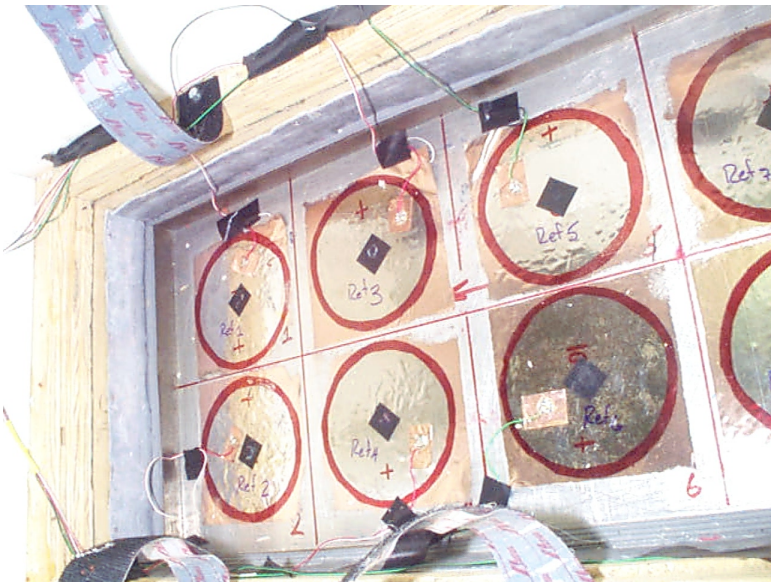

Figure 7.11: The shaped PVDF spatial reference sensors were bonded to the vibrating panel and were designed to have a low–pass cut–off frequency of 800 Hz.

PVDF sensors were mounted to the vibrating plate using a thin coat of ordinary spray glue below the eight Smart Foam elements. Control simulations conducted using distributed PVDF reference sensors were performed using error sensor arrays placed in the near field 100 mm above the tops of the Smart Foam elements with observer microphones placed in the observer plane.

Figure 7.12 depicts the wiring diagram used to obtain time histories for control simulations using PVDF reference sensors. PVDF sensor output was conditioned using an ICP signal conditioner and then acquired. Error array signals were summed using the analog summing amplifier discussed in Appendix B.

Data acquisition was performed using a custom written LabView interface with National Instruments SCXI hardware including analog anti–aliasing filters. The sampling rate was 4000 Hz with anti–aliasing filters set to 2000 Hz. Reference, error, and observer signals were appropriately conditioned and acquired simultaneously without filtering. These time histories were used in the control simulations. System identification paths used for this configuration were the same as used for the single and multiple point reference control

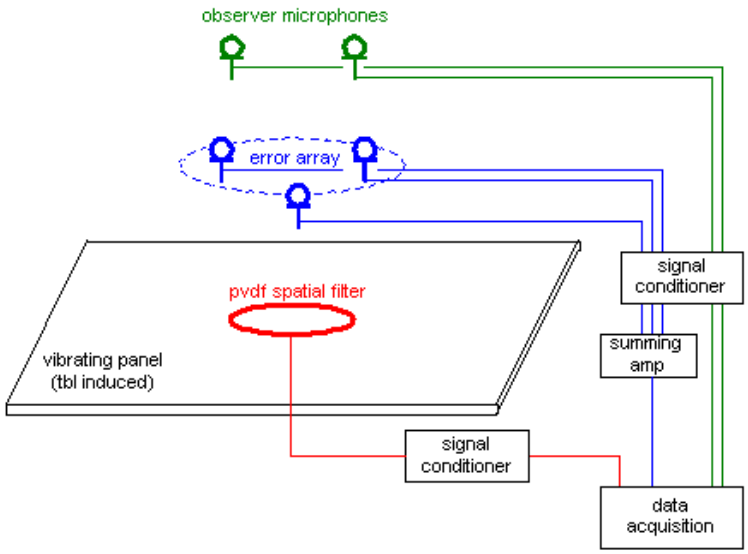

Figure 7.12: Primary paths were determined for the eight channel control configuration for use in the control simulation. The reference sensor used for this case was a single, shaped PVDF spatial sensor per channel.

simulations as discussed above.

Running and Processing Control Simulations

Control simulations were run using a software entitled *lmsfilterx* with permission from the programmer [78]. This code runs in a DOS window and is shown in Figure 7.13.

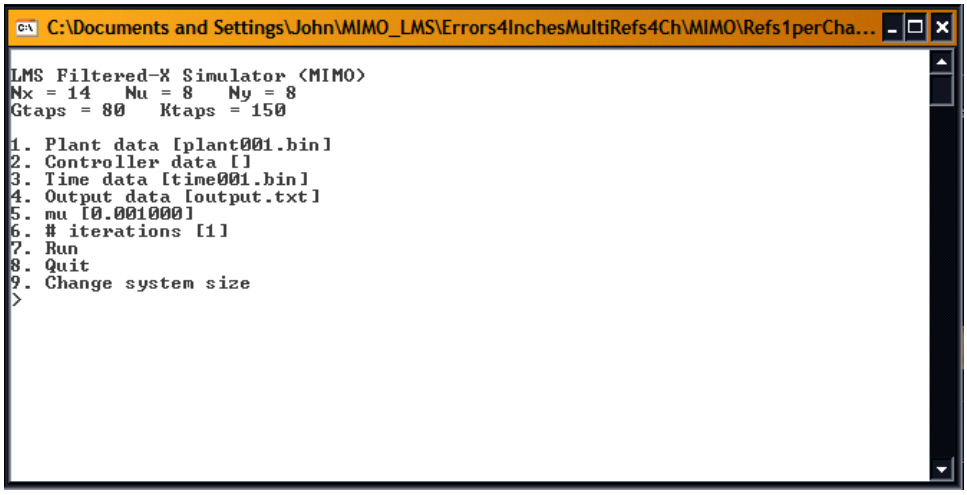

Figure 7.13: The lmsfilterx Control Panel (shown in reverse color).

Data prescribed to *lmsfilterx* was generated using a Matlab script entitled *MakeSim* which is included in Appendix C—Matlab Scripts. This script reads the measured reference, error and observer time histories and converts their format to binary data files. System identification filters, read by *MakeSim*, were generated from measured actuator voltages and microphone data using a Matlab script entitled *SysId* which is included in the Appendix C. Further, the number of references, errors and observers, as well as the lengths of the control and system identification filters are specified within the data files. Matlab format (MAT) data files are also constructed for the all–pass and the band–passed error and observer data. These MAT files are used during post–processing such that baseline and control runs may be compared.

Data generated is input to the control system using the command prompts shown. Keying the respective number allows the user to specify the filename of the input or output data file and values such as the convergence coefficient (mu, #5), the number of iterations (#6), or the system size (#9).

Binary files of the plant and time histories generated in *MakeSim* are input using selections #1 and #3, respectively. Control filters generated from a previous run may be specified as input to a following run using selection #2. The system size is specified in the following order: number of references, number of actuators, number of errors, length of system identification filter, length of control filter, and coupling. A coupling value of "1" specifies MIMO control whereas a value of "0" specifies fully decoupled (diagonalized or

mSISO) control; partial coupling is not permitted. It should be noted, however, that fully decoupled control still computes the cross–terms however the values are simply set to zero. Therefore, the number of computations required to run a fully decoupled control scheme is the same as if running a MIMO scheme given the same controller size and filter lengths.

Control is initiated by entering "7" and may be terminated prematurely by entering "8". When the simulation ends, either by completing the specified number of iterations or when terminated by the user, the output data will be saved to the prescribed text file name and the updated control filters will be saved to a binary data file named *cntrlfilters.bin*.

Results generated by *lmsfilterx* were then post–processed using a Matlab script entitled *CSimPost* which is included in Appendix C—Matlab Scripts.

The post–processing script prompts the user for the filenames of several data files. Two time history data files, one all–pass and the other band–passed over the control band, of the baseline errors generated in *MakeSim* are first read. This is followed by the combined error time history generated by *lmsfilterx* as well as the data file containing calibration data for each microphone. Time histories are then converted to the frequency domain for data presentation.

An example of mean squared all–pass and band–pass baseline errors are shown in the frequency domain in Figure 7.14 for the 400–800 Hz control band. The unconditioned baseline is white noise. Note that it is the band–passed time history which is minimized by *lmsfilterx*.

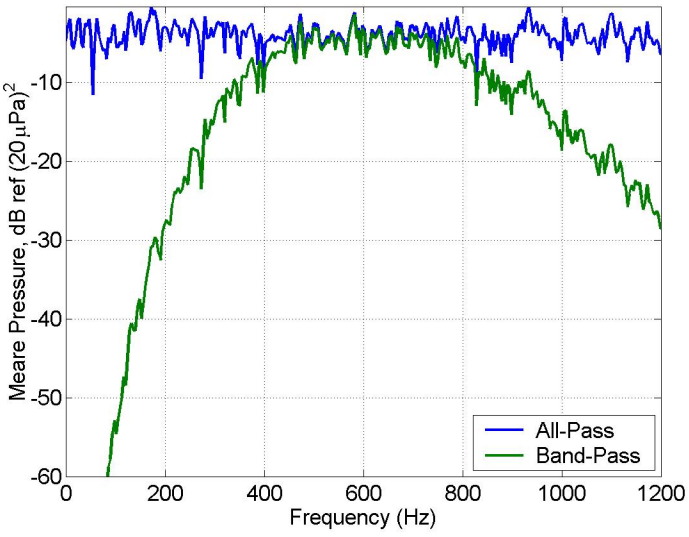

Figure 7.14: Example of all–pass and band–passed (400–800 Hz) baseline errors.

The mean square sums of the combined error is subtracted from that of the band–passed baseline errors to compute the reduction achieved. Reduction values are then added

to the all–pass baseline frequency response data to determine the controlled error field. The resulting, mean squared pressure of the combined error field is shown in Figure 7.15 relative to the band–passed baseline. The overall, spatially averaged reduction is then computed for the control band and from 0–1000 Hz.

This process is then repeated using the time histories at the observer microphones to determine the resulting control achieved in the observer plane.

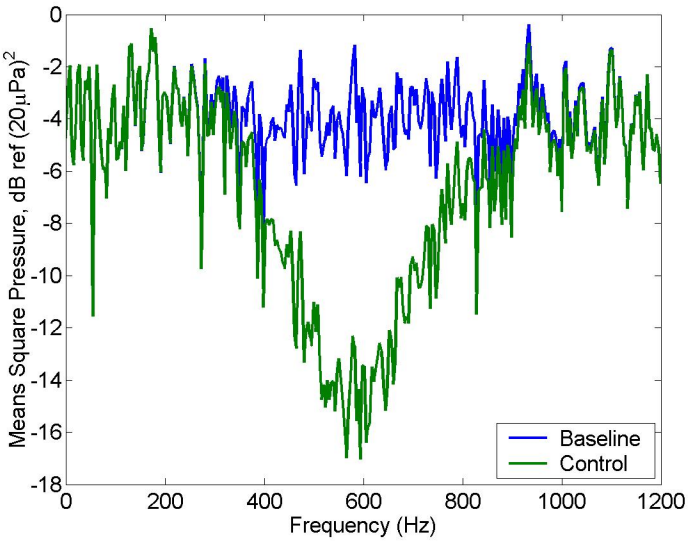

Figure 7.15: Example of control versus baseline data.

Qualification of Control Simulation Software

These studies were performed to confirm that the control software, including the pre- and post-processing routines discussed earlier in this chapter, worked properly. Control was performed using simulated reference, error and observer time histories and system identification filters.

Control simulations provided results only at the locations where the interior field is being minimized (error sensors). Since performance at the observer plane was also desired, the means by which to determine the performance at the observer microphones was necessary. Knowing the system identification paths between the control sources and the observer locations, the performance at the observer locations may be estimated using the control filters determined while minimizing at the error locations. Running the control simulation for one iteration using reference and observer time histories, the observer system identification filters, and setting the global convergence factor to zero generates the control results at the observer locations. These studies confirmed that this process worked correctly.

The control simulation software was qualified by running three simple control cases. These cases involved a single control source (loudspeaker) with a single reference and a single error, both acoustic pressure. Further, an additional acoustic pressure at an observation point was used allowing the process to determine control performance at a point other than where the acoustic pressure was minimized by the control system. The three cases studied were

- **Case 1**, A pure tone at 400 Hz with zero time delay between the error and observer acoustic pressure measurement locations
- **Case 2**, A pure tone at 400 Hz with the observer having three additional samples of delay relative to the error signal
- **Case 3**, Random noise band-passed from 400-800 Hz with the observer having three additional samples of delay relative to the error signal

The sampling rate used for all three cases was 4000 Hz. This then resulted in a time step of 1/4000 Hz = $2.5(10)^{-4}$ s or 0.25 ms. A time history $2^{13} = 8192$ points long was generated resulting in a 2.05 second duration. Fast Fourier transforms were generated using 1024 spectral lines without the use of windows.

Case 1 had the error and observer points collocated. Each used the same system identification filter having 10 coefficients as shown in Figure 7.16. Coefficient #3 was set to unity with all others set to zero. This then modelled a delay of two samples or 0.50 ms. The reference, error and observer signals, shown in Figure 7.17, were sinusoids with the reference having unit magnitude. The error and observer signals were identical with magnitude 0.9 and phased by -0.50 ms relative to the reference.

Only one iteration was required to achieve a 93 dB reduction of the 400 Hz tone used in Case 1. A comparison between baseline and controlled response is shown in Figure 7.18. Note that the performance was the same at both the error and observer points as would be expected for the collocated sensors.

Case 2 was the same as Case 1 but with the observer located downstream of the error location. The system identification filter describing the relation between the source and observer was increased in delay to five samples or 1.25 ms. Therefore, as noted in Figure 7.20 the sixth coefficient (time step five) of the system identification filter for the observer path is set to unity and is set to zero elsewhere.

Only one iteration was required to again achieve 93 dB reduction of the 400 Hz error signal as shown above in Figure 7.18. Performance at the observer location was 89 dB as shown in Figure 7.21. This difference in performance may be attributed to the difference in phase of the two signals.

Case 3 then used the same system identification filters as used for the Case 2 (Figure 7.20) configuration to control a broadband disturbance band-passed from 400–800 Hz. The reference used was a vector of random numbers. This vector was also used for the error signal, which was delayed by two samples, and the observer signal, which was delayed by five

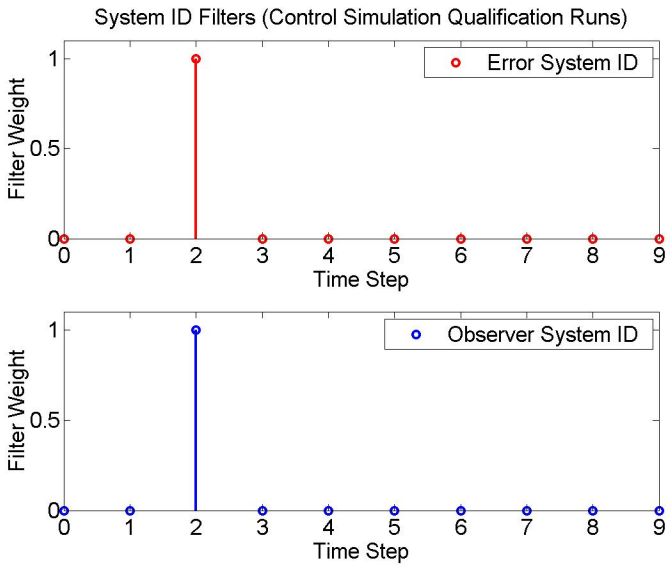

Figure 7.16: System ID filters used for Case 1.

samples. The all-pass (unconditioned) and the band-passed baseline error spectra, conditioned using 4th order Butterworth filters[1], are shown in Figure 7.22. The band-passed error time history was minimized by the controller using seventy-five coefficients in the control filter. System identification filters were the same as those used for Case 2 and are shown in Figure 7.20.

Case 3 achieved 11 dB attenuation averaged over the 400–800 Hz control band at both the error and observer locations. Figure 7.23 compares performance with the error baseline.

[1]Same as in the analog filters used for experiments.

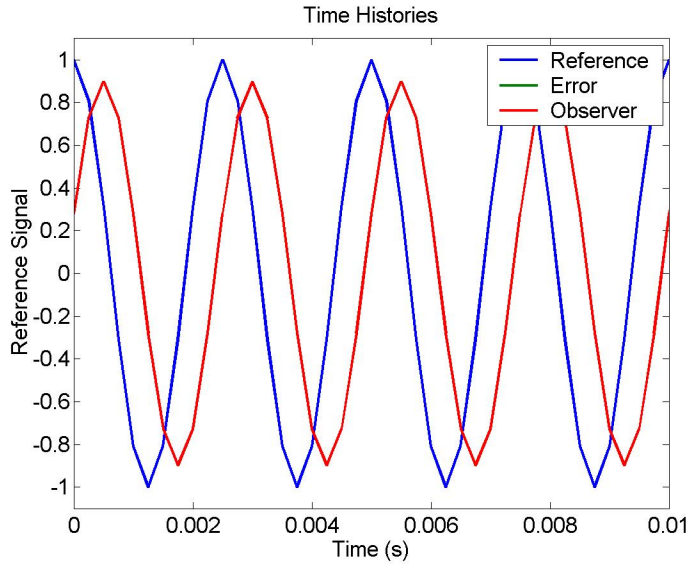

Figure 7.17: Time histories used for Case 1.

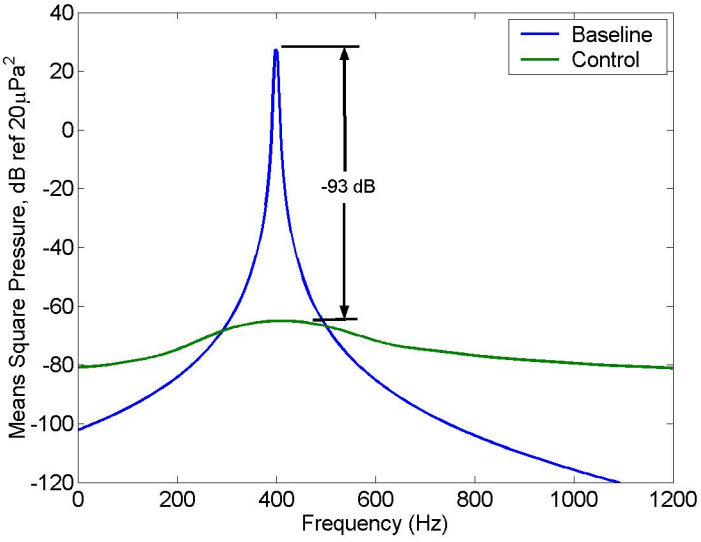

Figure 7.18: Performance achieved for Case 1.

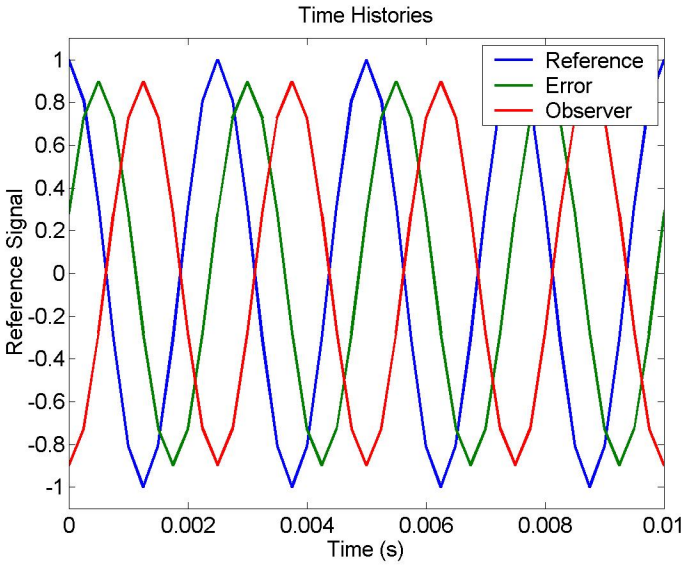

Figure 7.19: Time histories used for Case 2.

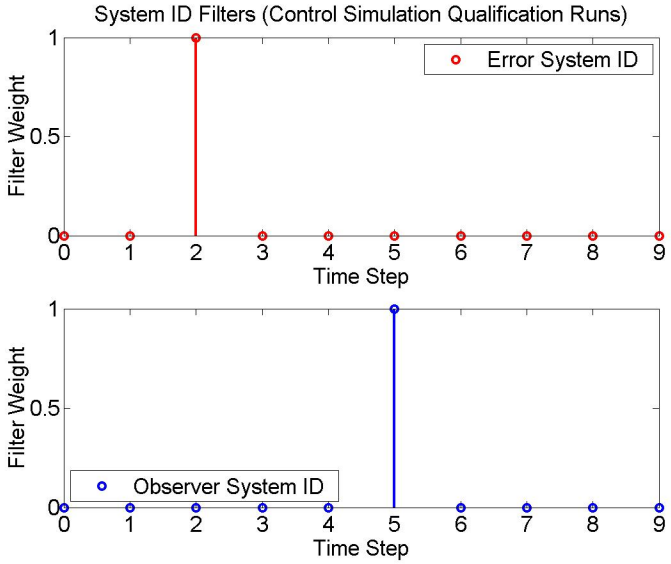

Figure 7.20: System ID filters used for Case 2.

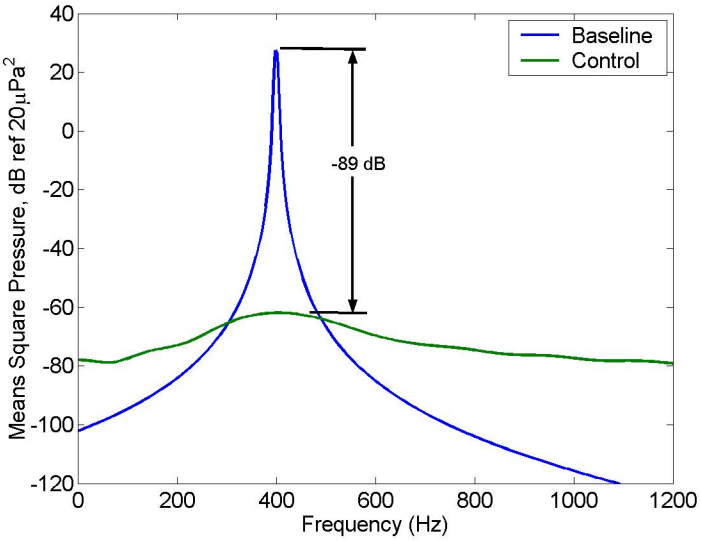

Figure 7.21: Performance achieved for Case 2.

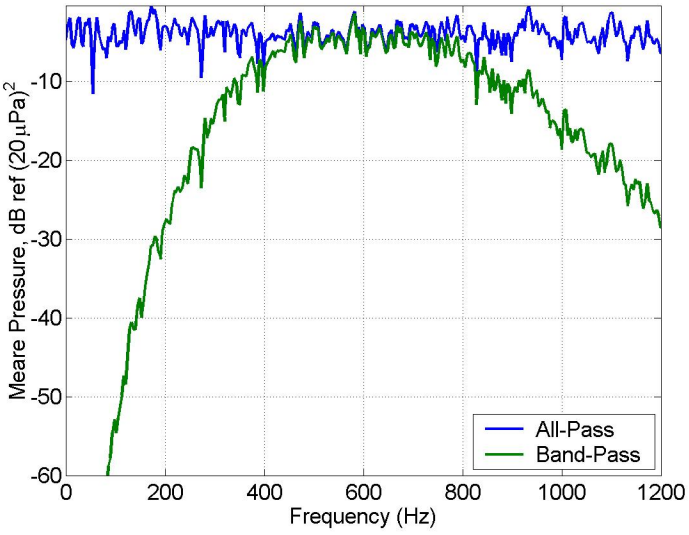

Figure 7.22: Baseline data used for Case 3.

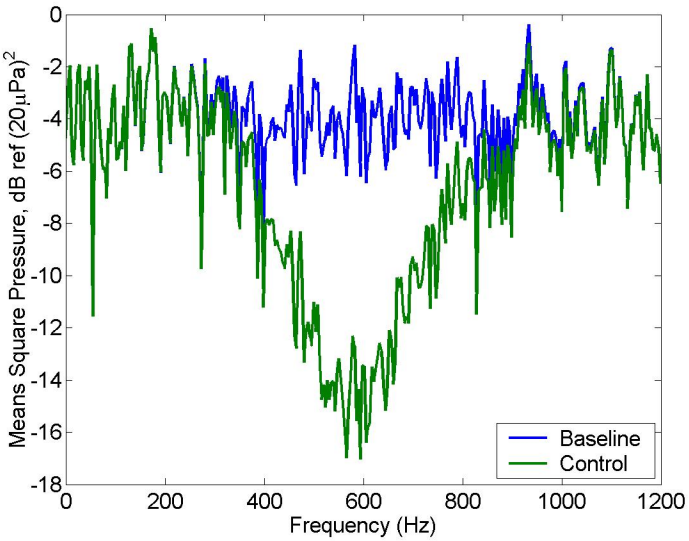

Figure 7.23: Performance achieved at the error location for Case 3.

7.2 Results for Four Channel Control Experiments

In *Experiment Setup* of this chapter, two actuator arrangements were described—the four element and eight element arrangements. In this section, experimental results are presented for experiments using the four element Smart Foam configuration.

The first of the two configurations of this arrangement had the four Smart Foam elements mounted directly to the radiating panel. The second configuration added tuning masses to each element. Tuning masses were used for the reduction of noise due to the relatively low frequency fundamental panel mode (1,1) by means of reactive vibration suppression. Baseline interior noise fields at the observer microphones for the three configurations are shown in Figure 7.24.

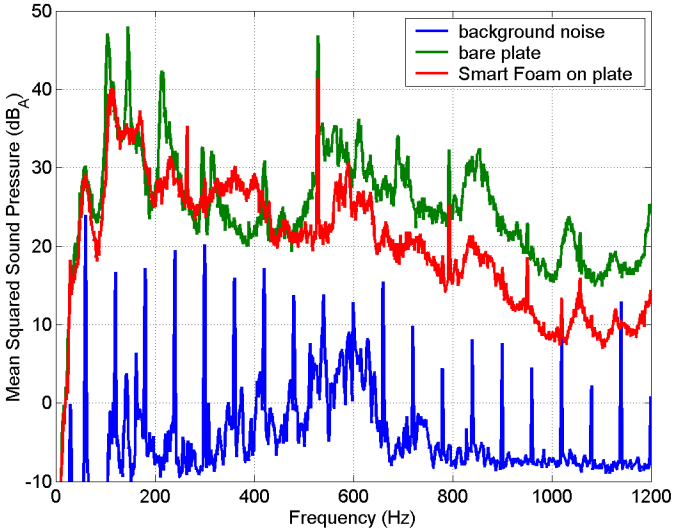

Figure 7.24: Baseline comparison of interior noise field at observer microphones due to background noise, bare plate, and with actuators.

Two controller coupling schemes were investigated. The first involved a fully coupled control strategy where filters were used to describe each reference–to–actuator relation and each actuator–to–error relation. A fully decoupled control strategy was also explored. Here, reference–to–actuator and actuator–to–error relations were considered only for the reference, actuator, and error of a particular channel with no cross–coupling. Fully decoupled control is also referred to as diagonalized control or multiple–SISO (single input, single output) control whereas fully coupled control may be referred to as MIMO (multiple input, multiple output) control. Note that diagonalizing the control scheme may still require performing the same number of computations as the fully coupled or MIMO case since coupling terms are often still computed with their values simply zeroed. However, a truly multiple–SISO scheme

involves several SISO systems with no cross–coupling terms being computed. Although various coupling schemes are possible, partial coupling was not considered within the scope of this research effort.

As was described in Chapter 1, a multiple–SISO (mSISO) control scheme requires significantly fewer computations to estimate the control filters. A significant reduction in the number of computations may be achieved, however control performance will in general be less than for the fully coupled control scheme. For a system having four actuators each with a single reference and a single error, the fully coupled control scheme requires $S+I(S^4+S^3+S^2)$ computations to determine the control filters each having I taps (coefficients) whereas the mSISO case requires only $S(3I+1)$ computations. For a system having four actuators and control filters each having 100 taps, 33,604 computations are required for the fully coupled case whereas only 1201 computations are required for mSISO.

Knowing the control filters, the number of computations required to estimate the control signals is I^2S^5 for MIMO and $SI(I-1)$ for diagonal. For the case above, this would require $1.024(10)^7$ computations for MIMO but only 39,600 computations for mSISO.

Four Element Smart Foam Active Control Experiments

The four element Smart Foam configuration was placed on the plate. Error sensors consisted of either a single microphone or one error array per actuator. For the reference sensors, either a single accelerometer was placed at the center of each actuator, or reference arrays were used.

The first test compared performance of fully coupled and mSISO control. Reference accelerometers were mounted on the plate and centered under their respective actuators. Single error microphones were located over their respective actuators in the observer plane. Although only four of the microphone signals were used for controller error signals, a total of twelve were observed which allowed for the detection of global control performance in the observer plane. In short, this control scenario had the error microphones and observer microphones in the same plane. Figure 7.26 is a plot of results for this case and a summary of results is presented in Table 7.3. Using fully coupled control, 3.2 dB_A of attenuation was achieved over the 400–800 Hz control band and 2.3 dB_A using mSISO control (the equivalent of four SISO control systems). The first harmonic (528 Hz) of the fan blade passage frequency was reduced by 10 dB_A using fully coupled control and by 6 dB_A for diagonalized control.

The error microphones were then dropped to a height of 75 mm (three inches) above the actuators. Four microphones were then placed at the observer locations. For this configuration, three combinations of reference and error signals were observed: single error with single reference, summed error with single reference, and summed error with reference arrays. These three cases were compared to the uncontrolled baseline in Figure 7.27 and in a detailed plot of the control band in Figure 7.28. Over the control band of 400–800 Hz, the single error with single reference case attenuated the mean squared acoustic pressure (P^2_{rms}) by -1.6 dB_A. The summed error with single reference case had an increase in performance of 0.3 dB_A to -1.9 dB_A and using both summed error and summed reference, the control

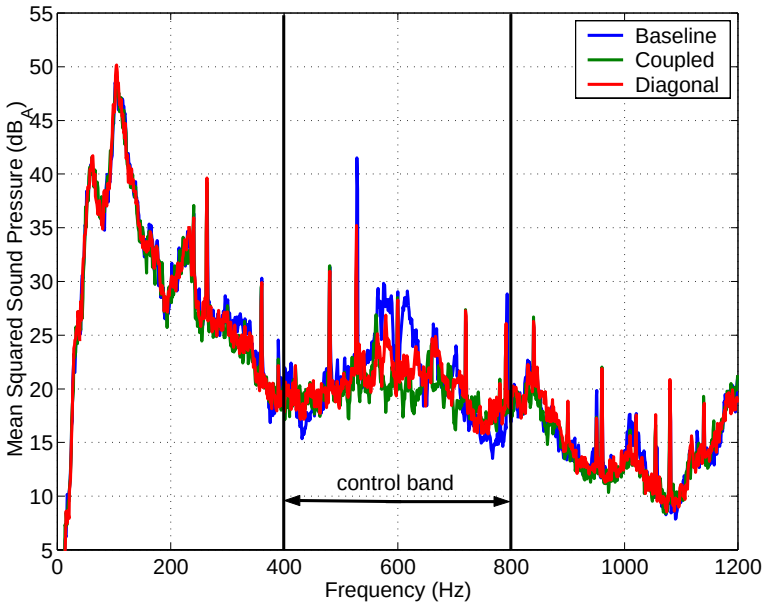

Figure 7.25: Comparison of performance between fully coupled and diagonalized control for 4x4x4 configuration between 400–800 Hz using single references and single errors. Data acquired at error microphones in the observer plane.

performance again increased to -2.3 dB$_A$. These increases in performance indicated the effectiveness of using the summed error signal in the control algorithm when error sensors were placed in the near field. In addition, the use of the discrete reference array also showed promise for control of turbulent boundary layer induced interior noise.

Tests were repeated using two channel (2x2x2) and three channel (3x3x3) control configurations over two control bands: 200–400 Hz and 400–800 Hz.

For the two channel configuration, actuators #2 and #4—the two actuators located in the center—were used. Here, reference accelerometer arrays were placed under each respective actuator and error arrays were located 75 mm above. Two control scenarios were used. The first used summed errors with a single reference per actuator and the second used summed errors with summed references. Band widths investigated were from 200–400 Hz and 400–800 Hz.

For 200–400 Hz control, -0.7 dB$_A$ reduction was achieved at the error microphones using summed errors with a single reference accelerometer per channel and a fully coupled control scheme. Using the reference arrays, the performance was -1.0 dB$_A$. This test configuration was not observed for the mSISO control case. The sum of squared sound pressure at the observer microphones using a single reference accelerometer per actuator was increased by +4.0 dB$_A$ and using the summed reference array it was increased by +3.5 dB$_A$. It should be noted that this increase occurred at varying magnitudes for frequencies above 150 Hz.

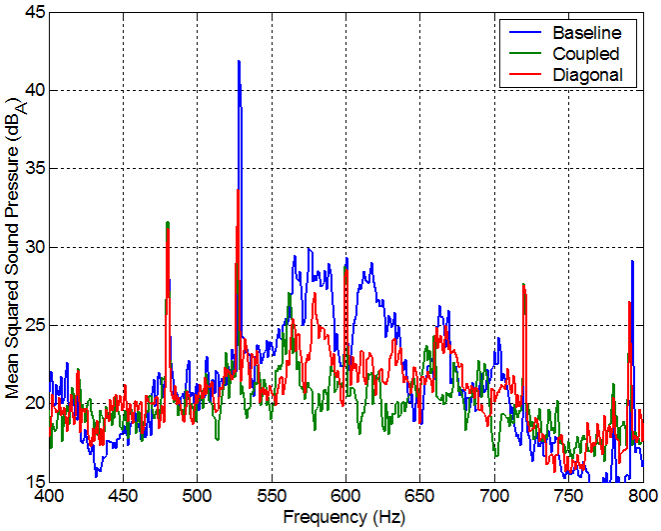

Figure 7.26: Detailed plot of control band for Figure 7.26].

Changing to the 400–800 Hz control band, -0.9 dB$_A$ reduction was achieved at the error microphones using summed errors with a single reference accelerometer per channel and a fully coupled control scheme. Using the accelerometer arrays, the performance was -1.6 dB$_A$. In addition, between 750–850 Hz, there was -1.5 dB$_A$ of control using the single reference and -4.3 dB$_A$ using the summed references. The sum of squared sound pressure at the observer microphones using a single reference accelerometer per actuator was increased by +2.0 dB$_A$ and using the summed reference array it was increased by +0.7 dB$_A$. It should be noted that this increase occurred at varying magnitudes for frequencies above 150 Hz.

The three channel control experiments were then run using the four element Smart Foam configuration shown in Figure 5.7. Here, actuators #2 and #4 were wired in phase

Table 7.2: Summary of results from Figure 7.26. Comparison of four channel control performance using fully coupled or diagonalized control. Single error microphones were placed in the observer plane with single reference accelerometers.

Coupling	**Control Band (Hz)**	**CB Performance** errors(observers)	**Comments**
Fully	400–800	-3.2(-3.2) dB$_A$	-10 dB$_A$ @ 528 Hz
Diagonalized	400–800	-2.3(-2.3) dB$_A$	-10 dB$_A$ @ 528 Hz

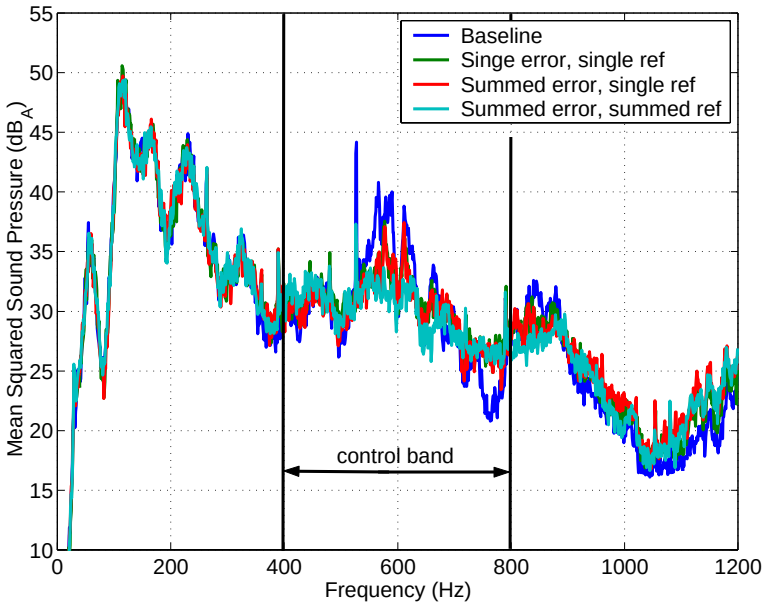

Figure 7.27: Comparison of four channel performance using either single mics or error arrays and either single references or reference arrays. Control was from 400–800 Hz and performance shown was at error mics placed at 100 mm from actuators.

as a single channel—control channel #2. Actuator #1 was used for control channel #1 and actuator #3 for control channel #3. Three error arrays were used and were placed one per actuator at three inches above the Smart Foam. Error array #1 was placed over actuator #1, error array #3 was placed over actuator #3, and centered between the remaining two actuators was placed error array #2. Three reference arrays were arranged directly below the error arrays on the panel. Summed error was used as the error signal for all three–channel controls experiments. The reference signals used were both single reference and summed reference as noted.

Over the 200–400 Hz band, -2.4 dB$_A$ reduction was achieved at the error microphones, using summed errors with a single reference accelerometer per channel and a fully coupled control scheme. Using the reference arrays, the performance was increased by 0.5 dB$_A$ to -2.9 dB$_A$. Diagonalizing this control scheme resulted in -2.3 dB$_A$ of reduction. Note, too, that the peak at 216 Hz was attenuated by -9 dB$_A$ using the coupled/summed references scheme. The other two methods reduced the level of this peak by -8 dB$_A$. Performance at the observer microphones using a single reference accelerometer per actuator was -1.5 dB$_A$. This performance was -1.8 dB$_A$ when the accelerometer array was used. Diagonalizing the controller and using the accelerometer array gave -1.2 dB$_A$ at the observer microphones.

At the error microphones, using the 400–800 Hz control band, a -1.7 dB$_A$ reduction was achieved using summed errors with a single reference accelerometer per channel and a

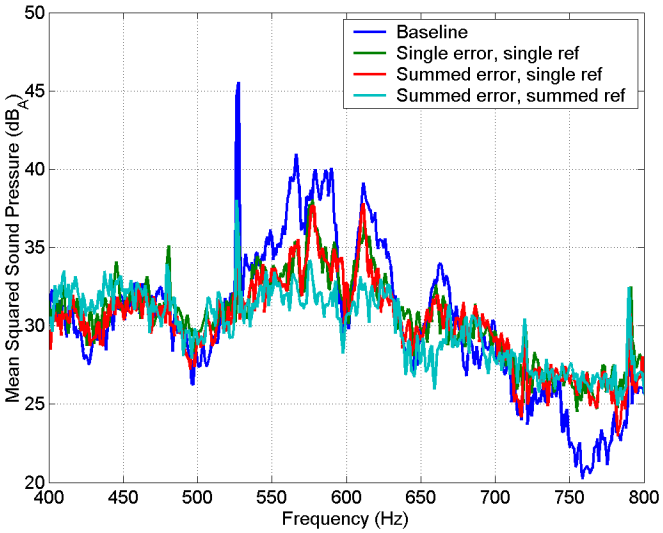

Figure 7.28: Detailed plot of control band for Figure 7.27.

fully coupled control scheme. Using the reference arrays, the performance was -1.5 dB$_A$. Diagonalizing this control scheme resulted in only -0.1 dB$_A$ of reduction. Note, too, that the peak at 216 Hz was shifted to 210 Hz for all three control cases. Performance at the observer microphones using a single reference accelerometer per actuator was -1.0 dB$_A$. This performance dropped to -0.7 dB$_A$ when the accelerometer array was used. Diagonalizing the controller and using the accelerometer array gave -0.5 dB$_A$ at the observer microphones.

Reactive/Active Hybrid Control Using Tuned Smart Foam

The four element Smart Foam configuration was then used for reactive/active hybrid control tests. Actuators #2 and #4 were again wired in phase and used for control channel #2. Control channels #1 and #3 used actuators #1 and #3, respectively. All four Smart Foam elements were tuned to 112 Hz using 1.6 mm (0.063″) thick aluminum plates as described in Chapter 5—Actuators. Tuning masses were mounted using spray glue. Since the 25 cm by 51 cm fuselage panel had the same thickness as the tuning mass layers, the increase in weight (or mass) is simply the ratio of the total tuning mass area to the area of the fuselage panel. This application resulted in a weight increase of 41%. The autospectrum, given a random acceleration input to the tuning mass, of one of the tuned Smart Foam elements is shown in Figure 7.29.

The performance of the reactive treatment is observed in Figure 7.30 with a detailed plot of the vicinity of the (1,1) peak shown in Figure 7.31. Here, reactive/passive control was compared to the passive (foam only) performance. The target frequency, 112 Hz, had

Table 7.3: Summary of results for sound pressure minimization using near field error sensing.

Coupling	**Control Band (Hz)**	**CB Performance** errors(observers)	**Reference**	**Error**	**Comments**
two channel control					
MIMO	200–400	-0.7(+42.0) dB_A	array	single	
MIMO	200–400	-1.0(+3.5) dB_A	array	array	
MIMO	400–800	-0.9(+2.0) dB_A	array	single	
MIMO	400–800	-1.6(+0.7) dB_A	array	array	
three channel control					
MIMO	200–400	-2.4(-1.5) dB_A	array	single	-8 dB_A @ 216 Hz
MIMO	200–400	-2.9(-1.8) dB_A	array	array	-9 dB_A @ 216 Hz
mSISO	200–400	-2.3(-1.2) dB_A	array	array	-8 dB_A @ 216 Hz
MIMO	400–800	-1.7(-1.0) dB_A	array	single	
MIMO	400–800	-1.5(-0.7) dB_A	array	array	
mSISO	400–800	-0.1(-0.5) dB_A	array	array	
four channel control					
MIMO	400–800	-1.6(n/a) dB_A	single	single	-5 dB_A, 550–680 Hz
MIMO	400–800	-1.9(n/a) dB_A	single	array	-5 dB_A, 550–680 Hz
MIMO	400–800	-2.3(n/a) dB_A	array	array	up to -8 dB_A, 550–680 Hz

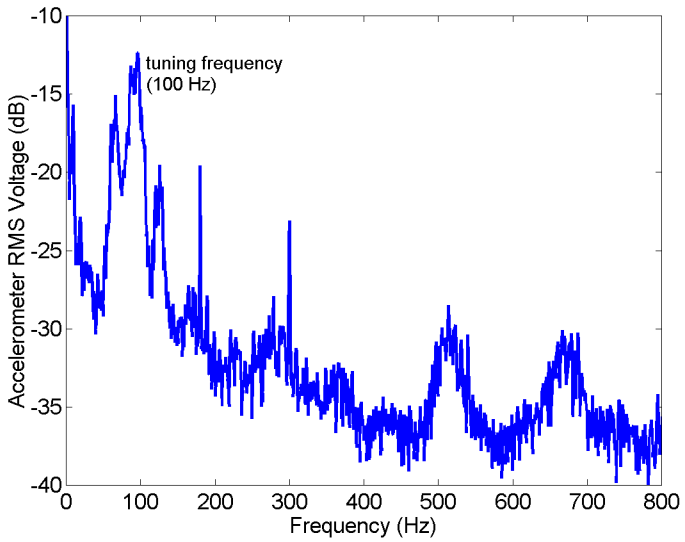

Figure 7.29: Autospectrum of a 3″ by 7 ″ smart foam element tuned to the fuselage panel (1,1) mode (actuator #3 shown).

a peak attenuation of -6.0 dB_A (-6.0 dB_A) at the error (observer) microphones along with an average attenuation of -3.1 dB_A (-3.9 dB_A) over a 25 Hz band centered about the target frequency. In addition, over the 0–1200 Hz band, the reactive/passive treatment had an average attenuation of -1.2 dB_A (-2.5 dB_A).

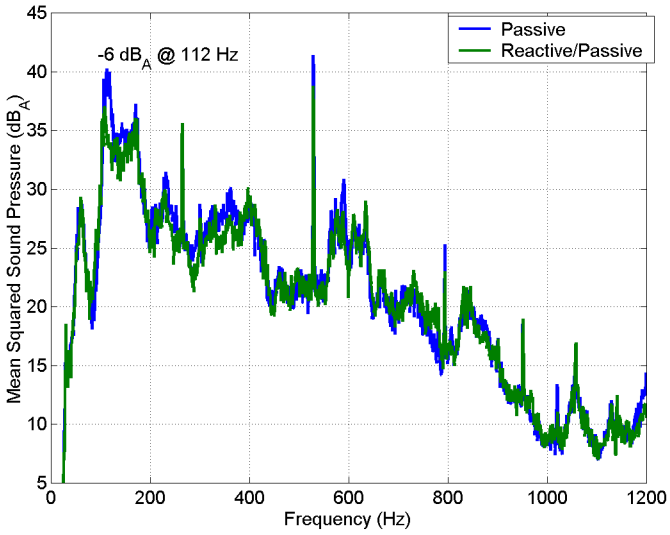

Figure 7.30: Comparison of Reactive/Passive and Passive control techniques. Smart Foam elements were tuned to the (1,1) panel vibration mode.

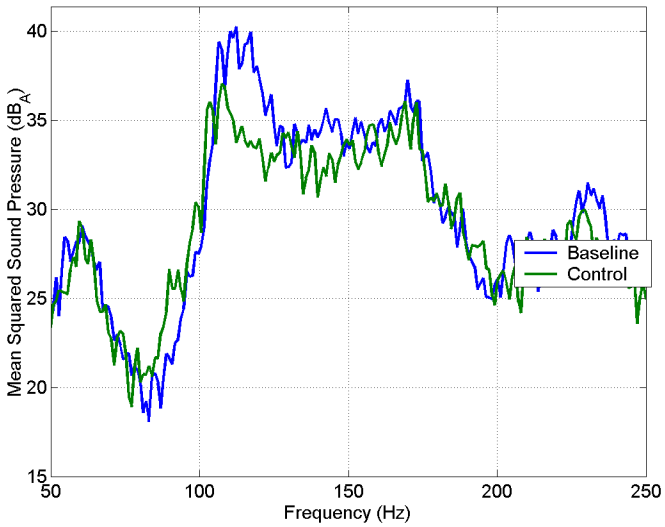

Figure 7.31: Detailed plot of Figure 7.30.

Active control was then performed both with and without the reactive treatment. In an attempt to increase the low frequency performance, the band of active control was set from 100–200 Hz. Reactive/passive control gave -1.8 dB_A (-3.2 dB_A) from 100–200 Hz and -1.2 dB_A (-2.5 dB_A) from 0–1200 Hz. Using active/passive control (no tuning masses) gave -0.8 dB_A (-1.3 dB_A) from 100–200 Hz and +1.9 dB_A (-0.7 dB_A) from 0–1200 Hz was realized. Note, that at the error microphones, there was a significant increase in the mean squared sound pressure at frequencies above 280 Hz. Combining both reactive and active control strategies with the passive treatment resulted in improved performance over both observed bands. From 100–200 Hz, the combined control performance was -1.9 dB_A (-3.3 dB_A) and from 0–1200 Hz it was -1.4 dB_A (-2.5 dB_A).

The control band was then changed to 200–400 Hz. Over this control band, the reactive treatment resulted in an average attenuation of -1.0 dB_A (-2.2 dB_A) and -1.2 dB_A (-2.5 dB_A) from 0–1200 Hz. Active control over the same bands gave -0.3 dB_A (-1.0 dB_A) and -0.4 dB_A (-1.0 dB_A), respectively. Using the combined RAP control gave the best performance with -1.4 dB_A (-2.3 dB_A) over the control band and -1.7 dB_A (-2.6 dB_A) from 0–1200 Hz. The reactive control performance at the tuning frequency was the same as for the previous case.

The tests were then repeated using a control band of 400–800 Hz, first with a coupled (Figure 7.32) controller and then using a diagonalized control scheme. For the coupled case, active control resulted in -2.8 dB_A (-1.8 dB_A) over the active control band, -0.7 dB_A (-0.7 dB_A) between 100–125 Hz, and -0.8 dB_A (-0.6 dB_A) from 0–1200 Hz. Performance was improved using the RAP scheme resulting in -3.0 dB_A (-2.7 dB_A) over the control band, -3.4 dB_A (-4.3 dB_A) between 100–125 Hz, and -1.8 dB_A (-2.7 dB_A) from 0–1200 Hz.

For the diagonalized case, active control resulted in -1.1 dB_A (-0.8 dB_A) over the control band, -0.8 dB_A (-0.8 dB_A) between 100–125 Hz, and -0.6 dB_A (-0.6 dB_A) from 0–1200 Hz. Performance was improved using the RAP scheme resulting in -1.8 dB_A (-2.2 dB_A) over the control band, -3.3 dB_A (-4.1 dB_A) between 100–125 Hz, and -1.7 dB_A (-2.7 dB_A) from 0–1200 Hz.

Table 7.4 suggests that this reactive control strategy is capable of narrow band noise reduction in the vicinity of the tuning frequency. In addition, it was shown that the tuning masses do not impede the active performance at higher frequencies, however, the tuning masses did result in further reduction at higher frequencies. This unexpected result is suspected to be due to higher order vibration modes of the tuned Smart Foam elements.

Table 7.4: Summary of results for sound pressure minimization—three channel control with actuators tuned to (1,1) panel mode. Actuators were mounted directly to the panel. Reference arrays were used along with error arrays placed at 100 mm from the tops of the actuators. For control schemes, R = reactive (tuning masses), P = passive (foam only), and A = active control.

Coupling	**Control Band (Hz)**	**Control Scheme**	**CB Performance** errors(observers)	**Comments**
n/a	RP	n/a	n/a	6 dB_A (6 dB_A) at tuning frequency with 3.1 dB_A (3.9 dB_A) between 100–125 Hz. Figure 7.30
n/a	100–200	RP	-1.8(-3.2) dB_A	
MIMO	100–200	AP	-0.8(-1.3) dB_A	
MIMO	100–200	RAP	-1.9(-3.3) dB_A	
n/a	200–400	RP	-1.0(-2.2) dB_A	
MIMO	200–400	AP	-0.3(-1.0) dB_A	
MIMO	200–400	RAP	-1.4(-2.3) dB_A	
n/a	400–800	RP	-0.5(-1.6) dB_A	Figure 7.32
MIMO	400–800	AP	-2.8(-1.8) dB_A	Figure 7.32
MIMO	400–800	RAP	-3.0(-2.7) dB_A	-3.4(-4.3) dB_A @ 100–125 Hz, Figure 7.32
mSISO	400–800	AP	-1.1(-0.8) dB_A	
mSISO	400–800	RAP	-1.8(-2.2) dB_A	-3.3(-4.1) dB_A @ 100–125 Hz

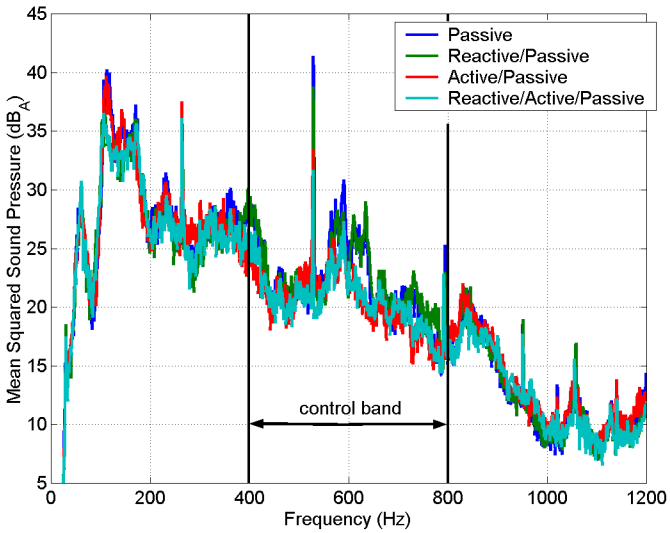

Figure 7.32: Reactive/Active/Passive attenuation results using a coupled three channel control system.

7.3 Results for Eight Channel Control Simulations

The eight actuator configuration is designed based on three parameters to more effectively control the turbulent boundary layer induced interior noise. First, the configuration was designed according to studies performed in Chapter 3 to have a sufficient number of reference locations. Second, the configuration was designed using spatial filters as one of the means used for determining the reference signal. Third, by having a square footprint, reference and error sensing could be conducted over an area better coordinated with the footprint of the respective actuator. This allowed the secondary signals to be generated based on a more accurate knowledge of the structure vibration in that vicinity. As dictated by the system design, eight channels of control were required thus requiring control simulations in place of experiments for reasons discussed previously.

Eight Channel Control Simulation Results

Control simulations were run using a control band of 400–800 Hz with the control performance monitored over the control band, from 50–1000 Hz and from 480–750 Hz. Performance within the 480–750 Hz band is presented to emphasize the achievable performance. As estimated in Chapter 6—Coherence and Causality Studies, the controller had six samples of delay given a sample rate of 4000 Hz. The controller delay was determined to be greater than the acoustic delay between the reference and the error locations and therefore the system was determined to be acausal. To identify the maximum performance achievable (least degree of acausality) given the 4000 Hz sample rate, control simulations were repeated using a delay of only one sample—the minimum delay achievable on an actual controller.

Simulation results are presented in the following two tables. Table 7.5 presents results using a controller having six samples of delay with results from simulations using only a single sample of delay presented in Table 7.6. MIMO and mSISO simulations were performed using either a single accelerometer or a PVDF reference sensor per actuator. An additional MIMO case used two references per actuator with a single sample of delay.

Table 7.5: Summary of control simulation performance given six samples of controller delay using a 400–800 Hz control band.

Reference	**Coupling**	**Performance at Errors (Observers)**		
		400–800 Hz	480–750 Hz	50–1000 Hz
1 Accel	MIMO	-2.2 dB_A (-0.9 dB_A)	-3.0 dB_A (-1.5 dB_A)	-1.0 dB_A (-0.2 dB_A)
1 Accel	mSISO	-0.2 dB_A (+0.2 dB_A)	-0.4 dB_A (+0.1 dB_A)	0.0 dB_A (+0.5 dB_A)
PVDF	MIMO	-1.5 dB_A (+0.3 dB_A)	-1.6 dB_A (-0.1 dB_A)	-0.9 dB_A (+52 dB_A)
PVDF	mSISO	0.0 dB_A (+0.9 dB_A)	0.0 dB_A (+0.7 dB_A)	-0.1 dB_A (+52 dB_A)

Table 7.6: Summary of control simulation performance given the minimum of one sample of controller delay using a 400–800 Hz control band.

Reference	**Coupling**	**Performance at Errors (Observers)**		
		400–800 Hz	480–750 Hz	50–1000 Hz
1 Accel	MIMO	-2.4 dB_A (-1.1 dB_A)	-3.6 dB_A (-1.9 dB_A)	-0.8 dB_A (0.0 dB_A)
1 Accel	mSISO	-0.5 dB_A (-0.1 dB_A)	-1.2 dB_A (-0.6 dB_A)	+0.1 dB_A (+0.5 dB_A)
PVDF	MIMO	-1.9 dB_A (-1.2 dB_A)	-2.2 dB_A (-1.2 dB_A)	-1.0 dB_A (-0.3 dB_A)
PVDF	mSISO	-0.2 dB_A (+0.7 dB_A)	-0.2 dB_A (+0.5 dB_A)	-0.1 dB_A (+52 dB_A)
2 Accels	MIMO	-3.1 dB_A (-1.4 dB_A)	-4.8 dB_A (-2.6 dB_A)	-1.2 dB_A (-0.2 dB_A)

Control simulation results are further discussed. Results obtained using six samples of delay are presented first followed by results obtained using one sample of delay.

Results summarized in Table 7.5 are presented here for the six sample delay simulations using a control band of 400–800 Hz. MIMO control using accelerometer references achieved a -2.2 dB_A reduction at the error sensors within the control band and is plotted in Figure 7.33 with a detailed plot of the control band in Figure 7.34. Within the 480–750 Hz band, performance at the error sensors was increased to -3.0 dB_A and was -1.0 dB_A over 50–1000 Hz.

Performance within the observer plane is plotted in Figure 7.35, with a detailed plot of the control band in Figure 7.36, and was greatest from 480–750 Hz having an attenuation of -1.5 dB_A. Observer plane performance was -0.9 dB_A within the control band and only -0.2 dB_A from 50–1000 Hz. However, from 560–640 Hz, -5.0 dB_A reduction was achieved at the observer plane with peak reductions up to -12 dB_A.

Decoupling the control system, the control performance decreased. Although results presented in Table 7.5 suggest minimal performance, by observation of Figure 7.37 it is shown that narrow band performance up to -6 dB_A was achieved. Performance in the observer plane was also poor however, -1.6 dB_A was achieved from 560–640 Hz with peak reductions of up to -6 dB_A as shown in Figure 7.39. Detailed plots of the control band are shown in Figure 7.38 and Figure 7.40, respectively.

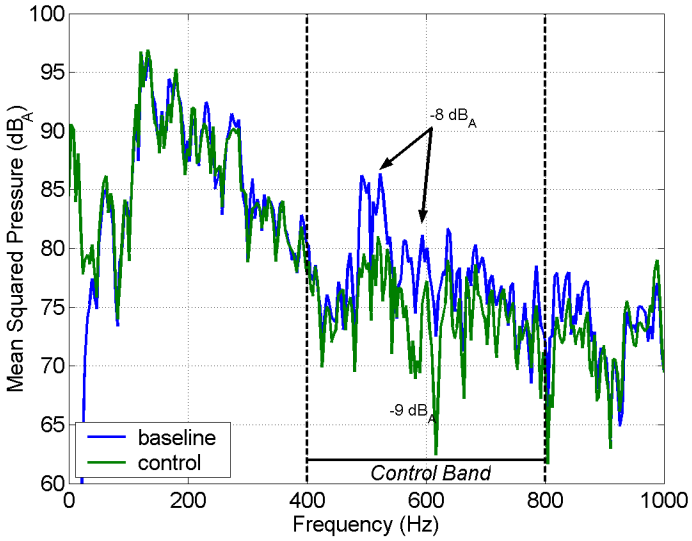

Figure 7.33: Control simulation performance *at the error sensors* using accelerometer references with MIMO coupling and six samples of delay.

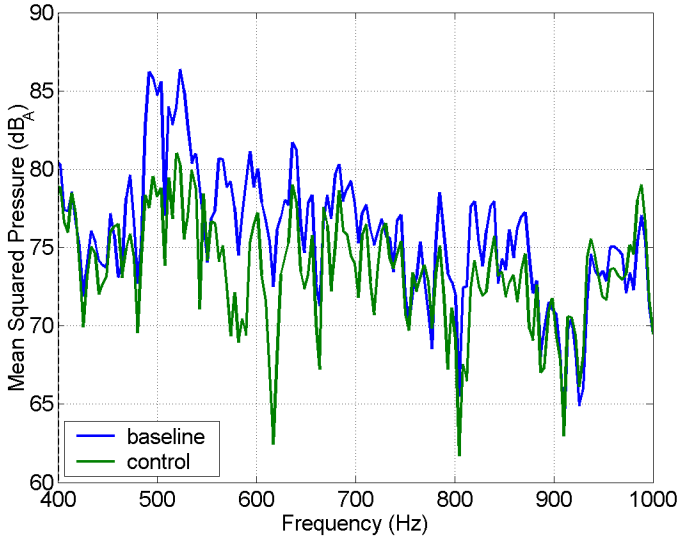

Figure 7.34: Control band detailed plot of Figure 7.33.

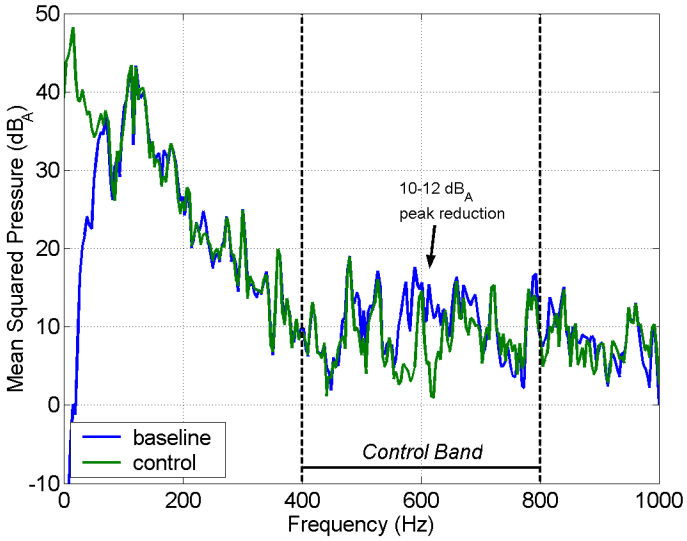

Figure 7.35: Control simulation performance *in the observer plane* using accelerometer references with MIMO coupling and six samples of delay.

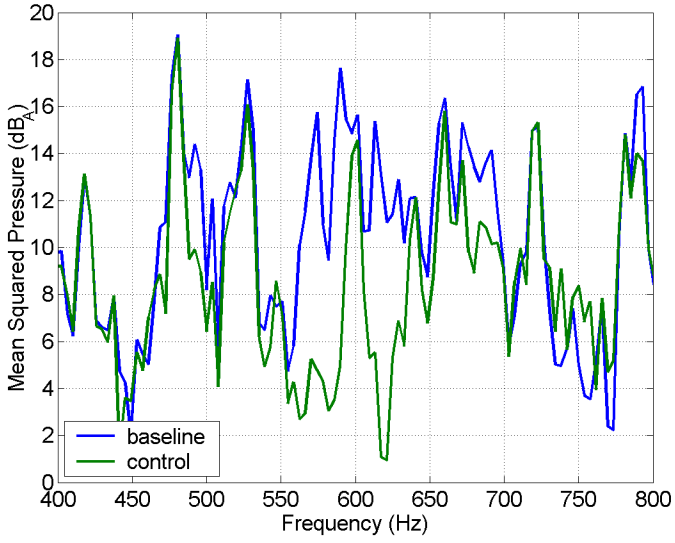

Figure 7.36: Control band detailed plot of Figure 7.35.

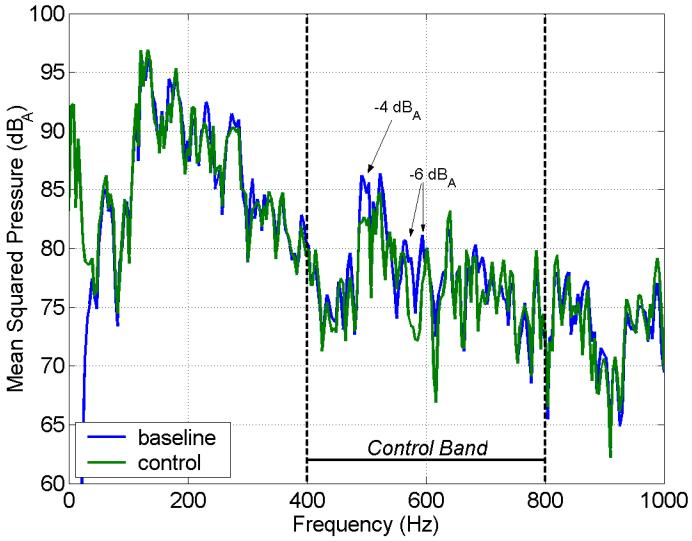

Figure 7.37: Control simulation performance *at the error sensors* using accelerometer references with mSISO coupling and six samples of delay.

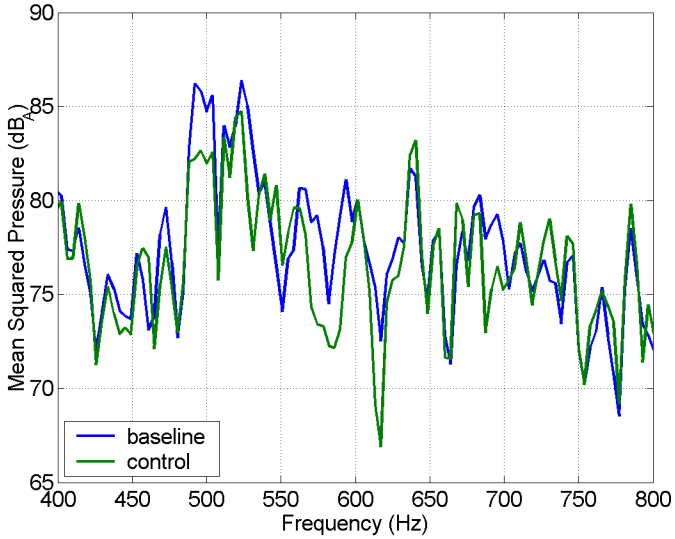

Figure 7.38: Control band detailed plot of Figure 7.37.

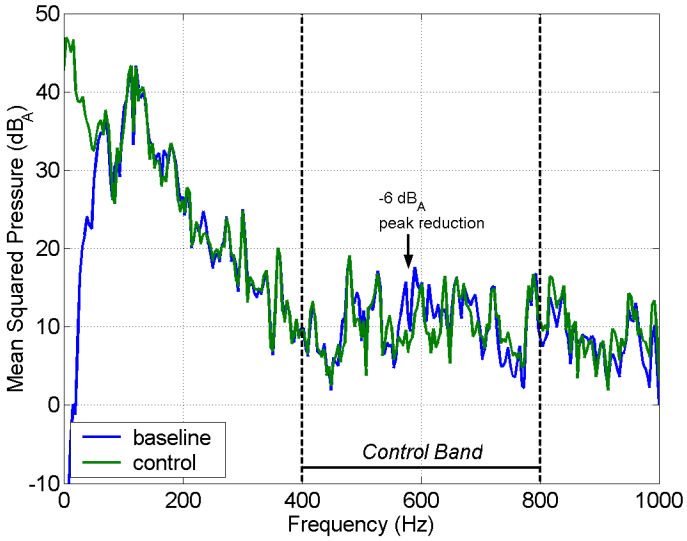

Figure 7.39: Control simulation performance *in the observer plane* using accelerometer references with mSISO coupling and six samples of delay.

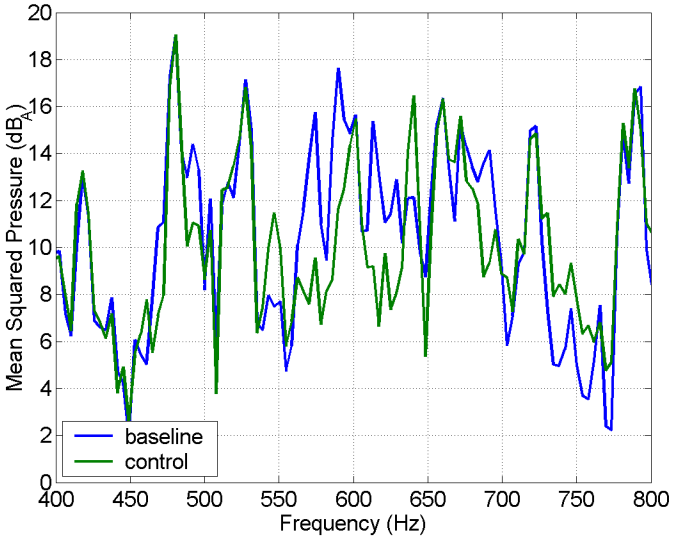

Figure 7.40: Control band detailed plot of Figure 7.39.

Performance using PVDF references was on par with performance obtained using accelerometer references. MIMO control using PVDF references achieved -1.5 dB_A reduction at the error sensors within the control band with up to -8 dB_A peak attenuation as shown in Figure 7.41 with a detailed plot of the control band shown in Figure 7.42. Within the 480–750 Hz band, performance at the error sensors increased marginally to -1.6 dB_A and was -0.9 dB_A over 50–1000 Hz. In the observer plane, negligible mean performance was achieved, however narrow band performance within the control band was as much as -12 dB_A. Mean square pressure increased outside the control band as shown in Figure 7.43 with a detailed control band plot shown in Figure 7.44. Decoupling the control system resulted in negligible control performance.

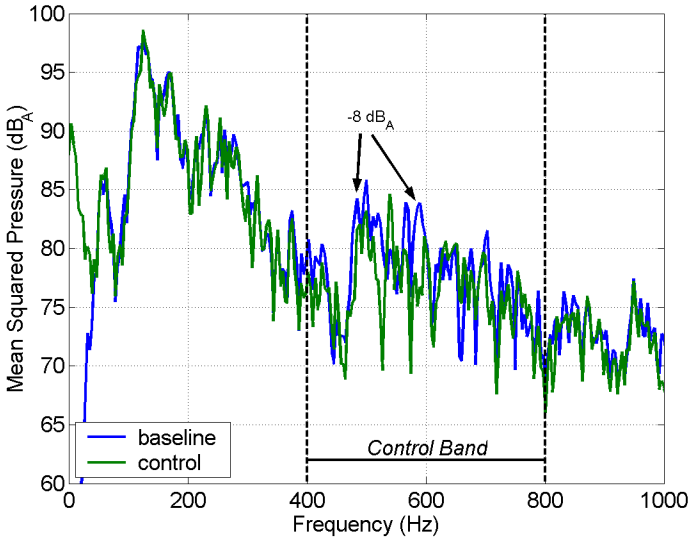

Figure 7.41: Control simulation performance *at the error sensors* using PVDF references with MIMO coupling and six samples of delay.

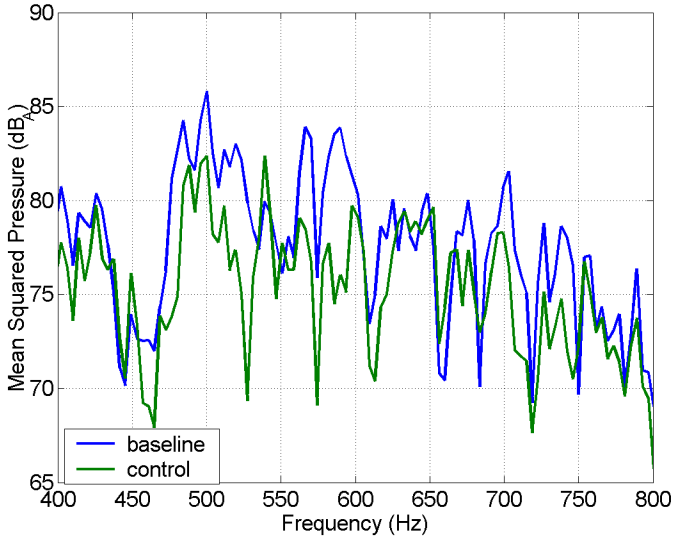

Figure 7.42: Detailed control band plot of Figure 7.41.

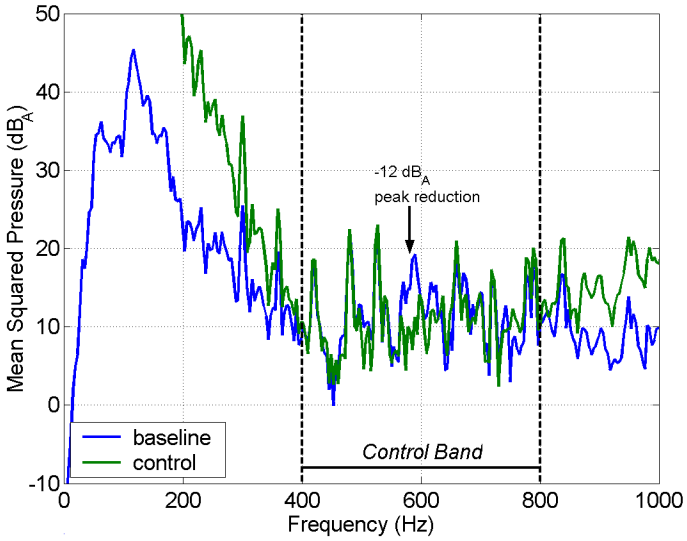

Figure 7.43: Control simulation performance *in the observer plane* using PVDF references with MIMO coupling and six samples of delay.

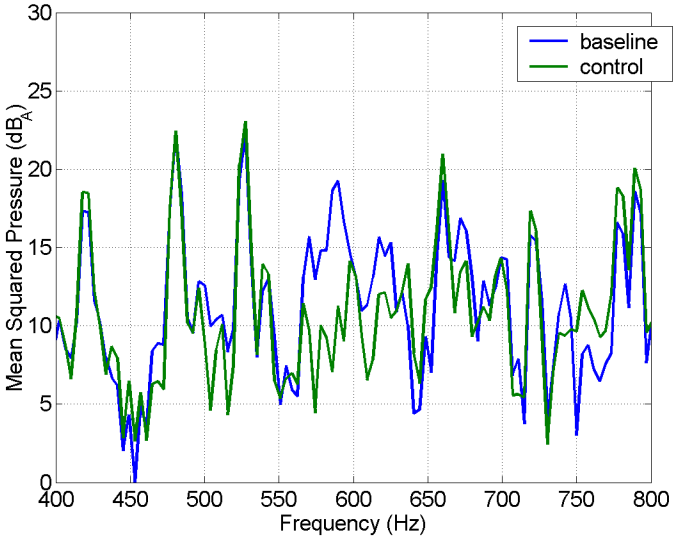

Figure 7.44: Detailed control band plot of Figure 7.43.

Control simulations were then repeated using only one sample of delay which is the minimum delay that a real digital control system may have. Reducing the controller delay would reduce the degree of acausality and therefore should result in better control performance. Results presented here are summarized in Table 7.6 and should be compared with results presented in Table 7.5. Observation of these two tables indicates that the more causal controller does indeed result in better control performance.

MIMO control using accelerometer references resulted in -2.4 dB_A within the 400–800 Hz control band and -3.6 dB_A from 480–750 Hz at the error sensors. Peak performance of up to -9 dB_A was achieved at the error sensors with an average attenuation of -4.8 dB_A from 490–630 Hz. These results are presented in Figure 7.45 and in a detailed plot of the control band in Figure 7.46.

Performance in the observer plane for these two bands was -1.1 dB_A and -1.9 dB_A, respectively. However, from 560–630 Hz, an average of -6.0 dB_A reduction was achieved with peak performance of up to -12 dB_A as shown in Figure 7.47 and in a detailed plot of the control band in Figure 7.48.

Decoupling the controller resulted in loss of performance. Using accelerometer references, only -1.2 dB_A was achieved from 480–750 Hz at the error sensors and only -0.6 dB_A in the observer plane. However, reduction of -2.2 dB_A was achieved at the error sensors from 490–630 Hz with peak attenuation of up to 6 dB_A as shown in Figure 7.49 with a detailed plot of the control band shown in Figure 7.50. Further, -2.2 dB_A was achieved in the observer plane from 560–700 Hz with peak reductions of up to -8 dB_A as shown in Figure 7.51 with a detailed control band plot shown in Figure 7.52.

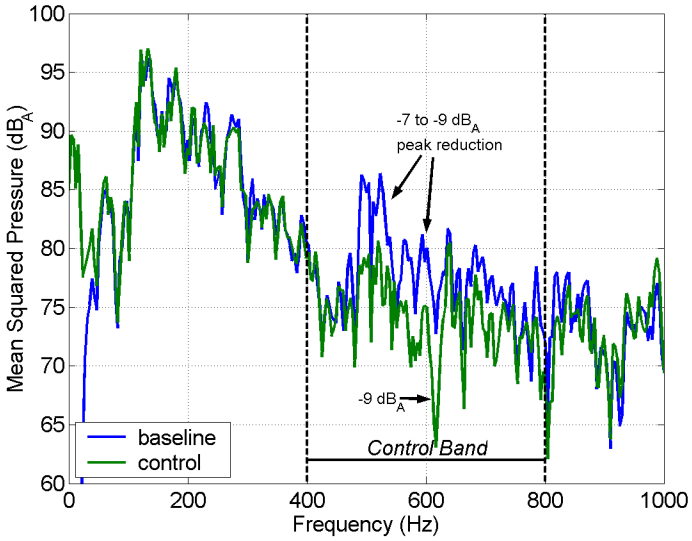

Figure 7.45: Control simulation performance *at the error sensors* using accelerometer references with MIMO coupling and one sample of delay.

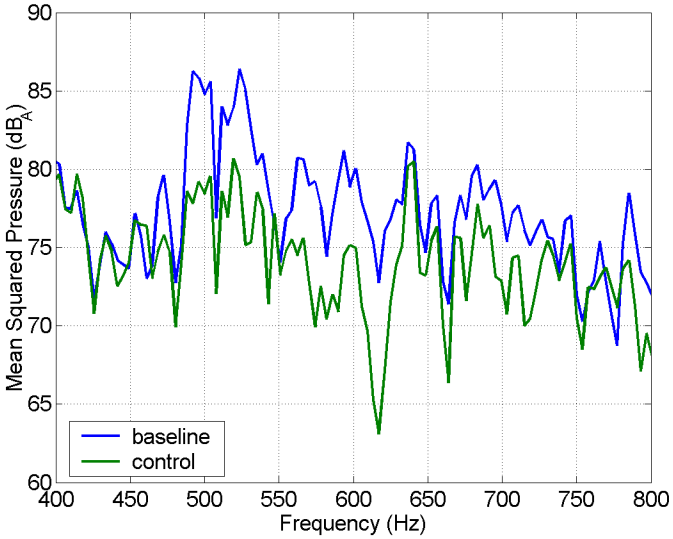

Figure 7.46: Detailed control band plot of Figure 7.45.

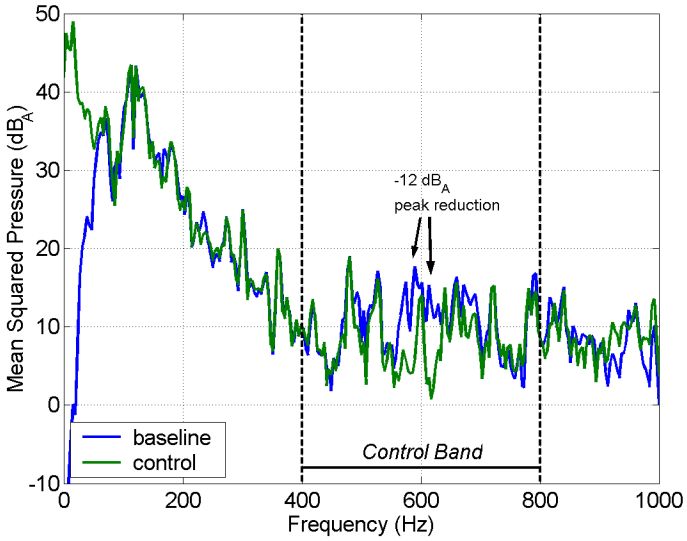

Figure 7.47: Control simulation performance *in the observer plane* using accelerometer references with MIMO coupling and one sample of delay.

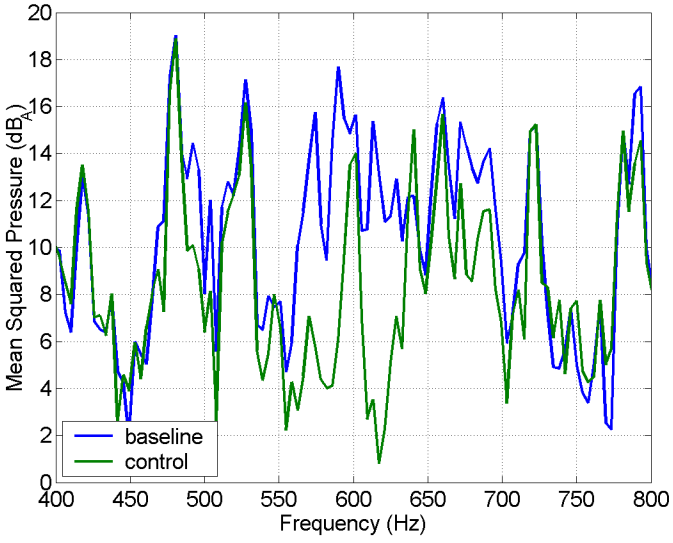

Figure 7.48: Detailed control band plot of Figure 7.47.

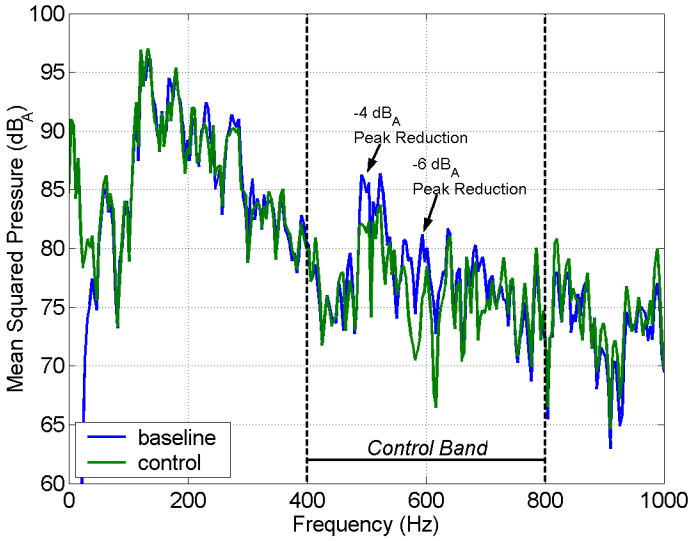

Figure 7.49: Control simulation performance *at the error sensors* using accelerometer references with mSISO coupling and one sample of delay.

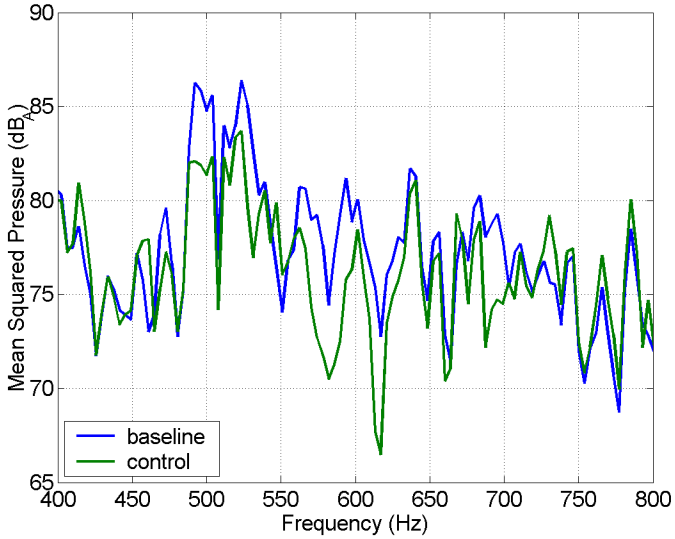

Figure 7.50: Detailed control band plot of Figure 7.50.

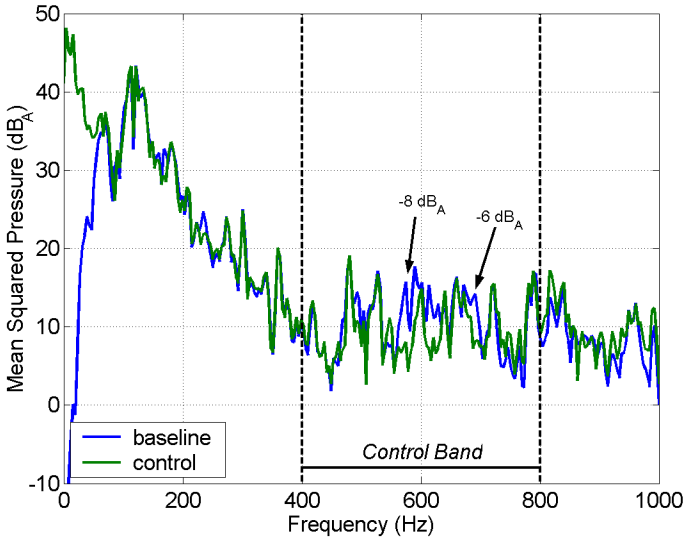

Figure 7.51: Control simulation performance *in the observer plane* using accelerometer references with mSISO coupling and one sample of delay.

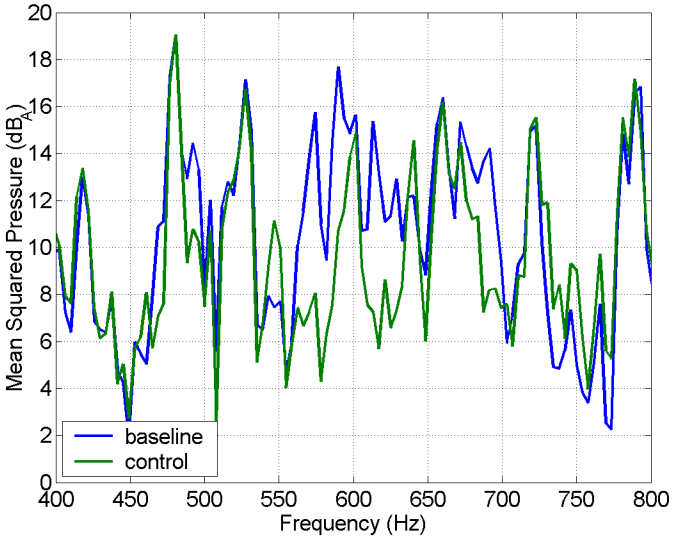

Figure 7.52: Detailed control band plot of Figure 7.52.

The use of PVDF references resulted in less performance than simulations using a single accelerometer reference per actuator. However, the performance achieved using the PVDF reference sensors was increased given only one, rather than six, samples of delay. The MIMO configuration, shown in Figure 7.53 resulted in -1.9 dB_A within the control band and -2.2 dB_A from 480–750 Hz at the error sensors. A peak attenuation of -4 dB_A was achieved at the error sensors.

Performance in the observer plane was -1.2 dB_A for the control band and from 480–750 Hz and is shown in Figure 7.54. Peak attenuation in the observer plane of up to -9 dB_A was achieved with -3.9 dB_A achieved from 570–630 Hz.

Decoupling the controller results in negligible broad band performance both at the error sensors and in the observer plane. However, peak performance of up to -4 dB_A was achieved at the error sensors as shown in Figure 7.55. Outside the control band, performance within the observer plane was unstable and suffered from an excessive increase of mean square pressure as shown in Figure 7.56.

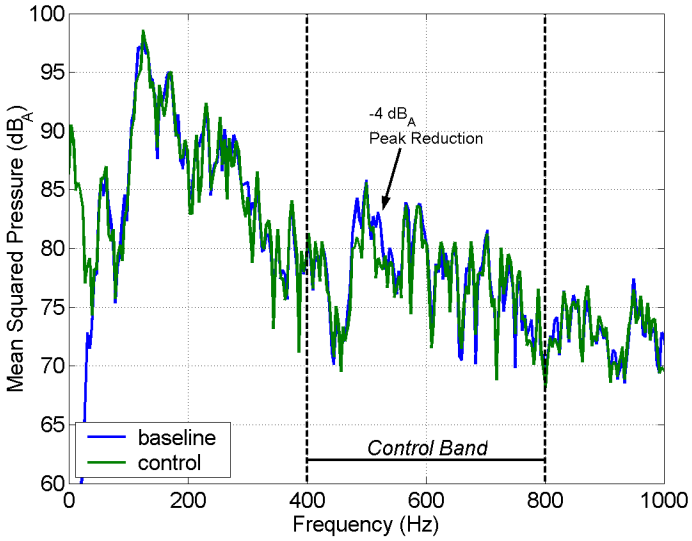

Figure 7.53: Control simulation performance *at the error sensors* using PVDF references with MIMO coupling and one sample of delay.

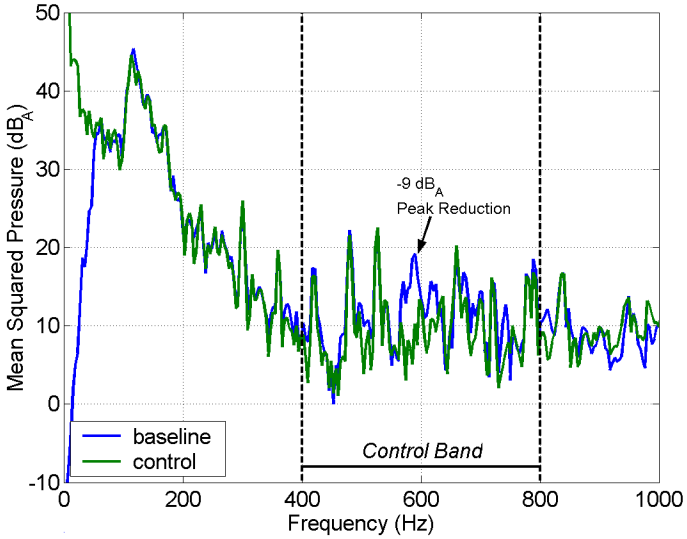

Figure 7.54: Control simulation performance *in the observer plane* using PVDF references with MIMO coupling and one sample of delay.

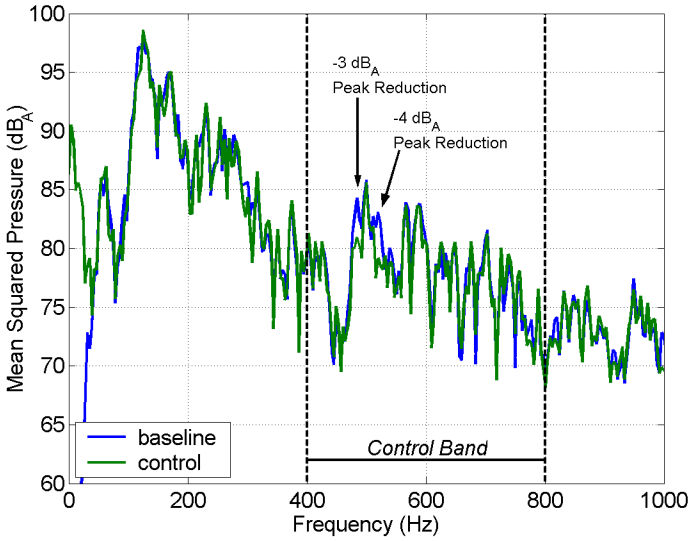

Figure 7.55: Control simulation performance *at the error sensors* using PVDF references with mSISO coupling and one sample of delay.

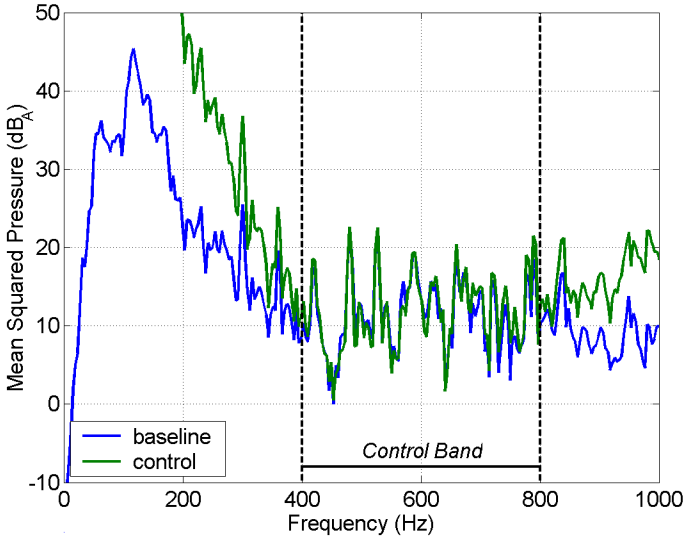

Figure 7.56: Control simulation performance *in the observer plane* using PVDF references with mSISO coupling and one sample of delay.

Based on multiple coherence studies performed in Chapter 6, simulations were performed using two independent (not summed) accelerometer references per actuator. These runs were performed using MIMO coupling only. Since *lmsfilterx* is not capable of partial coupling configurations, the multiple MISO approach could not be explored. However, the use of more than one reference per actuator was beyond the intended scope of this research effort and is presented here only to emphasize the benefits of increasing the coherence between the reference and error signals.

As shown in Table 7.6, the use of multiple references per actuator increases the control performance both at the error sensors and in the observer plane. Figure 7.57 shows the performance achieved at the error sensors with performance in the observer plane shown in Figure 7.59.

Within the control band, the two reference per actuator case resulted in -3.1 dB_A at the error sensors, a 0.7 dB_A performance improvement relative to the single reference case. Likewise, a 1.2 dB_A improvement was achieved from 480–750 Hz giving -4.8 dB_A of attenuation at the error sensors. As shown in Figure 7.57, and in a detailed plot of the control band in Figure 7.58, -12 dB_A peak attenuation was achieved.

Performance was also improved in the observer plane. Within the control band, performance in the observer plane was improved by 0.3 dB_A resulting in a -1.4 dB_A reduction. Further, a 0.7 dB_A improvement occurred in the 480–750 Hz band resulting in a -2.6 dB_A reduction. Peak attenuation in the observer plane of up to -12 dB_A was achieved as shown in Figure 7.59 and in a detailed plot of the control band in Figure 7.60.

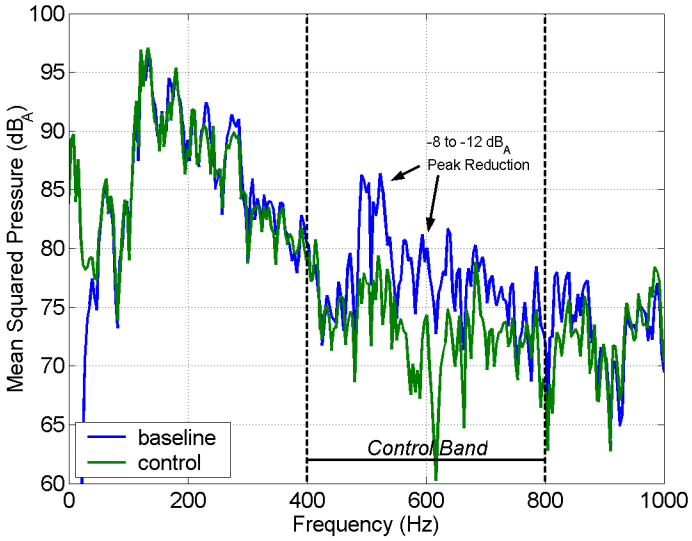

Figure 7.57: Control simulation performance *at the error sensors* using two accelerometer references per actuator with MIMO coupling and one sample of delay.

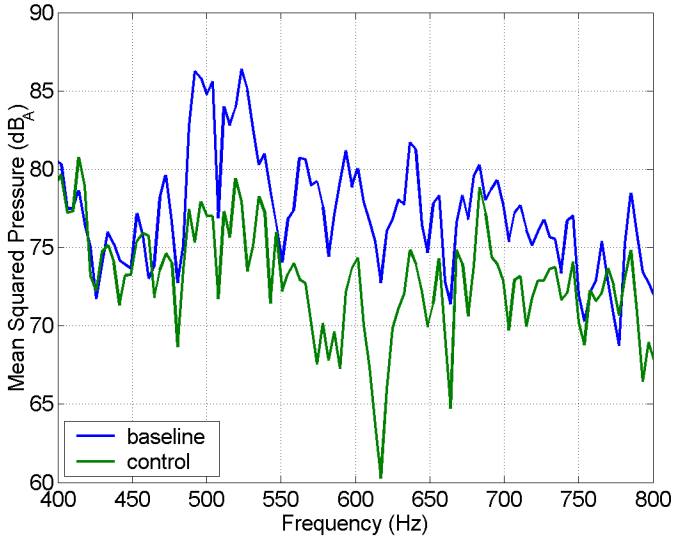

Figure 7.58: Detailed plot of control band for Figure 7.57.

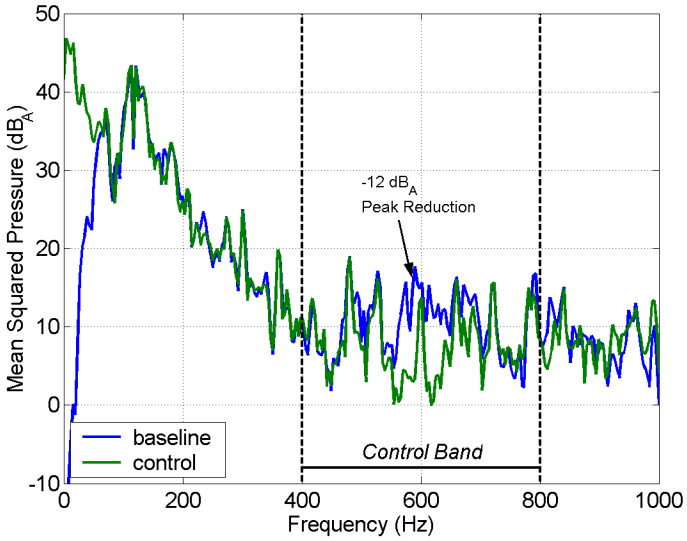

Figure 7.59: Control simulation performance *in the observer plane* using two accelerometer references with MIMO coupling and one sample of delay.

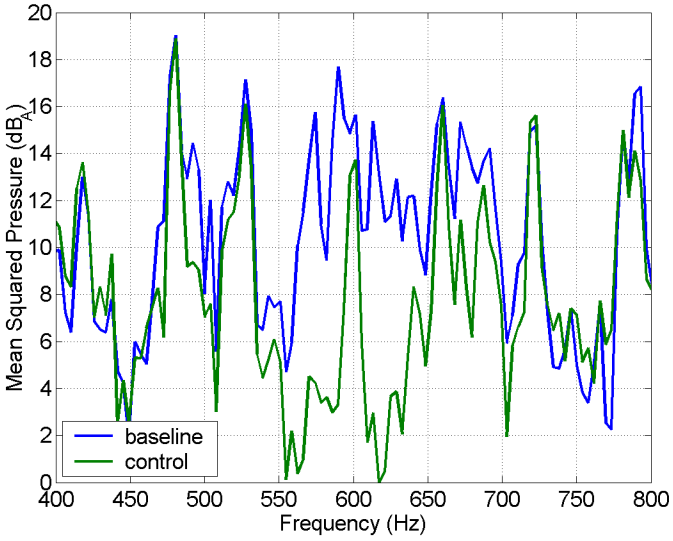

Figure 7.60: Detailed plot of control band for Figure 7.59.

7.4 Summary of Results

Active minimization of mean square sound pressure using Smart Foam was achieved at the error sensors and within the observer plane. Far field control was achieved using MIMO control and it was further shown that diagonalized or mSISO control may be implemented with success.

Four reference sensing methods were explored. The first method used one accelerometer mounted on the vibrating plate located under each respective actuator. In an effort to improve the relation between structure vibration and the interior noise field two methods of spatial filtering were explored. These methods allowed plate vibration to be filtered allowing only those vibrations in the band of interest to be sensed and therefore allow the control effort to be focussed where desired. Although these methods did allow for a limited degree of filtering they did not improve the coherence between the structure vibration and the interior noise field. Spatial filtering offered, at best, marginal improvement (fraction of a dB) in control performance when compared to using single, point measurements for reference signals. Overall, the use of spatial filters did not offer significant improvement in control performance. Of the reference sensing schemes studies, the best performance was achieved using two references per actuator.

Active control using microphone arrays allowed the placement of error sensors closer to the radiating structure. Control was achieved at error sensor arrays placed as close as 10 cm above the actuators. Placement closer to the Smart Foam elements resulted in significantly lesser control.

Three channel control experiments using the four element Smart Foam configuration with MIMO control from 400–800 Hz and near field error sensing resulted in -1.7 dB_A at the error sensors. In the observer plane -1.0 dB_A was achieved. Diagonalizing the controller resulted in negligible performance. However, using a 200–400 Hz control band, MIMO control resulted -2.9 dB_A at the near field error sensors and -1.8 dB_A in the observer plane. Using the mSISO approach, -2.3 dB_A and -1.2 dB_A was achieved at the error sensors and in the observer plane, respectively. Therefore, it has been shown that global control may be achieved using near field error sensing.

Using the eight Smart Foam element configuration with a 400–800 Hz control band resulted in better MIMO performance than that achieved using the four element configuration. Simulations using six samples of delay at 4000 Hz—the delay determined in the controller—resulted in -2.2 dB_A at the error sensors and -0.9 dB_A in the observer plane for MIMO control. From 480–750 Hz performance at the error sensors was -3.0 dB_A and -1.5 dB_A in the observer plane. However, minimal control was achieved using the mSISO approach with the eight Smart Foam element configuration.

Eight channel simulations were repeated using only a single sample of delay—the least amount of delay achievable in a real controller. Performance increased to -3.6 dB_A at the error sensors and -1.9 dB_A in the observer plane for MIMO control. Using the mSISO approach, -1.2 dB_A was achieved at the error sensors and -0.6 dB_A in the observer plane. The increase in performance suggests that the controller was indeed limited by the lack of

causality.

The use of PVDF shaped sensors was studied in place of accelerometers to obtain reference signals. Although they resulted in control, performance was greater using accelerometers.

The use two references per actuator was investigated based on the dependence of control performance on the coherence between reference and error signals. This method used acceleration measurements from neighboring actuators such that two references per actuator could be used. This sensing technique improved the coherence between the references associated with a particular actuator and each respective error signal. Relative to using a single accelerometer reference per actuator, MIMO control using two references per actuator had improved performance. In the control band, -3.1 dB_A was realized at the error sensors with -4.8 dB_A from 480–750 Hz. In the observer plane, -1.9 dB_A was achieved from 480–750 Hz.

Control using the multiple references per actuator technique was beyond the scope of this research effort. Further, the study was limited to only MIMO coupling due to limitations of the control simulation software and was therefore performed only to emphasize the effect of coherence on control performance. However, this study, does emphasize the need to increase the coherence between reference and error signals. Future research efforts may benefit by building on this study by using multiple, independent references per actuator with both MIMO and mMISO controller schemes. Such future studies may also benefit by using larger Smart Foam elements to increase low frequency control authority. Further, it was shown that better mSISO performance is achieved using fewer actuators. Therefore, the use of fewer, yet larger Smart Foam elements with multiple, independent references per actuator (mMISO) are recommended for future studies.

Active noise cancellation using Smart Foam is limited to higher frequencies (> 400 Hz). To increase control authority to lower frequencies, tuning masses were used to tune Smart Foam elements to have a fundamental bounce mode equal to a low frequency resonance of the radiating plate. The use such tuning masses adhered to the tops of Smart Foam actuators was shown to result in a globally attenuated interior noise field by reducing the structural response at the fundamental panel mode. Further, the use of tuning masses was shown to not inhibit active control. Peak attenuation using this reactive treatment was -6.0 dB_A at the 112 Hz fundamental panel mode with global control in excess of -3.0 dB_A achieved over a 25 Hz band about the 112 Hz (1,1) plate mode. This method was the most successful means of achieving global control, however their use resulted in a 41% weight penalty.

Chapter 8

Conclusions and Recommendations

A summary of conclusions for this research effort is presented along with recommendations for future research in active control of turbulent boundary layer induced interior noise in aircraft using integrated Smart Foam elements.

Correlation of the flow and resulting flow induced plate vibration was determined. Temporal and spatial correlation of the flow parallel to the plate was -3 dB at 0.4 ms and 30 mm, respectively with increasing time and distance resulting in reduced correlation. Resulting plate vibration had considerably better correlation due to modal filtering effects. Temporal and spatial correlation of the plate was -3 dB at 0.8 ms and 75 mm, respectively. Further, it was shown that the interior noise field was due to plate vibration excited by the turbulent flow.

Four reference sensing methods were observed: 1) the use of a single point acceleration measurement per actuator, 2) the use of a single, distributed PVDF spatial sensor per actuator, 3) the use of one discrete reference sensor array used per actuator, and 4) the use of multiple, independent point acceleration measurements per actuator. The scope of this research effort required the use of a single reference per actuator as used in the first three reference sensing methods. However, the use of PVDF spatial sensors and the discrete reference sensor arrays was shown to not benefit active control performance since they are not capable of increasing the coherence between the plate vibration (reference) and the interior noise field (error sensors). The use of multiple references per actuator was thus studied to highlight the need to increase the coherence between the reference and error sensors.

Multiple coherence was computed using each of the four reference sensing methods along with corresponding theoretical maximum achievable control from 400–800 Hz. The use of discrete reference sensor arrays and PVDF spatial sensors had theoretical maximum achievable control of up to 4.4 dB and 8.9 dB, respectively at error sensor arrays placed in the near field. In the observer plane, theoretical maximum achievable control using the discrete reference array and the PVDF spatial sensor was computed to be up to 3.5 dB and 6.3 dB, respectively.

The use of accelerometers for obtaining reference signals was also considered. Theoretically maximum achievable control of 9.4 dB was computed using a single reference per

actuator and up to 16.8 dB using three references per actuator with the error sensor arrays placed in the near field. Theoretical maximum achievable performance in the observer plane was up to 10.3 dB using a single reference per actuator and 13.4 dB using two references per actuator. Peak performance using two references per actuator was best, however using three references the performance was more global. Comparing results obtained using the two spatial sensing methods with those results obtained using independent accelerometers, it can be concluded that better performance may be achieved using the latter.

Directional error sensor arrays were developed to allow near field error sensing. These arrays were developed to sense primarily noise radiated from the vicinity of one Smart Foam element thus allowing a physical decoupling of acoustic paths radiating from the vicinities of neighboring actuators. Error array directivity was estimated to be 4.8 dB in the near field.

The error sensor arrays were also capable of sensing primarily the radiating component of the acoustic near field. The radiating component could then be minimize by the controller without expending effort minimizing the non–radiating acoustic waves of the near field. Near field rejection from 9.5 dB to 16.5 dB was obtained depending on source characteristics and array placement relative to the plate edges.

Three Smart Foam configurations were used. The first two had four Smart Foam elements with one configuration having tuning masses added for increased low frequency performance. The third configuration had eight Smart Foam elements in a two by four arrangement. Tuning masses were not used with the eight element configuration since their presence was determined to neither inhibit nor hinder active performance during the control experiments.

The four Smart Foam element configuration cut–on at 400 Hz whereas the eight element configuration did not effectively generate an acoustic field until 600 Hz. This difference in performance is due to the actuator geometry; Smart Foam elements used in the four element configuration were twice the length of the actuators used in the eight element configuration. For the eight element configuration, the actuators were limited by geometric restraints as well as the limited spatial correlation of the plate—poor spatial correlation requires a greater number of references, each associated with a corresponding Smart Foam element, yet low frequency authority of Smart Foam is proportional to the length of the actuator.

It was determined that the controller used for the control experiments using the four element Smart Foam configuration was acausal. The difference between the controller delay and the acoustic propagation time from the Smart Foam elements to the error arrays placed in the near field was 1.48 ms.

Active control was performed using either control experiments or simulations. Control experiments were performed using the four Smart Foam element configuration given either three or four channels; The four channel case used one actuator per channel whereas for the three channel case, channel 2 had two actuators wired in phase. Controller limitations required that channel counts greater than four be studied using control simulations.

Control experiments using the four channel Smart Foam configuration with MIMO control from 400–800 Hz resulted in -1.7 dB_A at the error sensors when placed in the near

field. In the observer plane -1.0 dB_A was achieved. Diagonalizing the controller resulted in negligible performance. However, using a 200–400 Hz control band, MIMO control resulted -2.9 dB_A at the near field error sensors and -1.8 dB_A in the observer plane. Decoupled control using the lower frequency control band resulted -2.3 dB_A and -1.2 dB_A at the error sensors and in the observer plane, respectively. Therefore, it has been shown that global control may be achieved using near field error sensing.

Tests were repeated using the same actuators wired for the three channel configuration. This configuration effectively allowed the use of one actuator having twice the size and thus better low frequency performance. For the 400–800 Hz control band, MIMO control of -2.8 dB_A at the near field sensors and -1.8 dB_A in the observer plane was achieved—approximately 1 dB_A better performance at each location. For mSISO control, -1.1 dB_A and -0.8 dB_A, respectively was achieved at the near field sensors and in the observer plane.

Control experiments were performed using references obtained from either a discrete reference sensor array or a single accelerometer per actuator. Performance was similar as was predicted by estimating the theoretical maximum achievable performance based on coherence studies. The use of discrete reference sensor arrays was thus shown to not have any advantage over using a single accelerometer per actuator for obtaining reference signals.

Active noise cancellation using Smart Foam is limited to higher frequencies (> 400 Hz). To increase control authority to lower frequencies, tuning masses were used to tune Smart Foam elements to have a fundamental bounce mode equal to a low frequency resonance of the radiating plate. The use of such tuning masses adhered to the tops of Smart Foam actuators was shown to result in a globally attenuated interior noise field by reducing structural response at the fundamental panel mode. Further, the use of tuning masses was shown to not inhibit active control. Peak attenuation using this reactive treatment was -6.0 dB_A at the 112 Hz fundamental plate mode with global control in excess of -3.0 dB_A achieved over a 25 Hz band about the 112 Hz (1,1) plate mode. This method was the most successful means of achieving global control, however their use resulted in a 41% weight penalty.

Controller delay was accounted for during control simulations by delaying the error signal by six samples relative to the reference signal. Further simulations were performed using only one sample of delay—the minimum delay of a real controller. This was done to determine the maximum control achievable given a controller with a minimum of delay.

Using the eight Smart Foam element configuration with a 400–800 Hz control band resulted in better performance than when using the four element configuration. However, the best performance was achieved using the four element/three channel Smart Foam configuration. Simulations using six samples of delay at 4000 Hz resulted in -2.2 dB_A at the error sensors and -0.9 dB_A in the observer plane for MIMO control. From 480–750 Hz, performance at the error sensors was -3.0 dB_A and was -1.5 dB_A in the observer plane. However, minimal control was achieved using the mSISO approach with eight actuators.

Eight channel simulations were repeated using only a single sample of delay—the least amount of delay achievable in a real controller. Performance increased to -3.6 dB_A at the error sensors and -1.9 dB_A in the observer plane for MIMO control. Using the mSISO approach, -1.2 dB_A was achieved at the error sensors and -0.6 dB_A in the observer plane.

This suggested that the controller was only marginally limited by the lack of causality.

Simulations were performed using PVDF shaped sensors in place of accelerometers. Although they resulted in control, performance was greater using accelerometers as was predicted in the estimates of theoretical maximum achievable control based on the coherence studies mentioned above.

The scope of this research effort was to use only a single reference per actuator. However, coherence studies suggested that the use of multiple, independent references per actuator would increase control performance.

MIMO simulations using two independent references per actuator, obtained from accelerometers, were studied. Results showed improved performance relative to using only a single reference accelerometer per actuator. Reductions of -4.8 dB_A and -1.9dB_A, respectively were achieved at the error sensors and in the observer plane from 480–750 Hz given the 400–800 Hz control band.

Based on this research effort, it is concluded that the use of multiple, integrated Smart Foam elements is capable of actively suppressing turbulent boundary layer induced interior noise. However, there is still room for improvement.

Larger Smart Foam elements were shown to be more effective at achieving higher control authority at lower frequencies. In addition, mSISO tests were more effective using smaller channel counts thus suggesting that lower frequency control must be performed with fewer, yet larger, Smart Foam elements. And, further, better coherence, and thus higher theoretical maximum achievable control, is achieved using multiple, independent references per actuator. Therefore, the next logical step would be to perform active control using a small channel count (2–4) of larger Smart Foam elements with multiple, independent references per actuator.

Suppression within the observer plane is a by–product of the performance achieved at the error sensors, and as was observed, performance in the observer plane was less than at the error sensors. It is therefore suggested that the control algorithm be modified such that estimates of the far field (observer plane) acoustic field be made using error measurements. Given a proper estimate of the far field along with the proper system identification filters of the secondary paths, the controller may then more effectively minimize the acoustic field within the desired zone of silence rather than as a by-product of suppressing the acoustic field at the error sensors.

A more capable controller would be necessary to achieve maximum control performance. The use of at least four actuators, with four or more references per actuator, and a minimum of delay would be necessary to perform the recommended control experiments. A higher channel count would be useful, however should only mSISO control experiments be required, then several SISO controllers may be used simultaneously. Further, mMISO runs would require several controllers each having multiple reference inputs with a provision for one error and one actuator.

Low noise levels generated by the low speed wind tunnel limited control performance. It is recommended that future efforts be performed using higher levels of turbulent boundary layer induced interior noise such that a greater signal–to–noise ratio will be achieved. Further,

it would be of benefit to use a larger enclosure such that true far field acoustic performance may be monitored. The acoustic field within the enclosure used for this research effort consisted primarily of the hydrodynamic and geometric near fields. At best, the far field was estimated to be present within the observer plane over a limited frequency band from 100–500 Hz. Within the majority of the desired control band, the observer plane was in the geometric near field where relative maxima and minima are encountered as opposed to the -6 dB drop–off of acoustic pressure given each doubling of distance. For future efforts, the enclosure should be built such that it is at least 100 cm deep. This would allow an observer plane to exist entirely in the far field given the desired 400–800 Hz control band.

The enclosure was mounted atop the enclosure for this research. Since it rested upon the wind tunnel, it was originally subjected to a structural transmission path which corrupted the interior field with noise not due to the turbulent flow. A vibration isolation stand was constructed to isolate the enclosure from such a path. However, this then resulted in an acoustic flanking path existing between the enclosure and tunnel walls requiring a compliant seal to be used. To alleviate such a problem, it is recommended that future efforts use a wind tunnel having the flexible plate located on a side wall. This would allow the enclosure to be placed to the side of the wind tunnel such that a stand may be built to the floor. A compliant gasket may then be used to seal the enclosure/test section interface. This configuration would prevent the weight of the enclosure from compressing the gasket which may then result in a new structural transmission path.

Appendix A

Wind Tunnel Setup and Qualification

The wind tunnel used for active noise control experiments and their supporting studies, as presented in the body of this dissertation, was a low speed, Mach 0.14, tunnel having a test section measuring 0.3 meters (one foot) square. Components of the wind tunnel included a fan with converging nozzle, lined duct preceded by Herschel–Quincke (HQ) tubes, test section, enclosure, vibration isolation stand for the enclosure, and terminated with a diverging nozzle. The fan, converging nozzle, and HQ tubes will not be discussed. The assembled unit used for this research is shown in Figure A.1. In the figure are shown, from left to right, the converging nozzle, Herschel–Quincke tubes, lined duct, test section with vibration isolation stand and enclosure mounted above, and the diverging nozzle. Not shown is the fan, mounted upstream of the converging nozzle. The Herschel–Quincke tubes were designed in previous research [58] to reduce the blade passage frequency of the fan. All other components are discussed below.

The lined duct was built as a means of reducing any upstream noise sources due to the fan. Most notably the fan blade passage frequency (264 Hz), and its first two harmonics (528 Hz and 792 Hz) whose mean squared pressure inside the enclosure were significantly greater than that of the interior noise spectrum due to TBL induced panel vibration. Design charts from [5] were used to design the lined duct with resulting dimensions as shown in Figure A.2.

To qualify the lined duct, a speaker was placed at one end with a microphone and another microphone was placed at the opposing end. The speaker was then given a random input and the noise level at each microphone was acquired. The transfer function between the two microphones was the gain in noise level across the lined duct and is shown in Figure A.3. Above 200 Hz, the attenuation of flow noise through the lined duct was more than 40 dB for all frequencies except at a small band centered at 250 Hz. Here, the attenuation was still greater than 32 dB. Aside for very low frequencies, the least attenuation occurs at 141 Hz. Attenuation at this frequency was approximately 12 dB.

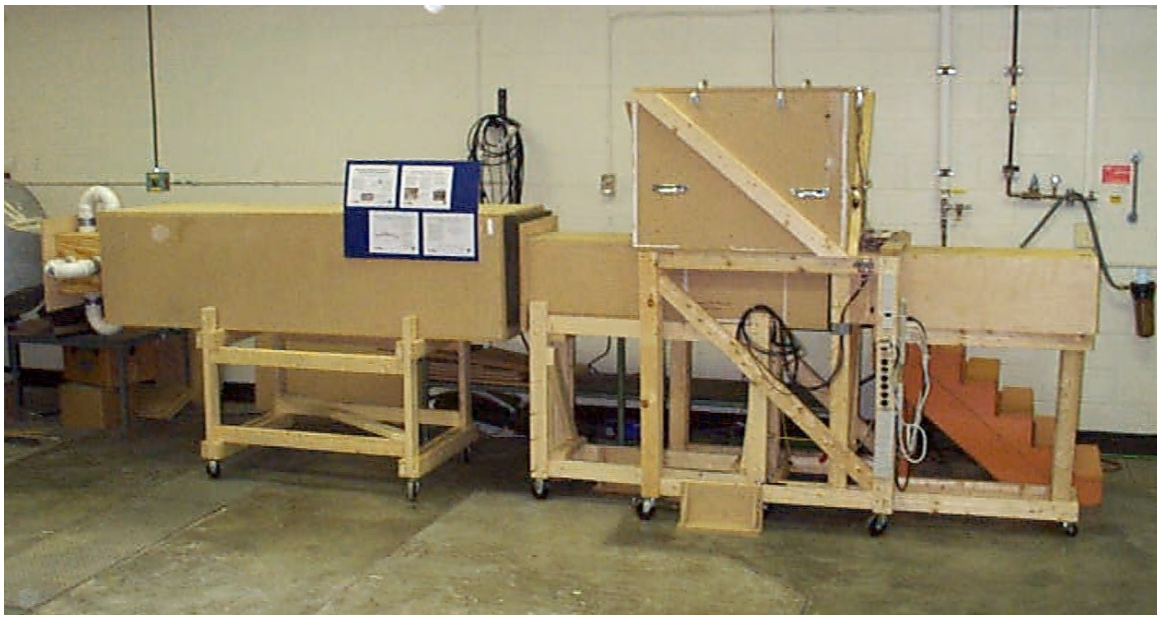

Figure A.1: The wind tunnel and its components.

.

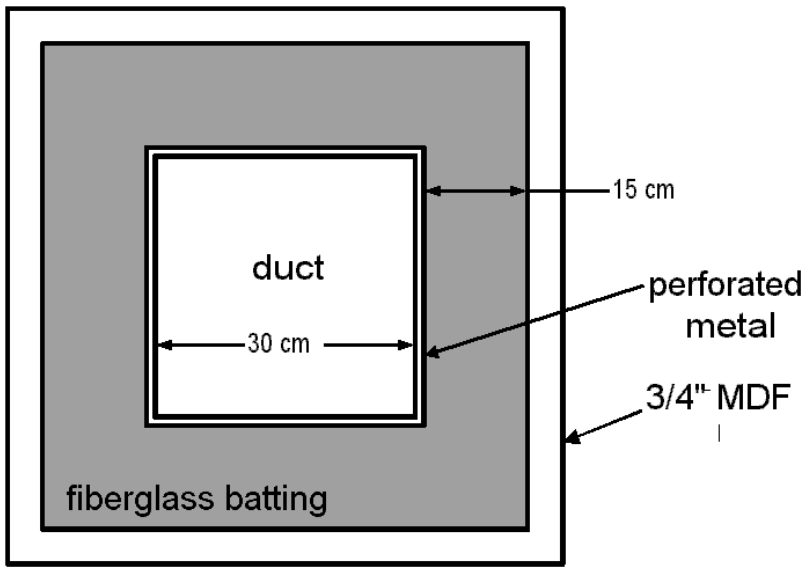

Figure A.2: The lined duct was designed to be 2.44 m long with the shown cross–section dimensions.

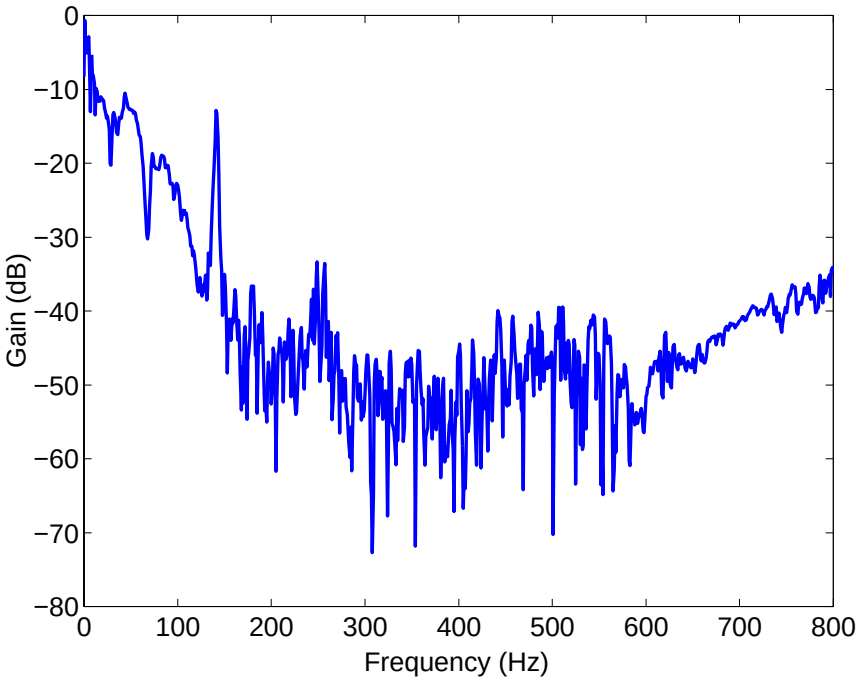

Figure A.3: Experimentally determined performance of the lined duct.

.

A.1 Wind Tunnel Test Section

The wind tunnel test section measured 0.3 meters (one foot) square in cross–section and 1.5 meters (five feet) in length. Originally, the test section was constructed of 3/4″ fiber board. Later, to reduce correlation between test section vibration and interior noise, the test section was wrapped with a thin layer of lead sheet and covered with 3/4″ MDF. The fuselage panel was mounted to a steel frame in the top wall of the test section flush to the duct interior. Clamped dimensions of the panel were 0.248 m (9–3/4″) in width and 0.51 m (20″) along the flow.

Higher order acoustic modes within the duct must be identified since they would have an effect on the disturbance power spectrum acting on the panel. These modes would result in higher magnitudes of panel excitation and should be identified since this phenomena would not exist in actual flight. At frequencies below cut–on, the phase speed is imaginary and no waves propagate, but above cut–on the phase speed is infinite. Phase speed in an infinite, rectangular duct may be expressed as

$$c_x = \omega \left\{ \left(\frac{\omega}{c}\right)^2 - \left(\frac{\pi n_y}{L_y}\right)^2 - \left(\frac{\pi n_z}{L_z}\right)^2 \right\}^{-1/2} \tag{A.1}$$

where n_y and n_z are the mode number pairs of the duct modes and L_y and L_z are the lengths of the duct walls, with phase speed in free space denoted as c, and angular frequency, ω [5]. Setting the phase speed to infinity gives

$$\frac{1}{\infty^2} = \omega \left\{ \left(\frac{\omega}{c}\right)^2 - \left(\frac{\pi n_y}{L_y}\right)^2 - \left(\frac{\pi n_z}{L_z}\right)^2 \right\} \tag{A.2}$$

or

$$\left(\frac{\omega}{c}\right)^2 = \left(\frac{\pi n_y}{L_y}\right)^2 + \left(\frac{\pi n_z}{L_z}\right)^2) \tag{A.3}$$

and dividing by 2π then gives

$$f_n = \frac{c}{2}\sqrt{(n_y/L_y)^2 + (n_z/L_z)^2} \quad \text{(Hz)} \tag{A.4}$$

Equation A.4 is then the same expression used for determining room modes with one dimension set to infinity. Note, that Equation (A.4) assumes that the duct has rigid walls and, with respect to wavelength, is sufficiently long. Theoretical values of duct mode frequencies and corresponding phase speed are shown in Table A.1. Duct cut–on was experimentally determined by Griffin to also be 563 Hz.

Since active control was considered for frequencies under 800 Hz, duct modes within this band would be of interest. Observation of Table A.1 suggests that noise within the duct propagates as a zero order duct mode (all in–phase) at frequencies below the 563 Hz cut–on frequency. Beginning at 563 Hz a (0,1) mode and a (1,0) mode cuts–on and at 796 Hz a (1,1) mode cuts–on.

Table A.1: Analytically Determined Resonant Frequencies and Corresponding Phase Speeds of the Tunnel Test Section

Frequency (Hz)	Phase Speed (m/s)	N_y (m/s)	N_z (Hz)
0	0	0	0
563	3535	0	1
563	3535	1	0
796	5000	1	1
1125	7071	0	2
1125	7071	2	0
1258	7905	1	2
1258	7905	2	1
1591	9999	2	2

A.2 Enclosure and Vibration Isolation Stand

The enclosure was mounted over the vibrating fuselage panel and was used to represent the interior of an aircraft cabin. Noise within the enclosure was required to be that due to the turbulent flow, however since excessive noise due to the wind tunnel fan and vibration of the test structure due to the flow were present, it was important that any flanking paths be minimized. For acoustic flanking paths, transmission loss through the enclosure walls needed to be increased, and for structural paths from the vibrating tunnel walls to the enclosure, it was required that the enclosure be placed on a vibration isolation stand. Originally, for Griffin's work, the enclosure was constructed of a double layer of $3/4''$ plywood and was placed directly on the tunnel test section. Acoustic modes of the enclosure may be found in Table A.2. See also [58] for a description of the original wind tunnel design and qualification.

Table A.2: Enclosure acoustic modes up to 1200 Hz using. Modal indices are 0,1,2,3.

Resonant Frequencies (Hz)
204.6
321.5
381.1
409.2
454.7
498.6
611.2
747.5
827.2
932.1
945.3
1037.1
1096.0
1097.2
1177.2

The resulting interior noise spectrum for the original configuration suffered from large peaks due to the fan blade passage frequency (BPF, 264 Hz) and its first two harmonics (528 Hz and 792 Hz). As mentioned previously, it was suspected that these tones propagated down the duct. Therefore, the lined duct was built to reduce interior noise at these frequencies. Although the BPF and its second harmonic were attenuated the first harmonic was not, thus indicating that the first harmonic was propagating by some other path. This other route was suspected to be due to an acoustic flanking path through the enclosure walls. In addition, structural vibration paths were suspected to be corrupting the interior noise field. To identify these possible acoustic and structural flanking paths, several tests were conducted; each one isolating the effect of a particular flanking path. The first involved running the tunnel with the enclosure mounted on the tunnel wall and a bare fuselage panel. This case allowed all noise sources to influence the interior field. A wooden plug (three layers of 3/4″ MDF) was then mounted to the panel and sealed with potters' clay. This eliminated interior noise due to the TBL. Therefore, in this configuration, the interior noise would consist only of noise due to acoustic and structural flanking paths. Then, the enclosure was removed and placed near the tunnel on a table so that it was of approximate height and location to its position on the tunnel eliminating any structural paths. These three configurations were then compared to background noise as shown in Figure A.4.

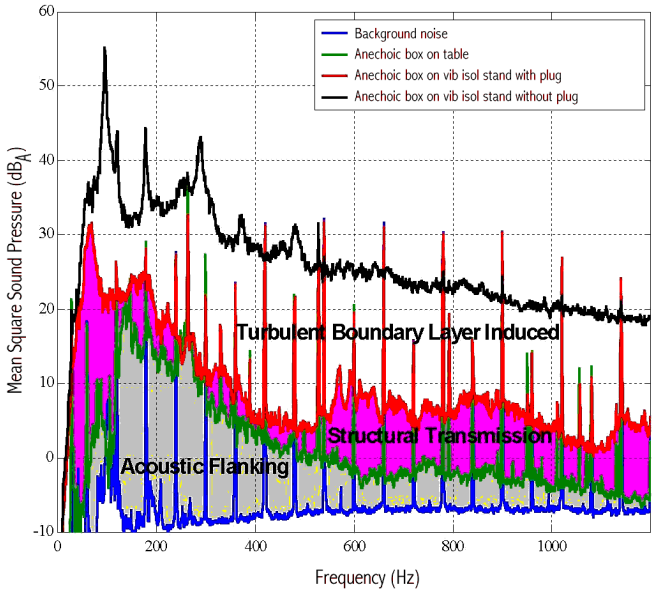

Figure A.4: The interior noise suffered from noise due to acoustic and structural flanking paths as identified here. Note that acoustic flanking was most significant at lower frequencies whereas structural paths were responsible for corrupting the acoustic field primarily above 500 Hz.

Therefore, modifications were made to reduce acoustic and structural flanking paths as shown in Figure A.5. Transmission loss of the enclosure was increased by adding a double layer of 3/4″ thick MDF to the original enclosure. It was characterized by placing it, both before and after applying the MDF, in a reverberation chamber with microphones placed both inside and outside the enclosure. The difference in the spatially averaged sum of squares pressure would be the increase in transmission loss. This increase in performance is shown in Figure A.6. An increase in transmission loss was achieved for frequencies above 200 Hz. Between 200–800 Hz, an average reduction of 7.9 dB was achieved resulting in enclosure transmission loss of greater than 20 dB for frequencies greater than 200 Hz.

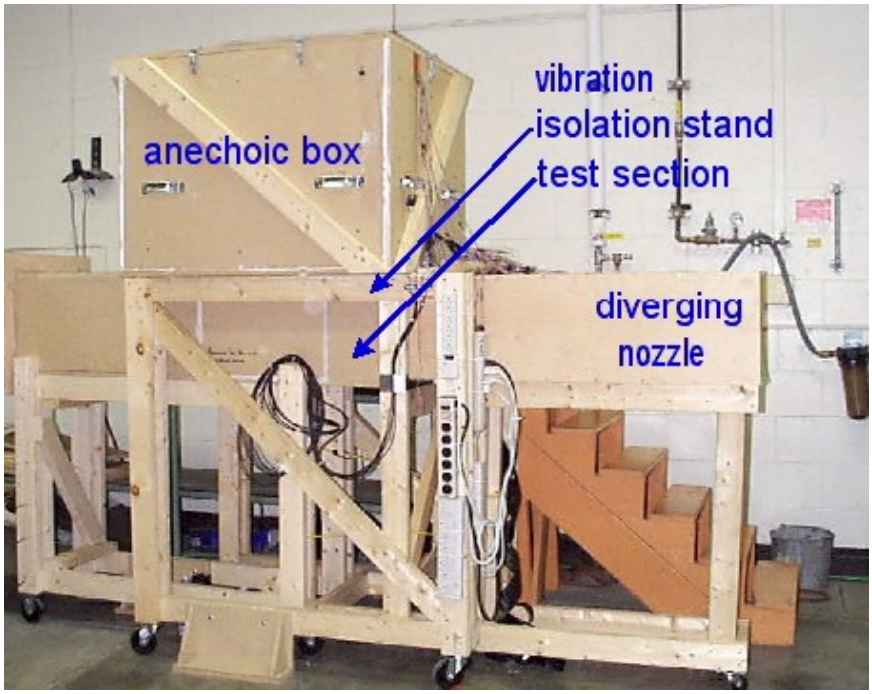

Figure A.5: Modifications to the enclosure included increased wall thickness to increase acoustic transmission loss through its walls and the use of a vibration isolation stand to minimize structural flanking paths originating at the tunnel walls.

The lid of the rebuilt enclosure was built in two pieces since the added mass would have made it difficult to lift. See Figure A.7. Since there was the possibility that the gaskets would not completely eliminate any sound propagating through the lid–enclosure interface, the lids were designed to increase the path length of an acoustic wave through the crack between the lid and box mating surfaces. Gaskets were placed at each step as shown in Figure A.8.

Structural flanking paths were then minimized by constructing a stand to support the enclosure. This stand held the enclosure above the wind tunnel test section decoupling

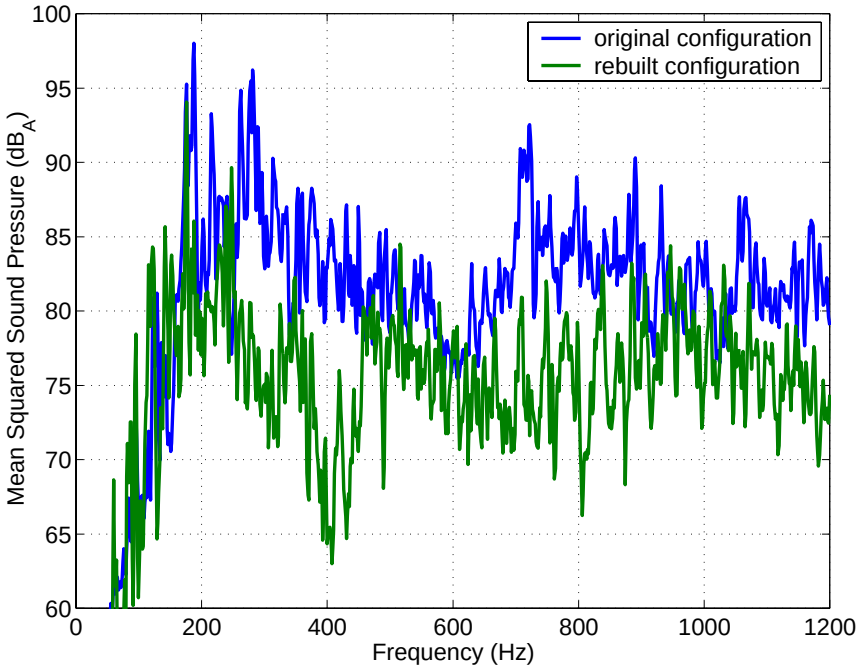

Figure A.6: The rebuilt enclosure had greater transmission loss than the original design at frequencies above 200 Hz. From 200–800 Hz there was a 7.9 dB increase in transmission loss.

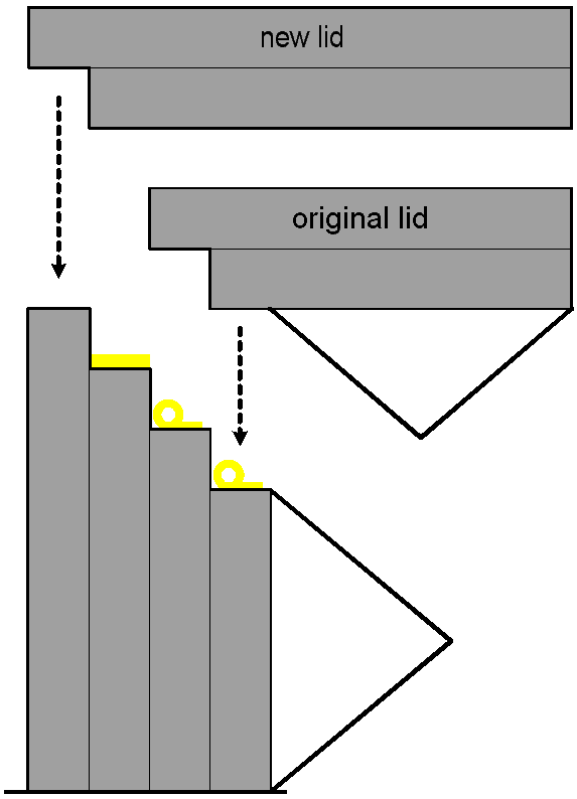

Figure A.7: The lid for the enclosure was built in two pieces to aid in removal. Mating surfaces were designed to increase the path length of an acoustic wave through the crack between the lid and box mating surfaces.

the structural path between the two. The only mating point between the enclosure and the wind tunnel wall was by compliant gaskets. The stand was designed so that a 1/4″ gap existed between the bottom of the enclosure and the top of the wind tunnel. This gap was then filled with the compliant gasket. The gasket was comprised of three components as shown in Figure A.9 with results for the rebuilt enclosure using the vibration isolation stand presented in Figure A.10.

The fuselage panel used was a flat aluminum plate bolted to a steel frame as shown in Figure A.11. The interior dimensions of the frame used to mount this panel measured 0.248 m (9–3/4″) in width and 0.51 m (20″) along the flow as shown in Figure A.12.

Experimentally determined panel modes for the 1.6 mm (0.063″) thick panel were reported by Griffin [58] and reproduced in Table A.3. Note, that the fundamental mode occurred at 119.4 Hz and therefore the interior noise due to this mode is significantly amplified due to the zeroeth order room mode of the enclosure. Other radiating modes occurred at 232.4 Hz, and 430.6 Hz. The interior noise field due to the turbulent flow, measured at 0.5 m from the 1.6 mm bare plate, is shown in Figure A.13.

Note, however, that the (1,1) panel mode had dropped in frequency to 112 Hz after the rebuilding of the wind tunnel test section. This occurred after the mounting procedure of the panel mounting frame was changed. Originally, the mounting frame was screwed into the wooden tunnel walls, but these screws were later replaced with adhesive since the mounting holes had stripped.

The (1,1) panel mode—the most efficient radiating mode—occurred at a frequency within the bandwidth of the zeroeth order mode of the enclosure. Low frequency responses within the enclosure were then significantly greater in magnitude than those in the desired active control band of 400–800 Hz. In an attempt to relieve these problems, the panel thickness was increased to 3.2 mm (0.125″). This gave an experimentally determined (1,1) panel mode of 230 Hz. The resulting interior noise field is shown in Figure A.14.

Although the plate (1,1) mode was moved outside the effects of the zeroeth order acoustic mode of the enclosure, the controllable region had a significant reduction in noise level. Therefore, the 1.6 mm plate was used for all experiments and analysis.

A.3 Diverging Nozzle

A diverging nozzle, or diffuser, is required at the flow exit point to make a gentler transition from flow to free field thus promoting a slowly varying acoustic impedance. This slowly varying impedance minimizes acoustic reflections. In addition, if the diffused nozzle diverged too quickly, stagnation points between the flow and the nozzle would occur resulting in separation points in the boundary layer. These separation points would then allow for vortices to develop which would then generate undesired flow noise. Flow noise due to the vortices may then corrupt the TBL noise. Proper design of the divergence angle would eliminate the possibility of flow separation. In addition, the acoustic impedance changes over a longer distance thus reducing the chance of an acoustic wave to reflect back towards the test section.

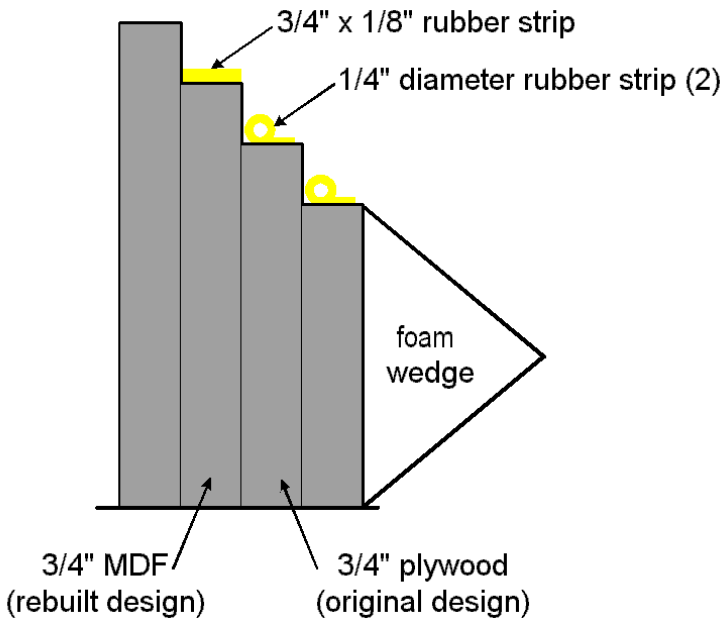

Figure A.8: A series of three gaskets were used to seal the lid of the enclosure.

Table A.3: Experimentally determined panel modes A.3. Griffin [58]

Mode	Frequency (Hz)
(1,1)	119.4
(1,2)	164.9
(1,3)	232.4
(2,1)	285.4
(1,4)	320.3
(2,2)	330.8
(2,3)	388.4
(1,5)	430.6
(2,4)	475.9
(3,1)	534.3
(1,6)	563.8
(2,5)	581.1

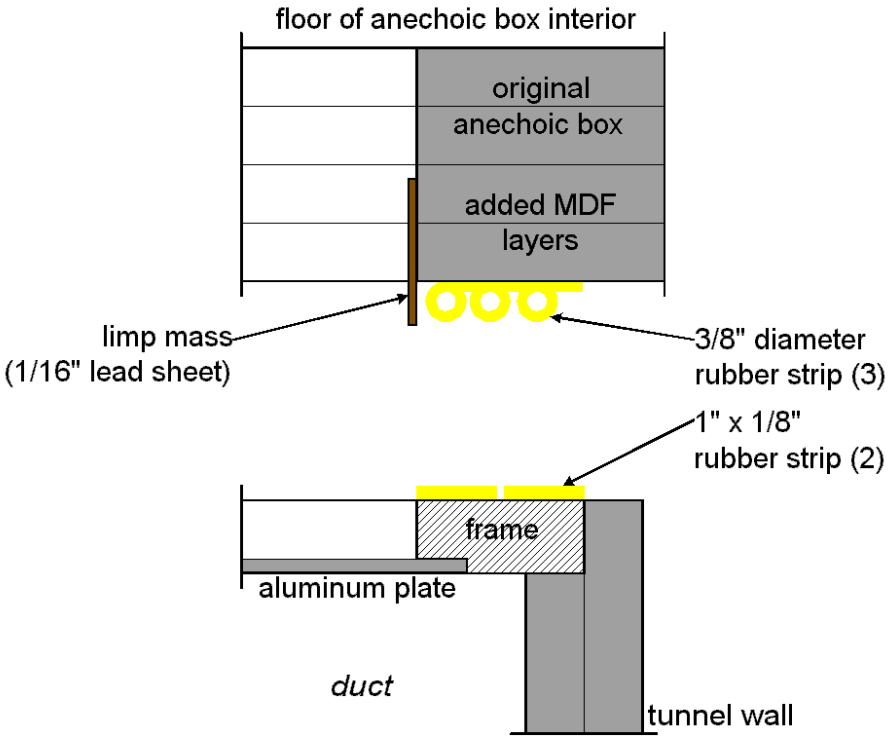

Figure A.9: The base gasket of the enclosure was designed using three componets:flat rubber weather stripping adhered to the panel frame, round weather stripping mounted to the bottom of the enclosure, and a thin lead sheet.

The original diffused nozzle measured 19 cm (48″) in length but was made with too great of a divergence angle. This excessive divergence angle resulted in flow separation. The nozzle was rebuilt to specifications as given in [61].

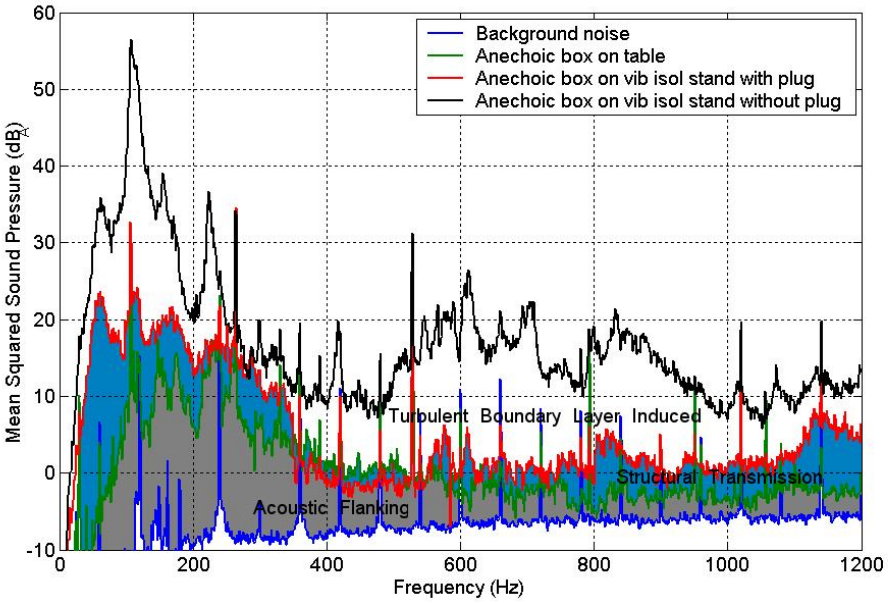

Figure A.10: Qualification of rebuilt enclosure with vibration isolation stand.

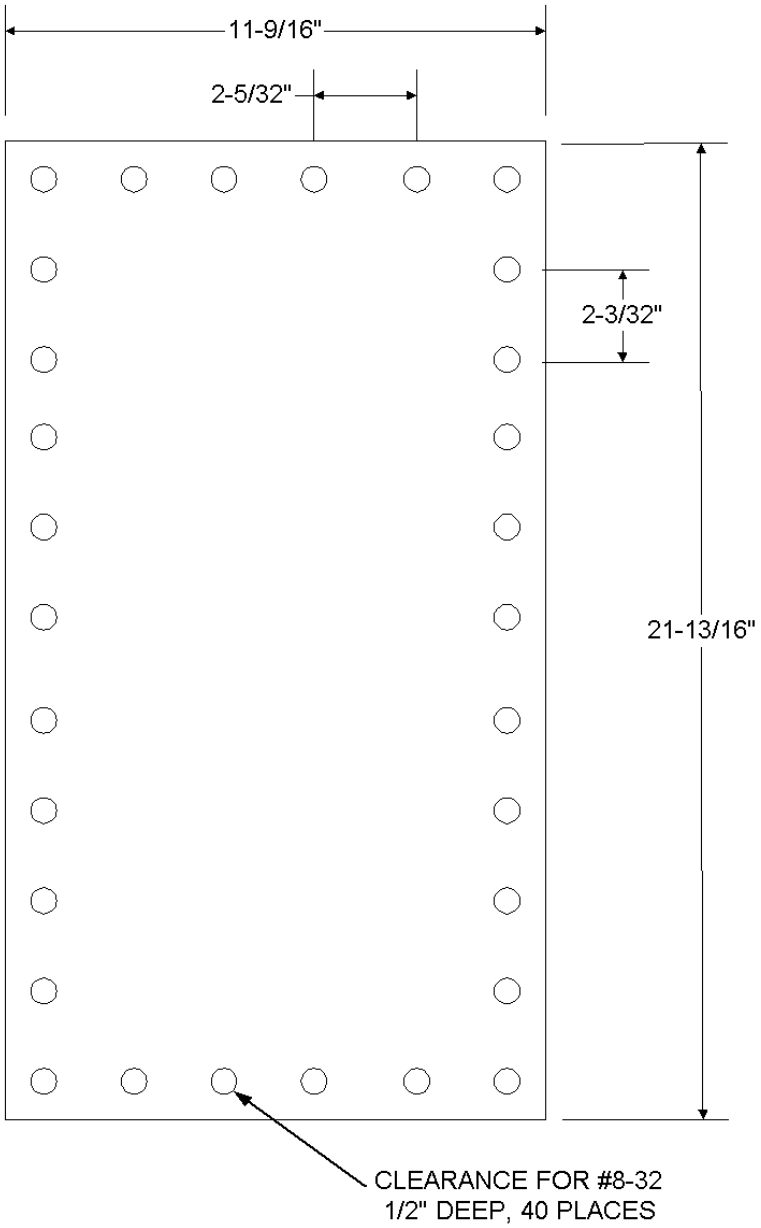

Figure A.11: The fuselage panels used measured 0.294 m (11-9/16″) by 0.554 m (21-13/16″). Thickness included 1.6 mm (0.063″), and 3.2 mm (0.125″)

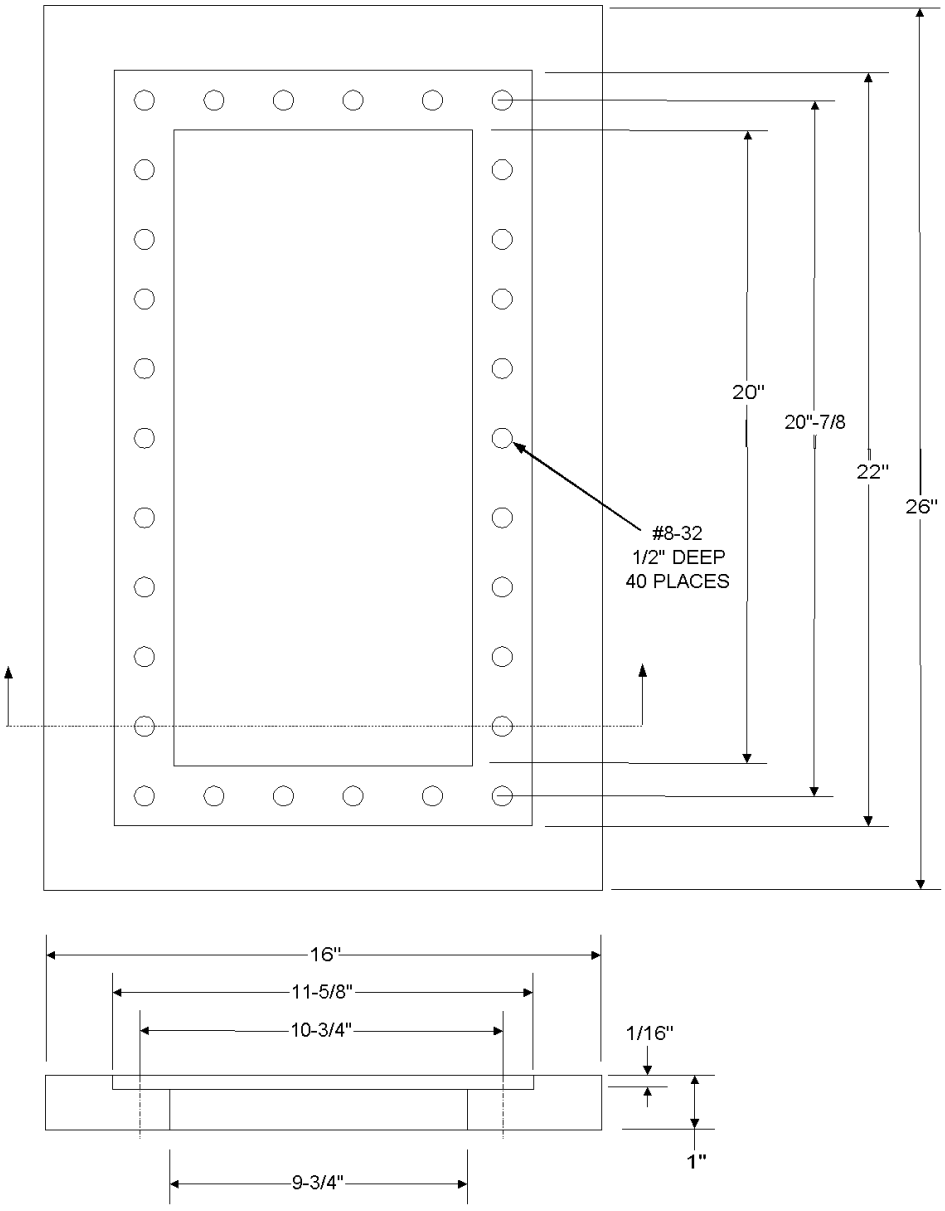

Figure A.12: Fuselage panel mounting frame.

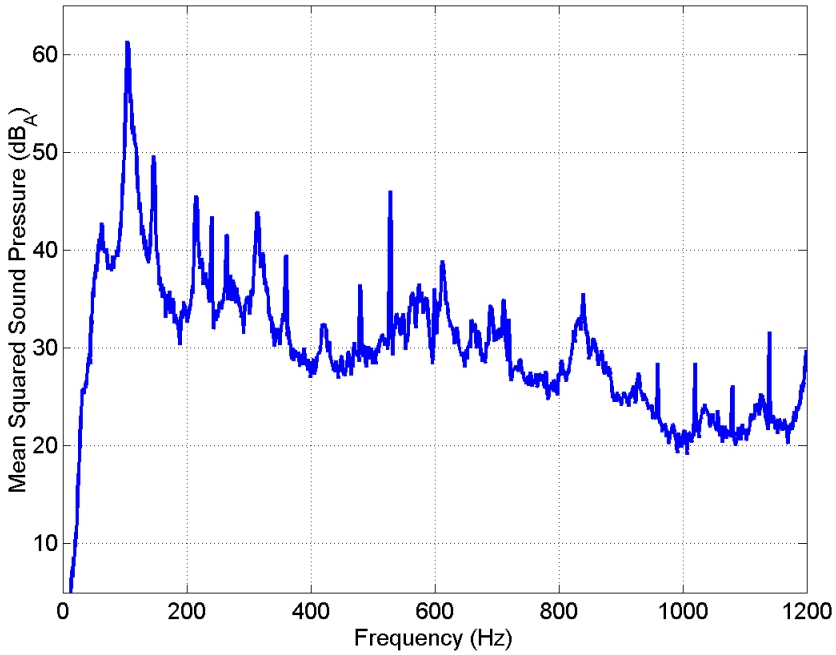

Figure A.13: The (1,1) plate mode occurred within the zeroeth order acoustic mode of the enclosure resulting in very high noise levels at low frequencies.

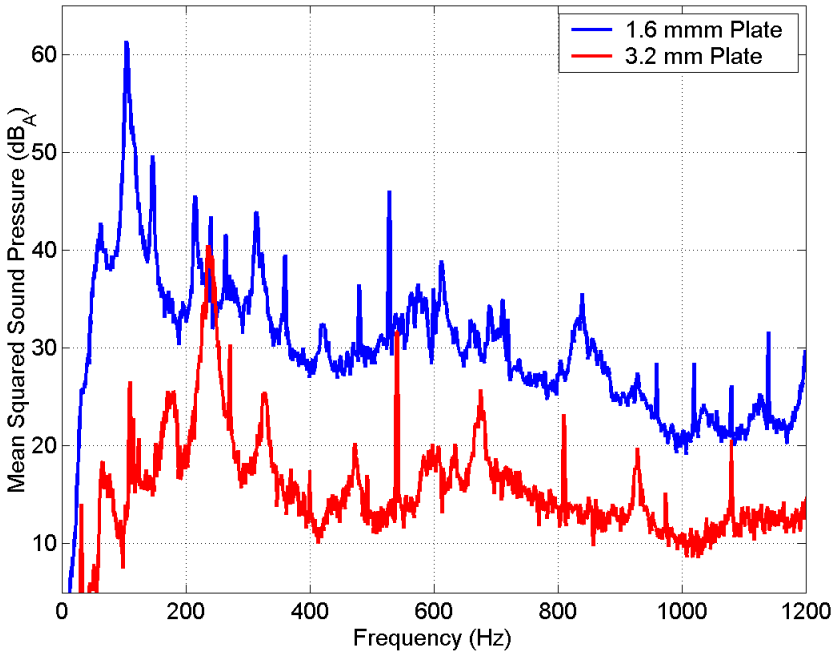

Figure A.14: Interior noise levels using the 3.2 mm plate were greater than 10 dB less than when using the 1.6 mm plate. The resonant frequency of the 3.2 mm plate occurred outside the zeroeth order acoustic mode of the enclosure but the controllable spectrum was of lesser magnitude than when using the 1.6 mm plate.

Appendix B

Summing Amplifier Design

Chapter 4—Error Sensing illustrated the theory and design of the error sensor arrays used for near field sensing and physical decoupling of the control units. This chapter presents the development and qualification of the summing amplifiers used to sum the individual microphone signals used in each error array.

The summing amplifiers used for the error arrays required summing three voltage inputs (from three microphones) each with similar gain. The output, then, was the summed array output.

Summing amplifiers consist of an operational amplifier, or OpAmp, and resistors used to adjust signal gains. A schematic of a summing amp with three inputs is shown in Figure B.1. The resulting output may then be represented as

$$v_{out} = -\left(v_1 \frac{R_f}{R_1} + v_2 \frac{R_f}{R_2} + v_3 \frac{R_f}{R_3}\right) \tag{B.1}$$

Since each channel is to have the same gain, the three resistors R_1, R_2, R_3, may each be set to some value R_{in}. The output may then be expressed

$$v_{out} = -\frac{R_F}{R_{in}} \left(v_1 + v_2 + v_3\right) \tag{B.2}$$

The response is then the negative of the sum of all inputs when $R_F = R_{in}$. Note, however, that each of these inputs were the outputs of voltage followers, or buffers. The buffer has a high input impedance and low output impedance thus isolating the summing amplifier from the instrumentation. Figure B.2 depicts the buffer schematic.

The schematic of the summing amplifier with buffers on each input is shown in Figure B.3. Note, the input and output voltages of the buffer are equal in magnitude but negated. Therefore, using buffers with the summing amplifier shown, the output voltage of the buffered summing amplifier would be in phase with the inputs.

A maximum of eight control channels were used for this research effort, each with a single error array. Therefore, eight summing amplifiers were required with each of these having three inputs. The OpAmps used were Analog Devices AD620AN, eight pin dips and were mounted to solderless breadboards, each having four distribution buses.

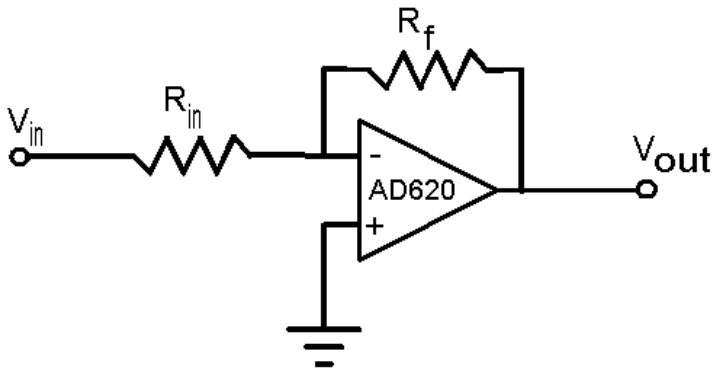

Figure B.1: Schematic of a summing amplifier with three inputs. Resistors are used to adjust gains.

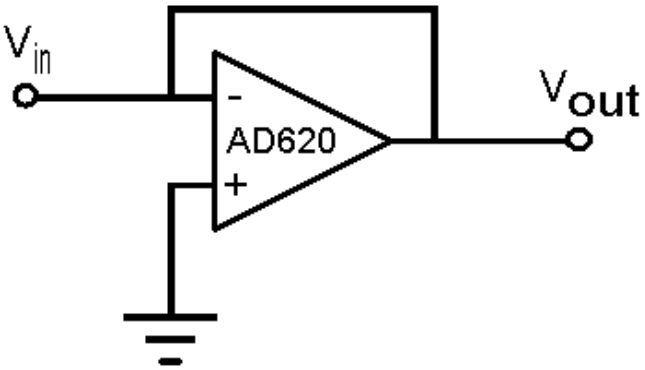

Figure B.2: Schematic of a voltage follower (buffer).

The gain across the OpAmp could be adjusted by changing the feed back resistor, denoted R_f, relative to the resistors applied to the inputs, R_{in}. These resistors were chosen to be 10 kΩ giving unity gain for each input. The OpAmp was powered using two 9 volt batteries wired to give a ±9 volt supply. The summing amp circuitry was placed inside metal boxes with BNC connectors mounted on the box sides as shown in Figure B.4.

The summing amplifiers were then qualified. The resulting output was then expected to be three times greater than the input voltage (since three inputs of equal magnitude were summed). This was first confirmed given a sinusoidal input of 50 Hz, 0.5 V_{peak}. The spectrum analyzer used was a Hewlett–Packard 35665A and was configured with a Hanning window, 400 spectral lines, and 20 averages. The output was shown to be 1.5 V_{peak} and in phase with the input. Broadband performance was then determined using white noise (0–12.8 kHz) applied in phase to each of the three inputs. The transfer function across the

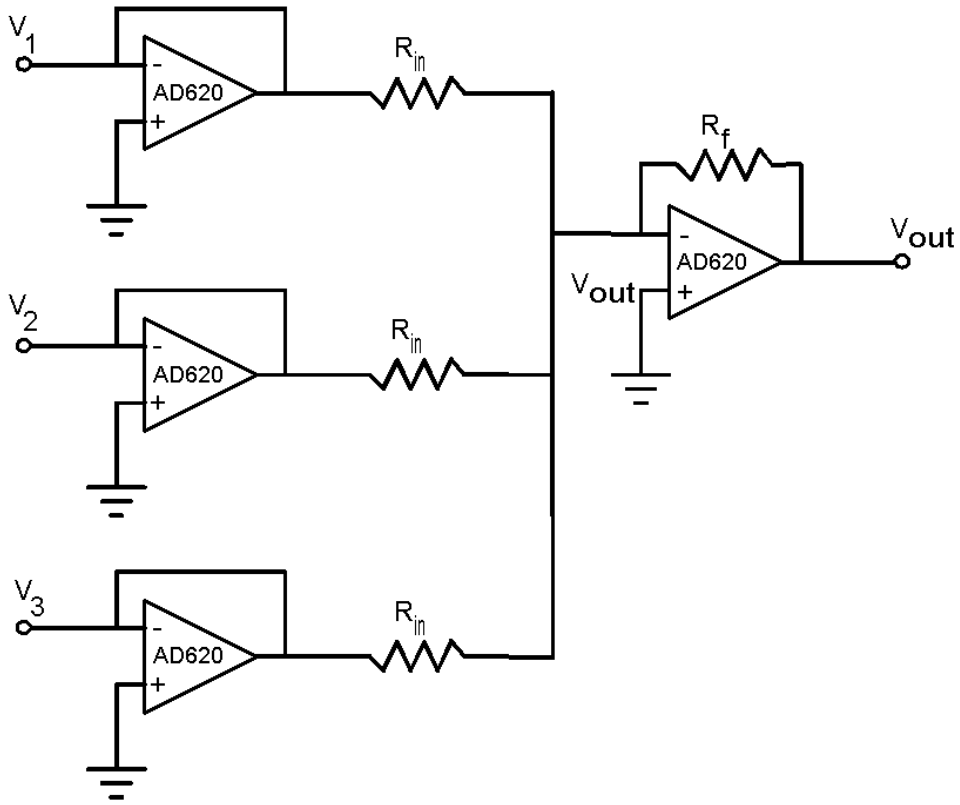

Figure B.3: Schematic of the summing amplifier with buffered inputs.

summing amplifier was determined to be 15.5 dB[1] broadband thus corresponding to a factor of six gain in power or a factor of three gain in voltage as expected.

[1]Note, at 0 Hz, the gain was 16.5 dB.

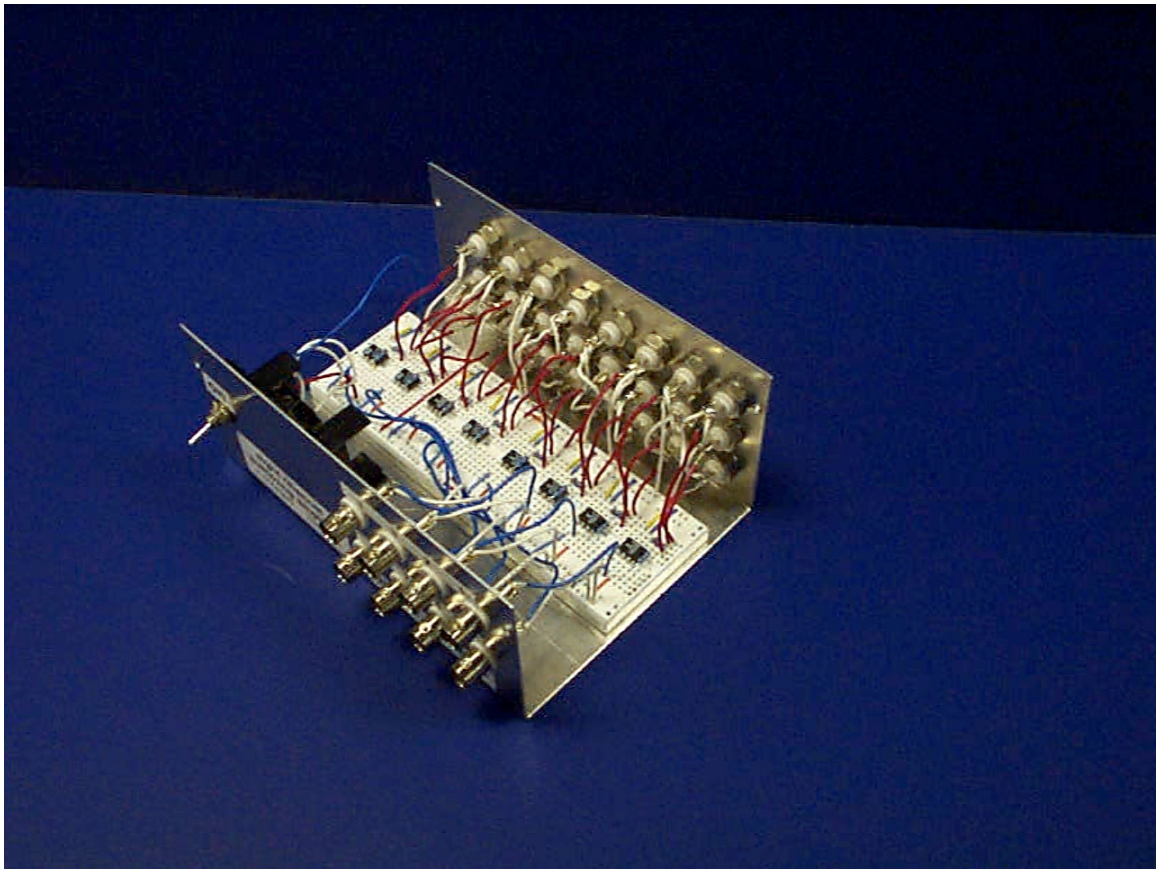

Figure B.4: The completed summing amplifier.

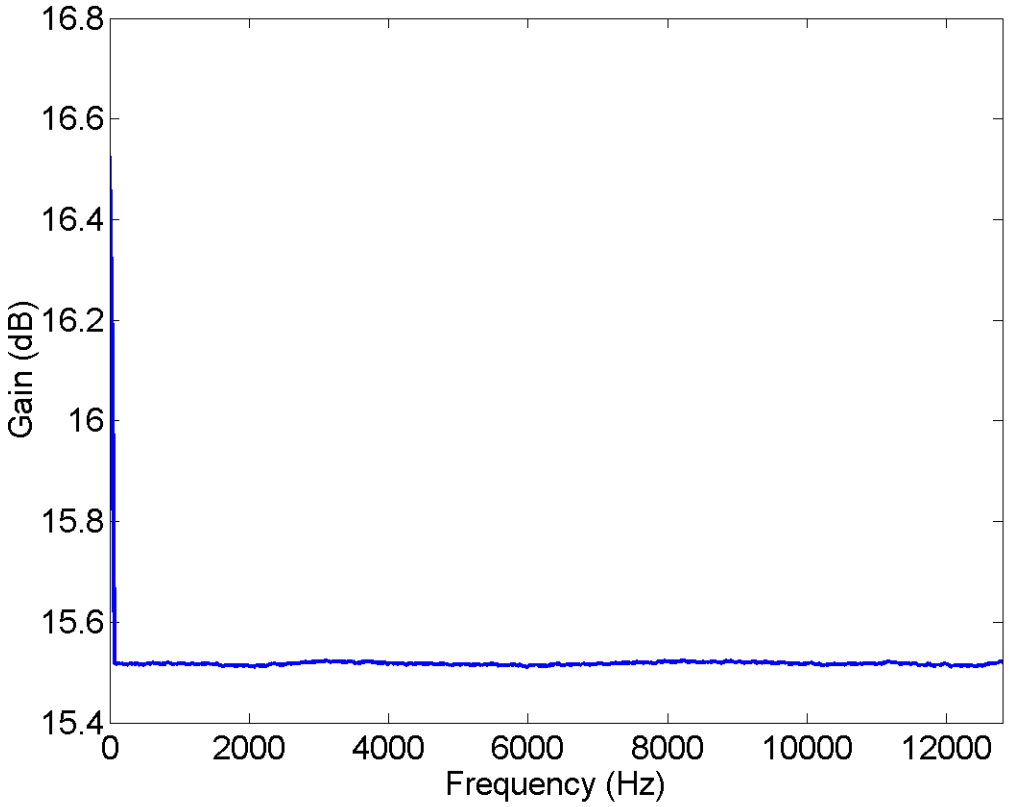

Figure B.5: The transfer function across the buffered summing amplifier was determined to be 15.5 dB.

Appendix C

Matlab Scripts

Matlab simulation codes written for use in this research are presented in this appendix. Each code is preceeded by a brief description of its use.

C.1 Distributed Reference Sensor Analysis

DistRef.m was written by the author to determine the sizing of the distributed, spatial reference sensor as discussed in Chapter 3—Reference Sensing.

```
%John D'Angelo
 %January 9, 2002
%
%
%Distributed PVDF reference sesnsor
clear;close all;
%
%Set Plot Default Values
set(0,'DefaultAxesFontSize',16) set(0,'DefaultLineLineWidth',2)
set(0,'DefaultAxesFontName','arial')
%

%%%%%%%%%%%% DESIGN CRITERIA %%%%%%%%%%%%

%%%% Structure properties and geometry
h = 0.0016;   % 0.063" thick plate
%h = 0.0023;   % 0.090" thick plate
E = 70e9; %Pa
rho = 2710; %kg/m^3
nu = 0.33;

%cut-off properties
fc1 = 500;
```

```
%Desired cut-off freq (Hz) of the filter
fc2 = 800;

%filter cut-ON wavenumber
kc1 = (2*pi*fc1).^(1/2) * ( 12*rho*(1-nu^2) /(E*h^2) ).^(1/4);

%filter cut-OFF wavenumber
kc2 = (2*pi*fc2).^(1/2) * ( 12*rho*(1-nu^2) /(E*h^2) ).^(1/4);

%wavelength (m) of cut-off freq
xc = 2*pi/kc2;

xc1 = 2*pi/kc1;


%Anti-aliasing properties
faa = 20000;            %anti-aliasing frequency
kaa = (2*pi*faa).^(1/2) * ( 12*rho*(1-nu^2) /(E*h^2) ).^(1/4);

%wavelength of cut-off frequency to minimize aliasing (use at least
%2.56 rings / wavelength )
raa = 2*pi/kaa;

%maximum sensor radius in meters (equals 2.43" = 0.062 m)
rmax = 0.062;
Nlines = 512;


%Spatial sampling resolution
k_xmax = 2*pi/rmax;

%f_xmax = 4064.7 Hz using 1.6 mm alum, 0.062 m sensor radius
f_xmax = k_xmax^2 * (12*rho*(1-nu^2)/(E*h^2))^(-0.5) / (2*pi);

%Define the wavenumber domain response
Nlinesd = 2*Nlines;

%Use for plotting the single-sided spatial response
x = [1/Nlines:1/Nlines:1]'*rmax;

%Use for 2-sided spatial respones
x2 = [1/Nlines/2:1/Nlines/2:1]'*2*rmax;
xd = [-flipud(x); x];
```

```
%Need to know wavenumbers all the way up to at least twice the
%fold-line wavenumber, kaa
k = [1/Nlines:1/Nlines:1]'*kaa;

%use to generate the desired, 2-sided k-domain response
k2 = [1/Nlines/2:1/Nlines/2:1]'*2*kaa;

kd = [-1+1/Nlinesd:1/Nlinesd:1]'*kaa;


%%%%%%%%%%%% SIMPLE DISK -- Lowpass filter %%%%%%%%%%%%

%Cut-off frequency given geometric restraint of maximum sensor radius
frmax = (2.3367/rmax^2) * sqrt(E*h^2/(12*rho*(1-nu^2))); krmax =
(2*pi*frmax).^(1/2) * ( 12*rho*(1-nu^2) /(E*h^2) ).^(1/4); ka =
k*rmax; Srmax = 2*rmax^2*pi * besselj(1,ka)./(ka); Srmax =
Srmax/max(Srmax);

%Required radius for a simple disk sensor to cut-off at fc2
rc = sqrt(2.3367/fc2) * (E*h^2/(12*rho*(1-nu^2)))^(0.25);

ka = k*rc;

%k-domain response of a simple disk
Sc = 2*rc^2*pi * besselj(1,ka)./(ka);
Sc = Sc/max(Sc);

Sc2 = Sc.^2; Sc4 = Sc.^4;

figure plot(k,10*log10(abs(Srmax)),k,10*log10(abs(Sc)))
xlabel('Wavenumber (m^{-1})') ylabel('Sensitivity (dB)') xlim([0
max(k)]) legendtext1 = ['Using max allow radius of '
num2str(rmax*1000) ' mm']; legendtext2 = ['Using ' num2str(fc2) '
Hz cut-off (' num2str(rc*1000,2) ' mm)'];
legend(legendtext1,legendtext2)

%Determine the diameter of a single disk to give -3 dB @ kc2
a = rmax; da = rmax/200; Sis3db=-100; intcount=0;

while Sis3db <-3 intcount = intcount+1;
    ka = k*a;
    Sdisk = 2*a^2*pi*besselj(1,ka)./(ka);
    Sdisk = Sdisk/max(Sdisk);
    Sdisk = 10*log10(abs(Sdisk));
```

```
    Sis3db(intcount,1) = real(floor(Sdisk( kc2/max(k) *length(k))));
    a = a - da;
end %end while

%Desired performance of the simple disk
figure plot(k,Sdisk) xlabel('Wavenumber (m^{-1})')
ylabel('k-domain Sensitivity (dB)') xlim([0 max(k)]) grid texttext
= ['disk radius ' num2str(a,2) ' m' ] text(0,-40,texttext)
```

C.2 Discrete Reference Sensor Array Analysis

RefArray.m was written by Dr. Mike Kidner and was used to determine the spacing of the accelerometers used in the discrete reference sensor array as discussed in Chapter 3—Reference Sensing.

```
function RefArray(freq)

%Set Plot Default Values
set(0,'DefaultAxesFontSize',16) set(0,'DefaultLineLineWidth',2)
set(0,'DefaultAxesFontName','arial')

%plate sensor wavenumber transfroms
N = 256/2; %number of points of plate
g = zeros(N,N);
xmax  = 0.508;                      %Plate length (20")
ymax = 0.2476;                      %Plate width (9.75")
x = linspace(-xmax,xmax,N); y = linspace(-ymax,ymax,N);
h =   0.0013;                       %Plate thickness (0.05")
D = 7e10*(h)^2./(12*2700*(1-0.3^2)); Q = 100; Res = 1000; for q =
1:Q
    r = q/Res; %distance of on y axis sensor from origin,

    % for 3 accels in a circluar pattern plus one in center
        a = r*cos(pi/3); % offset in y direction
        b = r*sin(pi/3); % iffset in x direction
        r_ind = round(r./(y(2)-y(1))); %get number of grid points
        a_ind = round(a./(y(2)-y(1))); %that correspond to the dims
        b_ind = round(b./(x(2)-x(1))); %r,a,b

        %place three sensors in a cicle on plate and one in center
        g(N/2,N/2)=1;
        g(N/2+r_ind,N/2)= 0.5;
        g(N/2-a_ind,N/2-b_ind) = 0.5;
        g(N/2-a_ind,N/2+b_ind) = 0.5;

    %figure
    G = fft2(g,N,N);

    kxmax =  1./(x(2)-x(1));
    kymax =  1./(y(2)-y(1));

    kx = linspace(-kxmax,kxmax,size(G,1));
    ky = linspace(-kymax,kymax,size(G,2));
    maxfreq = 2*pi*freq;
```

```
    ka = maxfreq./343; %acoustic wavenumber at max freq
    kmax = sqrt(maxfreq*D^(-0.5));
    kxind2 = max(find(kx<=kmax));
    kyind2 = max(find(ky<=kmax));
    kxind1 = min(find(kx>=-kmax));
    kyind1 = min(find(ky>=-kmax));

%shifts the quadrantsa so that 0 wavnuber is in the center
    G = fftshift(G);
     %xlabel('k_{x}')
     %ylabel('k_{y}')
     %zlabel('Sensor output')
    %freq = (k.^2.*sqrt(D))./(2*pi);
    [KX,KY]=meshgrid(kx,ky);

[KINDI KINDJ,TMP] = find(sqrt(KX.^2+KY.^2)<=ka);

RadiatingRatio(q) = sum(sum(abs(diag(G(KINDI,...
KINDJ)).^2))./(sum(sum(abs(G).^2)));

    %power of radiating wavenumbers./total wavenumber power
end

XX = linspace(1/Res,r,Q); plot(XX*100, 10.*log10(RadiatingRatio))
xlabel('Accelerometer separation, cm') ylabel('Radiating
wavenumber power/ Total wavenumber power (dB)')
%title('Radiating content of reference signal...
% vs accelerometer separation')

[ratio,xx]=max(10.*log10(RadiatingRatio)); Spacing = XX(xx);
fprintf('Ideal spacing: %2.1f cm (%2.2f inches)  \n'...
,Spacing*100,Spacing*100/2.54);
```

C.3 Error Array Far Field Analysis

MicArray was used to analytically determine the performance of an error array placed in a far field acoustic field.

```
% Directiviuty of a circular array of Nmic microphones
% kRmic = micarray1(Rmic,f)
%   where kRmic = wave number * mic array radius
%           Rmic = mic array radius (m)
%           f = frequency (Hz)
%
function [kRmic] = micarray1(Rmic,f)

%number of mics
Nmic = 3; SignMic = ones(1,Nmic);
SignMic(2) = 1;    %create a dipole source

omega = 2*pi*f;

%Observer microphine radius = 1m  (make this the distance from mic
%plane to radiating source)
Robs = 50/39.37;

%In-Plane Sweep angle (radians) from x =0 anticlosckise trhough y
%axis to x = 0
dtheta = pi/30;
Theta = [0:dtheta:2*pi];


%Normal-to-Plane Sweep angle (radians) (anti colockwise from x-y
%plane through z axis to x-y plane) dphi = pi/30; Phi =
[0:dphi:2*pi];

Thetamic = 2*pi/Nmic;

for n = 1:Nmic
    Xmic(n) = [Rmic*cos((n-1)*2*pi/Nmic)];
    Ymic(n) = [Rmic*sin((n-1)*2*pi/Nmic)];
    Zmic(n) = 0; %mics always in the z=0 plane
end

%Wave speed
c = 343;        %m/s
k = omega/c;  %acoustic wavenumber
```

```
a = 1.5/1000;              %Mic orifice radius (m)

for tt = 1:length(Theta)
    %for pp = 1:length(Phi)
   for pp = 1:length(Phi); %pp=round(0.5*length(Phi));

            %Coordinatres
            Xobs = Robs*cos(Phi(pp))*cos(Theta(tt));
            Yobs = Robs*cos(Phi(pp))*sin(Theta(tt));
            Zobs = Robs*sin(Phi(pp));

            Xvect(tt,pp) = Xobs;
            Yvect(tt,pp) = Yobs;
            Zvect(tt,pp) = Zobs;

            r = sqrt((Xobs-Xmic).^2+(Yobs-Ymic).^2+(Zobs).^2);
            Pobs(tt,pp) = sum((exp(-j*k.*r))./r);

            %Add a centered mic
%             r0 = Robs;
%             P0 = (exp(-j*omega*r0*c))/r0;
%             Pobs(tt,pp) = P0 + Pobs(tt,pp);

    end %end Phi loop
end     %end Theta loop


figure(1) surf(Xvect,Yvect,Zvect, 20.*log10(abs(Pobs))) colorbar
vert shading interp xlabel('X dimension (m)') ylabel('Y dimension
(m)') zlabel('Z dimension, (m)') titlestr = ['k*Rmic = ',
num2str(k*Rmic)]; title(titlestr);

%kRmic = k*Rmic;
```

C.4 Design of the Error Microphone Array

MAD.m, **M**icrophone **A**rray **D**esigner, was used to analytically determined the directivity of the error array at a given design frequency. The array diameter and the number of equally spaced microphones placed on this diameter may be edited to achieve the desired performance. Chapter 4—Error Sensing discusses the development of the theory and presents theoretical gain, $E_{array}^{hemisphere}$ and corresponding plots. See also *MicArrayNF.m* which further characterizes the error array given acoustic near field effects.

```
%%%%%%%%%%%%%%%%%%%%%%%%%%%%%%%%%%%%%%%%%%%%%%%%%%%%%%%%%%%%%%%%%%%%%%%
%Program: MAD.m   MicrophoneArrayDesigner
%
%This script determines the required microphone array diamter
%given a desired frequency, number of mics and directivity of
%sound power. Array gain = # of dB's the focus of the array is
% above the remaining sensed sound power.
%
%
%Note,  0.0254 m/inch
%
%%%%%%%%%%%%%%%%%%%%%%%%%%%%%%%%%%%%%%%%%%%%%%%%%%%%%%%%%%%%%%%%%%%%%%%

%Directiviuty of a circular array of Nmic microphones
% kRarray = micarray1(Rarray,f)
%   where kRarray = wave number * mic array radius
%           Rarray = mic array radius (m)
%           f = frequency (Hz)
%
clear;close all;
%Set Plot Default Values
set(0,'DefaultAxesFontSize',16) set(0,'DefaultLineLineWidth',2)
set(0,'DefaultAxesFontName','arial')

%Prompt for inputs
prompt={'Frequency (Hz)','Number of Microphones in Array','Array
gain (dB)',...
      'Source dimension (m)','Distance of array from source (m)',...
      'Maximum array radius (m)',...
      'Resolution for calculating array radius (m)'};

if exist('defMAD.mat') ~= 2
   def={num2str(800),num2str(3),num2str(6),'3*0.0254',...
   '4*0.0254','3*0.0254','0.25*0.0254'};
else;load defMAD;end
```

```
xtitle='Analysis Parameters'; lineNo=1;
answer=inputdlg(prompt,xtitle,lineNo,def);
f=str2num(char(answer(1))); Nmic=str2num(char(answer(2)));
ArrayGainMin=str2num(char(answer(3)));
Dsource=str2num(char(answer(4))); Ddist=str2num(char(answer(5)));
RarrayMax=str2num(char(answer(6)))/2;
dRarray=str2num(char(answer(7)));

def={num2str(f),num2str(Nmic),num2str(ArrayGainMin),num2str(Dsource),...
      num2str(Ddist),'num2str(RarrayMax)','num2str(dRarray)'};
save defmmcoh def


%%  ??? dipole? for wha'?
%create a dipole source
%SignMic = ones(1,Nmic);
%SignMic(2) = 1;

omega = 2*pi*f;

%Cone half-angle of the array focus
% (radiated noise in this cone is what we want to measure)
Psi = atan2(Dsource/2,Ddist);       %actual cone angle

%Normal-to-Plane Sweep angle (radians)
% (anti clockwise from x-y plane through z axis and back to x-y plane)
dphi = (pi-Psi)/pi/30;
%Phi = [0:dphi:2*pi]; %for entire sphere (accounts for the effect of reflections)
Phi = [0:dphi:pi]; %for hemisphere (free field radiation -- no reflections)

%closest cone angle to the Phi grid
Psi = floor(Psi/dphi)*dphi;

%In-Plane Sweep angle (radians) from x =0 anticlockwise
%though y axis and back to x = 0
dtheta = pi/30; Theta = [0:dtheta:2*pi];

%Observer microphine radius = 1m
Robs = 1;

%Element of area on imaginary sphere of radius Robs
dA = Robs^2*sin(dtheta)*sin(dphi);
```

```
%Angular spacing of microphones in array
Thetamic = 2*pi/Nmic;

%constants
c = 343;            %m/s
k = omega/c;    %acoustic wavenumber
rhoc = 415;     %air density x speed of sound, sea level, 20degC (kg/m^2/s)

%Iterate on array radius
Win=0; Wout=0;

%rz = 10*0.0254;            %out of plane distance for center mic
ArrayGain = 0;
Rarray = 0.5*0.0254;  %start array radius at 1/2"
ConeIn=0; ConeOut=0; index = 1; while ArrayGain < ArrayGainMin

   for n = 1:Nmic
    Xmic(n) = [Rarray*cos((n-1)*2*pi/Nmic)];
    Ymic(n) = [Rarray*sin((n-1)*2*pi/Nmic)];
    Zmic(n) = 0; %mics always in the z=0 plane
    end

    for pp = 1:length(Phi)
      for tt = 1:length(Theta)

            %Coordinates
            Xobs = Robs*cos(Phi(pp))*cos(Theta(tt));
            Yobs = Robs*cos(Phi(pp))*sin(Theta(tt));
            Zobs = Robs*sin(Phi(pp));

            Xvect(tt,pp) = Xobs;
            Yvect(tt,pp) = Yobs;
            Zvect(tt,pp) = Zobs;

            r = sqrt((Xobs-Xmic).^2+(Yobs-Ymic).^2+(Zobs).^2);
            Pobs(tt,pp) = sum((exp(-j*k.*r))./r);

            %Add a centered mic
            %r0 = sqrt(rz^2 +Robs^2 - 2*rz*Robs*cos(pi-Phi(pp)));
            %P0 = (exp(-j*omega*r0*c))/r0;
            %Pobs(tt,pp) = P0 + Pobs(tt,pp);


            %Calculate total power of array over desired focus
            if(( (Phi(pp) > pi/2 - Psi) & (Phi(pp) < pi/2 + Psi) ) )
```

```
               %inside the cone
               Win = Win + abs(Pobs(tt,pp)).^2 * dA / rhoc;
            else
               %outside the cone
               Wout = Wout + abs(Pobs(tt,pp)).^2 * dA / rhoc;
            end

         end %end Phi loop
    end      %end Theta loop


%Determine the array gain
if Win > 0; ArrayGain = 10*log10((Win+Wout)/Wout); end
fprintf('Array Diamter=%2.1f inches,...
 Array Gain(dB)=%2.2f \n',2*Rarray/0.0254,ArrayGain)

DiamVector(index) = 2*Rarray; GainVector(index) = ArrayGain;

if ArrayGain < ArrayGainMin; Win=0; Wout=0;end if Rarray >
RarrayMax;fprintf('Maximum array radius exceeded.\n');break;end


Rarray = Rarray + dRarray; index = index+1;

end % Array radius index loop
Rarray = Rarray - dRarray;


%Cone Geometry
ThetaCone = [0:2*dtheta:2*pi]; Dcone = atan(Psi)*2*Robs; XCircle =
Dcone*cos(ThetaCone); YCircle = Dcone*sin(ThetaCone); ZCircle =
Robs*ones(length(ThetaCone));

figure
%set(0,'DefaultLineLineWidth',0.5)
%plot3(diag(XCircle),diag(YCircle),eye(length(XCircle)),'k:' )
%hold on
plot3(XCircle,YCircle,Robs*ones(1,length(XCircle)),'k-' ) hold on
%surf(Xvect,Yvect,Zvect, 20.*log10(abs(Pobs)))
%surf(Xvect,Yvect,Zvect,10*log10(abs(Pobs)) /max(max(log10(abs(Pobs)))))
surf(Xvect,Yvect,Zvect,20*log10(abs(Pobs /abs(max(max(Pobs))) ))
) colorbar vert shading interp view(2) xlabel('X (m)') ylabel('Y
(m)')
%zlabel('Z (m)')
grid
```

C.5 Error Array Near Field Rejection Analysis

MicArrayNF.m was used to analytically determined the performance of an error array placed in the acoustic near field due to the plate used for noise control studies. This simulation was used to determine near field array gains and near field rejection gains as discussed in Chapter 4—Error Sensing.

```
% Directiviuty of a circular array of Nmic microphones
% kRmic = micarray1(Rmic,f)
%   where kRmic = wave number * mic array radius
%           Rmic = mic array radius (m)
%           f = frequency (Hz)
%
% John D'Angelo
% Modified September 4, 2003
%
%Cases:
%   1) Uniform
%   2) Monopole
%   3) Dipole
%   4) Quadrapole
%   5) Random phase
%
%function [kRmic] = MicArrayNF(Rmic,f)

clear;close all;
%Set Plot Default Values
set(0,'DefaultAxesFontSize',16) set(0,'DefaultLineLineWidth',2)
set(0,'DefaultAxesFontName','arial')

%Variable Parameters
type=2; %type = 1,2

VibDistIndex = 2; %1=uniform (orig), 2=Random, 3=monopole, 4=dipole, 5=quadapole
%NumElem = [10:10:100];          %Number of elements along x or
NumElem = 60;


%Simulation Parameters
f = 800;                        %Analysis frequency (Hz)
Rtarget = 5/2 /39.37;           %Desired target radius
h = 7 /39.37;                   %height of array from radiating panel
```

```
Rmic = 3/2 /39.37;                %Mic Array radius

omega = 2*pi*f;
c = 343;                          %acoustic wave speed
k = omega/c;                      %acoustic wavenumber


%%%%%%%%  PISTON ARRAY GEOMETRY (was originally a panel)

Wpanel = 9.75/39.37; Lpanel = 20/39.37;  %Width and Length of panel


for nn = 1:length(NumElem)

dXpanel = 2/NumElem(nn); dYpanel = dXpanel;

%Element center position along "X"
Xpanel = [-1+dXpanel/2:dXpanel:1-dXpanel/2]*Wpanel/2;

%Element center position along "Y"
Ypanel = [-1+dYpanel/2:dYpanel:1-dYpanel/2]*Lpanel/2;



%%%%%%%%  MICROPHONE GEOMETRY

a = (11/64)/2 / 39.37;  %Accousticel mics are 11/64" in diameter

%number of mics
Nmic = 3; SignMic = ones(1,Nmic);
%SignMic(2) = 1;    %create a dipole source


%Location of single, centered microphone
X0 = 0; Y0 = 0; H0 = h;

%Location of microphone array
for n = 1:Nmic
    Xmic(n) = [Rmic*cos((n-1)*2*pi/Nmic)];
    Ymic(n) = [Rmic*sin((n-1)*2*pi/Nmic)];
end
```

```
%%%%%%%%  TARGET GEOMETRY
Qtarget = [0:pi/10:2*pi]; Xtarget = Rtarget * cos(Qtarget);
Ytarget = Rtarget * sin(Qtarget); Ztarget = 3 *
(zeros(length(Xtarget)) + diag(diag(ones(length(Xtarget)))) );




%%%%%%%%  ARRAY AND TARGET PLACEMENT
if type == 0
    dX = 0; dY = 0;                     %Type 0 -- Center placement
elseif type==1
    dX = 2.44/39.37; dY = 7.5/39.37;    %Type I Array Position
elseif type==2
    dX = 2.44/39.37; dY = 2.5/39.37;    %Type II Array Position
else
    fprintf('Not a valid array position. \n\n')
    break
end


%Single Mic
X0 = X0 + dX; Y0 = Y0 + dY;

%Mic Array
Xmic = Xmic + dX; Ymic = Ymic + dY;

%Target
Xtarget = Xtarget + dX; Ytarget = Ytarget + dY;


%Plate Vibratrion Condition (uniform, random, monopole, dipole, quadrapole)
if VibDistIndex == 1 %Uniform
    VibDist = ones(NumElem(nn));

elseif VibDistIndex == 2 %Random
    VibDist = rand(NumElem(nn));

elseif VibDistIndex == 3 %Monopole
    Xpos = Xpanel + abs(min(Xpanel));
    Ypos = Ypanel + abs(min(Ypanel));
    for ii = 1:length(Xpanel)
        for jj = 1:length(Ypanel)
            VibDist(ii,jj) =...
             sin( Xpos(ii)/Wpanel *pi ) * sin( Ypos(jj)/Lpanel  *pi );
```

```
    end; end;

elseif VibDistIndex == 4 %Dipole
    Xpos = Xpanel + abs(min(Xpanel));
    Ypos = Ypanel + abs(min(Ypanel));
    for ii = 1:length(Xpanel)
        for jj = 1:length(Ypanel)
            VibDist(ii,jj) =...
             sin( Xpos(ii)/Wpanel *2*pi ) * sin( Ypos(jj)/Lpanel *pi );
    end; end;

elseif VibDistIndex == 5 %Quadrapole
    Xpos = Xpanel + abs(min(Xpanel));
    Ypos = Ypanel + abs(min(Ypanel));
    for ii = 1:length(Xpanel)
        for jj = 1:length(Ypanel)
            VibDist(ii,jj) =...
            sin( Xpos(ii)/Wpanel *2*pi ) * sin( Ypos(jj)/Lpanel *2*pi );
    end; end;

end




%%%%%%%%  RESULTING SOUND PRESSURE

%Sound pressure at Single Mic at the center of the array
%  (needed to calculate array gain)
for ii = 1:length(Xpanel)
    for jj = 1:length(Ypanel)

        R0 = sqrt( (Xpanel(ii)-X0)^2 + (Ypanel(jj)-Y0)^2 + H0^2 );

   %Pressure at center mic due to each (ii,jj) elemental radiating plate area
        Ponemic(ii,jj) = exp(-j*k*(R0-a))/R0;

    end  %end jj loop
end  %end ii loop

%sans near field
PonemicFF = Ponemic .* VibDist;

%Apply the near field effects
Ponemic(:,:) = j*k/(1+j*k*a) * Ponemic(:,:) .* VibDist;
```

```
%Sound pressure at sum of Mic Array
for ii = 1:length(Xpanel(:))
    for jj = 1:length(Ypanel(:))

   %Radial distance from (ii,jj) panel element
   %   to each microphone in the array
   R1 = sqrt( (Xpanel(ii)-Xmic(1))^2 + (Ypanel(jj)-Ymic(1))^2 + H0^2 );
   R2 = sqrt( (Xpanel(ii)-Xmic(2))^2 + (Ypanel(jj)-Ymic(2))^2 + H0^2 );
   R3 = sqrt( (Xpanel(ii)-Xmic(3))^2 + (Ypanel(jj)-Ymic(3))^2 + H0^2 );
   Parray(ii,jj) = exp(-j*k*(R1-a))/R1 +...
      exp(-j*k*(R2-a))/R2 + exp(-j*k*(R3-a))/R3 ;

    end  %end jj loop
end  %end ii loop

%sans near field
ParrayFF = Parray .* VibDist;

%Apply the near field effects
Parray(:,:) = j*k/(1+j*k*a) * Parray(:,:) .* VibDist; Parray(:,:)
= Parray(:,:)/3;



%%%%%%%%  ARRAY GAIN --- Directionality
%Mean square pressure within target and total pressure measured
% using single mic and mic array
PTargetArrayVal = 0; PTargetOneMicVal = 0; POneMicVal = 0;
PArrayVal = 0;

POneMicValFF = 0; PArrayValFF = 0;


for ii = 1:length(Xpanel(:))
    for jj = 1:length(Ypanel(:))

        if  sqrt(Xpanel(ii)^2 + Ypanel(jj)^2) <= Rtarget
            PTargetOneMicVal = PTargetOneMicVal + Ponemic(ii,jj);
            PTargetArrayVal =  PTargetArrayVal  + Parray(ii,jj);
```

```
        end  %end if

        POneMicVal = POneMicVal + Ponemic(ii,jj);
        PArrayVal = PArrayVal + Parray(ii,jj);


        %Farfield study (use to determine nearfield rejection gain)
        POneMicValFF = POneMicValFF + PonemicFF(ii,jj);
        PArrayValFF = PArrayValFF + ParrayFF(ii,jj);


    end  %end jj loop
end  %end ii loop


Gain(nn)  = 1/( 1 - ( (PTargetArrayVal.^2/PTargetOneMicVal.^2) /
(PArrayVal.^2/POneMicVal.^2) ) ); Gain(nn) =
10*log10(abs(Gain(nn)));

GainNFreject(nn)  = ( abs(POneMicVal)/abs(POneMicValFF) ) / (
abs(PArrayVal)/abs(PArrayValFF) ) ; GainNFreject(nn) =
10*log10(abs(GainNFreject(nn)));
fprintf(' Array Gain = %2.1f  dB \n Nearfield Rejection Gain = ...
%2.1f dB \n',Gain(nn),GainNFreject(nn))

end  %NumElem for loop


figure
surf(Xpanel,Ypanel,zeros(length(Parray)),20*log10(abs(Parray -
Ponemic) ./ max(max(abs(Parray - Ponemic))) )) xlim([min(Ypanel)
max(Ypanel)]) ylim([min(Ypanel) max(Ypanel)]) xlabel('Plate Width
(m)') ylabel('Plate Length (m)') colorbar vert shading interp
view(2) hold on plot(Xtarget,Ytarget,'k')


figure
surf(VibDist) colorbar vert shading interp view(2) hold on
xlabel('Element Number along Width') ylabel('Element Number along
Length')

figure plot(NumElem, Gain,'bo-', NumElem, GainNFreject,'ro-')
xlabel('Number of Elements per Side') ylabel('Gain (dB)')
legend('Near Field Sensor Aray Gain','Near Field Rejection
Gain',4)
```

```
%ylim([0 12])
```

C.6 Primary Path Multiple Coherence

Primary path multiple coherence codes are presented here. These codes were used for determining the coherence between the reference signal of a single control channel to all error sensor arrays and all observer microphones. This was performed for all reference designs presented in Chapter 3—Reference Sensing and Chapter 6—Coherence and Causality Studies.

Primary Path Multiple Coherence, MCoh.m

This code was used to process time domain data into coherence and theoretical maximum achievable control for references consisting of one, two, or three independent point reference measurements per actuator.

```
%%%%%%%%%%%%%%%%%%%%%%%%%%%%%%%%%%%%%%%%%%%%%%%%%%%%%%%%%%%%%%%%%%%%%%%%%%%%
%John D'Angelo
%November 14,2000
%%%%%%%%%%%%%%%%%%%%%%%%%%%%%%%%%%%%%%%%%%%%%%%%%%%%%%%%%%%%%%%%%%%%%%%%%%%%
%description:   Plots multiple coherence for several data sets
%                   Works with multicoh.m
%
%%%%%%%%%%%%%%%%%%%%%%%%%%%%%%%%%%%%%%%%%%%%%%%%%%%%%%%%%%%%%%%%%%%%%%%%%%%%
clear;close all;
%Set Plot Default Values
set(0,'DefaultAxesFontSize',16) set(0,'DefaultLineLineWidth',2)
set(0,'DefaultAxesFontName','arial')
%
cd D:\Users\John\research6_8ch_control_tests\TG47_8_Ch_Multicoh
channel = 5; chn = channel+2; eval(['load Channel_'
num2str(channel) '.mat' ])

Nerr=24;        %total number of mics
Nerr_obs = 6;       %number of observer mics
Nerr_error = 8;   %number of error rings
Nref=1;
%Fs=4000;
Fmax=1200; Nfft=1024;
df = Fs/Nfft; freq = [0:df:Fmax]';

%notes:
% Channel 1:      accelerometer reference
% Channel 2:      distributed pvdf reference
% Channels 3-10:  summed error rings
% Channels 11-16: observer mics
```

```
%multiple coherence to observer mics
data = data_in(:,[1 11:16]);
[mcoh_accel_obs]=multicoh_noplots(Nerr_obs,Nref,data,Nfft,Fs,Fmax);
MaxControl_accel_obs = -10*log10(1-mcoh_accel_obs.^2); clear data
figure subplot(2,1,1) plot(freq,abs(mcoh_accel_obs)) xlim([0
Fmax]) ylim([0 1]) subplot(2,1,2)
plot(freq,abs(MaxControl_accel_obs)) xlim([0 Fmax])

data = data_in(:,[2 11:16]);
[mcoh_pvdf_obs]=multicoh_noplots(Nerr_obs,Nref,data,Nfft,Fs,Fmax);
MaxControl_pvdf_obs = -10*log10(1-mcoh_pvdf_obs.^2); clear data
figure subplot(2,1,1) plot(freq,abs(mcoh_accel_obs)) xlim([0
Fmax]) ylim([0 1]) subplot(2,1,2)
plot(freq,abs(MaxControl_accel_obs)) xlim([0 Fmax])

%multiple coherence from accel to error rings
data = data_in(:,[1 3:10]);
[mcoh_accel_error]=multicoh_noplots(Nerr_error,Nref,data,Nfft,Fs,Fmax);
MaxControl_accel_error = -10*log10(1-mcoh_accel_error.^2); clear
data figure subplot(2,1,1) plot(freq,abs(mcoh_accel_error))
xlim([0 Fmax]) ylim([0 1]) subplot(2,1,2)
plot(freq,abs(MaxControl_accel_error)) xlim([0 Fmax])

%ordinary coherence from accel to corresponding error ring
data = data_in(:,[1 chn]);
[coh_accel_error]=multicoh_noplots(1,Nref,data,Nfft,Fs,Fmax);
MaxControl_coh_accel_error = -10*log10(1-coh_accel_error.^2);
clear data figure subplot(2,1,1) plot(freq,abs(coh_accel_error))
xlim([0 Fmax]) ylim([0 1]) subplot(2,1,2)
plot(freq,abs(MaxControl_coh_accel_error)) xlim([0 Fmax])

%multiple coherence from pvdf to coherence to error rings
data = data_in(:,[2 3:10]);
[mcoh_pvdf_error]=multicoh_noplots(Nerr_error,Nref,data,Nfft,Fs,Fmax);
MaxControl_pvdf_error = -10*log10(1-mcoh_pvdf_error.^2); clear
data figure subplot(2,1,1) plot(freq,abs(mcoh_pvdf_error)) xlim([0
Fmax]) ylim([0 1]) subplot(2,1,2)
plot(freq,abs(MaxControl_pvdf_error)) xlim([0 Fmax])

%ordinary coherence from pvdf to corresponding error ring
data = data_in(:,[1 chn]);
[coh_accel_error]=multicoh_noplots(1,Nref,data,Nfft,Fs,Fmax);
MaxControl_coh_pvdf_error = -10*log10(1-coh_accel_error.^2); clear
data figure subplot(2,1,1) plot(freq,abs(coh_accel_error)) xlim([0
Fmax]) ylim([0 1]) subplot(2,1,2)
```

```
plot(freq,abs(MaxControl_coh_pvdf_error)) xlim([0 Fmax])
```

Primary Path Coherence Using PVDF Reference Sensors, Coh.m

This code was used to process time domain data into coherence and theoretical maximum achievable control using either the discrete reference sensor arrays or the PVDF reference sensors.

```
% This script is used to determine the ordinary coherence between reference
% sensors and error arrays.
% Reference sensors were the round PVDF spatial sensors
%
% Data is derived from TG48 test
%
% John D'Angelo
% October 2, 2003
%
% %%%%%%%%%%%%%%%%%%%%%%%%%%%%%%%%%%%%%%%%%%%%%%%%%%%%%%%%%%%%%%%%%%%%%%%%%%%
clear;close all;clc
%Set Plot Default Values
set(0,'DefaultAxesFontSize',16) set(0,'DefaultLineLineWidth',2)
set(0,'DefaultAxesFontName','arial')

% Use for Discrete Reference Sensor Arrays
%  cd 'C:\Documents and
%  Settings\John\Data\TG36_ContrSimPathsAndMCohSumRefs\'
%  %load PrimaryPathSummedRefsSPKR
%  load PrimaryPathSummedRefsTBL


%Use for PVDF Reference Sensor
cd 'C:\Documents and Settings\John\Data\research6b\COH using...
PVDF\' load TG48_Error4inch_PvdfRefs
%      % %loaded variables:
%      % Fs = 4000 Hz, Sample rate in Hertz
%      % time_data(:,ch#)  Acquired time-domain data
%      % time_data(:,1:8)  Accelerometer reference signals
%      % time_data(:,9:16)  error array (summed) signals
%      % time_data(:,17:22)  Observer signals
diary Act8.txt RR = 8;

Npts = 35*Fs; Ref = time_data(1:Npts,1:8); Err =
time_data(1:Npts,9:16); Nerr = 8; Nobs = 6; Nref = 1; Obs =
```

```
time_data(1:Npts,17:22); clear time_data

%% ----  COHERENCE AT ERROR ARRAYS ---
%----Actuator #1
[mcoh1,cperf1,cperfbw1,freq]=multicoh(Nerr,Nref,[Err,
Ref(:,RR)],1024,Fs,1000,400,800); cperfbw1 figure subplot(2,1,1)
plot(freq,real(mcoh1))
%xlabel('Frequency (Hz)')
ylabel('Coherence') subplot(2,1,2) plot(freq,cperf1)
xlabel('Frequency (Hz)') ylabel('Theoretical Max Control (dB)')
legend('1','2','3','4','5','6','7','8')
%text(-100,-15,'Actuator #1, 1 Reference, Error Arrays')
pause print -dpng Act8_AtErrors_PVDF
%clear freq mcoh cperf


%% ----  COHERENCE AT OBSERVER MICROPHONES ---
%----Actuator #1
[mcoh1,cperf1,cperfbw1,freq]=multicoh(Nobs,Nref,[Obs,
Ref(:,RR)],1024,Fs,1000,400,800); cperfbw1 figure subplot(2,1,1)
plot(freq,real(mcoh1))
%xlabel('Frequency (Hz)'
ylabel('Coherence') subplot(2,1,2) plot(freq,cperf1)
xlabel('Frequency (Hz)') ylabel('Theoretical Max Control (dB)')
legend('1','2','3','4','5','6')
%text(-100,-15,'Actuator #1, 1 Reference, Observer Mics')
pause print -dpng Act8_AtObsMics_PVDF
%clear freq mcoh cperf

diary
```

C.7 Feed Forward, Filtered–x Control Simulation

Pre– and post–processing codes used with the feed forward, filtered–x control simulation program, *LMSFilterX*, are presented in this section. Two codes were used for pre–processing—*SysId.m* and *MakeSim.m*. The remaining four codes were used for post–processing of the results obtained from the control simulation. Each of these codes was written by the author.

Simulations using these software tools are presented in Chapter 7—Active Noise Control.

System Identification, SysId.m

System identification, or error path, filters were generated using *SysId.m*. Here, the error paths between each actuator and each error or observer location were determined. These filters were then used in *MakeSim.m*.

```
%John D'Angelo
%February 12, 2002
%
%file: SysID.m
%This script is used to identify the system id of the adaptive,
%filtered-x feedforward controller.
%Secondary path filters determined in this script are then to be
%used in the controller script, FFC_8ch.m
%
clear;close all;
%
%Set Plot Default Values
set(0,'DefaultAxesFontSize',16) set(0,'DefaultLineLineWidth',2)
set(0,'DefaultAxesFontName','arial')
%
%Set filter parameters
Ncc = 8;                    %Number of control channels
I = 60;                     %Number of Sys ID filter coeffs
CoeffVect = [1:1:I];
Fmax = 1200;                %Cut-off frequency
FcHP = 400; FcLP = 500;     %Band pass freqs (Hz)
alpha = 0.003;       %Covergence parameter

%Change to working directory
cd D:\Users\John\research6_8ch_control_tests\TG48and49
%cd D:\Users\John\research6_8ch_control_tests\TG48and49\ErrorMicsInObsPlane
%cd d:\users\john\research6_8ch_control_tests\ControlSimCheck

%Loop through each control channel
for cc=1:Ncc
```

```
    fprintf('\n')

    %load actuator "cc" data file
    eval(['load TG49_Error4inch_Actuator' num2str(cc) '.mat ;'])
    %eval(['load TG49_Error20inch_Actuator' num2str(cc) '.mat ;'])

    %eval(['load SecondaryPathAct' num2str(cc) '.mat ;']);
    %time_data=data_in;
    %clear data_in
    %Fs=2000;  %remove for Fs=4000 Hz

    if cc==1;
        Fny = Fs/2;
        N=4;                    %4th order filter
        Werror = [FcHP FcLP]/Fny; [Berror,Aerror]=butter(N,Werror);
        Wvoltage = FcLP/Fny; [Bvoltage,Avoltage]=butter(N,Wvoltage);
        clear FcHP FcLP Fny N Werror Wvoltage
    end


    %Decimate input data to Fs = 2000 Hz  *** comment out for Fs = 4000 Hz
    %time_data = time_data(2:2:length(time_data),:);

    InputVoltage = time_data(:,size(time_data,2));
    time_data = time_data(:,1:size(time_data,2)-1);

%     %use these for ControlSimCheck
%     InputVoltage = time_data(:,1);
%     time_data = time_data(:,2:size(time_data,2));

    fprintf('System Id Filter Converged, Actuator #%1i: ',cc);

    %index through each error ring and observer mic
    for mm=1:size(time_data,2)

        SysIdTime = time_data(:,mm);
        ErrorPathIRold = zeros(I,1);
        nn=1;  %Time step index
        conv=0;

        Voltage = InputVoltage;  %resests the values of the input voltage

        while conv==0

            VoltageLP = filter(Bvoltage,Avoltage,InputVoltage(nn:nn+I-1));
```

```
            SysIdTimeBP = filter(Berror,Aerror,SysIdTime(nn:nn+I-1));

            [ErrorPathTF, Freq] = tfe(VoltageLP,SysIdTimeBP,I,Fs,I);
            ErrorPathTF2sided = [ErrorPathTF(1:I/2);
            conj(ErrorPathTF(I/2:-1:1))];
            ErrorPathIR = ErrorPathIRold + ifft(ErrorPathTF,I);

           %convergence threshold
            Threshold=max(abs((ErrorPathIRold-ErrorPathIR)/max(ErrorPathIR)));
            if Threshold < alpha;
                if mm <= Ncc;
                if mm==1;
                    fprintf('\n   Error #%1i',mm);
                    else fprintf(',%1i',mm);
                end
                else
                if mm-Ncc==1;
                    fprintf('\n   Observer #%1i',mm-Ncc);
                    else; fprintf(',%1i',mm-Ncc);
                end
                end
                conv=1;
            end

            ErrorPathIRold = ErrorPathIR;

           clear SysIdFilterCurrent ErrorPathIR
           nn = nn+1;

        end; clear nn conv Threshold
        %store filter in appropriately named variable
        if mm <= Ncc
            eval(['SysId_Actuator' num2str(cc) '_Error' num2str(mm)...
            '= ErrorPathIRold;'])
        else
            eval(['SysId_Actuator' num2str(cc) '_Obs' num2str(mm-Ncc)...
            '= ErrorPathIRold;'])
        end
        clear SysIdTime SysIdTimeBP SysIdFilterPrevious VoltageLP
        clear ErrorPathTF ErrorPathTF2sided Voltage ErrorPathIRold

    end; clear mm
    clear time_data
end;
```

```
%summon completion
for bb = 1:4;beep; pause(0.4);end;

clear bb cc alpha I Ncc  Aerror Berror Avoltage Bvoltage time_data
InputVoltage

%Save filter coeffs and other parameters to .mat file
eval(['save ' uiputfile('*.mat','Save error path variables to file
for use in control algorithm');])
```

C.8 Control System Pre–Processing Code, MakeSim.m

MakeSim.m was originally written by Chris Park of Vasci. The code was then modified by the author specifically for simulations performed in this research.

MakeSim.m was used to generate binary files of the primary acoustic field, vibration field, and of the error paths. In addition, *mat* files of the conditioned and unconditioned error primary field were generated for use in *AnaTimeFFSim.m*.

```
% create binary files for use by LMS Filterd-X simulation
% original code written by Chris Park
% modified as shown here by John D'Angelo
clear; close all
%
% Notes:
%
% 1. G and K are stored backwards such that Gij[1]
% is the END of the impulse response
% 2. G = [g11 g12 g13 ... g21 g22 ... gij ...] where i = err sensor
%  & j = actuator
% 3. K = [k11 k12 k13 ... k21 k22 ... kjh ...] where
% j = actuator & h = ref sensor
%
tau = -6;         % artificial time delay, 1.577 mS delay in controller
                  %    @ 2000 Hz, tau = -3.2 samples,  (use -3)
                  %    @ 4000 Hz, tau = -6.3 samples,  (use -6)

i1 = 1;         % 1st data point of time data
i2 = 2^12; Npts = i2-i1+1;

gain = 100000;  %remove gain in

%CHANGE
Fhp = 400; Flp = 500;   %low and high pass notch freqs
prefilter = 1;


%CHANGE
GerrFilename = 'plantEr.bin';   %name of file for all error paths
GobsFilename = 'plantOb.bin';   %name of file for all error paths
XZerrfiltFilename = 'timeEr400to500Hz.bin'; XZobsfiltFilename =
'timeOb400to500Hz.bin'; XZerrFilename = 'timeEr.bin';
XZobsFilename = 'timeOb.bin';

clear Kfilename;
```

```
%CHANGE
Nx = 4;                     % number of references?
Nu = 4;                     % number of controllers?
Ny = 4;                     % number of errors?
No = 6;                     % number of observers
Gtaps = 60;                 % number of sys id coeffs
Ktaps = 250;                % number of control coeffs
%Fs, sample rate (Hz)   (input in reference/error data file)


%********** INPUT ***********
%inputs required:
%       1) System Id coeffs from SysId.m
%       2) Reference and primary errors

%System Id Filters (from SysId.m)
%format: G11[N] G11[N-1]... G12[N]... Gij[N] where i = err sensor &
% j = actuator

%CHANGE
% cd d:\Users\John\CD1\M_Files\MIMO_LMS\ErrorsAt4inches
% load SysId_ErrorRings4inches_30coeffs_2000Hz_400to800HzBW.mat
cd d:\Users\John\CD1\M_Files\MIMO_LMS\ErrorsAt20inches load
SysId_ErrorRings20inches_60coeffs_4000Hz_400to500HzBW.mat


breaknow=0; if Nx==8
    %error paths
    kk=1;
    for yy = 1:Ny
    for uu = 1:Nu
        eval(['Gcurrent = SysId_Actuator' num2str(uu) '_Error'...
        num2str(yy) ';'])
        G(:,kk) = flipud(Gcurrent);
        kk=kk+1;
    end
    end

    %observer paths
    kk=1;
    for oo = 1:No
    for uu = 1:Nu
        eval(['Gcurrent = SysId_Actuator' num2str(uu) '_Obs'...
         num2str(oo) ';'])
```

```
        Gobs(:,kk) = flipud(Gcurrent);
        kk=kk+1;
    end
    end

elseif Nx==4
    %error paths
    kk=1;
    for yy = 3:Ny+2
    for uu = 3:Nu+2
        eval(['Gcurrent = SysId_Actuator' num2str(uu) '_Error'...
         num2str(yy) ';'])
        G(:,kk) = flipud(Gcurrent);
        kk=kk+1;
    end
    end

    %observer paths
    kk=1;
    for oo = 1:No
    for uu = 1:Nu
        eval(['Gcurrent = SysId_Actuator' num2str(uu) '_Obs'...
         num2str(oo) ';'])
        Gobs(:,kk) = flipud(Gcurrent);
        kk=kk+1;
    end
    end
else
    fprintf('This code setup only for 4 or 8 channels \n')
    breaknow=1;
end if breaknow==1; break; end



%Reference and primary error signals
% Format: time_data(:,1:Nx) = refs, time_data(:,Nx+1:Nx+Ny) =
% errors,
% time_data(:,Ny+1:Nx+Ny+Nobs) = observers
%load TG48_Error4inch_AccelRefs.mat
%load TG48_Error4inch_PvdfRefs.mat
load TG48_Error20inch_AccelRefs.mat
%load TG48_Error20inch_PvdfRefs.mat

if Nx==4
 %4 channel config: all refs, all errors, all obsevers
```

```
 % (1000x gain applied for lmsfilterx.exe)
    time_data=gain*time_data([2:2:length(time_data)],[3:6,11:14,17:22]);
else
 %8 channel config: all refs, all errors, all obsevers
    time_data = gain * time_data([2:2:length(time_data)],:);
end

b = ones(1,Nx);  % ref accelerometers
c = ones(1,Ny);  % err mics
cob = ones(1,No);  % obs mics
V_per_Pa = ones(1,Ny+No); % cal factors for mics

%for a real system, the error will lag the reference or at best
%have zero lag.  So, real systems have -tau values. if tau>=0,
  X = time_data([i1:i2]+tau,find(b==1));
  Y = time_data([i1:i2],Nx+find(c==1))*...
   diag(1./V_per_Pa(find(c==1)));
  Yob = time_data([i1:i2],Nx+Ny+find(cob==1))*...
   diag(1./V_per_Pa(find(cob==1))); else,
  X = time_data([i1:i2],find(b==1));
  Y = time_data([i1:i2]-tau,Nx+find(c==1))*...
   diag(1./V_per_Pa(find(c==1)));
  Yob = time_data([i1:i2]-tau,Nx+Ny+find(cob==1))*...
   diag(1./V_per_Pa(find(cob==1)));
end

%filter the references (X) and errors (Y)
if prefilter == 1,
  orderlp = 12;
  orderhp = 12;
  [B,A] = butter(orderlp,2*Flp/Fs);
  for n=1:Nx,
    Xh(:,n) = filter(B,A,X(:,n));
  end
  for n=1:Ny,
    Yh(:,n) = filter(B,A,Y(:,n));
  end
  for n=1:No,
    Yhob(:,n) = filter(B,A,Yob(:,n));
  end

  [B,A] = butter(orderhp,2*Fhp/Fs,'high');
  for n=1:Nx,
    Xh(:,n) = filter(B,A,Xh(:,n));
  end
```

```
  for n=1:Ny,
    Yh(:,n) = filter(B,A,Yh(:,n));
  end
  for n=1:No,
    Yhob(:,n) = filter(B,A,Yhob(:,n));
  end
else
    Xh = X; Yh = Y;
end


%/*****************************************************************/
%/* save the plant model, G                                       */

%/* file format: Ny Nu Gtaps G11[N] G11[N-1]... G12[N]... Gij[N] */
%/*****************************************************************/
%
%for errors
datafile = fopen(GerrFilename,'w+');
fwrite(datafile,Ny,'long');             %number of errors
fwrite(datafile,Nu,'long');             %number of controllers
fwrite(datafile,Gtaps,'long');          %number of sys id taps
for n=1:Nu*Ny,
  fwrite(datafile,G(:,n),'double');
end fclose(datafile);
%
%for observers
datafile = fopen(GobsFilename,'w+');
fwrite(datafile,No,'long');             %number of obs
fwrite(datafile,Nu,'long');             %number of controllers
fwrite(datafile,Gtaps,'long');          %number of sys id taps
for nn=1:Nu*No,
  fwrite(datafile,Gobs(:,nn),'double');
end fclose(datafile);



%/*****************************************************************/
%/* save the control filter, K                                    */

%/* file format: Nu Nx Ntaps K11[N] K11[N-1]... K12[N]... Kjh[N] */
%/*****************************************************************/
%
if exist('Kfilename'),
  datafile = fopen(Kfilename,'w+');
```

```
  fwrite(datafile,Nu,'long');
  fwrite(datafile,Nx,'long');
  fwrite(datafile,Ktaps,'long');
  for n=1:Nu*Nr,
    fwrite(datafile,K(n,:),'double');
  end
  fclose(datafile);
end


%/*****************************************************************/
%/* save the time data, X and Z                                   */

%/* file format: Nx Nz Npts X1[0] X2[0]...X1[1] X2[1]...  Z1[0]... */
%/*****************************************************************/
%
%filtered X and Z for errors (for generating the control coeffs)
datafile = fopen(XZerrfiltFilename,'w+');
fwrite(datafile,Nx,'long'); fwrite(datafile,Ny,'long');
fwrite(datafile,Npts,'long'); for k=1:Npts,
  fwrite(datafile,Xh(k,:),'double');    %save the band passed refs
end for k=1:Npts,
  fwrite(datafile,Yh(k,:),'double');    %save the band passed errors
end fclose(datafile);


%filtered X and Z for observers
datafile = fopen(XZobsfiltFilename,'w+');
fwrite(datafile,Nx,'long'); fwrite(datafile,Ny,'long');
fwrite(datafile,Npts,'long'); for k=1:Npts,
  fwrite(datafile,Xh(k,:),'double');    %save the band passed refs
end for k=1:Npts,
  fwrite(datafile,Yhob(k,:),'double');  %save the band passed errors
end fclose(datafile);



% UNfiltered X and Z (for determining the secondary error)
datafile = fopen(XZerrFilename,'w+'); fwrite(datafile,Nx,'long');
fwrite(datafile,Ny,'long'); fwrite(datafile,Npts,'long'); for
k=1:Npts,
  fwrite(datafile,X(k,:),'double');     %save the unconditioned refs
end for k=1:Npts,
  fwrite(datafile,Y(k,:),'double');     %save the unconditioned errors
end fclose(datafile);
```

```
%
%
% UNfiltered X and Z (for determining the secondary observers)
datafile = fopen(XZobsFilename,'w+'); fwrite(datafile,Nx,'long');
fwrite(datafile,Ny,'long'); fwrite(datafile,Npts,'long'); for
k=1:Npts,
  fwrite(datafile,X(k,:),'double');     %save the unconditioned refs
end for k=1:Npts,
  fwrite(datafile,Yob(k,:),'double');   %save the unconditioned observers
end fclose(datafile);


%/*****************************************************************/
%/* save the time data Z for use with ana_time                    */

%/*                                                               */
%/*****************************************************************/
%
data_in=Y/gain; save BaselineErrors Fs data_in

data_in=Yob/gain; save BaselineObservers Fs data_in

data_in=Yh/gain; save BaselineErrors400to500Hz Fs data_in

data_in=Yhob/gain; save BaselineObservers400to500Hz Fs data_in
```

C.9 Post–Processing of Control Simulation Data

CSimPost.m was used to post–process results obtained from lmsfilterx. The code is run once for the error and observation runs of each control simulation configuration. The script calls three subroutines, *PerfHist.m*, *ErrorHist.m*, *AnaTimeFFSim.m*, and *PerfComp.m* which are each listed below.

PerfHist.m is used to monitor the controller convergence by plotting the overall performance at each iteration of control. *ErrorHist.m* is used to extract output from *lmsfilterx*, and *AnaTimeFFSim.m* is used to convert time histories to the frequency domain. *PerfComp.m* was used to compute the mean reduction achieved over a prescribed frequency band.

The *CSimPost.m* code is:

```
% This script is use to post-process conttrol simulations
%   performed in LMSFilterX.exe
%   Sub-routines are called for each required task
%
% This routine...
%   ...was created to steamline the steps required to
%      post-process lmsfilterx results
%   ...was used only for the second set of control
%      simulations (2004 runs)
%
%                                              John D'Angelo
%                                              December 30, 2003
%
%JDAJDAJDAJDAJDAJDAJDAJDAJDAJDAJDAJDAJDAJDAJDAJDAJDAJDAJDAJDA
clear; close all;
%
%Set Plot Default Values
set(0,'DefaultAxesFontSize',16) set(0,'DefaultLineLineWidth',2)
set(0,'DefaultAxesFontName','arial')

fprintf('ATTENTION!!!\n') fprintf('The following modifications
must be made prior to running this script ....\n\n') fprintf('The
LOG and OUTPUT files generated by LMSFilterX.exe must have their
first lines REMOVED.')

cd 'C:\Documents and Settings\John\MIMO_LMS'

%Select the calibration file
a=['READ -- Select calibration file (Cal file must be in directory
containing the data)']; [file,path]=uigetfile('*.mat',a,0,0);
cd(path); load (file); cal=cal'; cal=10.^(cal/20);
```

```
%Plot limits
xmin=0; xmax=1000; CBmin=400; CBmax=800; if length(cal)==6
    ymin=-10; ymax=50;
    hliney=-8; %y-coord for horiz line in plot
    textx=500; texty=-6;  %"Control Band" text placement
else
    ymin=60; ymax=100;
    hliney=62; %y-coord for horiz line in plot
    textx=500; texty=63;  %"Control Band" text placement
end


%---Observe the Control Filters
a=['READ -- Select controlfilter BIN file'];
[file,path]=uigetfile('*.bin',a,0,0); cd(path) fid =
fopen(file,'r'); Ctaps = fread(fid); clear file path
% NumActs = Ctaps(1); %Number of actuators
% NumRefs = Ctaps(5); %Number of references
% NumTaps = Ctaps(9); %Number of Control filter taps
Ctaps = Ctaps(13:length(Ctaps));


%---Observe control convergence (PerfHist.m)
[Nsteps,perf] = perfhist(15,20); perfdb = -10*log10(perf);

figure plot([1:Nsteps],-10*log10(perf)) xlabel('Iteration Number')
ylabel('Overall Attenuation (dB)') xlim([1 Nsteps])
ylim([min(perfdb)-1 max(perfdb)+1])
%set(gcf,'Position',[0 50 1024 650])


%---Read the BAND PASSED TIME DOMAIN signals of the combined
%  error field and control voltages (ErrorHist.m)
[J,VactTime,dtimeBP,Fs] = errorhist;
%       J, value of the cost function
%       Vact, actuator voltage
%       dtimeBP, band passed combined error field
%       Fs, sample rate (Hz) as specified in "errorhist" input prompt

data_in = dtimeBP; %ana_time_ffsim wants inputs as "data_in"
eval(['save ' uiputfile('CombErrorTimeDataBP_.mat','SAVE -- Save
time domain combined errors') ' data_in Fs' ;]) clear data_in dt =
1/Fs; time = [0:dt:dt*(length(dtimeBP)-1)];

%Compute the frequency domain ALL-PASS Baseline data
```

```
[freq,Pxx,AW,RedNull] = ana_time_ffsim(1,cal,'All Pass');
BaselineAP = Pxx; BaselineAWAP = BaselineAP + AW; clear RedNull
Pxx

%---Compare primary and combined error fields conditioned over
%  the control band (AnaTimeFFsim.m)
[freq,Pxx,aw2,Reduction] = ana_time_ffsim(2,cal,'Band Pass');
eval(['save ' uiputfile('ReductionFreq_.mat','SAVE -- Save
spectral reduction data in dB with frequency vector ') ' freq
Reduction' ;])
BaselineBP = Pxx(1,:);              %Band-passed baseline
CombErrorBP = Pxx(2:size(Pxx,1),:); %Band-passed combined errors
BaselineAWBP = BaselineBP + AW;     %Band-passed, a-weighted baseline
CombErrorAWBP = CombErrorBP + AW;   %Band-passed, a-weight combined errors
clear Pxx aw2


eval(['save ' uiputfile('CombinedErrorsFreq_.mat','SAVE -- Save
combined error data in dB ') ' CombErrorBP CombErrorAWBP  ' ;])

figure plot(freq,BaselineAWAP,freq,(BaselineAWAP+Reduction))
xlabel('Frequency (Hz)') if exist('AW'); ylabel('Mean Squared
Pressure (dB_A)'); else; ylabel('Mean Squared Pressure (dB)'); end
xlim([min(freq) max(freq)]) legend('baseline','control',3) grid
xlim([xmin xmax]) ylim([ymin ymax]) line([CBmin CBmin],[ymin
ymax],'Color',[0 0 0],'LineStyle','--') line([CBmax CBmax],[ymin
ymax],'Color',[0 0 0],'LineStyle','--') line([CBmin CBmax],[hliney
hliney],'Color',[0 0 0]) text(textx,
texty,'\fontsize{16}\itControl Band')

%---Compare the undconditioned primary spectral response with the
%  unconditioned combined error field (PerfComp.m)
RdB_400to800Hz = perfcomp(Reduction,freq,400,800) RdB_50to1000Hz =
perfcomp(Reduction,freq,50,1000) RdB_480to600Hz =
perfcomp(Reduction,freq,480,600)
```

Control Performance History, PerfHist.m

PerfHist.m allows the monitoring of control filter convergence by plotting control versus iteration number. Before running this code, however, the *log* file saved by *LMSFilterX.m* must first have its first line (J_0) removed. In addition, the bracketed numbers in the right most column must all start at the same column number with the appropriate range specified in *PerfHist.m* on the following line:

```
perf(nn) = str2num(perfchar(16:21));
```

This code was set to read from the 16^{th} through the 21^{st} values.

```
function [Niter,perf] = perfhist(istart,iend)
% clear;clc;istart = 15; iend = 20;  %used for debuging function
% cd 'C:\Documents and Settings\John\MIMO_LMS'

%
% Reads the log file from lmsfilterx.exe and plots the overall
% attenuation in dB for each iteration.
%
%   Inputs
%       istart, Index to begin reading of reduction values per step
%       iend, Index to end reading of reduction values per step
%
%   Outputs
%       Niter, Number of iterations performed during lmsfilterx run
%       perf, Vector of performance acheived (linear scale)
%
%
%                                                   John D'Angelo
%                                                   April 22, 2002
%
%
%JDAJDAJDAJDAJDAJDAJDAJDAJDAJDAJDAJDAJDAJDAJDAJDAJDAJDAJDAJDAJDAJDA

%Get the FILENAME and PATH of the LOG file generated by LMSFILTERX.EXE
fprintf('\n\n Log file used:\n') a=['READ -- Select log file  for
analysis']; [filename,pathname]=uigetfile('*.log',a,0,0);
fprintf('\t %s%s \n',pathname,filename)
clear i a nn=1; terminate=0; cd(pathname) fid = (fopen(filename));
while terminate==0
    perfchar = fgets(fid);
    if perfchar(2) == 'J'

        %these indices must be set according to lms.log
        perf(nn) = str2num(perfchar(istart:iend));
        nn=nn+1;
    else
        terminate=1;
    end
    clear perfchar
end fclose(fid) Niter = nn-1;
```

Control Error History, ErrorHist.m

ErrorHist.m generate the time domain signals of the combined error field and of the actuator control voltages. The first line of the *txt* file, output by *LMSFilterX.m* must first be removed.

```
function [J,v,e,Fs] = errorhist
%
% Generates the time-domain signals of the combined error fields
% and actuator voltages.
% NOTE: The first line of output text file from lmsfilterx.exe
% must be removed prior to running
%
%
%   [J,v,e,Fs] = errorhist
%
%   Inputs
%       SELECTED during run
%
%   Outputs
%        J, value of the cost funtion
%        v, Actuator voltage time history
%        e, Combined error time history
%        Fs, Sample rate (Hz)
%
%                                                  John D'Angelo
%                                                  December 30, 2003
%
%JDAJDAJDAJDAJDAJDAJDAJDAJDAJDAJDAJDAJDAJDAJDAJDAJDAJDAJDAJDAJDA

%loading information about number of test cases
prompt={'High Pass Frequency (Hz)','Low Pass Frequency
(Hz)','Sampling Rate (Hz)',...
        'Number of Actuators','Number of Errors',...
        'Linear Gain (must be same as in MakeSim)'};
def={'400','800','4000','8','8','1'}; lineNo=1; xtitle='Selecting
number of test cases'; answer=inputdlg(prompt,xtitle,lineNo,def);
fhp=char(answer(1)); fhp=str2num(fhp); flp=char(answer(2));
flp=str2num(flp); Fs=char(answer(3)); Fs=str2num(Fs);
Nact=char(answer(4)); Nact=str2num(Nact); Nerr=char(answer(5));
Nerr=str2num(Nerr); gain=char(answer(6)); gain=str2num(gain);

%select and load the file
%(This data file is output by LMSFILTERX.EXE and therefore
%   is the BAND PASSED combined errors)
fprintf('File used:\n') a=['READ -- Select the data file obtained
by the control system (Output_*.text)'];
```

```
[filename,pathname]=uigetfile('*.txt',a,0,0);
fprintf('\t %s%s \n',pathname,filename)
cd(pathname) data = textread(filename); clear i a filename
pathname

N = [1:1:length(data)];                  %iteration number vector

J = data(:,1);                           %value of cost function
v = data(:,2:Nact+1);                    %actuator voltage
eap = data(:,Nact+2:Nact+Nerr+1);        %combined error

eap = eap/gain;
e=eap;%e = BandPass(eap,Fs,fhp,flp,4,4);
```

Time–to–Frequency Analysis, AnaTimeFFSim.m

AnaTimeFFSim.m is a modification of *AnaTime.m* written by Dr. Marty Johnson of the Vibration and Acoustics Laboratory at Virginia Tech.

AnaTimeFFSim.m was used to compare the primary and combined error fields conditioned over the control band. From this program is generated the *reduction* file—the control performance achieved.

```
function [freq,Pxxs,AW,reduction] =
ana_time_ffsim(num_case,cal,msg)
%
% Creating sum of the squared signals from time data recording
% made on the NI acquisition system. Simply run the program and
% select all of the relevant calibration and data files%
%
%
%
%   [freq,Pxxs,AW,reduction] = ana_time_ffsim(num_case,cal,msg)
%
%   Inputs
%       num_case, Number of cases to compare
%       cal, Calibration data
%       msg, Message used in prompt for loading data files
%        (ex. 'All Pass' or 'Band Pass')
%
%   Outputs
%       freq, Frequency vector used for plotting performance
%       Pxxs, autospectrae of the input signals (dB scale)
%           (Each selected file is a column in order selected,
%              ie. baseline is in first column)
%       AW, vector of A-weighted coefficients (dB scale)
%                To apply A-weight, ADD "AW" to a vector
%       reduction, Reduction vs. freq achieved (dB scale)
%
%   Function calls
%       aweight(freq), Computes A-weight vector for freqs
%
%
%                                              John D'Angelo
%                                              December 2003
%
%JDAJDAJDAJDAJDAJDAJDAJDAJDAJDAJDAJDAJDAJDAJDAJDAJDAJDAJDA

%loading files for analysis
```

```
data=[];si=[0];%si=[];
for i=1:num_case
    if i==1
     a=['READ -- Select ' msg ' ...
     Baseline time history data file'];
    else
     a=['READ -- Select ' msg ' ...
     Combined Error time history data file,...
     Case # ', num2str(i-1),' for analysis'];
    end
    [file,path]=uigetfile('*.mat',a,0,0);
    cd(path);
    load (file);

    %rem this line
    %(some daq programs call it data_in and some time_data)
    if exist('data_in')==0
        data_in = time_data;
    end

    if size(data_in,1) > 24000
        data_in = data_in(1:24000,:);
    end

    data=[data data_in.*(ones(length(data_in),1)*cal)];

    if i==1
        si = [si min(size(data_in))];
    else
        %si=[si si(i-1)+min(size(data_in))];
        si=[si si(i)+min(size(data_in))];
    end

    clear data_in
end


%loading information about signals
prompt={'Enter number of first data string :','Enter number of
last data string',...
      'Enter cut-off frequency:','Enter number of samples',...
      'Enter length of FFT', 'Include A-weighting? 1=Yes 0=No'};
def={'1',num2str(si(2)),'1200',num2str(length(data)),'1024','1'};
%def={'1',num2str(si(1)),'1200',num2str(length(data)),'1024','1'};
xtitle='Analysis Parameters'; lineNo=1;
```

```
answer=inputdlg(prompt,xtitle,lineNo,def);

mfs=char(answer(1)); mf=str2num(mfs); mls=char(answer(2));
ml=str2num(mls); cfreqs=char(answer(3)); cfreq=str2num(cfreqs);
num_maxs=char(answer(4)); num_max=str2num(num_maxs);
NFFTs=char(answer(5)); NFFT=str2num(NFFTs); aws=char(answer(6));
aw=str2num(aws);

%calculating autospectrum
if num_case==1
    %Pxx=zeros(1+(NFFT/2),1);
    [Pxx,freq]=PSD(data(1:num_max,1),NFFT,Fs);
    Pxxs=Pxx'/(freq(2));
    bin_max=1+floor(cfreq/freq(2));
else
    for o=1:num_case
        Pxx=zeros(1+(NFFT/2),ml-mf+1);
        for i=1:ml-mf+1
         [Pxx(:,i),freq]=PSD(data(1+si(o):num_max,i-1+mf+si(o)),NFFT,Fs);
        end

        size(freq)

        %calculating highest bin
        bin_max=1+floor(cfreq/freq(2));

        if ml-mf==0
            Pxxs(o,:)=Pxx'/(freq(2));
        else
            Pxxs(o,:)=sum(Pxx')/((ml-mf+1)*freq(2));
        end
    end
end

bin_max size(freq)

%calculating a weighting
if aw==1
    AW=ones(num_case,1)*aweight(freq(1:bin_max));
    aw=0;
else
    AW=zeros(num_case,bin_max);
end

Pxx=Pxx';
```

```
freq=freq(1:bin_max); Pxxs=10*log10(Pxxs(:,1:bin_max));
if num_case>1
    reduction = AW + Pxxs;
    %Subtract columns 2,3,... from column 1 (the baseline column)
    reduction = reduction - ones(size(reduction,1),1)*reduction(1,:);
    reduction = reduction(2:size(reduction,1),:);
else reduction = 0; end
```

Control Performance Comparison, PerfComp.m

PerfComp.m is the final stage required for analyzing the control achieved by *LMSFilterX.exe*. Here, control performance determined, as given in the *reduction* file, by *AnaTimeFFSim.m* is subtracted in the frequency domain from the unconditioned primary error field. The primary and combined error fields are then compared spectrally.

```
function [RdB] = perfcomp(reduction,freq,fs1,fe1)
%
%   This function computes the overall reduction (in dB) within
%   the specified control band and the overall reduction (in dB)
%   across the useable frequency band specified as freq
%
%   The overall sound pressure reduction is calculated over two bands.
%
%       Inputs
%           Reduction, reduction vs. frequency data
%           freq, frequency vector (Hz)
%           fs1, Begining of control band (Hz)
%           fe1, End of control band (Hz)
%
%       Outputs
%           RdBcb, Mean reduction (in dB) over the control band
%           RdBall, Mean redcution across the observed freq range
%
%
%                                                 John D'Angelo
%                                                 December 30, 2003
%
%JDAJDAJDAJDAJDAJDAJDAJDAJDAJDAJDAJDAJDAJDAJDAJDAJDAJDAJDAJDAJDAJDA
ii = find(freq>fs1); bin_start1=ii(1); clear ii ii =
find(freq>fe1); bin_end1=ii(1); clear ii RdB = 10*log10(
mean(10.^(reduction(:,bin_start1:bin_end1)/10) ) );
```

References

[1] R.B. Lindsay. The story of acoustics. *The Journal of Acoustic Society of America*, 39(4):629–644, 1966.

[2] S. M. Kuo and D. R. Morgan. *Active Control of Noise Systems*. John Wiley and Sons, New York, NY, first edition, 1996.

[3] B.S. Murray R.E. Hayden and M.A. Theobald. Boundary layer induced noise in the interior of aircraft. *NASA CR 172152*, 1983.

[4] M.E. Johnson C.R. Fuller and J.R. Griffin. Active-passive control of aircraft interior boundary layer noise using smart foam. *AIAA*, 2000.

[5] David A. Bies and Colin H. Hansen. *Engineering Noise Control, Theory and Practice*. E & FN Spon, London, second edition, 1996.

[6] W.O. Hughes and A.M. McNelis. Cassini/titan iv acoustic blanket development and testing. In *Proceedings—Institute of Environmental Sciences*, pages 205–221, 1996.

[7] L. Bradford and J.E. Manning. Attenuation of the cassini spacecraft acoustic environment. *Journal of Sound and Vibration*, pages 30–37, 1996.

[8] D.A. Carne M.D. Long and C.M. Fuller. Acoustic blanket effect on payload fairing vibration. In *Proceedings—Institute of Environmental Sciences*, pages 222–233, 1996.

[9] B.H. Lu Y.C. Ding and C.H. Ku. A new method for predicting the dynamic behaviors of three-layer viscoelastically sandwiched structures. In *10th International Modal Analysis Conference*, volume I, pages 637–641, San Diego, CA, 1992. Society for Experimental Mechanics.

[10] S. Nadella and M.D. Rao. Damping of composite structures using embedded viscoelastic layers. In *13th International Modal Analysis Conference*, volume I, pages 233–239, Nashville, TN, 1995. Society for Experimental Mechanics.

[11] K. Mukhopadhyay and H.B. Kingsbury. On the dynamic response of a rectangular sandwich plate with viscoelastic core and generally orthotropic facings. *Journal of Sound and Vibrations*, 47(3):233–239, 1976.

[12] N.W. Hagood and A. von Flotow. Damping of structural vibrations with piezoelectric materials and passive electrical networks. *Journal of Sound and Vibrations*, 146(2):243–265, 1991.

[13] A.S. Bicos D.L. Edberg and J.S. Fechter. On piezoelectric energy conversion for electronic passive damping enhancement. In *Proceedings of Damping '91*, pages Paper GBA–1, San Diego, CA, 1991.

[14] J.J Hollkamp. Multimodal passive vibration suppression with piezoelectric materials and resonant shunts. *Journal of Intelligent Material Systems and Structures*, 5:49–57, January 1994.

[15] M. Mercadel C.R. Fuller, J.P. Maillard and A.H. von Flotow. Control of aircraft interior noise using globally detuned vibration absorbers. *Journal of Sound and Vibration*, 82:615–624, 1995.

[16] M.R. Jolly and J.Q. Sun. Passive tuned vibration absorbers for sound radiation reduction from vibrating panels. *Journal of Sound and Vibration*, 191(4):577–583, 1996.

[17] C. Wang Z Sun, J. Sun and Y. Dai. Dynamic vibration absorbers used for increasing the noise transmission loss of aircraft panels. *Journal of Applied Acoustics*, 48(4):311–321, 1996.

[18] Y.M. Huang and C.R. Fuller. The effects of dynamic absorbers on the forced vibration of a cylindrical shell and its coupled interior sound field. *Journal of Sound and Vibration*, 200(4):401–418, 1997.

[19] M. Abè and T. Igusa. Semi-active dynamic vibration absorbers for controlling transient response. *Journal of Sound and Vibration*, 198(5):547–569, 1996.

[20] J.P. Maillard C.R. Fuller and A.H. von Flotow. Control of aircraft interior noise using globally mis-tuned vibration absorbers. In Proceedings of the First Joint CEAS/AIAA Aeroacoustics Conference, editor, *AIAA paper 85-0879*, Germany, 1995.

[21] K. Nagaya and L. Li. Control of sound noise radiated from a plate using dynamic absorbers under the optimization by neural network. *Journal of Sound and Vibration*, 208(2):289–298, 1997.

[22] C.R. Fuller P. Marcotte and P. Cambou. Control of the noise radiated by a plate using a distributed active vibration absorber (dava). In Proceeding of Active 99, editor, *Active 99*, pages 447–456, Fort Lauderdale, FL, 1999.

[23] C.R. Fuller P. Marcotte and M.E. Johnson. Numerical modelling of a distributed active vibration absorbers (dava) for control of noise radiated by a plate. In Proceeding of Active 2002, editor, *Active 2002*, pages 535–546, ISVR, Southampton, UK, July 2002.

[24] J.D. Powell G.F. Franklin and A. Emami-Naeini. *Feedback Control of Dynamic Systems*. Addison–Wesley, Reading, MA, third edition, 1994.

[25] S. Elliott. *Signal Processing for Active Control*. Academic Press, San Diego, first edition, 2001.

[26] J.D. Powell G.F. Franklin and M.L. Workman. *Digital Control of Dynamic Systems*. Addison–Wesley, Reading, MA, second edition, 1992.

[27] John G. Proakis and Dimitrius G. Manolakis. *Digital Signal Processing, Principles, Algorithms, and Applications*. Prentice Hall, Upper Sadle River, New Jersey, third edition, 1996.

[28] P.A. Nelson and S.J. Elliot. *Active Control of Sound*. Academic Press, London, first edition, 1995.

[29] S.J. Elliot B. Rafaely and J. Garcia-Bonito. Broadband performance of an active headrest. *Journal of the Acoustical Society of America*, 106(2):787–793, August 1999.

[30] S.J. Elliot P. Joseph and P.A. Nelson. Near field zones of quiet. *Journal of Sound and Vibration*, 172(5):605–627, 1994.

[31] C. Kestell and C.H. Hansen. Active noise control with virtual sensors in a long narrow duct. *International Journal of Acoustics and Vibration*, 5(2), Accepted April 2000.

[32] C. Kestell and C.H. Hansen. Virtual sensors in active noise control. *Journal of Acoustics*, September Accepted September 2000.

[33] X. Qiu A. Berry and C.H. Hansen. Near–field sensing strategies for the active control of the sound radiated from a plate. *The Journal of Acoustic Society of America*, 106(6):3394–3406, December 1999.

[34] S.J. Elliott and M.E. Johnson. Radiation modes and the active control of sound power. *Journal of the Acoustical Society of America*, 94(4):2194–2204, October 1993.

[35] Z. Li C. Guigou and C.R. Fuller. The relationship between volume velocity and far–field radiated pressure of a planar structure. *Journal of Sound and Vibration*, 1996.

[36] M.E. Johnson and S.J. Elliott. Active control of sound radiation using volume velocity cancellation. *Journal of the Acoustical Society of America*, 98(4):2174–2186, October 1995.

[37] P. Gardonio C. Maury and S.J. Elliott. Model for active control of flow-induced noise transmitted through double partitions. *AIAA Journal*, 40(4):1113–1121, 2002.

[38] P. Gardonio C. Maury and S.J. Elliott. Active control of flow-induced noise transmitted through a panel. *AIAA Journal*, 39(10):1860–1867, 2001.

[39] G. Cousin. Sound from tbl-induced vibration. *AIAA Journal*, 2216, June 1998.

[40] C.K. Barton and J.S. Mixson. Noise transmission and control for a light twin-engined aircraft. *Journal of Aircraft*, 18(7):570–575, 1981.

[41] J.S. Mixson and J.F. Wilby. Aeroacoustics of flight vehicles, theory and practice. *NASA Reference Publication 1258*, pages 271–335, 1995.

[42] K.W. Eure G.P. Gibbs and J.W. Lloyd. Active control of turbulent boundary layer induced sound radiation from aircraft style panels. In *Proceedings of Active-99*, Ft. Lauderdale, FL, December 1999. Technomic Press, Lancaster, PA.

[43] J. Juang G.P. Gibbs, R.H. Cabell. Controller complexity for active control of tbl induced sound radiation from panels. In *6th AIAA/CEAS Aeroacoustics Conference*, volume AIAA 2000-2043, Lahaina, HI, June 2000. Technomic Press, Lancaster, PA.

[44] G.P. Gibbs and R.H. Cabell. Active control of turbulent boundary layer induced sound radiation from multiple aircraft panels. *AIAA Paper*, 2496, 2002.

[45] A.B. Coppens L.E. Kinsler, A.R. Frey and J.V. Sanders. *Control of Aircraft Interior Noise Using Globally Detuned Vibration Absorbers*. John Wiley and Sons, New York, NY, third edition, 1982.

[46] K. Uchino. *Materials Science and Technology*. Number 12. VCH Publishers, Inc., 1994.

[47] G.C. Tibbets. Transducer having piezoelectric film arranged with alternating curvatures. *U.S. Patent #4056742*, November 1977.

[48] J. Pan C. Guigou, C.A. Gentry and C.R. Fuller. Active control of sound with foam-pvdf composite material. *Journal of Canadian Acoustics*, 23(3):105–106, September 1995.

[49] E.R. Green. *An Examiniation of Smart Foams for Active Noise Control*. PhD thesis, Purdue University, West Lafayette, IN, 1995.

[50] J.S. Bolton and E.R. Green. Smart foams for active absorption of sound. In *Second Conference on Recent Advances in Active Control of Sound and Vibration*, pages 139–149, Blacksburg, VA, 1993. Technomic Press, Lancaster, PA.

[51] C.A. Gentry C.R. Fuller, M.J. Bronzel and D.E. Whittington. Control of sound radiation/reflection with adaptive foams. In *Noise-Con 94*, pages 429–436, Fort Lauderdale, FL, 1994.

[52] B.D. Johnson and C.R. Fuller. Broadband control of plate radiation using a piezoelectric, double amplifier active skin and radiation senssing. *Journal of the Acoustic Society of America*, 107(2):876–884, 2000.

[53] and C.R. Fuller C.A. Gentry, C. Guigou. Smart foam for applications in passive-acitive noise radiation control. *Journal of the Acoustical Society of America*, 101(4):1771–1778, April 1997.

[54] C. Guigou and C.R. Fuller. Foam-pvdf smart skin for aircraft interior sound control. In *Proceedings of the SPIE's 4th Symposium on Smart Structures and Materials*, San Diego, CA, March 1997.

[55] C. Guigou C.R. Fuller and B.D. Johnson. Control of sound radiation from structures using active skins. In *Submitted to the Proceedings of the 1st Ibroamericano de Acoustica*, pages 186–197, Florianopolis, SC, Brasil, April 1998.

[56] C. Guigou and C.R. Fuller. Foam-pvdf smart skin for aircraft interior sound control. In *SPIE's 4th annual Symposium on Smart Structures and Materials*, San Diego, CA, March 1997.

[57] C. Guigou and C.R. Fuller. Control of aircraft broadband interior noise with foam-pvdf smart skin. *Journal of Sound and Vibration*, 220(3):541–557, 1999.

[58] J.R. Griffin. The control of interior cabin noise due to a turbulent boundary layer noise excitation using smart foam elements. Master's thesis, Virginia Polytechnic Institute and State University, Department of Mechanical Engineering, Vibration and Acoustics Lab, 1999.

[59] A.J. Raudkivi and R.A. Callander. *Advanced Fluid Mechanics, An Introduction*. Wiley, New York, first edition, 1975.

[60] Alan Mironer. *Engineering Fluid Mechanics*. McGraw–Hill, New York, first edition, 1994.

[61] Frank M. White. *Fluid Mechanics*. McGraw–Hill, New York, third edition, 1994.

[62] Ejup N. Ganic and Tyler G. Hicks. *Engineering Companion*. McGraw–Hill, New York, 2003.

[63] Richard J. Gross Philip M. Gerhart and John I. Hochstein. *Fundamentals of Fluid Mechanics*. Addison-Wesley Publishing Company, Reading, Massachusetts, second edition, 1992.

[64] J.S. Bendat and A.G. Piersol. *Random Data Analysis and Measurement Procedures*. Wiley–Interscience, New York, second edition, 1986.

[65] Steven W. Smith. *The Scientist and Engineer's Guide to Digital Signal Processing*. California Technical Publishing, San Diego, California, second edition, 1998.

[66] Tuncer Cebici and A. M. O. Smith. *Analysis of Turbulent Boundary Layers*. Academic Press, New York, first edition, 1974.

[67] Frank Fahy. *Sound and Structural Vibration: Radiation, Transmission and Response*. Academic Press, London, first edition, 1998.

[68] S.J. Elliot C.R. Fuller and P.A. Nelson. *Active Control of Vibration*. Academic Press, London, first edition, 1996.

[69] L. Cremer and M. Heckl. *Structure–Borne Sound*. Springer–Verlag, Berlin, second, translated e.e. ungar edition, 1988.

[70] J. Juang. *Applied System Identification*. Prentice Hall, Englewood Cliffs, NJ, first edition, 1994.

[71] Daniel Zwillinger. *CRC Standard Mathematical Tables and Formulae*. CRC Press, New York, NY, thirtieth edition, 1996.

[72] Erwin Kreyszig. *Advanced Engineering Mathematics*. John Wiley and Sons, New York, NY, seventh edition, 1993.

[73] D.W. Miller S.A. Collins and A.H. von Flotow. Distributed sensors as spatial filters in active structural control. *Journal of Sound and Vibration*, 173(4):471–504, 1994.

[74] M.R.F. Kidner and M.E. Johnson. 2d shaped sensors for feedback control. In *The 2001 International Congress and Exhibition on Noise Control Engineering*, The Hague, Holland, August 2001.

[75] Y. Lin M. R. Bai and J. Lai. Reduction of electronic delay in active noise control systems–a multirate signal processing approach. *The Journal of Acoustic Society of America*, 111(2):916–924, February 2001.

[76] J.S. Vipperman R.A. Burdisso and C.R. Fuller. Causality analysis of feedforward-controlled systems with broadband inputs. *Journal of the Acoustical Society of America*, 94(1):234–242, July 1993.

[77] S.J. Elliot P.A. Nelson T.J, Sutton and L. Moore. Active control of multiple–source random sound in enclosures. In *Proceedings of the Institute of Acoustics*, volume 12, pages 689–693, 1990.

[78] Chris Park. lmsfilterx.exe. Feed Forward, Filtered-X, LMS Control Simulation Software.

Vita

John Patrick D'Angelo was born on February 27, 1973 in Cambridge, Massachusetts to Arlene and Giovanni D'Angelo and has a sister, Laura. John currently resides just north of Boston in Medford, Massachusetts.

Dr. D'Angelo studied mechanical drawing at Medford Vocational Technical High School where he graduated top in his class. He later attended University of Massachusetts Lowell where he achieved a Bachelor of Science and Master of Science in Mechanical Engineering in 1996 and 1998, respectively. Research for his Master of Science degree was funded by NASA—Goddard Space Flight Center and regarded the active isolation of very low frequency vibration.

Engineering work experience began as a Junior in high school where he worked in the Consumer Products Division of Polaroid Corporation in Cambridge and Norwood, Massachusetts. He interned at Polaroid as a computer aided draftsman and later as an engineering intern until completing his Bachelor of Science degree. Dr. D'Angelo later interned at IDEO Product Development in Lexington, Massachusetts. Prior to finishing his Doctorate, he worked from his Medford, Massachustts home for his former Master of Science advisor at MERLAB, P.C. and later as a contractor at DRS Electric Power Technologies in Hudson, Massachusetts.

Dr. D'Angelo is currently a Technical Staff Member at MIT / Lincoln Laboratory in Lexington, Massachusetts. He also performs consultation in the fields of vibration, acoustics and mechanical design through his company, Coherence One, which he founded in 2003.